

2017

Nanoporous materials chemistry: From gas separation to high pressure chemistry

Cong Liu
Lehigh University

Follow this and additional works at: <http://preserve.lehigh.edu/etd>

 Part of the [Chemistry Commons](#)

Recommended Citation

Liu, Cong, "Nanoporous materials chemistry: From gas separation to high pressure chemistry" (2017). *Theses and Dissertations*. 2692.
<http://preserve.lehigh.edu/etd/2692>

This Dissertation is brought to you for free and open access by Lehigh Preserve. It has been accepted for inclusion in Theses and Dissertations by an authorized administrator of Lehigh Preserve. For more information, please contact preserve@lehigh.edu.

Nanoporous materials chemistry: From gas separation to high pressure chemistry

by

Cong Liu

A Dissertation

Presented to the Graduate and Research Committee

of Lehigh University

in Candidacy for the Degree of

Doctor of Philosophy

in

Chemistry

Lehigh University

Jan 2017

© 2016 Copyright
Cong Liu

Approved and recommended for acceptance as a dissertation in partial fulfillment of the requirements for the degree of Doctor of Philosophy

Cong Liu

Nanoporous materials chemistry: From gas separation to high pressure chemistry

Defense Date

Approved Date

Dissertation Director
Dr. Kai Landskron

Committee Members:

Dr. Dmitri Vezenov

Dr. Xiaoji Xu

Dr. Bruce Koel

TABLE OF CONTENTS

LIST OF FIGURES	viii
LIST OF TABLES	xiii
ABSTRACT	1
1 Introduction to nanoporous materials.....	3
1.1 Background on nanoporous materials	3
1.2 Overview about synthesis of mesoporous materials	6
1.2.1 Synthesis of periodic mesostructures using the soft-templating route	6
1.2.2 Hard templated synthesis of ordered mesoporous materials	13
1.2.3 Synthesis of disordered porous carbon materials	16
1.3 Common applications for nanoporous materials	22
1.3.1 The application of mesoporous material in catalysts	22
1.3.2 Application of mesoporous material in drug delivery.....	25
1.3.3 Nanoporous materials for energy storage applications	26
1.3.4 Nanoporous materials for high pressure chemistry.....	27
1.4 References:	28
2 Characterization techniques for nanoporous materials and electrochemical measurements.....	31
2.1 Transmission Electron Microscopy.....	31
2.2 Scanning electron microscopy.....	35
2.3 Powder X-ray scattering.....	37
2.4 Small angle X-ray scattering techniques	39
2.5 Gas adsorption techniques.....	41
2.6 Electrochemical measurement methods	50
2.6.1 Cyclic voltammetry.....	52
2.6.2 Galvanostatic charge/discharge measurements	55
2.7 References.....	58
3 Carbon dioxide capture and concept of Supercapacitive Swing Adsorption.....	59
3.1 Global warming caused by carbon dioxide.....	59
3.2 Carbon capture and sequestration techniques	62

3.2.1	Oxy fuel combustion	63
3.2.2	Pre-combustion CO ₂ capture	63
3.2.3	Post-combustion CO ₂ capture	64
3.2.4	Disadvantages of current carbon capture techniques.....	76
3.3	Concept of supercapacitors	79
	Fig 3-13. Electric flux and Guass' Law. Source: [4].....	80
3.4	Concept of supercapacitive swing adsorption (SSA)	87
3.4.1	Electric field swing adsorption	87
3.4.2	Supercapacitive swing adsorption.....	89
3.5	References.....	91
4	Supercapacitive swing adsorption: Experimental results	94
4.1	Static mode SSA experiments with ionic liquid as electrolyte	94
4.1.1	Apparatus and experimental setup.....	94
4.1.2	SSA experiment with radial type supercapacitor	96
4.1.3	SSA experiments with asymmetrical electrode configurations	99
4.2	Static mode SSA experiments with aqueous electrolyte.....	103
4.2.1	SSA experiment with carbon monoliths.....	103
4.3	SSA experiments in flow-through mode	115
4.3.1	Background and experimental setup.....	115
4.3.2	Experimental results	121
4.4	Possible SSA mechanism and optimizations	136
4.5	References:	138
5	High pressure chemistry of nanoporous materials.....	139
5.1	Introduction to the high pressure chemistry of mesoporous materials.....	139
5.2	Introduction to high-pressure apparatus.....	142
5.3	Synthesis of high-pressure phases from mesoporous precursors	146
5.3.1	Synthesis of stishovite nanocrystals from mesoporous silica	146
5.3.2	Synthesis of mesoporous coesite form mesoporous silica	151
5.3.3	Synthesis of nanopolycrystalline diamond from mesoporous carbon.....	156

5.4	Synthesis of high pressure phase with periodic mesostructures via nanocasting at high pressure	158
5.4.1	Synthesis of periodic mesoporous coesite	159
5.4.2	Synthesis of periodic mesoporous quartz.....	162
5.5	Summary.....	167
5.6	References.....	169
6	Synthesis of cubic BN from nanoporous precursors	171
6.1	Introduction to boron nitride materials.....	171
6.2	Experimental setup and procedures:.....	173
6.2.1	Synthesis of C-ORNL-1 mesoporous carbon template.....	174
6.2.2	Synthesis of mesoporous carbon / borazane composite	174
6.2.3	Removal of the carbon template	175
6.2.4	HPHT experiments.....	175
6.3	Product characterization and analysis:.....	175
6.3.1	Characterization of the mesoporous carbon template C-ORNL-1	177
6.3.2	Characterization of mC/mBN composite	179
6.3.3	Characterization of mesoporous boron nitride precursor	181
6.3.4	Single-crystalline mBN nanoparticles obtained at 14 GPa and 1300 °C	182
6.3.5	Nanopolycrystalline cBN obtained at 10 GPa and 1000 °C.....	185
6.3.6	Mesoporous boron nitride treated at 8 GPa and 1000 °C	190
6.4	Discussion and conclusion:.....	192
6.5	References.....	195
7	Synthesis of diamond nanowires by nanocasting at high pressure with a hard template	197
7.1	Introduction and background	197
7.2	Materials and experimental procedures.....	202
7.3	Product characterization and analysis.....	206
7.3.1	Treatment of sample at 14GPa and 1300°C.....	206
7.3.2	Treatment of composite at 14 GPa and 1600 °C.....	207
7.4	Discussion and conclusions:	210

7.5	Reference.....	213
	VITA.....	215

LIST OF FIGURES

Fig 1-1. Selected zeolite structures. From top to bottom: zeolite X and Y, ZSM-12, ZSM-5, ZSM-22. Ref[14].....	4
Fig 1-2. Bronsted and Lewis acid sites on zeolites. Ref[12]	5
Fig 1-3. CTAB templated synthesis of mesoporous carbon. Ref [1]	8
Fig 1-4. Structural illustration of tri-block copolymer	8
Fig 1-5. Preparation of mesoporous carbon with triblock copolymer and resin. Ref[13] ..	9
Fig 1-6. Phase diagram of CTAB in water. Ref[4]	10
Fig 1-7. Schematic drawing of surfactant-precursor interaction models. Ref[9]	13
Fig 1-8. Top: casting concept at macroscale, Bottom: casting concept at nanoscale. Ref[3]	15
Fig 1-9. Pore size distribution of nanoporous carbon prepared from TEOS and FA. Ref[8]	17
Fig 1-10. Nitrogen adsorption isotherm and pore size distribution of mesoporous carbon prepared from cyclodextrin and TMOS. Ref[7]	18
Fig 1-11. Typical physical activation apparatus 1) Nitrogen gas feed; 2) flask heater; 3) water saturator; 4) tube furnace; 5) reaction chamber; 6) sample; 7) liquid waste collector; 8) furnace thermocouple; 9) sample thermocouple 10) temperature monitor; 11) temperature controller. Ref[15].....	19
Fig 1-12. Carbon lattice expansion from metallic potassium. Ref[11].....	21
Fig 1-13. Schematic illustration of hierarchical pore structure of activated carbon. Ref[10]	22
Fig 1-14. Catalytic cycle on solid mesoporous surface. Ref[2]	23
Fig 1-15. Cu complex grafted MCM-41 for epoxidation of hydrocarbon molecules. Ref[6].....	24
Fig 1-16. Top: Functionalization of silica pore wall, Bottom: Drug loading. Ref[5].....	26
Fig 2-1. Structural illustration of TEM compared with light microscope. Ref[4]	34
Fig 2-2. Structure illustration of SEM. Ref[6].....	36
Fig 2-3. Electron-specimen interaction of SEM.....	37
Fig 2-4. Principle of X-ray diffraction. Ref [2].....	38
Fig 2-5. Bragg's law illustration. Ref[3]	39
Fig 2-6. Lattice parameter d_k of MCM-41 and SBA-15. Ref[5].....	40
Fig 2-7. Type of isotherms.....	43
Fig 2-8. Parameters of Kelvin equation.....	45
Fig 2-9. Ink-bottle pore model.....	46
Fig 2-10. Langmiur plot. Ref[7]	47
Fig 2-11. Structure of potentiostat. Ref[1].....	50
Fig 2-12. 2-electrode setup and 3-electrode setup.....	51

Fig 2-13. Theoretical CV graph of an ideal EDLC with 3 Farads capacitance. Ref[1]	52
Fig 2-14. CV curve of Nesscap ESHSR-0003C0-002R7. Ref[1].....	54
Fig 2-15. Ideal cyclic charge discharge for an EDLC. Ref[1].....	55
Fig 2-16. Cyclic charge discharge curve of damaged EDLC. Ref[1].....	56
Fig 3-1. The rise of atmospheric CO ₂ concentration since industrial revolution. Source: [5]	59
Fig 3-2. Global average temperature trend. Source:[5]	60
Fig 3-3. Worldwide demand for power. Source:[3]	61
Fig 3-4. Overview of CCS techniques. Ref[15].....	62
Fig 3-5. Post-combustion CO ₂ capture techniques. Source:[8].....	64
Fig 3-6. Common amine species for CO ₂ absorption. Ref[16].....	66
Fig 3-7. Membrane-based CO ₂ separation. Source: [1]	69
Fig 3-8. Working capacity for PSA. Ref[9]	72
Fig 3-9. Typical PSA operating cycle. Ref[10].....	73
Fig 3-10. Working capacity for TSA. Image source: [6].....	74
Fig 3-11. Combined TSA and PSA cycle. [14].....	76
Fig 3-12. Parallel plate capacitor. Ref[11]	80
Fig 3-13. Electric flux and Gauss' Law. Source: [4].....	80
Fig 3-14. Electric fields between plates. Source:[2]	81
Fig 3-15. Charge and discharge cycle of EDLC. Source:[7].....	83
Fig 3-16. Ragone chart of energy storage systems. Ref[12].....	85
Fig 3-17. Cell design for EFSA. Image: Dr. David Moore, Nina Jarrah	88
Fig 4-1. EDLC in radial configuration. Source: [1]	94
Fig 4-2. Molecular structure of EMIM FAP ionic liquid.....	95
Fig 4-3 Schematic Illustration of the glass cell fabricated or testing SSA effect.....	96
Fig 4-4. SSA experiment with CO ₂ , each point is taken in 1 min. Red dots: charging cycle, black dots: discharging cycle. Green line: Temperature.....	98
Fig 4-5. SSA experiment with Helium, each point is taken in 1 min. Red dots: Bias on, black dots: bias off.:Green line: Temperature	99
Fig 4-6. SSA experiment cell with asymmetrical electrode setup.	100
Fig 4-7. SSA experiment with asymmetrical electrode configuration. Black: discharged state, red: charged state	101
Fig 4-8. Left: Styrofoam housing for SSA experiments, right: 2L tempered beaker.....	104
Fig 4-9. N ₂ adsorption isotherm of BPL carbon. (inset: pore size distribution)	106
Fig 4-10. Modified SSA cell setup.	107
Fig 4-11. SSA experiments with BPL carbon monolith. Red: charged state, black: discharged state.	108
Fig 4-12. Top: SSA experiment repeated 100 cycles (only 50 shown for clarity) Red: charged state, Blue: Discharged state	109

Fig 4-13. Left: Following SSA experiment repeated 20 cycles. Red: charged state, Blue: Discharged state.....	110
Fig 4-14. Cyclic voltammetry with 3.7 g BPL electrodes and 1 mV/s scanning rate	113
Fig 4-15. Charge/Discharge curve of 3.7 g BPL monolith electrodes with 5 mA from 0 V to 1 V.....	114
Fig 4-16. Construction of SSA gas separation device, cross-sectional view. 1. Valve, 2. Aluminum block. 3. Graphite plate with gas diffusion channels. 4. Carbon cloth. 5. Top electrode. 6. Separator. 7. Bottom electrode.....	116
Fig 4-17. Gas channel of the top graphite plate.....	119
Fig 4-18. SSA experiment with electrodes having a 0.0487 g mass. Red: Charged state, black: discharged state.....	123
Fig 4-19. Gas separation device with pressure transducer removed. 1: Aluminum block. 2. Graphite plate with gas diffusion channels. 3. Carbon cloth. 4. Exposed electrode. 5. Separator. 6. Submerged electrode.....	125
Fig 4-20. CO ₂ breakthrough curve of 0.197g electrode.....	127
Fig 4-21. Carbon dioxide breakthrough without SSA.....	129
Fig 4-22. Breakthrough curve with 0.1 cc/min mixture flow.....	130
Fig 4-23. 2nd adsorption cycle with 0.1 cc/min gas flow.....	132
Fig 4-24. CV curve of the thin film electrodes with 1 mV/s scanning rate.....	134
Fig 4-25. Charge/discharge curve for thin film carbon electrodes with a constant current of 1mA.....	135
Fig 5-1. Structures of mesoporous silica: a) hexagonal, b) gyroid, c) lamellar	140
Fig 5-2. Left: Piston-cylinder press. Right: Diamond anvil cell. Ref[1].....	143
Fig 5-3. Sample assembly in a multi-anvil apparatus. Ref[3].....	144
Fig 5-4. Illustration of multi-anvil assembly. Ref[2].....	144
Fig 5-5. Multi-anvil press at Geophysical Labs	145
Fig 5-6. Crystal structure of Stishovite. Grey: Silicon, Red: oxygen.....	146
Fig 5-7. Images of stishovite nanoparticles. Left: SEM, Right: TEM.....	147
Fig 5-8. XRD spectra of stishovite nanocrystals.....	147
Fig 5-9. XRD of stishovite nanocrystals from KIT-6.....	148
Fig 5-10. SEM(left) and TEM (right) of stishovite nanocrystals from KIT-6.....	149
Fig 5-11. TEM(left) and SEM(right) of coesite from SBA-15.....	149
Fig 5-12. XRD spectra of coesite from SBA-15.....	150
Fig 5-13. Phase diagram of silicon dioxide.....	151
Fig 5-14. SEM images of mesoporous coesite nanocrystals	152
Fig 5-15. TEM (a-c) and SAED (d) of mesoporous coesite nanocrystals.....	152
Fig 5-16. Depth sectioned TEM image (a) and pore size distribution of coesite nanocrystals	153

Fig 5-17. TEM (left) and XRD (right) experiment of SBA-16 treated under 12 GPa and 200 °C.	154
Fig 5-18. Pore collapse and reformation mechanism.....	155
Fig 5-19. Microscopy(A) and XRD (B) of diamond nanocrystals from CMK-8.....	156
Fig 5-20. TEM (A), SAED (B) and SEM (E) of mesoporous diamond nanocrystals.....	157
Fig 5-21. Nanocasting at high pressure.....	159
Fig 5-22. SAXS(A), XRD(B), TEM with FFT inset(C) and SAED(D) of ordered mesoporous coesite.....	160
Fig 5-23. Nitrogen adsorption isotherm of mesoporous coesite(inset: pore size distribution).....	161
Fig 5-24. TEM (a) and SEM (b,c) of mesoporous quartz produced at 4 GPa.....	162
Fig 5-25. SAXS(a) and XRD(b) of mesoporous quartz.....	163
Fig 5-26. Nitrogen adsorption isotherm of mesoporous quartz (inset: pore size distribution).....	163
Fig 5-27. Nitrogen isotherm of mesoporous quartz produced under 2 GPa.....	164
Fig 5-28. TEM (top left and right) and SEM of mesoporous quartz produced at 2 GPa.....	165
Fig 5-29. XRD products produced at 2 GPa(left) and 1 GPa(right).....	165
Fig 5-30. SEM(left) and TEM(right) of quartz obtained at 2 GPa after hydrothermal treatment.....	166
Fig 6-1. Phase transition schematics. Top: from graphite to diamond, Bottom: from hBN to cBN (white: boron, black: nitrogen). Ref[3]	172
Fig 6-2. Removal of carbon by ammonia etching	175
Fig 6-3. TEM images of the mesoporous carbon template with FFT inset.....	178
Fig 6-4. SEM of mesoporous carbon template.....	178
Fig 6-5. Nitrogen adsorption isotherm of mesoporous carbon template. (Inset: pore size distribution).....	179
Fig 6-6. TEM image of mC/mBN nanocomposite.....	180
Fig 6-7. Nitrogen adsorption isotherm of mC/mBN composite	180
Fig 6-8. TEM image of mBN precursor.....	181
Fig 6-9. Nitrogen adsorption isotherm for mBN precursor. (Inset: pore size distribution)	182
Fig 6-10. XRD of mBN treated at 14 GPa and 1300 °C.....	183
Fig 6-11. TEM of mBN treated at 14 GPa and 1300 °C (inset: SAED).	183
Fig 6-12. SEM of mBN treated at 14 GPa and 1300 °C.....	184
Fig 6-13 DLS particle size of cBN obtained at 14 GPa and 1300 °C.....	185
Fig 6-14. TEM images of mBN treated at 10 GPa and 1000 °C	186
Fig 6-15. SEM image of mBN treated at 10 GPa and 1000 °C	186
Fig 6-16. XRD spectra of mBN treated at 10 GPa and 1000 °C	187
Fig 6-17. DLS CONTIN of mBN treated at 10 GPa and 1000 °C.....	187

Fig 6-18. Nitrogen adsorption isotherm of mBN treated at 10 GPa and 1000 °C.....	188
Fig 6-19. The principle of 3D TEM by tilting. Ref[1]	189
Fig 6-20. One slice from 3D TEM images. (No scale bar shown).....	189
Fig 6-21. Pore size distribution of mBN treated at 10 GPa and 1000 °C	190
Fig 6-22. TEM (left) and SEM (right) of mBN treated at 8 GPa and 1000 °C	191
Fig 6-23. XRD of mBN treated at 8 GPa and 1000 °C	191
Fig 6-24. DLS CONTIN analysis of mBN treated at 8 GPa and 1000 °C	192
Fig 7-1. Low-dimensional sp ² carbon structure. Fullerene (a), carbon nanotube (b), graphene (c). Ref[5].....	197
Fig 7-2. One dimensional sp ³ carbon structure, blue: carbon, white: hydrogen. Ref[1].	198
Fig 7-3. Production of diamond nanowire by masked etching. Ref[4]	199
Fig 7-4. Mask deposition of diamond nanowires. Left: scheme, right: SEM image. Ref[3]	200
Fig 7-5. Proposed synthetic scheme for 1D diamond nanostructures.	201
Fig 7-6. The Double-Pass AAO Templates obtained from ACS materials.....	202
Fig 7-7. SEM image of top (left) and cross-sectional (right) view of ACSAAO50 template.	203
Fig 7-8. SEM image of AAO/C composite.....	204
Fig 7-9. N ₂ adsorption isotherm of the AAO template before and after the infiltration of mesophase pitch.	204
Fig 7-10. XRD of AAO/C composite before HPHT. The diffraction peaks correspond to alpha-alumina (PDF 46-1212).	205
Fig 7-11. AAO/C composite after heat treatment at 1300 °C.	205
Fig 7-12. AAO/C composite after 14 GPa and 1300 °C.	207
Fig 7-13. XRD of the AAO/diamond composite. D refers to diamond, Pt refers to Platinum, all other peaks can be assigned to alpha alumina (PDF 46-1212).....	208
Fig 7-14. Raman spectra of AAO/Diamond after HPHT.....	208
Fig 7-15. SEM of AAO/Diamond composite.....	209
Fig 7-16. SEM image of AAO/Diamond after etching.....	210
Fig 7-17. Carbon phase diagram. Source: [2].....	211

LIST OF TABLES

Table 1-1. Geometrical relationships for spherical, cylindrical and lamellar micelles	11
Table 2-1. Kinetic diameters of gas molecules.....	42
Table 3-1. Physical and chemical properties of sorbents. Ref[16].....	67
Table 3-2. Comparison of different CCS techniques	78
Table 4-1. Change in gas compositions during SSA experiment with 3.7 g and 7.5 g electrodes.....	112
Table 4-2 List of materials for the gas separation device assembly.....	118
Table 4-3. CO ₂ composition after each charge and discharge cycle.....	124
Table 4-4. CO ₂ concentration in the effluent gas at vs time.	126
Table 4-5. CO ₂ concentration in effluent gas without SSA effect.	128
Table 4-6. CO ₂ breakthrough data from experiment without applied voltage.....	129
Table 4-7. CO ₂ concentration in the desorption cycle.	131
Table 4-8. CO ₂ concentration in 2 nd desorption cycle.....	132
Table 5-1. Comparison of bulk precursor and nanoporous precursor for HPHT synthesis.	167

ABSTRACT

Nanoporous materials are classified into three categories according to the pore sizes: microporous (< 2 nm), mesoporous (2 – 50 nm), and macropores (> 50 nm). Due to their large surface to volume ratio and tunable pore size, nanoporous materials has gained significant research attention in recent years and has been used in many applications such as adsorbent, gas separation, catalysts, supercapacitors, drug delivery and so on.

In this thesis, two aspects of nanoporous material application will be discussed. In the first part, a concept called capacitive Swing Adsorption (SSA) for carbon dioxide separation will be introduced. Unlike Pressure Swing Adsorption (PSA) and Temperature Swing Adsorption (TSA), SSA works at ambient conditions and utilizes charging and discharging of nanoporous carbon materials to alter the adsorption and desorption behaviors. In this thesis, an inexpensive gas separation device is built on top of the SSA concept. It is demonstrated that the device can reversibly capture and release CO₂ from a flow of 15 % CO₂ and 85 % N₂ gas mixture with an energy efficiency on par with current CO₂ capture techniques. With further optimizations, SSA will be promising concept for the next generation carbon dioxide capture technology.

Nanoporous can be also used as unique starting materials for high-pressure material synthesis. To obtain high-pressure phases of materials, usually high-temperature high-pressure (HTHP), experiments are performed. Porous materials exhibit higher reactivity than their bulk counterparts during HTHP, thus reducing the pressure and temperature required to obtain a high pressure phase. Furthermore, the tunability of pore structures gives the potential to control the crystal size and morphology. The second part of the thesis will introduce a synthetic pathway to obtain two forms cubic boron nitride (cBN) materials: nanopolycrystalline cBN and single-

crystalline cBN nanoparticles. In addition, it is also demonstrated that diamond nanowires can be obtained with the aid of a nanoporous alumina template.

1 Introduction to nanoporous materials

1.1 Background on nanoporous materials

The development of human history has always been accompanied with advancements in chemistry and materials science. Take porous materials for example, its earliest documented application appeared in 1500 BC, when the Egyptians used charcoal to eliminate odorous smell from infected human wounds. As early as 450 BC, the Hindu and Phoenicia people found that charcoal is useful for purifying drinking water, which is possible due to the porosity of carbon materials. Even though the ancient people were only able to find limited applications of porous materials without understanding the mechanism how they worked, it is undoubted that porous materials have shown crucial importance in many aspects. With the technological advancements today, we are able to scientifically understand porous materials and tailor them at the nanoscale to meet our demands.

According to the International Union of Pure and Applied Chemistry (IUPAC), nanoporous materials can be classified into three categories: microporous (pore size up to 2 nm), mesoporous (pore size between 2 and 50 nm, *meso-* is the Greek for “in between”), and macroporous (pore size larger than 50 nm). The development of nanoporous materials originates from the study of zeolite materials. Zeolite is a family of materials microporous crystalline aluminosilicates first discovered by Swedish mineralogist and chemist Axel Cronstedt in 1756 when he heated an unknown silicate mineral and found the evolution of bubbles and gas steam. The mineral was then later named to zeolite, a Greek name for “bubbling stone”. The modern study of zeolite dates back to 1932 when McBain found that chabazite, a zeolite mineral was able to adsorb molecules that are smaller than 5 angstroms[16]. The subsequent scientific research found that chabazite

can effectively separate nitrogen and oxygen. Later on, Breck and co-workers had produced a series of zeolites[17], including zeolite A, zeolite X and zeolite Y and enabled the mass production of zeolites for separation and purification applications. With the development of modern characterization techniques such as X-ray diffractometers, scientists were able to determine the structure of zeolites by diffraction. The basic building blocks for zeolites are SiO_4 and AlO_4 tetrahedrons. These building blocks are bridged by oxygen atoms to create porous three-dimensional frameworks. Since zeolites can pass/block molecules by their size, they are often referred as “molecular sieves”.

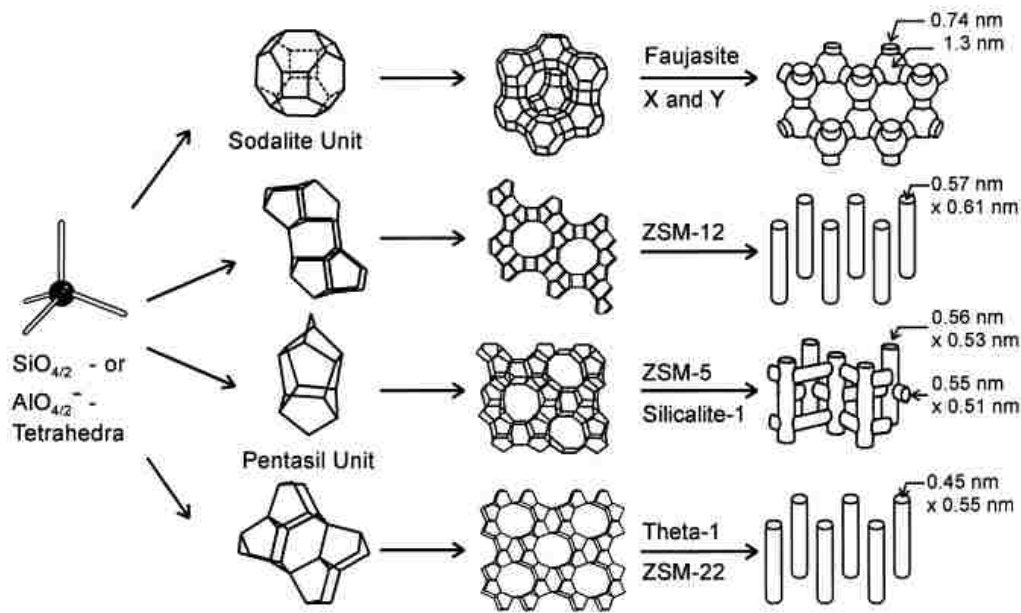


Fig 1-1. Selected zeolite structures. From top to bottom: zeolite X and Y, ZSM-12, ZSM-5, ZSM-22. Ref[14]

Due to the charge imbalance in the AlO_4 , there are counter ions in the pores to maintain neutrality. The counter ions can be alkali metal, alkaline earth metal, or ammonium, which make zeolites useful in ion exchange applications. If the cation is H^+ , then zeolite can act as Bronsted acid (proton donor), or the framework can be de-hydrolyzed to act as Lewis acid (electron donor). The acidity,

combined with stability, high activity, and size selectivity have enabled zeolites to be used as petroleum cracking catalysts over conventional liquid phase acids.

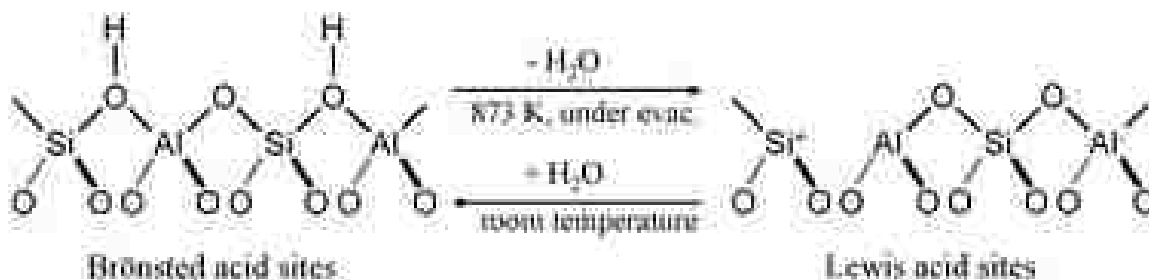


Fig 1-2. Brønsted and Lewis acid sites on zeolites. Ref[12]

Due to the nature of zeolite formation, most zeolites have pores smaller than 2 nm, which limits their abilities to process larger molecules. For example, the small pore diameter limits the diffusion and penetration of long-chain hydrocarbons. In order to go around this issue, Charles Kresge from Mobil Corporation Laboratories synthesized the MCM (Mobil Composition of Matter) family silica materials M41S with a highly periodic mesoporous structure in 1992[18]. The key for forming a mesoporous material is the combination of a sol-gel process and surfactant self-assembly. Depending on the synthesis conditions, the mesostructure can be hexagonal (MCM-41), cubic (MCM-48), or lamellar (MCM-50) and the pore size can range from 1.5 to 10 nm. Compared with zeolite materials, the MCM family materials have a highly ordered porous structure with significantly larger pore sizes. The original research paper by Kresge has triggered widespread studies about the synthesis application of mesoporous silica materials.

Another notable milestone on mesoporous material research is the synthesis of SBA (Santa Barbara Amorphous) family mesoporous silica by Galen Stucky, including SBA-15 (hexagonal), SBA-16 (cubic), SBA-1 (cubic) and etc[19]. Compared with M41S, SBA has larger pore sizes from 5 to 30nm and their pore channels are interconnected by micropores. Instead of using an ionic

surfactant in MCM synthesis, the SBA family used tri-block copolymer as pore-forming surfactants. With a similar route, the Zhao group was able to synthesize FDU (Fudan University) series mesoporous materials as well[20, 21].

In addition to silicate materials, researchers also attempted to produce three-dimensional structured carbon in addition to 0D (fullerene[22]), 1D (carbon nanotube[23]), 2D (few layer graphite, later graphene[24]) structured carbons. In 1999, Ryong Ryoo applied the concept of mold-casting to the nanoscale, using sucrose to infiltrate MCM-41 template and carbonizing the sucrose[25]. The template was then removed to obtain mesoporous carbon with a replicate structure of MCM-41. Later, the Dai group at Oak Ridge National Lab[26] and Zhao group[27] were able to make mesoporous porous carbon with tri-block copolymer surfactants as well. Tanaka et, al. was able to produce mesoporous carbon films using a spin coating with the concept of evaporation-induced self-assembly (EISA)[28, 29].

Since the work in this thesis primarily relates to mesoporous silica and carbon systems, only these types of porous material will be discussed in this chapter. However, a wide range of nanoporous materials with other chemical components has been made, such as mesoporous metal oxides[30], mesoporous polymers[31], and metal-organic frameworks[32, 33]. A handful of information can be found about these systems in the related literature[34-36].

1.2 Overview about synthesis of mesoporous materials

1.2.1 Synthesis of periodic mesostructures using the soft-templating route

Prior to the discovery of periodic mesoporous materials, mesoporous materials such as aerogels and pillared layer clay mostly showed disordered pore structure and broad pore size distribution, therefore there were attempts from both academia and industry to design and synthesize mesoporous materials with tailored mesostructure and uniform pore size distribution. The

breakthrough was made by Kresge and co-workers in 1992 produced M41S silica with cetyltrimethylammonium bromide (CTAB)[18]. Researchers then have proposed the formation mechanism of the mesostructure made by the soft-templated self-assembly route. By definition, self-assembly refers to the spontaneous organization of materials by non-covalent forces (for example, Van der Waals force, hydrogen bonding, electrostatic force etc.) without external aid[37, 38]. The templates in these scenarios are structures of organic molecules around which a material (usually inorganic) nucleates and grows in a skin-wrapping pattern, and upon template removal, the structure and geometry are replicated by the inorganic material. There are different thoughts about whether the formation of the mesostructure follows a cooperative assembly route (precursor and surfactant assemble together) or “true” liquid crystal template route (surfactant first pack into structures, then precursor fills the void), however, in both cases the surfactant plays a vital role in structure formation. To obtain a mesostructure with the soft-templating approach, there are four conditions to fulfill: 1) the soft template must be able self-assemble into nanostructures, 2) there has to be at least one precursor which can interact with the template to form a framework, 3) the template must not decompose before the precursor transform to a rigid structure 4) the ability for the precursor to form a highly crosslinked framework strong enough to support the porous structure without collapse[16].

In the case of M41S silica synthesis, depending on concentration, surfactant structure and temperature, CTAB surfactants in the solution form micelles, which further pack into hexagonal, cubic or lamellar structures to reduce free energy. The anionic silicate species interact with the hydrophilic cations of the surfactant (CTA⁺) by electrostatic force to form layers around the surfactant micelles. Upon condensing, the silica framework is then captured as a fossil of the

surfactant micelles. Then, through calcining, the surfactant is removed to leave an ordered mesoporous silica product.

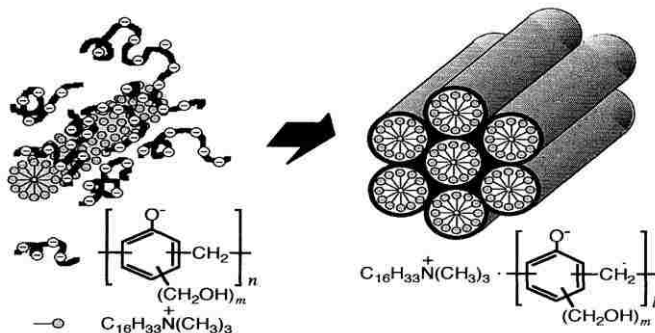


Fig 1-3. CTAB templated synthesis of mesoporous carbon. Ref [1]

In 1999, Moriguchi and co-workers extended the concept of liquid crystal templating to produce carbon materials with periodic mesoporous structure[1] (Fig 1-3). The carbon-yielding resol-formaldehyde resin with negative charge interacts with the cation of CTAB, which leads to the mesostructure formation. Both lamellar and hexagonal phases were obtained by adjusting the ratio between resin and surfactant.

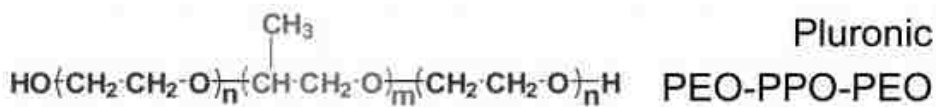


Fig 1-4. Structural illustration of tri-block copolymer

Besides ionic surfactants, nonionic surfactants were also explored to form mesostructures. Compared with ionic surfactants, they have relatively low cost, low toxicity, and better degradability. The variability of non-ionic surfactants can lead to structures with different pore shape and geometry as well. Attard and co-workers first demonstrated synthesis of mesostructure from nonionic surfactants by using $\text{C}_{25}\text{H}_{25}\text{EO}_8$. The short chain surfactant created a mesoporous silica with 3 nm pore size[39]. In 1998, Stucky and co-workers obtained mesoporous SBA-15 with Pluronic P123 surfactant (Fig 1-4). The Pluronic surfactant is a family of

surfactants made of poly (alkylene-oxide) block copolymer. Due to the longer chain length, the pore size of SBA-15 was much larger, up to 30 nm.

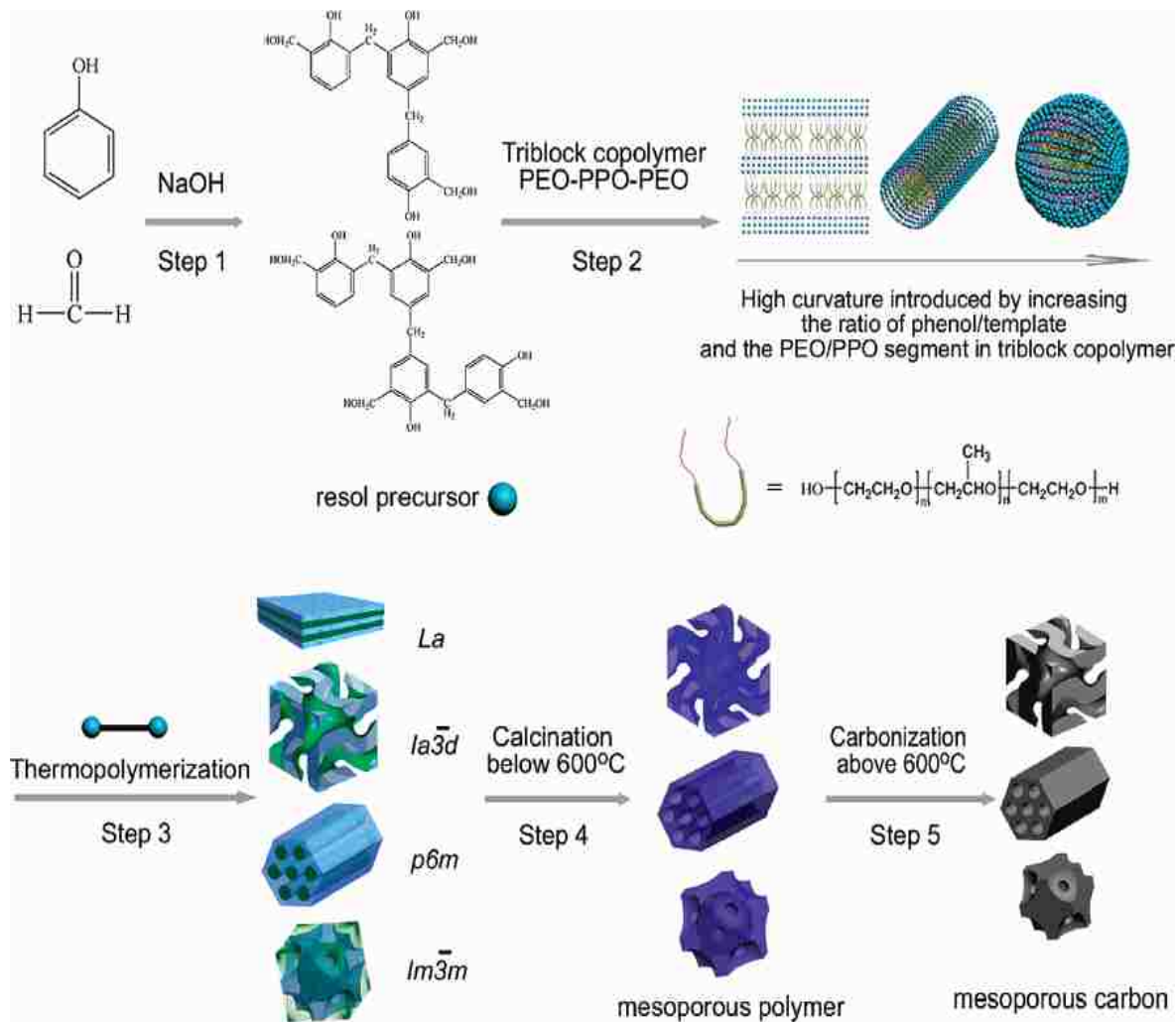


Fig 1-5. Preparation of mesoporous carbon with triblock copolymer and resin. Ref[13]

The tri-block copolymer surfactant was also used to create a series of mesoporous carbon structures[13]. Usually, a phenol (resorcinol or phloroglucinol) and formaldehyde resin is used, since the fairly high carbon yield from the highly crosslinked aromatic framework. By hydrogen bond interaction, the resin interacts with the hydrophilic tail group of the surfactant to form different mesostructures. Due to the low stability and low carbon yield of the linear structure, the surfactant will decompose into small, volatile molecules at lower temperature ($< 600^\circ\text{C}$) and

leaves nothing but void after decomposing and carbonization. Therefore, the carbon-rich resin can be converted to a porous carbon framework (Fig 1-5).

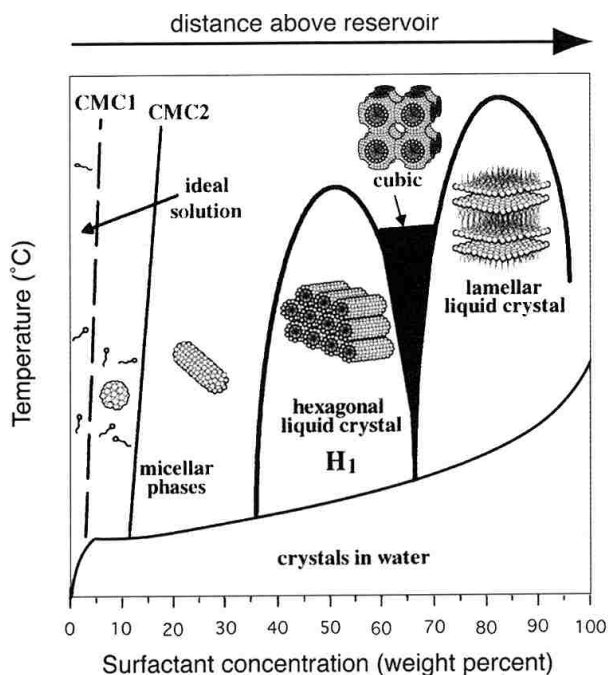


Fig 1-6. Phase diagram of CTAB in water. Ref[4]

In the soft-templating synthesis route of ordered mesoporous materials, the mesostructure formation is guided by surfactants[4] (Fig 1-6). Take CTAB for example, the ability of surfactant to form mesostructure is related to the critical micelle concentration (CMC). At low concentrations, CTAB exists as free molecules. As the concentration rises, the surfactants assemble into micelles driven by surface tension and free energy. Then the micellar phase further transforms into cylindrical rods and further into a close-packed hexagonal array structure. As the concentration of surfactants further goes up, the mutually parallel rods are pushed into planar lamellar phase. In some cases, cubic structure is also observed[40].

From the perspective of thermodynamics, the packing, and structure of micelles are governed by free energy. Tanford was the first to describe this topic mathematically by using opposing forces

to formulate a quantitative expression for free energy on micelle aggregation. Ninham and co-workers proposed the concept of packing parameter to predict the size and shape of micelle aggregation with thermodynamic principles [41].

Molecular packing parameter contains three parts: the volume and length of the surfactant tail (v_0/l_0) and the surface area of the micelle hydrophobic core (a). Mathematically it is expressed as v_0/al_0 . Sphere, cylinder, and bilayer structures are three common structures with known molecular packing parameters. The geometrical relationship of micelles containing g molecules can be listed in the following table 1-1[42].

Packing	Sphere	Cylinder	Lamella
Volume of core $V = gv_0$	$4\pi R^3/3$	πR^2	$2R$
Surface area of core $A = ga$	$4\pi R^2$	$2\pi R$	2
Area per molecule a	$3v_0/R$	$2v_0/R$	v_0/R
Packing parameter v_0/al_0	$0 \leq v_0/al_0 \leq 1/3$	$1/3 \leq v_0/al_0 \leq 1/2$	$1/2 \leq v_0/al_0 \leq 1$

Table 1-1. Geometrical relationships for spherical, cylindrical and lamellar micelles

In Tanford's model, the free energy is contributed by three factors: 1) the free energy arising from the surfactant tail's contact with water or the hydrocarbon micelle core, 2) even though most surface area of the micelle core is covered by surfactant tails, there is still residual contact between the core and water, 3) the repulsive interaction and electrostatic interactions between headgroups at the micelle core. It is not the intention of this introduction to discuss the mathematical details for calculating the free energy and geometry, but the following conclusions

summarized by R. Nagarajan can serve as a rule of thumb when predicting the micelle structure form surfactants[42].

1. For non-ionic surfactants with ethylene oxide (EO) as headgroup, as the number of EO units increase in the headgroup, the micelle packing will favor lamellar, then cylindrical, and finally spherical packing.
2. Ionic surfactants have stronger repulsion at the micelle core compared with non-ionic surfactant. So ionic surfactants will form smaller micelles compared with non-ionic surfactants with the same length.
3. Adding salt to an ionic surfactant solution will decrease headgroup repulsion, leading to a larger packing parameter. So it is possible to transform from special micelles to cylindrical micelles by increasing the ionic concentration of the solution.
4. Comparing double tail and single tail surfactants with the same area a , the packing parameter of double tail surfactants will be twice compared to that of single tail surfactants. So double tail surfactants form lamellar structure more easily than single tail ones.
5. If aqueous-organic mixture solvent is used instead of water, the interfacial tension decreases, which will lead to a decrease in packing parameter. So lamellar micelles might transform to cylindrical or spherical micelles under such condition.

The interaction between precursor and surfactants is also of great importance for the assembly of mesostructures[9]. Depending on charges of the surfactants, researchers have postulated several models. In the case of ionic surfactants, the interactions are primarily Columbic forces between two parties, which can be described by S^+I^- , S^-I^+ , S^+X^- and S^-X^+ , where S is the surfactant

ion, I is the inorganic precursor (organic in the case of mesoporous carbon), X is the case where the counter ion is involved in the assembly, and the superscript refers to the corresponding charge. Later this notation is also used to describe non-ionic surfactants as well with S^{0I^0} or N^{0I^0} . In some cases, there is also a direct formation of covalent bond between the surfactant and precursor, which is denoted as SI (Fig 1-7), for example, Ying synthesized SBA-15 like mesoporous niobium oxide (Nb-TMS1) by linking $Nb(OEt)_5$ to long-chain amine surfactant ($C_{12}H_{25}NH_2$) by NB-N bond[43].

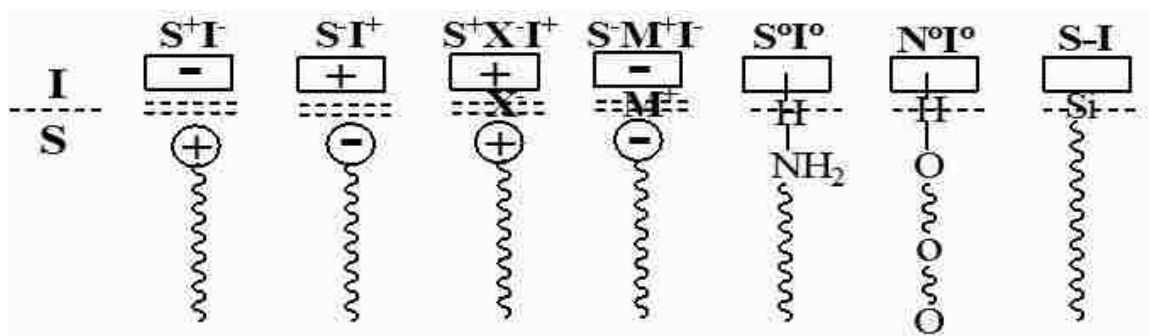


Fig 1-7. Schematic drawing of surfactant-precursor interaction models. Ref[9]

1.2.2 Hard templated synthesis of ordered mesoporous materials

In the soft templating route, a successful synthesis of the mesostructure depends on the precursor, the surfactant and the interaction between them, therefore many mesoporous materials cannot be obtained this way. A hard templating route, also known as nanocasting, is also widely used to create materials with periodic mesopores. In fact, the hard-templating route appeared before soft-templated synthesis. The first hard-templated mesoporous carbon was reported by Knox and co-workers in 1983, where phenol-hexamine mixture was filled into silica gel with mesoporous structure. A disordered mesoporous carbon was obtained with high surface area. It was not until 1999 that Ryoo and co-workers obtained highly periodic mesoporous carbon CMK-

1 by hard templated route. MCM-41 type mesoporous aluminosilicate with interconnected pore channels was used as the template and infiltrated with sucrose. At temperatures from 1073 to 1373 °C, sucrose was carbonized with the aid of sulfuric acid catalyst. Then the silica template was removed by hot base solution, creating an inverse replica carbon framework of the mesoporous silica.

In general, three steps are involved in the hard templating synthesis route: 1) infiltration of precursor material into the void spaces of templates, 2) Condensing of the precursor into a robust interconnected framework, 3) removal of the template by selective etching. To obtain a continuous mesoporous product, one critical prerequisite is the pore channel needs to be interconnected to avoid the collapse of the porous structure upon template removal (Fig 1-8). For instance, by using pure MCM-41 silica, mesoporous carbon cannot be obtained due to lack of interconnected mesopores. On the other side, SBA-15 shares the same hexagonal structure with MCM-41, but its pore channels are interconnected by micropores created by the calcination of poly (ethylene oxide) chains of surfactants. CMK-3 was successfully replicated from SBA-15 with a robust three-dimensional porous framework.

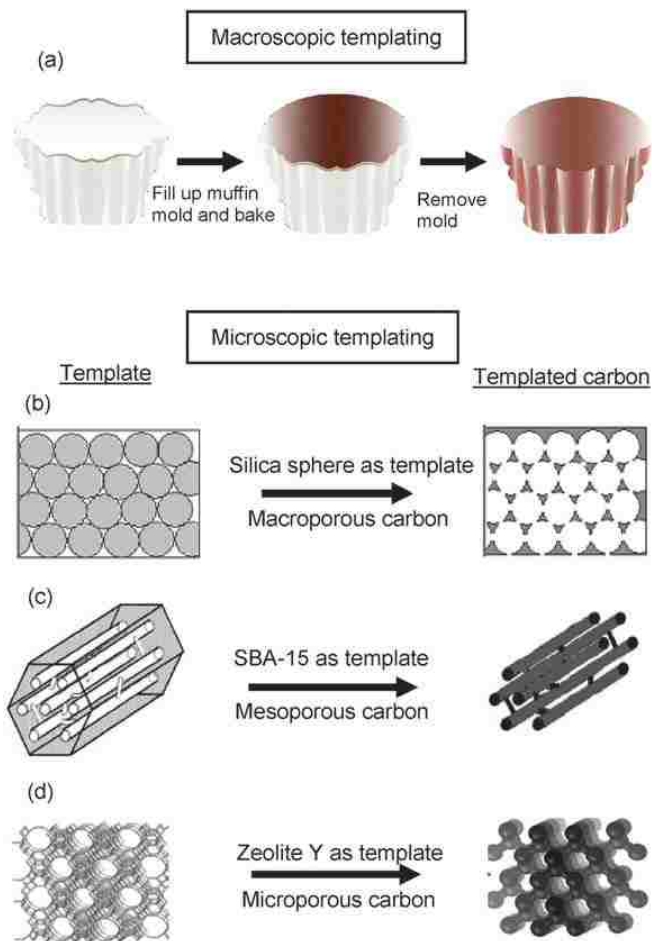


Fig 1-8. Top: casting concept at macroscale, Bottom: casting concept at nanoscale. Ref[3]

In the hard-templating synthesis route, the product structure can be controlled and tuned by the structure of templates. For example, by varying the hexadecyltrimethylammonium bromide (HTAB) to the surfactant ratio, Ryoo was able to produce mesoporous SBA-15 with tailor wall thicknesses between 1.4 to 2.2 nm, and the pore sizes of corresponding carbon materials can be controlled accordingly[44]. Due to the development of mesoporous silica with different structures, a number of mesoporous carbons were made, including cubic, body centered cubic, gyroid, and hexagonal structures. Therefore, with the synthesis of new nanoporous silicas, it is anticipated that nanoporous carbon with replicating structure will be produced as well.

In addition to three-dimensional framework templates, colloidal silica spheres are explored as the template for porous carbon materials. Compared with mesoporous silica, colloidal silica can be prepared with simple Stober methods and do not need complicated synthesis procedures. In addition, it is also available commercially at a relatively low cost. In addition, the wide selection in particle diameter enables the synthesis of mesoporous carbon with tunable pore sizes. The first synthesis of ordered mesoporous carbon templated by silica spheres was reported by the Mallouk group at Pennsylvania State University. Silica particles with 35 nm diameter were sintered under pressure to create an ordered inorganic template, divinylbenzene (DVB) and ethylene glycol dimethacrylate (EDMA) was used as carbon source. After the carbonization of precursors, silica template was removed by HF, leaving a porous carbon replica. Due to different thermal contraction rate of DVB and EDMA, the pore size can be continuously varied from 15 to 35 nm[45]. Li and Jaroniec had also synthesized mesoporous carbon with commercial colloidal silicas with mesophase pitch as the carbon source to obtain a non-microporous carbon framework[46].

1.2.3 Synthesis of disordered porous carbon materials

In addition to the research and exploring of ordered mesoporous materials, there is significant interest in disordered porous materials as well with controlled pore sizes. Despite having disordered pore structure, the synthesis of disordered porous structures usually include fewer steps than that of ordered structures and the controlled pore size can still provide excellent properties for adsorption, separation and energy storage applications. Kyotani and co-workers were able to synthesize mesoporous carbon from a carbon/silica nanocomposite, which was prepared by copolymerization of tetraethoxy silane (TEOS) and furfuryl alcohol (FA) in a sol-gel process. The silica component was removed by HF to obtain a carbon-only framework. The pore size distribution can be easily tuned by changing the TEOS/FA ratio and temperature (Fig 1-9).[8]

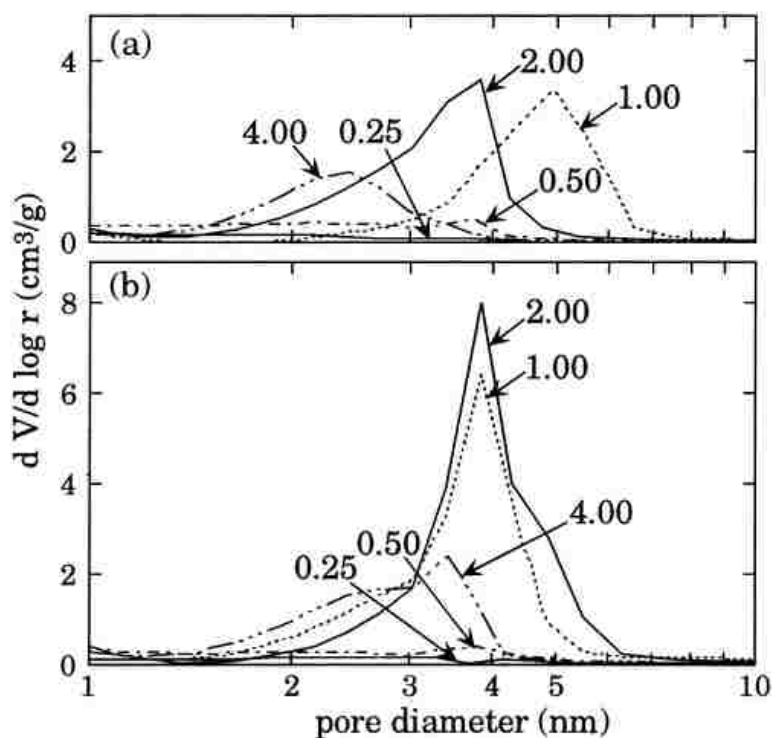


Fig 1-9. Pore size distribution of nanoporous carbon prepared from TEOS and FA. Ref[8]

In a similar approach, Sayari also prepared mesoporous carbon with monodisperse pore size by co-condensing silica with a carbon source[7]. In Sayari's approach, beta-cyclodextrin was used as carbon-yielding agent and co-polymerized with tetramethyl orthosilicate (TMOS) to produce a carbon-silicate hybrid monolith (Fig 1-10). In this case, cyclodextrin served as the pore forming agent for silica framework, and later as carbon source. After the etching of silica content, a carbon-only framework was obtained.

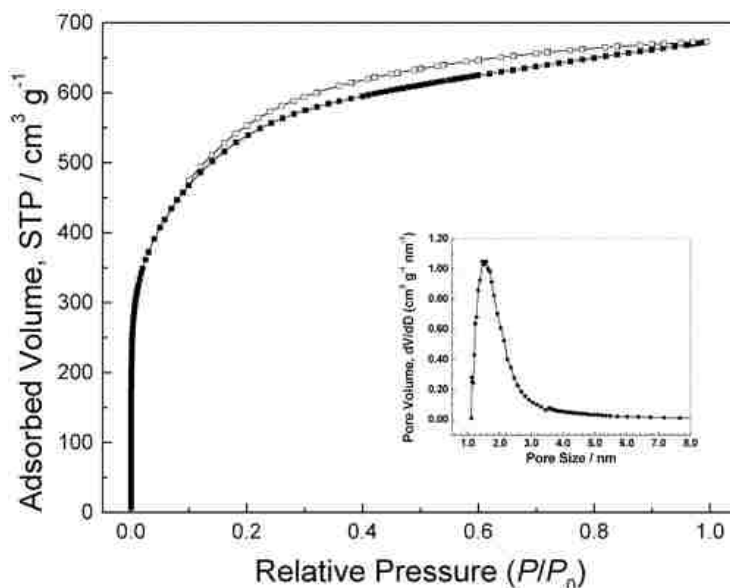


Fig 1-10. Nitrogen adsorption isotherm and pore size distribution of mesoporous carbon prepared from cyclodextrin and TMOS. Ref[7]

Activated carbon (AC) is another important type of disordered nanoporous carbon. AC is an amorphous carbon form which is treated from low-cost carbon sources to create porosity. The porosity of ACs is usually contributed by interconnected micropores smaller than 2 nm, leading to surface areas over 3000 m²/g[47]. A common carbon source for producing ACs is charcoal. More recently, there is also rising interest for producing ACs from agricultural products such as coconut shell, cotton stalks, durian shells, olive stones, wood and so forth[48]. Due to their low cost, high porosity and high surface area, over 275,000 tons of ACs are produced annually for industrial applications like water and air purification, food de-coloring, catalyst loading and so forth.

The production of ACs from raw materials usually starts with a few pre-treatment steps, from crushing, milling to sieving the particles to the right mesh size, then followed by the activation step. There are primarily two routes for producing ACs: physical activation and chemical activation[49]. The former is generally a two-step treatment, where the carbonaceous content

first undergoes a pyrolysis step at relatively low temperatures ($< 700\text{ }^{\circ}\text{C}$) under protective atmosphere (Nitrogen), followed by activation by an activating agent such as carbon dioxide or steam[50], where carbon is removed by partial oxidation. The activation temperature is chosen with respect to the specific carbon sources and oxidizing agents. Below is a typical experimental apparatus for physical activation of carbon using steam (Fig 1-11).

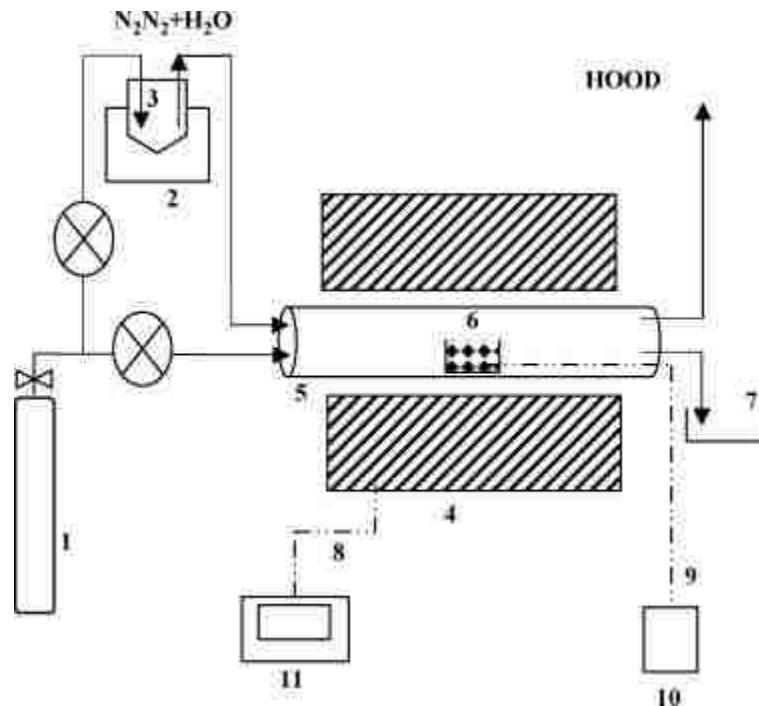


Fig 1-11. Typical physical activation apparatus 1) Nitrogen gas feed; 2) flask heater; 3) water saturator; 4) tube furnace; 5) reaction chamber; 6) sample; 7) liquid waste collector; 8) furnace thermocouple; 9) sample thermocouple 10) temperature monitor; 11) temperature controller. Ref[15]

In contrast, chemical activation is a one-step activation process by heating the precursor with activating agents together, where pores are created by chemicals impregnating the precursor[51]. Common activating agents include KOH, H_3PO_4 , K_2CO_3 , ZnCl_2 , etc. Chemical activation is a well-demonstrated method for producing ACs, however, due to a large number of variables such as

complexity of precursor, activating agent choices and so forth, the activation mechanism is still not well understood. For example, KOH activation of carbon is driven from a series of reactions at a wide temperature range. Otowa and co-workers have proposed that below 700 °C, the following reactions is responsible for carbon etching[52].



The main products of KOH activation include hydrogen, water, carbon monoxide, carbon dioxide, potassium oxide and potassium carbonate. KOH is first dehydrated into K₂O at 400 °C, then carbon is removed by the reaction with water. The Linares-Solano group further studied the gas evolution process by temperature-programmed reaction (TPR) and further proposed another reaction about carbon etching[11].



At temperatures higher than 700 °C, the formed K₂CO₃ decomposes into K₂O and CO₂, where the CO₂ can be further reduced to CO. The potassium content can be possibly reduced to metallic state as well.



Wang and Kaskel summarized the mechanism of KOH activation to be three steps[47]: 1) Initial removal of carbon content by redox reactions between potassium contents with carbon such as in reaction 1-5, 2) further development of porous structures by gas evolution reactions such as reaction 1-1, 1-7, 3) the intercalation of metallic potassium into carbon matrix to allow the expansion of carbon lattice as indicated in Fig 1-12. High surface area and porosity are generated after the removal of potassium species by washing.

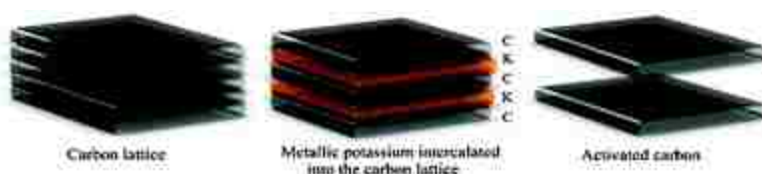


Fig 1-12. Carbon lattice expansion from metallic potassium. Ref[11]

Depending on the choice of precursor material, activating method, activating agents and conditions, the porosity of ACs can be comprised of micropores, mesopores and sometimes macropores as depicted in Fig 1-13. In general, the surface area of ACs is mostly contributed from micropores, however, mesopores and macropores are also of vital importance since they provide pathways for molecules and ions to access the micropores. The internal surface of ACs is primarily made up of microcrystalline graphitic sites packed in a random order to form pores. This also leads to a relatively broad pore size distribution in ACs. From a chemistry perspective, the surface of ACs can be terminated by a variety of functional groups, for example, hydroxyl group, ketone group, and carboxylate group[53].

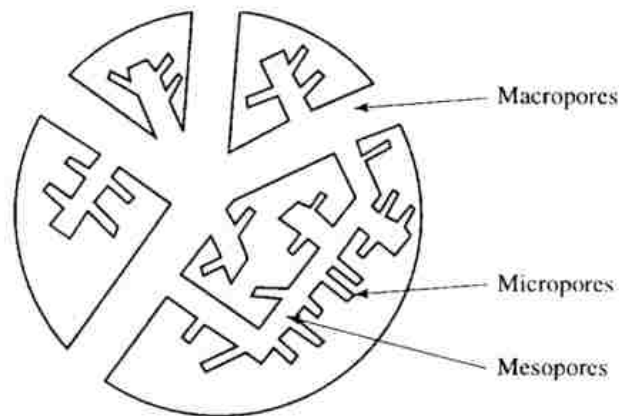


Fig 1-13. Schematic illustration of hierarchical pore structure of activated carbon. Ref[10]

1.3 Common applications for nanoporous materials

After over several decades of research and development, the properties of nanoporous materials have been gradually understood, giving rise to a number of applications in various field in chemistry and chemical engineering.

1.3.1 The application of mesoporous material in catalysts

When the Mobil researchers synthesized the M41S family materials, they were intended to substitute to zeolite materials for catalyst applications in the petroleum cracking industry, as the larger pore channels could lead to better diffusion kinetics and would fit large molecules as well, but the amorphous pore walls of mesoporous silica could not provide the hydrothermal stability required for petroleum cracking. However, the successful synthesis of order mesoporous materials triggered widespread research interest on mesoporous materials and subsequently lead to their applications in heterogeneous catalysis.

Generally, in a heterogeneous catalyst-driven reaction, several fundamental steps are involved as depicted in Fig 1-14. First, the reactants first diffuse to the catalyst and get adsorbed on the surface, then the chemical reaction happens on the surface. Afterwards, the products are desorbed from the solid surface to regenerate the catalysts for the next cycle. Since the reaction happens on the catalyst surface, materials with high surface area are strongly desired for such applications[54]. Mesoporous materials are good candidates for heterogeneous catalysts for the following reasons[2]: 1) Their high surface area can provide a large number of active sites for chemical reactions; 2) Their pore dimensions can be tuned during synthesis to provide selectivity of molecules based on size; 3) The ability to adjust the surface texture and functionalize the surface chemistry properties, i.e., hydrophobicity, hydrophilicity, polarity and so forth; 4) They are suitable for industrial applications due to relatively low-cost, non-corrosive and non-toxic properties.

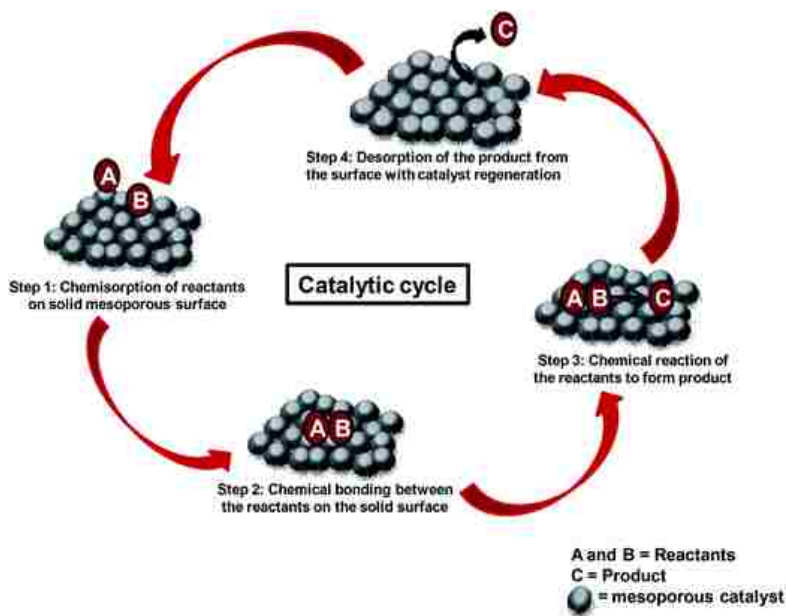


Fig 1-14. Catalytic cycle on solid mesoporous surface. Ref[2]

Pure mesoporous silica, despite having high surface area, has limited reactivity for practical applications, therefore it is often doped with heteroatoms (usually metal) or functionalized with surface groups to provide catalytic activity[55].

For example, metal modified mesopores exhibit great catalytic properties for redox reactions, especially on the controlled oxidation of hydrocarbon molecules. In this case, redox catalysts are grafted onto the pore walls of mesoporous materials. Koner and co-workers embedded copper complexes into MCM-41 using post-synthesis modification, which was applied as an oxidation catalyst for epoxidation of various olefin molecules such as styrene, cyclohexene, and cyclooctene using tert-butylhydroperoxide (TBHP) as an oxidant (Fig 1-15)[6].

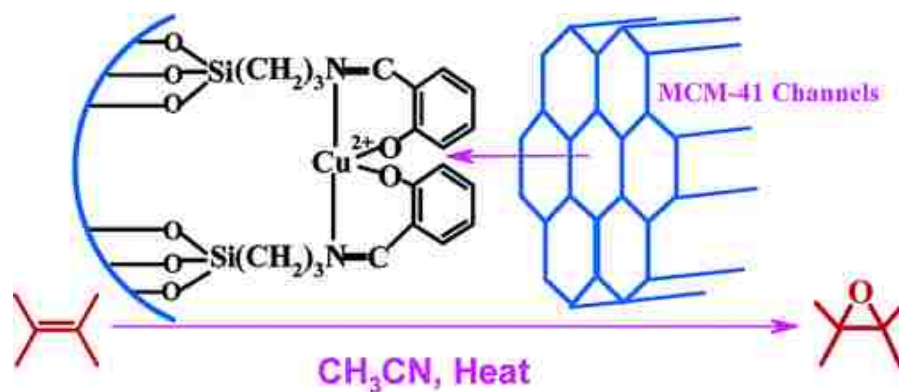


Fig 1-15. Cu complex grafted MCM-41 for epoxidation of hydrocarbon molecules. Ref[6]

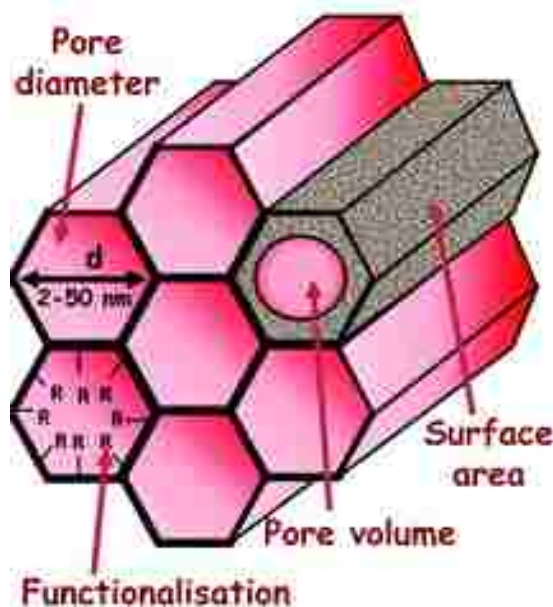
In addition to redox catalyst activity, mesoporous silica can also act as a solid acid catalyst. Pure siliceous framework does not exhibit any acid or base properties, so research efforts were put into incorporating heteroatoms like aluminum into silica framework to create active acid sites[55]. When aluminum substitutes silicon atoms in an isomorphic manner, AlO₄⁻ sites are created, and when the charge imbalance is compensated by H⁺ ions, the framework will show Bronsted acidity[56]. For example, Chmelka et al. have prepared SBA-15 type aluminosilicate using a

cooperative assembly of TMOS and aluminum chloride in the presence of hydrochloric with F127 or P123 as surfactants, and the product with a Si to Al ratio of 72 showed improved catalytic activity for Friedel-Crafts alkylation compared with conventional zeolite Beta catalyst[57].

1.3.2 Application of mesoporous material in drug delivery

Due to their stable porous framework, continuous variable pore size and the ability to be surface modified, mesoporous silica has been adapted for drug delivery applications. The pioneering work in this field was contributed by Vallet-Regi and co-workers[58], where MCM-41 mesoporous silica with different channel sizes were synthesized with C16TAB and C12TAB templates and loaded with isobutylphenylpropanoic acid (Ibuprofen) to act as a reservoir for controlled drug delivery. Since then, a number of other drug molecules, including Diflunisal (Dolobid), Amoxicillin, Erythromycin, Alendronate, Cis-platin and so forth.

Mazano and Vallet-Regi have summarized that mesoporous silica materials are suitable for biotechnological application due to the following properties[5]: 1) the high pore volume can provide confined space for large amounts of drug or biologically active species; 2) the large surface area can provide high potential for drug molecule adsorption; 3) the homogeneous porous structure with narrow pore-size distribution can ensure reproducibility during drug adsorption and release tests; 4) the pore walls of mesoporous silica can be easily modified for anchoring different drug molecules and enhanced control over drug loading and release (Fig 1-16).



FUNCTIONALISATION GROUP
-Si-CH ₃
-Si-CH ₂ -CH ₂ -CH ₃
-Si-CH ₂ -CH ₂ -CH ₂ -CH ₃
-Si-CH ₂ -CH ₂ -CH ₂ -CH ₂ -CH ₂ -CH ₂ -CH ₂ -CH ₂ -CH ₃
-Si-CH ₂ -CH ₂ -CH ₂ -NH ₂
-Si-CH ₂ -CH ₂ -CH ₂ -SH
-Si-CH ₂ -CH ₂ -CH ₂ -CN
-Si-CH ₂ -CH ₂ -CH ₂ -COOH
-Si-CH ₂ -CH ₂ -CH ₂ -Cl
-Si-Ph
-Si-Bz
-Si-CH ₂ -CH ₂ -CH ₂ -N ⁺ -(CH ₃) ₃
-Si-CH ₂ -CH ₂ -CH ₂ -N ⁺ -(CH ₃) ₂ (CH ₂) ₁₇ -CH ₃
-Si-CH ₂ -CH ₂ -PO-(O-CH ₂ -CH ₃) ₂
-Si-CH ₂ -CH ₂ -CH ₂ -OCOC(CH ₃)=CH ₂
-Si-CH ₂ -CH ₂ -CH ₂ -NH-CH ₂ -CH ₂ -NH ₂
-Si-CH ₂ -CH ₂ -CH ₂ -NH-CO-NH-PPi(NH ₂) _x

PPi= Poly(propylene imine) dendrimers, x=3, 7 and 15

DRUG LOADING

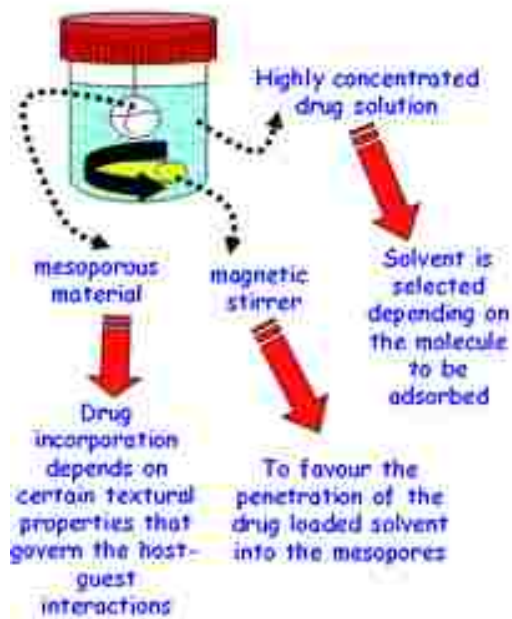


Fig 1-16. Top: Functionalization of silica pore wall, Bottom: Drug loading. Ref[5]

1.3.3 Nanoporous materials for energy storage applications

With the growing market of electronic devices and electric vehicles recently, there has been a strong demand for high power density energy storage devices. Nanoporous materials, especially

carbon-based materials, are extensively studied for supercapacitors[3, 10]. The details of carbon-based supercapacitors will be explained in Chapter 3.

1.3.4 Nanoporous materials for high pressure chemistry

In recent years, the Landskron group has found that nanoporous materials are excellent precursors for high pressure synthesis. Owing to their high surface area and porous structure, they usually exhibit higher reaction activity during high pressure reaction than their bulk counterparts. An overview of high pressure chemistry of nanoporous chemistry will be given in Chapter 5.

1.4 References:

1. Moriguchi, I., et al., *Micelle-Templated Mesophases of Phenol-Formaldehyde Polymer*. Chemistry Letters, 1999. **28**(11): p. 1171-1172.
2. Pal, N. and A. Bhaumik, *Mesoporous materials: versatile supports in heterogeneous catalysis for liquid phase catalytic transformations*. RSC Advances, 2015. **5**(31): p. 24363-24391.
3. Zhang, L.L. and X.S. Zhao, *Carbon-based materials as supercapacitor electrodes*. Chemical Society Reviews, 2009. **38**(9): p. 2520-2531.
4. Raman, N.K., M.T. Anderson, and C.J. Brinker, *Template-Based Approaches to the Preparation of Amorphous, Nanoporous Silicas*. Chemistry of Materials, 1996. **8**(8): p. 1682-1701.
5. Manzano, M. and M. Vallet-Regi, *New developments in ordered mesoporous materials for drug delivery*. Journal of Materials Chemistry, 2010. **20**(27): p. 5593-5604.
6. Jana, S., et al., *Anchoring of Copper Complex in MCM-41 Matrix: A Highly Efficient Catalyst for Epoxidation of Olefins by tert-BuOOH*. Langmuir, 2007. **23**(5): p. 2492-2496.
7. Han, B.-H., W. Zhou, and A. Sayari, *Direct Preparation of Nanoporous Carbon by Nanocasting*. Journal of the American Chemical Society, 2003. **125**(12): p. 3444-3445.
8. Kawashima, D., et al., *Preparation of Mesoporous Carbon from Organic Polymer/Silica Nanocomposite*. Chemistry of Materials, 2000. **12**(11): p. 3397-3401.
9. Soler-Illia, G.J.d.A.A., et al., *Chemical Strategies To Design Textured Materials: from Microporous and Mesoporous Oxides to Nanonetworks and Hierarchical Structures*. Chemical Reviews, 2002. **102**(11): p. 4093-4138.
10. Simon, P. and Y. Gogotsi, *Charge storage mechanism in nanoporous carbons and its consequence for electrical double layer capacitors*. Philosophical Transactions of the Royal Society of London A: Mathematical, Physical and Engineering Sciences, 2010. **368**(1923): p. 3457-3467.
11. Lozano-Castelló, D., et al., *Carbon activation with KOH as explored by temperature programmed techniques, and the effects of hydrogen*. Carbon, 2007. **45**(13): p. 2529-2536.
12. Kondo, J.N., et al., *A comparative IR characterization of acidic sites on HY zeolite by pyridine and CO probes with silica-alumina and [gamma]-alumina references*. Physical Chemistry Chemical Physics, 2010. **12**(37): p. 11576-11586.
13. Liang, C., Z. Li, and S. Dai, *Mesoporous Carbon Materials: Synthesis and Modification*. Angewandte Chemie International Edition, 2008. **47**(20): p. 3696-3717.
14. Weitkamp, J., *Zeolites and catalysis*. Solid State Ionics, 2000. **131**(1-2): p. 175-188.
15. Bouchelta, C., et al., *Preparation and characterization of activated carbon from date stones by physical activation with steam*. Journal of Analytical and Applied Pyrolysis, 2008. **82**(1): p. 70-77.
16. AlOthman, Z., *A Review: Fundamental Aspects of Silicate Mesoporous Materials*. Materials, 2012. **5**(12): p. 2874.
17. Breck, D.W., W.G. Eversole, and R.M. Milton, *NEW SYNTHETIC CRYSTALLINE ZEOLITES*. Journal of the American Chemical Society, 1956. **78**(10): p. 2338-2339.
18. Kresge, C.T., et al., *Ordered mesoporous molecular sieves synthesized by a liquid-crystal template mechanism*. Nature, 1992. **359**(6397): p. 710-712.
19. Zhao, D., et al., *Triblock Copolymer Syntheses of Mesoporous Silica with Periodic 50 to 300 Angstrom Pores*. Science, 1998. **279**(5350): p. 548-552.

20. Yu, C., Y. Yu, and D. Zhao, *Highly ordered large caged cubic mesoporous silica structures templated by triblock PEO-PBO-PEO copolymer*. *Chemical Communications*, 2000(7): p. 575-576.
21. Fan, J., et al., *Cubic Mesoporous Silica with Large Controllable Entrance Sizes and Advanced Adsorption Properties*. *Angewandte Chemie International Edition*, 2003. **42**(27): p. 3146-3150.
22. Kroto, H.W., et al., *C60: Buckminsterfullerene*. *Nature*, 1985. **318**(6042): p. 162-163.
23. Iijima, S., *Helical microtubules of graphitic carbon*. *Nature*, 1991. **354**(6348): p. 56-58.
24. Novoselov, K.S., et al., *Electric Field Effect in Atomically Thin Carbon Films*. *Science*, 2004. **306**(5696): p. 666-669.
25. Ryoo, R., S.H. Joo, and S. Jun, *Synthesis of Highly Ordered Carbon Molecular Sieves via Template-Mediated Structural Transformation*. *The Journal of Physical Chemistry B*, 1999. **103**(37): p. 7743-7746.
26. Wang, X., C. Liang, and S. Dai, *Facile Synthesis of Ordered Mesoporous Carbons with High Thermal Stability by Self-Assembly of Resorcinol-Formaldehyde and Block Copolymers under Highly Acidic Conditions*. *Langmuir*, 2008. **24**(14): p. 7500-7505.
27. Meng, Y., et al., *Ordered Mesoporous Polymers and Homologous Carbon Frameworks: Amphiphilic Surfactant Templating and Direct Transformation*. *Angewandte Chemie International Edition*, 2005. **44**(43): p. 7053-7059.
28. Tanaka, S., et al., *Synthesis of ordered mesoporous carbons in film morphology using organic-organic interaction approach*, in *Studies in Surface Science and Catalysis*, P.M. Antoine Gédéon and B. Florence, Editors. 2008, Elsevier. p. 657-660.
29. Tanaka, S., et al., *Synthesis of ordered mesoporous carbons with channel structure from an organic-organic nanocomposite*. *Chemical Communications*, 2005(16): p. 2125-2127.
30. Yang, P., et al., *Generalized syntheses of large-pore mesoporous metal oxides with semicrystalline frameworks*. *Nature*, 1998. **396**(6707): p. 152-155.
31. Sang, X., et al., *Template-free synthesis of mesoporous polymers*. *Chemical Communications*, 2014. **50**(60): p. 8128-8130.
32. Li, H., et al., *Design and synthesis of an exceptionally stable and highly porous metal-organic framework*. *Nature*, 1999. **402**(6759): p. 276-279.
33. Yaghi, O.M., G. Li, and H. Li, *Selective binding and removal of guests in a microporous metal-organic framework*. *Nature*, 1995. **378**(6558): p. 703-706.
34. Furukawa, H., et al., *The Chemistry and Applications of Metal-Organic Frameworks*. *Science*, 2013. **341**(6149).
35. Ren, Y., Z. Ma, and P.G. Bruce, *Ordered mesoporous metal oxides: synthesis and applications*. *Chemical Society Reviews*, 2012. **41**(14): p. 4909-4927.
36. Majoulet, O., et al., *Preparation, Characterization, and Surface Modification of Periodic Mesoporous Silicon-Aluminum-Carbon-Nitrogen Frameworks*. *Chemistry of Materials*, 2013. **25**(20): p. 3957-3970.
37. Whitesides, G.M. and M. Boncheva, *Beyond molecules: Self-assembly of mesoscopic and macroscopic components*. *Proceedings of the National Academy of Sciences of the United States of America*, 2002. **99**(8): p. 4769-4774.
38. Darling, S.B., *Directing the self-assembly of block copolymers*. *Progress in Polymer Science*, 2007. **32**(10): p. 1152-1204.
39. Attard, G.S., J.C. Glyde, and C.G. Goltner, *Liquid-crystalline phases as templates for the synthesis of mesoporous silica*. *Nature*, 1995. **378**(6555): p. 366-368.

40. Brinker, C.J., et al., *Evaporation-Induced Self-Assembly: Nanostructures Made Easy*. *Advanced Materials*, 1999. **11**(7): p. 579-585.
41. Israelachvili, J.N., D.J. Mitchell, and B.W. Ninham, *Theory of self-assembly of hydrocarbon amphiphiles into micelles and bilayers*. *Journal of the Chemical Society, Faraday Transactions 2: Molecular and Chemical Physics*, 1976. **72**(0): p. 1525-1568.
42. Nagarajan, R., *Molecular Packing Parameter and Surfactant Self-Assembly: The Neglected Role of the Surfactant Tail*. *Langmuir*, 2002. **18**(1): p. 31-38.
43. Antonelli, D.M. and J.Y. Ying, *Synthesis of a Stable Hexagonally Packed Mesoporous Niobium Oxide Molecular Sieve Through a Novel Ligand-Assisted Templating Mechanism*. *Angewandte Chemie International Edition in English*, 1996. **35**(4): p. 426-430.
44. Lee, J.-S., S.H. Joo, and R. Ryoo, *Synthesis of Mesoporous Silicas of Controlled Pore Wall Thickness and Their Replication to Ordered Nanoporous Carbons with Various Pore Diameters*. *Journal of the American Chemical Society*, 2002. **124**(7): p. 1156-1157.
45. Johnson, S.A., P.J. Ollivier, and T.E. Mallouk, *Ordered Mesoporous Polymers of Tunable Pore Size from Colloidal Silica Templates*. *Science*, 1999. **283**(5404): p. 963-965.
46. Li, Z. and M. Jaroniec, *Mesoporous Carbons Synthesized by Imprinting Ordered and Disordered Porous Structures of Silica Particles in Mesophase Pitch*. *The Journal of Physical Chemistry B*, 2004. **108**(3): p. 824-826.
47. Wang, J. and S. Kaskel, *KOH activation of carbon-based materials for energy storage*. *Journal of Materials Chemistry*, 2012. **22**(45): p. 23710-23725.
48. Alslaibi, T.M., et al., *A review: production of activated carbon from agricultural byproducts via conventional and microwave heating*. *Journal of Chemical Technology & Biotechnology*, 2013. **88**(7): p. 1183-1190.
49. Ioannidou, O. and A. Zabaniotou, *Agricultural residues as precursors for activated carbon production—A review*. *Renewable and Sustainable Energy Reviews*, 2007. **11**(9): p. 1966-2005.
50. Demiral, H., et al., *Production of activated carbon from olive bagasse by physical activation*. *Chemical Engineering Research and Design*, 2011. **89**(2): p. 206-213.
51. Juan, Y. and Q. Ke-qiang, *Preparation of Activated Carbon by Chemical Activation under Vacuum*. *Environmental Science & Technology*, 2009. **43**(9): p. 3385-3390.
52. Otowa, T., R. Tanibata, and M. Itoh, *Production and adsorption characteristics of MAXSORB: High-surface-area active carbon*. *Gas Separation & Purification*, 1993. **7**(4): p. 241-245.
53. Figueiredo, J.L., et al., *Modification of the surface chemistry of activated carbons*. *Carbon*, 1999. **37**(9): p. 1379-1389.
54. Corma, A., *From Microporous to Mesoporous Molecular Sieve Materials and Their Use in Catalysis*. *Chemical Reviews*, 1997. **97**(6): p. 2373-2420.
55. Taguchi, A. and F. Schüth, *Ordered mesoporous materials in catalysis*. *Microporous and Mesoporous Materials*, 2005. **77**(1): p. 1-45.
56. Chandra Mouli, K., et al., *Effect of pore diameter of Ni–Mo/Al-SBA-15 catalysts on the hydrotreating of heavy gas oil*. *Applied Catalysis A: General*, 2011. **404**(1–2): p. 21-29.
57. Chiu, J.J., et al., *Friedel–Crafts alkylation properties of aluminosilica SBA-15 meso/macroporous monoliths and mesoporous powders*. *Journal of Catalysis*, 2004. **221**(2): p. 400-412.
58. Vallet-Regi, M., et al., *A New Property of MCM-41: Drug Delivery System*. *Chemistry of Materials*, 2001. **13**(2): p. 308-311.

2 Characterization techniques for nanoporous materials and electrochemical measurements

In order to investigate chemical and structural characteristics of nanoporous materials, a number of instrumental techniques are required, including but not limited to electron microscopes, gas adsorption techniques, diffractometers, potentiostats and so forth. This chapter will briefly describe the working principles of the instruments that are commonly used for the characterization of porous materials.

2.1 Transmission Electron Microscopy

Transmission Electron Microscopy (TEM) is a type of microscope using high energy electron beam as the light source for imaging. The first TEM was invented by Ruska and Knoll in Germany in 1933 and later commercialized by Siemens in 1939, improving the image resolution up to 20 times compared with optical microscopes. Since then, the TEM technique has evolved into an important characterization technique in physics, materials science, chemistry, biological sciences and so forth[8]. The current state-of-the-art TEM, the TEAM 0.5 at Lawrence Berkeley National Laboratory, is able to reach an imaging resolution of 50 pm[9].

The most important parameter for microscopes is the resolution, i.e., the smallest distance between two points on the specimen that can be differentiated as two separate parts. For example, the average resolution of human eyes is 0.2 mm, which means we cannot distinguish two objects that are closer than 0.2 mm.

The theoretical resolution of an optical microscope is limited by the wavelength of visible light, as described by Abbe's equation:

$$d = \frac{0.612 * \lambda}{n \sin \alpha} \quad \text{Eq. 2-1}$$

where:

d is the resolution

λ is the wavelength of the light source

n is the refractive index of the medium between the point source and lens

α is the cone half angle from the light source to the sample specimen.

If the aberrations and astigmatisms are eliminated in an optical microscope, the resolution limit by diffraction is proportional to the wavelength of the light source. The wavelength of visible light is 390 – 700 nm, leading to a roughly 200 nm resolution limit for traditional microscopes. Scientists have tried to use ultraviolet light (UV) as the light source to improve the resolution, however, UV can only improve the resolution by a factor of 2. In addition to electron beams, X-ray was explored as the light source. However, X-ray cannot be focused by electromagnetic lens, therefore it is much more difficult to make X-ray microscopes with high-resolution compared with electron microscopes[10].

According to the wave-particle duality theory proposed by Louis de Broglie, moving particles have wave-like properties and their wavelength can be described by the de Broglie's equation:

$$\lambda = \frac{h}{mv} \quad \text{Eq. 2-2}$$

where:

h is the Plank's constant

m is the mass of the particle

v is the velocity of the particle.

When an electron passes through an electric field, it will be accelerated, so the kinetic energy would be equal to the energy from the electric field. This can be stated as the following:

$$E \text{ (eV)} = \frac{1}{2}mv^2 \quad \text{Eq. 2-3}$$

By combining Eq. 2-2 and Eq. 2-3, assuming that electron mass does not change after acceleration, we can derive the wavelength of an accelerated electron beam:

$$\lambda = \sqrt{\frac{m}{2E}} \frac{h}{m} = \sqrt{\frac{h}{2Em}} \quad \text{Eq. 2-4}$$

Putting the numbers and constants into Eq. 2-4, the wavelength of electron beam can be calculated as the following:

$$\lambda = \frac{1.23}{\sqrt{V}} \text{ nm} \quad \text{Eq. 2-5}$$

where V is the accelerating voltage in volts. So the diffraction limited resolution of electron beam can be calculated as the following:

$$d = \frac{0.753}{\sin \alpha * \sqrt{V}} \text{ nm} \quad \text{Eq. 2-6}$$

since α in electron microscopy is generally very small, like 10^{-2} , we can just substitute *sin* α with α , giving us the equation:

$$d = \frac{0.753}{\alpha * \sqrt{V}} \text{ nm} \quad \text{Eq. 2-7}$$

where:

d is the diffraction limited resolution

α is the aperture half angle

V is the accelerating voltage in volts.

So for an electron microscope operating at 200 kV, the theoretical resolution limit is 0.17 nm calculated from the equation, approximately 1,000 times better than optical microscopes. Based on the assumption, scientists were able to make transmission electron microscopy with the development of electromagnetic lenses for electron beams.

The structure of TEM was analogous to that of a transmission optical microscope, as illustrated in Fig 2-1. A typical TEM is usually made with 3 sections, 1) the electron source, which is responsible

for generating and focusing the electron beam, 2) the imaging system, which contains a series of electromagnetic lenses to lead the beam pass the specimen and generate a highly magnified electron image and 3) the recording system, using fluorescent imaging plates to render the electronic image visible to human eye and recording the image by CCD devices.

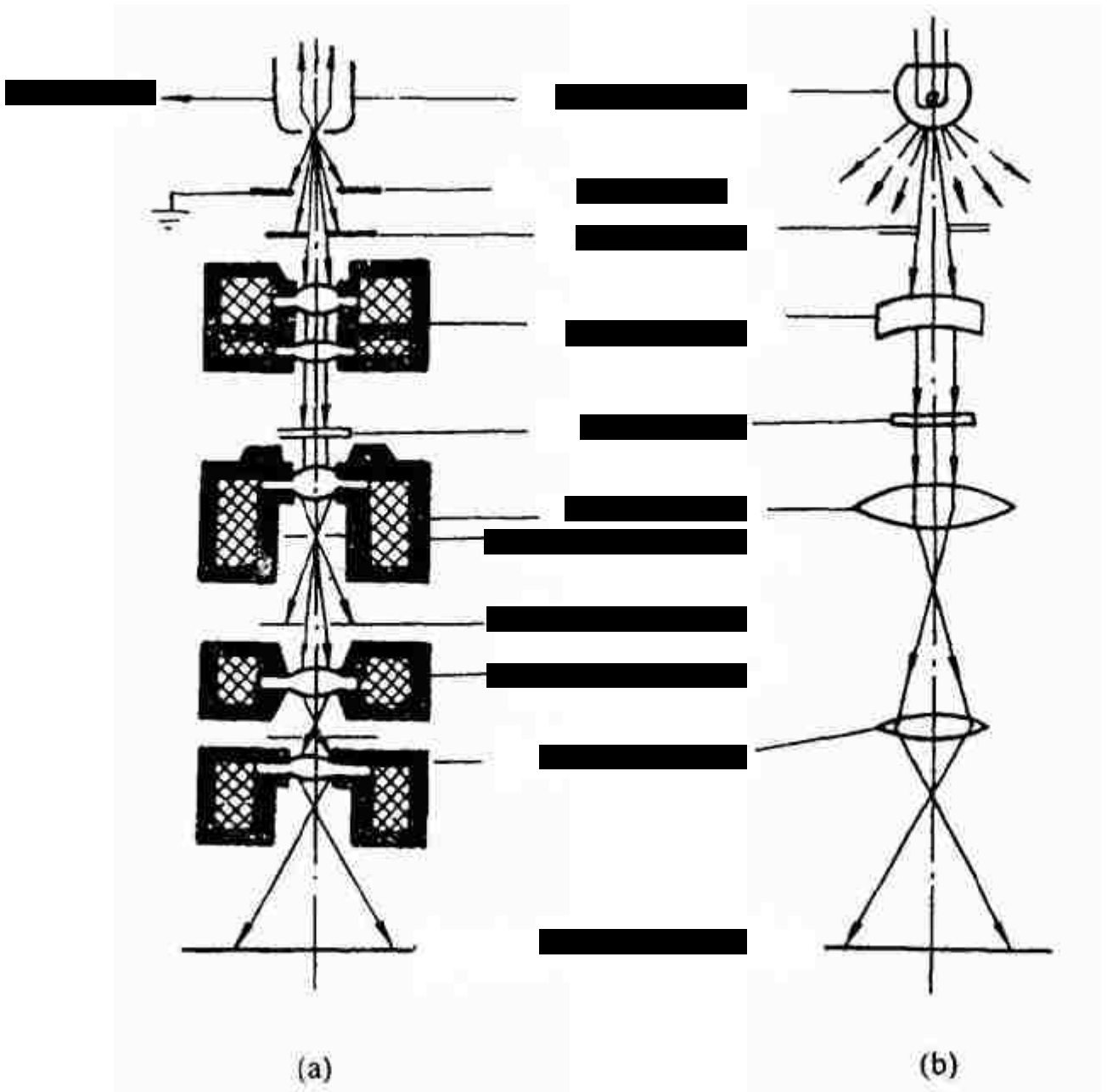


Fig 2-1. Structural illustration of TEM compared with light microscope. Ref[4]

The electron source, cathode, is usually a tip shaped tungsten filament, on some higher end models, the electron gun can be Lanthanide hexaboride or field emission tips. The electron beam is then accelerated through a high voltage and then focused through the condenser lens and turned into a parallel beam and focused onto the specimen.

The specimen is usually mounted on a copper mesh with a thin layer carbon coating. After the electron beam passes through the specimen, the objective lens focuses the beam into a real image that is further magnified by intermediate lens and objective lens. Modern microscopes are often equipped with one intermediate lens and one projector lens, to provide wider magnification ranges without the need to increase the column size to fit one large lens.

After the image is finally adjusted and magnified, the electron beam falls on a fluorescent screen located in the imaging chamber to generate an image that is visible to human eyes. Modern TEMs are usually equipped with charge-coupled device (CCD) to record monochromatic electronic image to digital image for further processing and analysis.

2.2 Scanning electron microscopy

Unlike TEM, scanning electron microscopy uses a focused high energy electron beam to scan over the specimen surface and detects various signals that are generated by the electron beam, and processes the signals to digital images. The signals primarily come from the interaction between the incident electron beam and the specimen, therefore they contain information about the surface morphology, sample texture, chemical composition and so forth. In a typical SEM application, data is generated over a selected area of the sample with a magnification from 50 X to 50,000 X. Some high-performance SEM instruments can reach a spatial resolution as low as 1 nm[11].

Similar to TEM, SEM is made from three sections as well, the electron source, the scanning system, and the detection system. After accelerator and condenser, the electrons from the gun is converged into a tiny beam, which is then scanned over the specimen surface in a zig-zag pattern under the control of the scanning coil. Signals generated from the scan is then collected by the

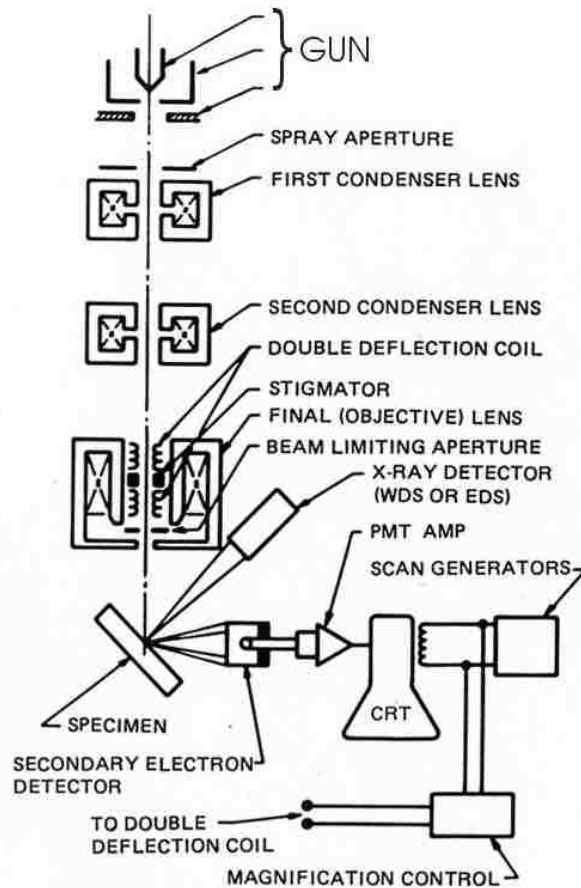


Fig 2-2. Structure illustration of SEM. Ref[6]

detector and rendered into a scanning motion on the digital screen that is in synchronization with the electron beam moves (Fig 2-2).

Accelerated electron beam with high kinetic energy is targeted towards solid sample. As a result of the electron-sample interaction, a number of signals are generated, as shown below. Both backscattered electrons (BSE) and secondary electrons (SE) are used for imaging purposes. BSEs

are valuable for providing electron contrast between different phases and chemical compositions of the specimen while SEs are useful for surface morphology and structure. X-rays are generated from inelastic collision between incident electrons and the orbital electrons of the specimen atoms. Therefore, characteristic X-rays can be used for element identification of the specimen (Fig 2-3).

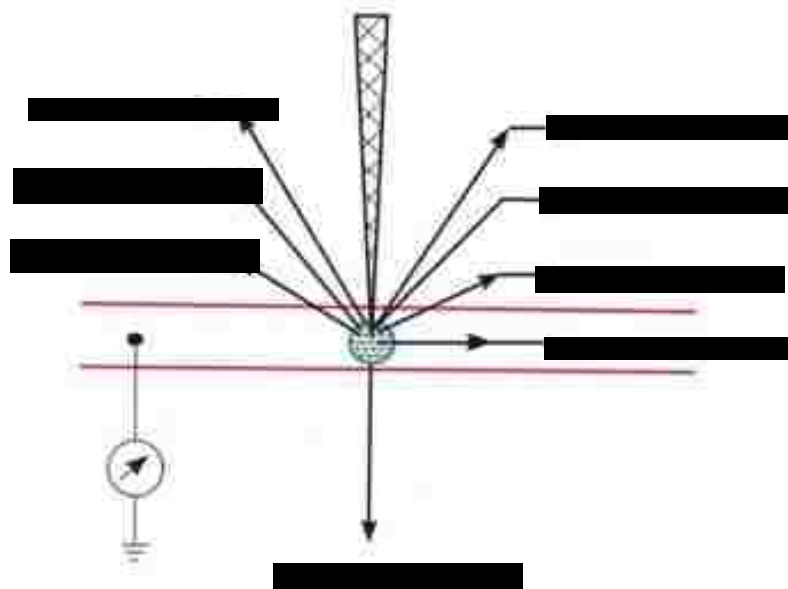


Fig 2-3. Electron-specimen interaction of SEM.

2.3 Powder X-ray scattering

X-ray is a type of electromagnetic wave that has wavelengths from 0.01 to 10 nm, it was first discovered by WC Rontgen in 1895. Later in 1912, the first X-ray diffraction image was taken from $\text{CuSO}_4 \cdot 5\text{H}_2\text{O}$ by Von. Laue and later in 1913, W. H. Bragg and W. L. Bragg derived Bragg's law by studying X-Ray interaction with NaCl crystals[3].

The foundation of modern X-ray diffractometers can be illustrated by the drawing in Fig 2-4. An X-ray beam is generated by hitting accelerated electrons on a metal target (Usually Cu, Mo) to remove K-shell electrons from the orbital and as a result, X-rays with characteristic wavelengths are generated by electrons dropping back from L and M orbitals. The beam from the source (usually Cu $K\alpha$) incidents the sample with an angle of θ , and is then scattered by the sample. The detector (scintillation counter) is placed at the angle 2θ to the beam source so it is always detecting the beam reflected from the sample.

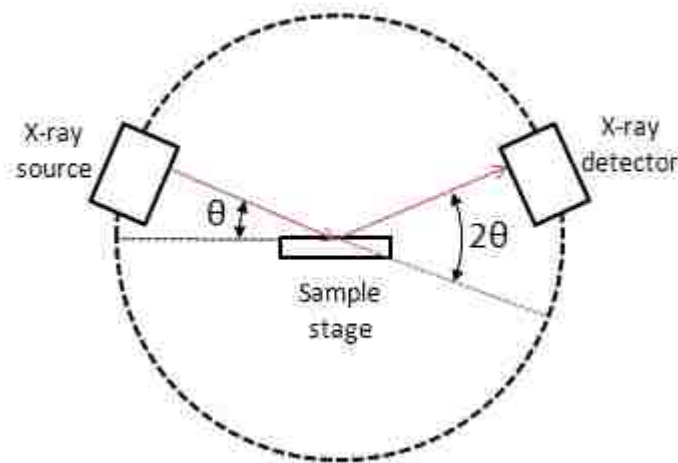


Fig 2-4. Principle of X-ray diffraction. Ref [2]

The working foundation of X-ray diffraction is built on Bragg's Law in Fig 2-5. There are some basic assumptions in deriving the Bragg's equation: 1) Crystals are made of atoms repeating periodically, so 2) X-ray can hit different facets of a crystal due to its penetrating abilities, 3) Since the source and detector is so far away from the sample compared with the interplanar spacing so the incident beam and reflected beam can both be considered as parallel beams.

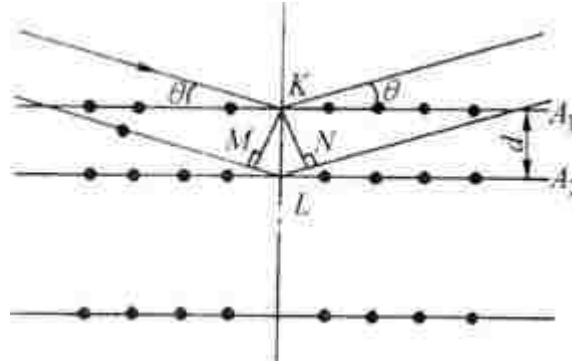


Fig 2-5. Bragg's law illustration. Ref[3]

When a beam of parallel X-rays hit a series of crystal planes (hkl) at an angle of θ , the beam is reflected by each individual crystal plane. Considering the beam hitting two adjacent planes A_1 and A_2 , assuming the interplanar spacing is d , the optical path difference (OPD) can be calculated as:

$$\delta = ML + LN = 2d\sin\theta \quad \text{Eq. 2-8}$$

For the two beams to interfere constructively, the OPD has to satisfy the following condition:

$$\delta = n\lambda \quad \text{Eq. 2-9}$$

combining the two equations, we can get

$$2d\sin\theta = n\lambda. \quad \text{Eq. 2-10}$$

So when the incident angle fits the criteria for the Bragg's law, an X-ray diffraction peak would occur and be recorded by the detector. So crystals with different space group would have X-ray diffractions at different 2θ angles. Even if two crystals share the same space group and structure, their structure factors will lead to diffraction patterns. For this reason, XRD is widely used for identifying crystal phases of materials.

2.4 Small angle X-ray scattering techniques

In addition to wide angle X-ray diffraction, small angle X-ray diffraction (SAXS) is another important technique for the characterization of porous materials on the mesoscale. According to the Bragg's Law mentioned above, the lattice constant is inversely proportional to the scattering angle. Conceptually, SAXS operates according to the same principle as wide-angle X-ray diffraction.

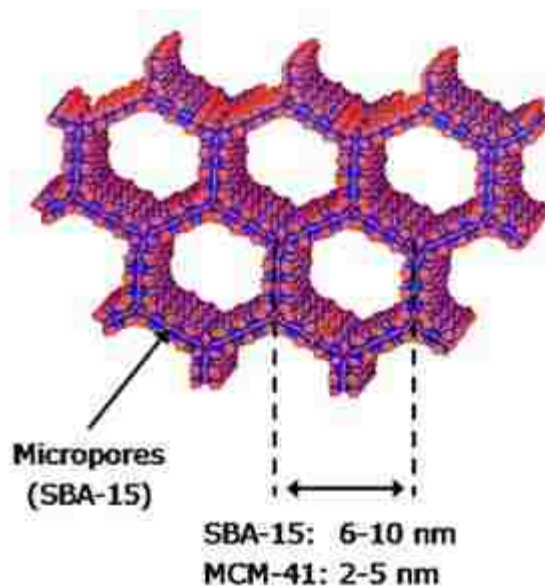


Fig 2-6. Lattice parameter d_k of MCM-41 and SBA-15. Ref[5]

In comparison, wide-angle X-ray scattering (WAXS) or usually measures the diffraction from 10° to 90° , which can reveal information about crystal structure and atomic arrangements, on the other hand, SAXS measures within the regime where the scattering angle (2θ) is usually less than 5° , therefore the measurement gives evaluation of the structure up to tens of nanometers. For example, in Fig 2-6, the lattice constant d_k in mesostructures is on the order of nanometers.

In addition, SAXS is capable of determining the structures for a number of other systems as well, including non-porous nanoparticles, micelles, proteins, etc. In some scenarios, the Cu radiation source can be substituted by synchrotron sources to gain additional sensitivity. However, this is beyond the scope for this thesis.

2.5 Gas adsorption techniques

Adsorption is a phenomenon that is observed and utilized by humans since ancient times. For example, wood charcoals are utilized for purifying and decolorizing water and sugars. C. Sheele performed the first scientific study of adsorption of gas on charcoals in 1773. A. Fontana reported the observation that charcoal can adsorb a certain amount of gases after degassing in 1777. In the 20th century, the adsorption phenomenon was studied further after the discovery of synthetic zeolites.

From a scientific point of view, adsorption can be defined as the phenomenon that gas or liquid molecules adhere to the surface of a solid material, where the solid is referred as the sorbent and the gas or liquid is referred as the sorbate. With the advancement of modern study of condensed state and interface science, gas adsorption is gradually understood from the molecular level and developed into a powerful characterization technique of solid materials. The kinetic diameters of some gas molecules are very small as listed below in Table 2-1. Since they have extremely small diameters and can move freely they can enter nanopores. Gas adsorption to the nanopores can be used to characterize the internal surface and porosity of porous materials. This is particularly useful for disordered porous materials since they are more difficult to characterize by electron microscopy techniques. In addition, adsorption measurements can provide a macroscopic average measurement of pore sizes compared with microscopy techniques which are local techniques.

Gas molecule	Kinetic diameter(Å)
CO ₂	3.3
N ₂	3.76
H ₂	2.89
Kr	3.6

Table 2-1. Kinetic diameters of gas molecules.

The amount of gas molecules adsorbed on a solid surface is a function of temperature, pressure, and the interaction between adsorbate and the adsorbent. For a specific gas-solid system at a given temperature, the adsorption uptake is only dependent on the pressure, and the measurement of the gas uptake as a function of pressure is called an adsorption isotherm.

In this work, the gas adsorption isotherm was measured by a Quantachrome AS-1 surface area & pore size analyzer. Solid sorbent sample was first degassed in a vessel by heating in vacuum. The heating temperature was chosen so that the sample is degassed sufficiently without structural damage. Afterwards, the vessel was transferred to the measurement station where it was cooled to cryogenic temperature (usually 77K), then a series of small doses of sorbate gas was added to the sample vessel while pressure change in the vessel was constantly monitored. The volume of gas adsorbed on the sample was calculated from the pressure change after each dose since there is a direct relationship between pressure and volume. The adsorption uptake was measured with the pressure up to the saturated vapor pressure (p_0) of N₂ at 77K. Then the adsorbed amount is plotted against the relative pressure (p / p_0) to obtain an adsorption isotherm curve.

There are various types of adsorption isotherms for gas molecules on solid surfaces. Brunauer, Deming, Teller, and Sing et, al have classified the adsorption isotherms into six categories

according to the adsorption curve (Fig 2-7). In reality, most adsorption isotherms are different combinations of one or more types of curves listed in the classifications.

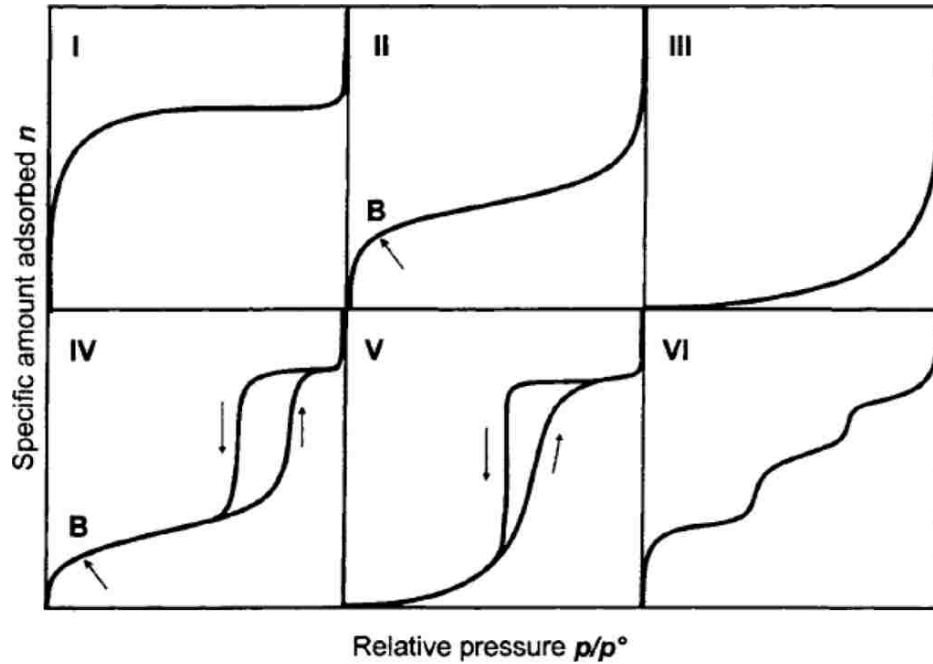


Fig 2-7. Type of isotherms.

Zeolites and many activated carbons with very small micropores usually exhibit type I isotherm. The steep rise of adsorption curve in the low pressure region indicates that most of the adsorption happens inside the micropores where the adsorption potential is very large. In addition, this type of isotherm is also observed when there is a strong interaction between the gas molecules and sorbents, for example, carbon monoxide and hydrogen adsorption on metal surfaces.

A type II adsorption isotherm is commonly observed when multi-layer gas adsorption happens on a non-porous solid surface, e.g., N_2 on the metal oxide surface. At $p/p_0 = 0.3$ (point B), the slope

change on the adsorption curve indicates that a monolayer of gas molecules has been adsorbed on the surface. As the pressure increases, multi-layer adsorption occurs.

A Type III isotherm is seen when the adsorbate gas has a low affinity with the sorbent surface, i.e., the interaction between the gas molecules is stronger than that between gas molecules and solid surfaces, for example, water vapor adsorption on hydrophobic graphite surface. At low pressures, the adsorption uptake is very low and rises when the pressure increases.

A type IV isotherm is typical for mesoporous and macroporous solids. If the sorbent has micropores or the affinity of the sorbate molecules is high, the adsorption curve exhibits a similar pattern with type II isotherm at low pressure regions. When the pressure goes above $p/p_0 = 0.4$, the gas molecules condense inside the mesopore in a liquid state, which is called capillary condensation, resulting in a steep rise in the adsorption curve. After the adsorption is finished at $p = p_0$, the desorption curve does not exactly fit the adsorption curve but shows an adsorption hysteresis. Since the hysteresis happens at the pressure corresponding to mesopores, it is very useful for determining size, distribution and geometry of the mesopores. There are several theories to explain different types and origins of hysteresis. Zsigmondy has proposed that adsorption is a process of wetting the pore surface while the desorption process is a process of liquid exiting the surface so the hysteresis is caused by the difference between the contact angle[12]. Kramer and McBain used an ink bottle model to describe the hysteresis. Foster and Cohan had a more general explanation of this phenomenon by establishing a mathematical model for the liquid meniscus forming during adsorption and desorption[13]. There are also many other models for explaining the hysteresis. For the sake of simplicity here, the ink bottle model will be described here.

In the adsorbed state, gas molecules in the pores are in liquid form, therefore the pore-adsorbate interaction can be described by the Kelvin equation, as depicted in Fig 2-8.

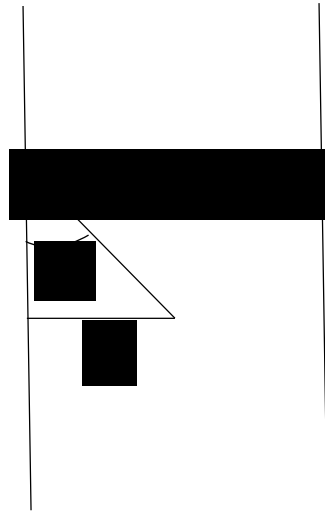


Fig 2-8. Parameters of Kelvin equation.

$$\ln \frac{p}{p_0} = - \frac{2\gamma V_m}{rRT} \cos\theta,$$

Eq. 2-11

where:

p is the saturated vapor pressure inside the capillary,

p_0 is the saturated vapor pressure when the liquid surface is flat,

γ is the surface tension of the liquid,

r is the radius of the capillary,

V_m is the liquid molar volume,

R is the gas constant,

T is the temperature.

According to Eq. 2-11, the saturated vapor pressure p inside the capillary is lower than p_0 on a flat surface, causing the capillary condensation phenomenon inside mesopores and macropores. In an ink bottle pore model in Fig 2-9, the adsorption first happens at the bottle with a radius of R_b , and the desorption first happens at the neck with a radius of R_n . Due to the difference in R_h and R_b , the desorption pressure is going to be smaller than the adsorption pressure, creating the hysteresis in the isotherm curve.

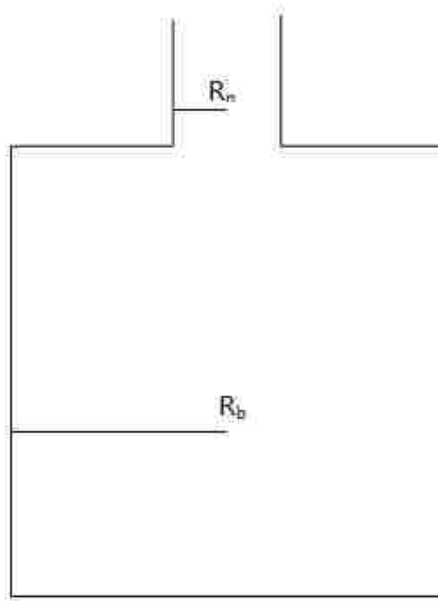


Fig 2-9. Ink-bottle pore model.

A type V isotherm is generally the same as a type IV except at low pressure, where the adsorbate has a low affinity towards the adsorbent, and a type VI isotherm is a very rear step-wise adsorption curve which is seen when a non-polar molecule adsorbs on a non-porous solid link nitrogen on graphitized carbon.

In order to interpret information about the surface area, pore size, and pore distribution of mesoporous materials, a variety of theoretical models have been developed. Among which, Langmuir and BET theories are the most widely used models to calculate the surface area of

porous materials. Langmuir derived an equation to describe the relationship between adsorption capacity and pressure with the following assumptions:

- 1) The adsorption is only monolayer, i.e., only a single layer of gas molecules covers the solid surface,
- 2) The sorbent has a uniform surface, and there is no interaction between the sorbate molecules.

Assuming the portion of the surface covered by gas molecules is θ , then the blank area is $(1 - \theta)$.

So the speed of adsorption and desorption can be described as

$$r_a = k_a p(1 - \theta), \quad \text{Eq. 2-12}$$

$$r_d = k_d p \theta, \quad \text{Eq. 2-13}$$

respectively. At equilibrium, the rate of adsorption and desorption is the same, so

$$\theta = \frac{k_a p}{k_d + k_a p}. \quad \text{Eq. 2-14}$$

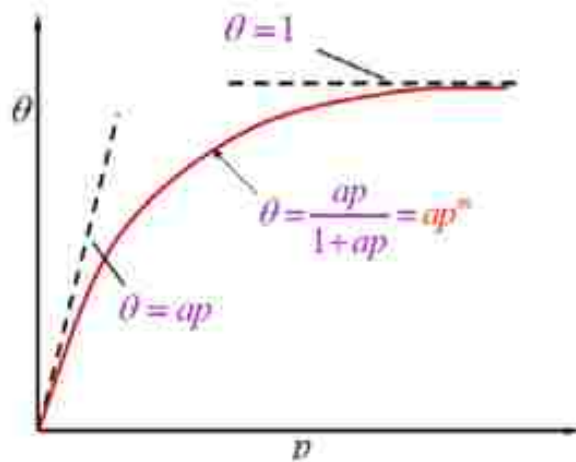


Fig 2-10. Langmuir plot. Ref[7]

The Langmuir plot is based on the assumption of monolayer adsorption and ideal gas behavior, which may not be valid in real applications.

Based on the idea of Langmuir theory, Brunauer, Emmett and Teller have extended the model from monolayer adsorption to multilayer adsorption[7]. The first layer of gas molecules covering the solid surface is still driven by the interaction by the chemical potential between the gas molecules and solid molecules. From the second layer and onwards, the adsorption is driven by the interaction between the gas molecules, so the heat of adsorption is close to the heat of condensation of the gas molecules. At equilibrium, the adsorption capacity is the sum of all layers of gas molecules. Applying these modifications to Langmuir equation, the BET equation can be derived as the following:

$$V = V_m \frac{Cp}{p_s - p} \frac{1 - (n+1)\left(\frac{p}{p_s}\right)^n + n\left(\frac{p}{p_s}\right)^{n+1}}{1 + (C-1)\frac{p}{p_s} - C\left(\frac{p}{p_s}\right)^{n+1}}, \quad \text{Eq.2-15}$$

where V_m is the volume of gas needed for monolayer coverage and p_s is the saturated vapor pressure at the given temperature, n is the layer of adsorption, C is the constant associated with adsorption heat.

If $n = 1$, the BET equation simplifies into the Langmuir equation.

If n is infinite, then $(p/p_s)^n$ is 0, the equation can be simplified into

$$\frac{p}{V(p_s - p)} = \frac{1}{V_m C} + \frac{C-1}{V_m C} \frac{p}{p_s}. \quad \text{Eq. 2-16}$$

Plotting $p / V(p_s - p)$ against p/p_s gives V_m , leading to the calculation of BET surface area

$$S = \frac{A_m L V_m}{22.4 \text{ dm}^3 \text{ mol}^{-1}}, \quad \text{Eq. 2-17}$$

where A_m is the cross section area of the gas molecule. It is noteworthy this equation only applies at partial pressures between 0.05 - 0.35. If the pressure is too low, then monolayer adsorption might not have completed yet, and if the partial pressure is higher than 0.35, capillary

condensation in the mesopores could already take place, breaking the multi-layer adsorption equilibrium.

In addition to surface area, pore volume and pore size distribution can also be obtained from the gas adsorption isotherm. The pore volume can be simply calculated from the volume of gas vapor adsorbed at the saturated vapor pressure when p / p_0 is close to 1. Since the sorbate molecules are condensed into liquid state inside the pores, the pore volume can be calculated accordingly.

The pore size distribution, however, is more complicated to calculate. A widely used method for calculating pore size was developed by Barrett, Joyner, and Halenda (BJH), for the evaluation of cylindrical shaped porous materials by simply considering the capillary condensation in the pore channels.

Because the pore shape was assumed to be cylindrical, pore size can be calculated from the Kelvin equation:

$$r = \frac{-2\gamma V_m}{RT \ln \frac{p}{p_0}}, \quad \text{Eq. 2-18}$$

where γ is the surface tension of the sorbate molecule at the temperature T , V_m is the molar volume of the sorbate.

The development of modern computers has enabled scientists to analysis the pore size by computational simulations. Since the interaction between gas molecules and sorbents are driven by potentials, the computational method aims to simulate an isotherm curve close to the measured curve, by changing different thermodynamic parameters like the affinity of the gas molecule and solid surface, the shape of the pores, isotropy and anisotropy of the molecules and so on. For example, Saito and Foley proposed a method for cylindrical porous materials by modeling 5 physical parameters to fit the adsorption curve[14]. The development of DFT theory

and Monte Carlo algorithm has enabled more accurate evaluation of porous structure by using more complicated functions and parameters[12].

2.6 Electrochemical measurement methods

Electrochemistry is an interdisciplinary subject studying chemical reactions that are subjected to electric voltage and current. Electrochemical characterization methods are of practical importance when determining the electrochemical behaviors of the SSA systems, including the capacitive behaviors and energy efficiency during sweeping. The characterization of electrochemical systems involves a potentiostat, which controls the voltage between a working electrode and a counter electrode while monitoring the current flow as shown in Fig 2-11.

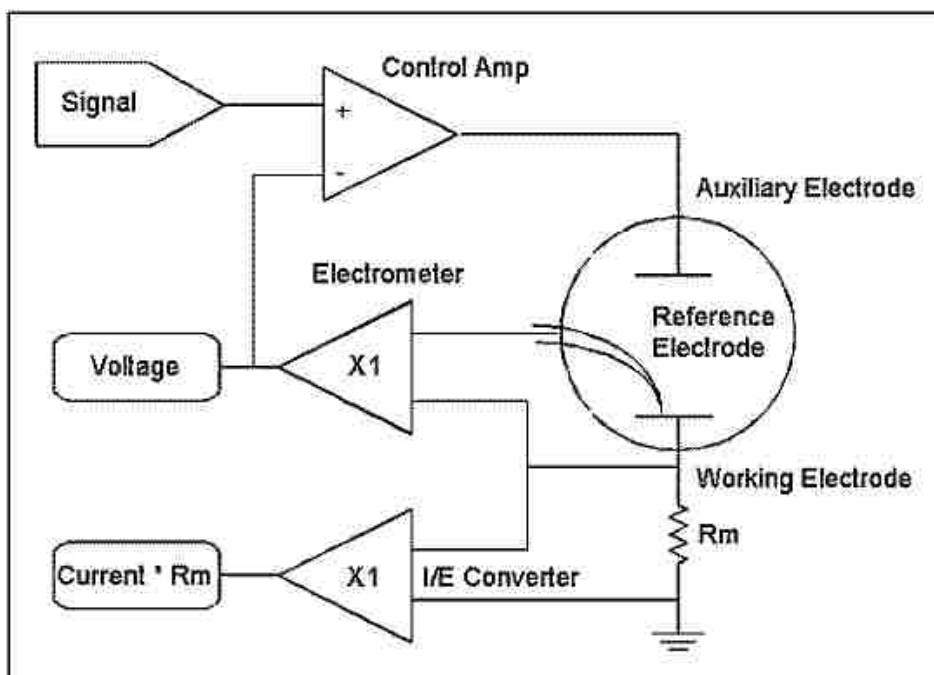


Fig 2-11. Structure of potentiostat. Ref[1]

The electrochemical measurement in this work is done by using a Gamry Ref 3000 series potentiostat. The Gamry can also work in a galvanostatic mode, in which it controls the current input between the working electrode and counter electrode while recording the voltage between them.

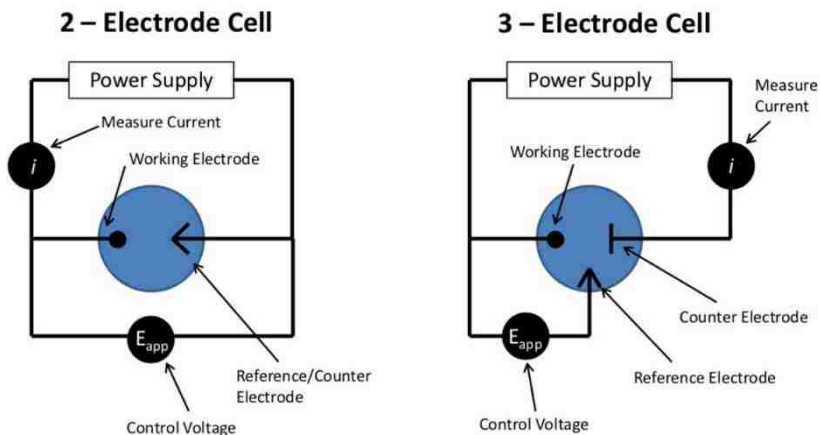


Fig 2-12. 2-electrode setup and 3-electrode setup.

A three-electrode configuration is typically used in an electrochemical measurement, using working electrode, counter electrode and reference electrode such as Ag/AgCl electrode, saturated calomel electrode (SCE), as shown in Fig 2-12. The reference electrode can provide a stable electrode potential and does not charge during the measurement, so it can be used for providing accurate measurement of electrochemical potential. For this reason, three-electrode is preferred in electrochemical measurements. However, most of the work in this paper is completed in a two-electrode configuration where only working electrode and counter reference electrode is included. This setup allows the measurement of electrochemical behaviors across the whole assembly, where accurate and fine measurement of potential is not critical. The two-

electrode setup is commonly used when evaluating energy storage devices in a whole assembly, such as electrochemical batteries, capacitors, fuel cells, solar panels and so on.

2.6.1 Cyclic voltammetry

Voltammetry was developed first in 1922 by Heyrovsky and has become a fundamental and versatile analysis method used for studying various types of electrochemical systems. The basic technique is to measure the current response at a given potential. Usually, in a voltammetry, the voltage of the working electrode is ramped up in a linear pattern versus time and after the set potential is reached, it is swept in the opposite direction to the starting voltage, the current recorded during the voltage scan is then plotted against the sweeping voltage to obtain a voltammetry. Cyclic voltammetry(CV) is the repeated voltammetry scanning on the assembled electrochemical cell.

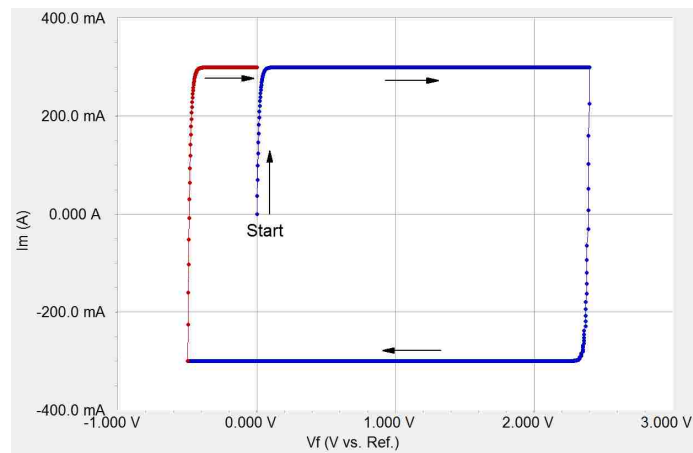


Fig 2-13. Theoretical CV graph of an ideal EDLC with 3 Farads capacitance. Ref[1]

The CV plot of ideal EDLCs shown in Fig 2-13 is a near rectangular shape with constant charging and discharging current, the slight drop at the end of charging cycle due to equivalent series resistance (ESR). The current response to voltage input is almost instant since the charge is stored electrostatically on the electrode with no red-ox reaction happening. Since there is no kinetic factor in the case of ideal EDLC, the electrical double layer forms almost instantly after the voltage ramping begins, then current remains a straight line with a slope of 0 until the voltage goes in the opposite direction. The capacitance can be derived from the following way:

$$C = \frac{Q}{V} = \frac{It}{V} = I \frac{t}{V} = \frac{I}{s} \quad \text{Eq. 2-19}$$

where Q is the charge, V is the voltage, I is the current and s is the scanning speed.

According to the equation, for a given EDLC with a fixed capacitance, the current is proportional to the scanning speed.

However, real-world capacitors are not perfectly ideal EDLCs, and the calculated capacitance is dependent on the scanning speed. Generally speaking, higher scanning speed will yield a lower capacitance and vice versa. This is because in real-world EDLCs, the electrolyte ions have to diffuse from the bulk electrolyte to the electrode surface to form the double layer, which is governed by multiple factors, like the electrolyte viscosity, pore geometry of the electrode, surface roughness and so forth. With a slower charging current, the electrolyte ions will be allowed to diffuse into the pore surface more thoroughly, creating a higher capacitance. So usually a series of scanning speed is chosen to evaluate the behavior of the EDLC versus scanning speed and an appropriate current density for the system, also to find a balance between capacitance and measurement time.

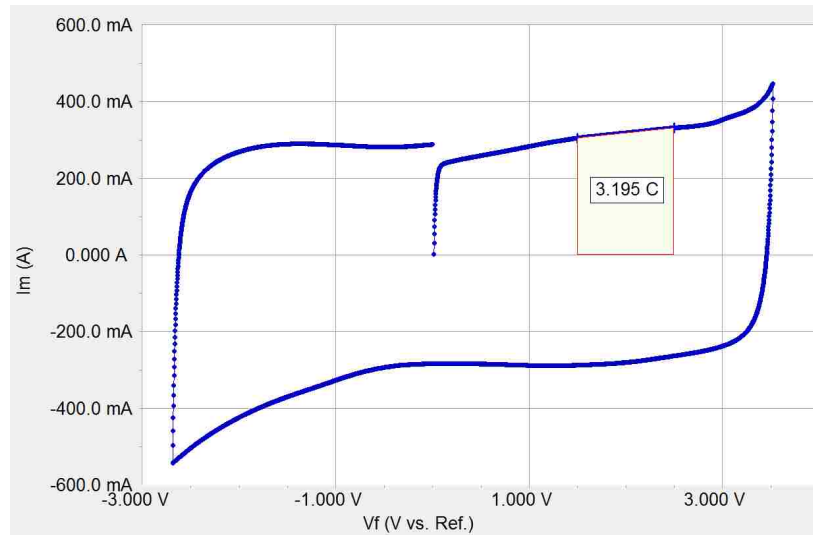


Fig 2-14. CV curve of Nesscap ESHSR-0003C0-002R7. Ref[1]

Shown in Fig 2-14 is a real-world example of commercial EDLC CV scan with a speed of 100 mV/s. The capacitor here shown is a 3F EDLC from Nesscap, part no ESHSR-0003C0-002R7. The CV curve is deviated from the ideal curve due to the diffusion resistance during the initial charging and double layer formation step. The same applies for the curve at the end of the charging cycle while the voltage goes to an opposite direction.

In this scenario, since the charging curve and discharging curve is not completely flat, the capacitance can be calculated from integration of a segment from the charging curve.

$$dQ = C dV,$$

$$\int_{t_1}^{t_2} dQ = C \int_{t_1}^{t_2} dV,$$

$$C = \frac{\Delta Q_{t_2 - t_1}}{\Delta V_{t_2 - t_1}} \quad \text{Eq. 2-20}$$

By choosing an appropriate segment, the capacitance of the Nesscap capacitor can be calculated to be 3.195 F by this method.

In addition to capacitance measurements, cyclic voltammetry can be used to study other electrochemical systems as well. For example, an electrochemical red-ox reaction will generate a peak in the CV curve. However, such applications are beyond the scope of this work.

2.6.2 Galvanostatic charge/discharge measurements

Unlike CV, galvanostatic charge-discharge measures the voltage response of an electrochemical system with a constant current. In this case, pre-set current is flown into the capacitor electrodes, and the voltage change of the EDLC is recorded and plotted against time. After the voltage of the system has reached the preset voltage limit, current is then withdrawn from the capacitor until the voltage reaches the lowest set limit. Repeated scanning is called cyclic charge-discharge (CCD), which is used commonly to evaluate the cycle life, capacitance and power efficiency of an EDLC. The choice of charge/discharge current can also have an impact on the capacitance and energy efficiency, due to the diffusion kinetics mentioned above. A higher current will result in lower capacitance and efficiency while lower current will lead the opposite direction.

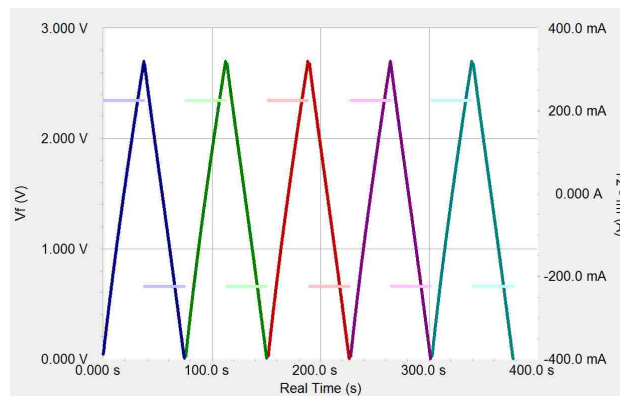


Fig 2-15. Ideal cyclic charge discharge for an EDLC. Ref[1]

Shown in Fig 2-15 is a CCD curve of a nearly ideal EDLC curve. The lighter, horizontal curve represents current to the capacitor while the triangle shaped darker curve represents the voltage.

The capacitance can be calculated from the slope of the curve as the following:

$$C = I \frac{dt}{dV}. \quad \text{Eq. 2-21}$$

Energy efficiency can be calculated from CCD as well. In the charging cycle, energy put into the capacitor can be calculated by the integration area of the voltage with time and energy retrieved from the discharge curve in the same way.

$$E_{charge} = \int p dt = I \int \int dv dt \quad \text{Eq. 2-22}$$

$$E_{discharge} = \int p dt = -I \int \int dv dt \quad \text{Eq. 2-23}$$

Then the efficiency is obtained by dividing the retrieved energy by the input energy. In an ideal EDLC, the energy efficiency would be very close to 100%.

In reality, the CCD behavior of EDLCs is not always ideal. Shown in a Fig is the CCD of a non-ideal supercapacitor that has low power efficiency. The result is obtained from a Nesscap ESHSR-0003C0-002R7 EDLC damaged by overvoltage as an extreme example in Fig 2-16.

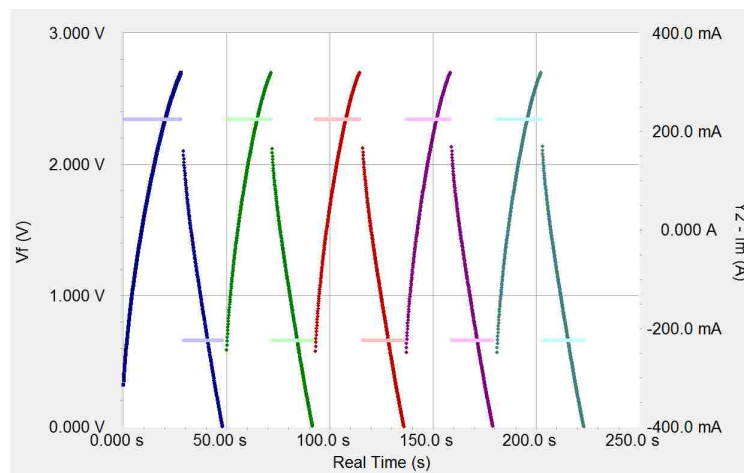


Fig 2-16. Cyclic charge discharge curve of damaged EDLC. Ref[1]

The behavior of this specific ELDC far from idea. The charging curve of the capacitor is closer to an exponential curve than a linear curve, which is caused by high self-discharge of the capacitor. There is also a noticeable voltage drop after at each half cycle, called the IR drop. This resulted from high equivalent series resistance (ESR) of the EDLC. The ESR is contributed from multiple factors, including the contact resistance between the current collector and the carbon electrode, and the diffusion resistance of the electrolyte. These non-ideal behaviors decrease the capacitance and energy efficiency of EDLCs but in reality, it is not possible to eliminate them.

2.7 References

1. Gamry, *Gamry Application Notes*. 2016.
2. *Reactions and characterization of solids*, in *Tutorial chemistry texts 2000*, Royal Society of Chemistry : distributor RSC Distribution Services : distributor Central Book Services : distributor Central Book Services, : Cambridge. p. 208 p.
3. Hammond, C. and ebrary Inc., *The basics of crystallography and diffraction*, in *International Union of Crystallography texts on crystallography 122009*, Oxford University Press, : Oxford ; New York. p. xiii, 432 p.
4. Williams, D.B., C.B. Carter, and SpringerLink (Online service), *Transmission Electron Microscopy A Textbook for Materials Science*, 2009, Springer US, : Boston, MA.
5. Manzano, M. and M. Vallet-Regi, *New developments in ordered mesoporous materials for drug delivery*. *Journal of Materials Chemistry*, 2010. **20**(27): p. 5593-5604.
6. Goldstein, J.I., et al., *Scanning Electron Microscopy and X-ray Microanalysis*, 2003, Springer US, : Boston, MA. p. 1 online resource.
7. Lowell, S., et al., *Characterization of Porous Solids and Powders: Surface Area, Pore Size and Density*, in *Particle Technology Series*, 2004, Springer Netherlands : Imprint: Springer, : Dordrecht. p. 1 online resource.
8. Pennycook, S.J., et al., *Transmission Electron Microscopy: Overview and Challenges*. *AIP Conference Proceedings*, 2003. **683**(1): p. 627-633.
9. Dahmen, U., et al., *An update on the TEAM project — first results from the TEAM 0.5 microscope, and its future development*, in *EMC 2008 14th European Microscopy Congress 1–5 September 2008, Aachen, Germany: Volume 1: Instrumentation and Methods*, M. Luysberg, K. Tillmann, and T. Weirich, Editors. 2008, Springer Berlin Heidelberg: Berlin, Heidelberg. p. 3-4.
10. Assoufid, L., et al., *Compact X-ray and Extreme-Ultraviolet Light Sources*. *Optics and Photonics News*, 2015. **26**(7): p. 40-47.
11. Shimizu, K., T. Mitani, and SpringerLink (Online service), *New Horizons of Applied Scanning Electron Microscopy*, in *Springer Series in Surface Sciences*, 2010, Springer-Verlag Berlin Heidelberg, : Berlin, Heidelberg.
12. Rouquerol, F., J. Rouquerol, and K.S.W. Sing, *Adsorption by powders and porous solids : principles, methodology and applications*. 1999, San Diego: Academic Press. xvi, 467 p.
13. Cohan, L.H., *Sorption Hysteresis and the Vapor Pressure of Concave Surfaces*. *Journal of the American Chemical Society*, 1938. **60**(2): p. 433-435.
14. Saito, A. and H.C. Foley, *Curvature and parametric sensitivity in models for adsorption in micropores*. *AIChE Journal*, 1991. **37**(3): p. 429-436.

3 Carbon dioxide capture and concept of Supercapacitive Swing Adsorption

3.1 Global warming caused by carbon dioxide

In the past three decades, the global surface temperature has been increasing steadily at a rate of 0.2 °C per decade[13]. Global warming could cause natural disasters such as glacier melting, desert expansion, decreased crop productivity and so forth[17]. It is one of the most serious environmental issues that humanity is facing today. This phenomenon is a long-term process associated with natural fluctuations in climate. However, human activity also has great influence as well.

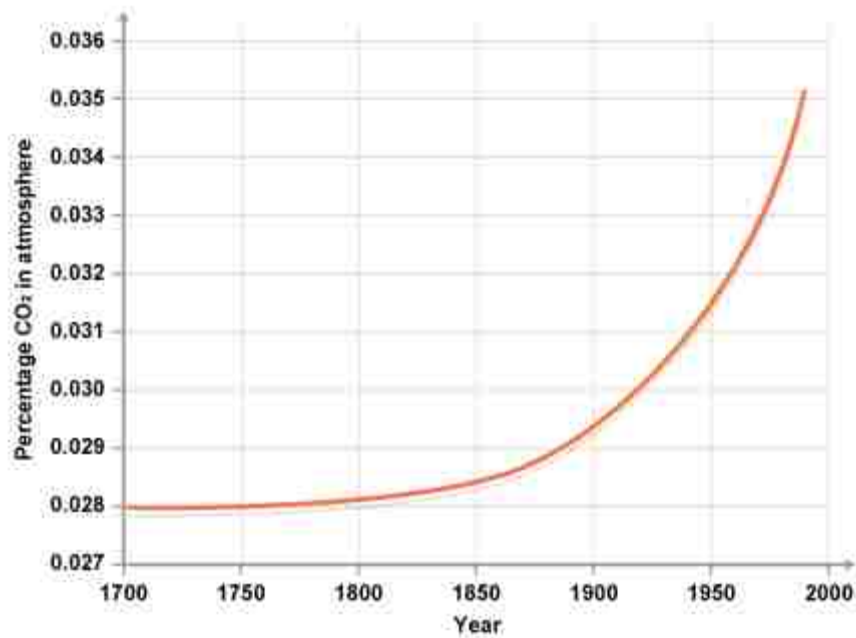


Fig 3-1. The rise of atmospheric CO₂ concentration since industrial revolution. Source: [5]

For centuries, the volume percentage carbon dioxide concentration in the atmosphere has stayed at a steady 0.028% (Fig 3-1), but after the industrial revolution, it started to increase dramatically by 40%, reaching 0.040% in mid-2013, and the global average temperature has increased in a similar pattern (Fig 3-2). Carbon dioxide is believed to be the major cause of global warming since it absorbs energy from infrared radiation. Therefore the energy is trapped in the atmosphere,

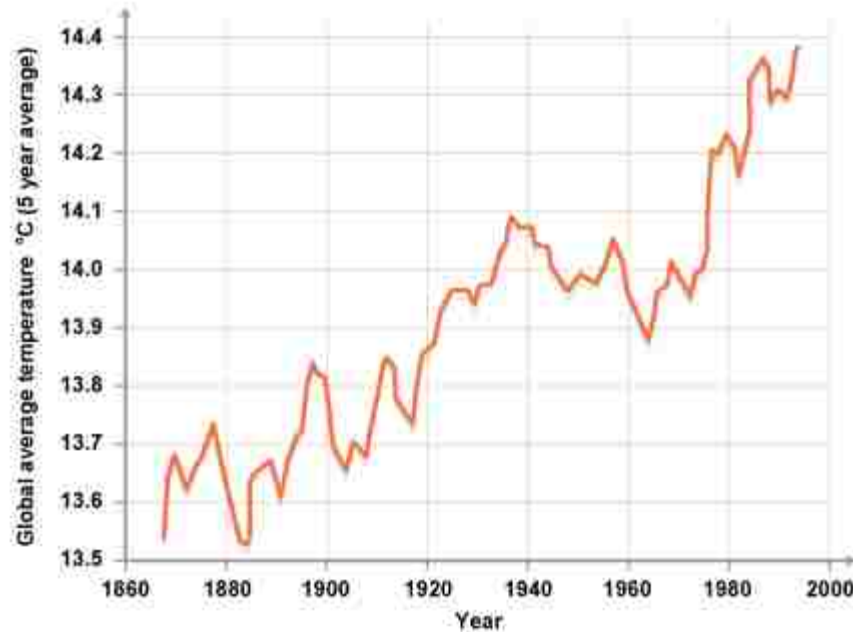


Fig 3-2. Global average temperature trend. Source:[5]

The Sun has a surface temperature at around 6000K and emits short-wave radiations in the range of 0.2 – 4 μm , while the earth with a surface temperature of 255K radiates in the range of 4-100 μm . Carbon dioxide is an inefficient short wave absorbing molecule but it captures the longwave emitted by earth surface, then the CO_2 molecules absorbs the energy emitted from the earth surface. Therefore the increased carbon dioxide concentration in the atmosphere can be the cause of global warming issue [18, 19].

The increase in carbon dioxide concentration is tightly associated with the consumption of fossil fuels, including coal, petroleum, natural gas and so forth[16]. Over the past several decades, over three-quarters of CO₂ emissions came from the combustion of fossil fuel. To reduce the carbon emissions, various approaches have been evaluated and adopted, including the following[20]:

- Improving the heat efficiency of power plants;
- Selecting fuel with low carbon contents, such as hydrogen and natural gas;
- Build renewable energy infrastructures like solar and wind energy;
- Carbon dioxide capture and sequestration (CCS).

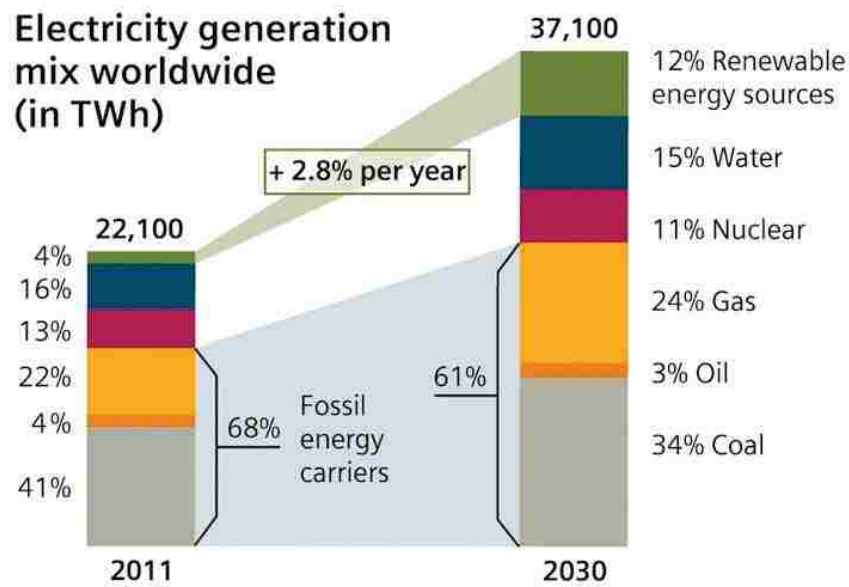


Fig 3-3. Worldwide demand for power. Source:[3]

With the development of human society, the global energy demand is expected to increase by 2.8 % per year (Fig 3-3). Although renewable energy is projected to grow steady over the next few decades, fossil fuel will still provide over 60% of generated electrical energy worldwide, due to its high abundance, low cost, and well-established global trading markets. Additionally, the transition to clean energy sources is hindered by their inherent limitations[21]. For example, solar energy

still has relatively high capital investment and low efficiency, water, and wind energy are severely limited by locations, and nuclear energy rose safety concerns in recent years especially since the Fukushima Daiichi nuclear disaster in 2011[22, 23].

3.2 Carbon capture and sequestration techniques

Due to these limitations, carbon capture and sequestration (CCS) techniques have gained significant attention. CCS captures CO₂ emissions from fossil fuel power plants and stores it in compressed cylinders for further utilization. The general scheme for CCS is illustrated in Fig 3-4. Depending on the combustion and capture methods, it can be divided into oxy-fuel combustion, pre-combustion capture, and post-combustion capture.

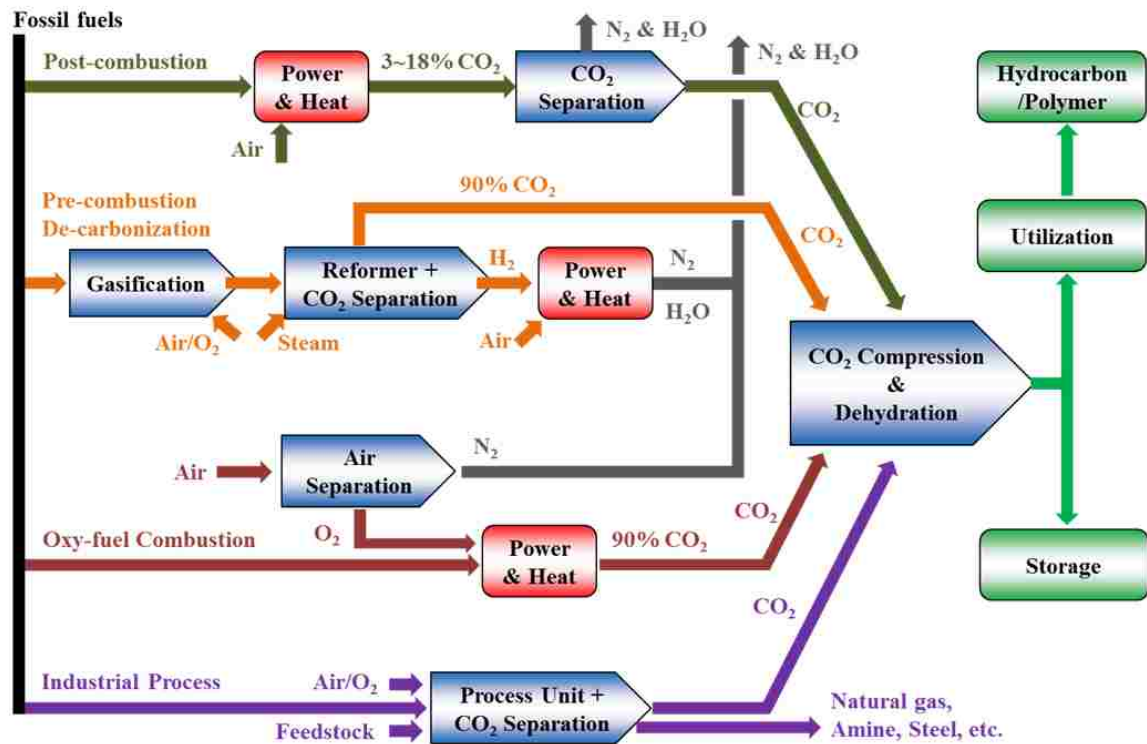


Fig 3-4. Overview of CCS techniques. Ref[15]

3.2.1 Oxy-fuel combustion

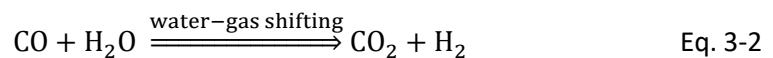
Oxy-combustion uses oxygen rather than air as oxidizing agents for the combustion to obtain exhaust gas with high carbon dioxide concentration. In this process, oxygen is usually obtained by cryogenic separation of air. During the combustion, part of exhaust CO₂ is mixed with fresh oxygen to reduce the total concentration of O₂ for combustion to avoid overheating. Carbon dioxide capture is easily accomplished by physical absorption techniques since the flue gas contains high concentrations of CO₂, H₂O and minor concentrations of sulfur species[24].

Due to the high combustion temperature, the heat efficiency of oxy-combustion is greater compared with air combustion, enabling the use of a wide range of fuels besides fossil fuel, including biomass and agricultural waste that has a lower heat of combustion. Since the flue gas does not contain nitrogen, the total emission from oxy-combustion is significantly reduced, eliminating the need for NO_x reducing devices, as well as increasing overall heat efficiency. Unfortunately, the high cost of oxygen separation and high parasitic load of operation has prohibited the widespread usage of oxy-fuel combustion.

3.2.2 Pre-combustion CO₂ capture

Pre-combustion of CO₂ is the procedure of removing carbon dioxide from fossil fuels before combustion, and it is best suitable for Integrated Gasification Combined Cycle (IGCC)[25]. When gasifying a fossil fuel like coal, air (oxygen) and H₂O pass through coal at high temperature to get syngas with high concentration of CO (40-60%) and H₂ (20-35%), then through a water-gas shift reaction, the syngas is converted to high concentration of CO₂ (up to 50%) and H₂.

The reactions can be described as the following.





The products of these reactions are primarily CO₂ and H₂, which can be easily separated by adsorption or membrane-based techniques[26]. Then the hydrogen gas is directly used as a clean fuel with only H₂O generated after the combustion.

3.2.3 Post-combustion CO₂ capture

Post-combustion capture refers to the process of capturing CO₂ from flue gas generated by combustion of coal with air. Post-combustion capture does not require major modifications to the combustion facilities and can be used in other CO₂ emission industries, for example, cement manufacturing, steel production and so forth[27]. Oxy-fuel combustion suffers from high oxygen production cost and oxygen related corrosion issues, pre-combustion requires retrofit of existing facilities to accommodate hydrogen combustion, therefore currently post-combustion capture is the economically most promising process, and the most studied technique (Fig 3-5).

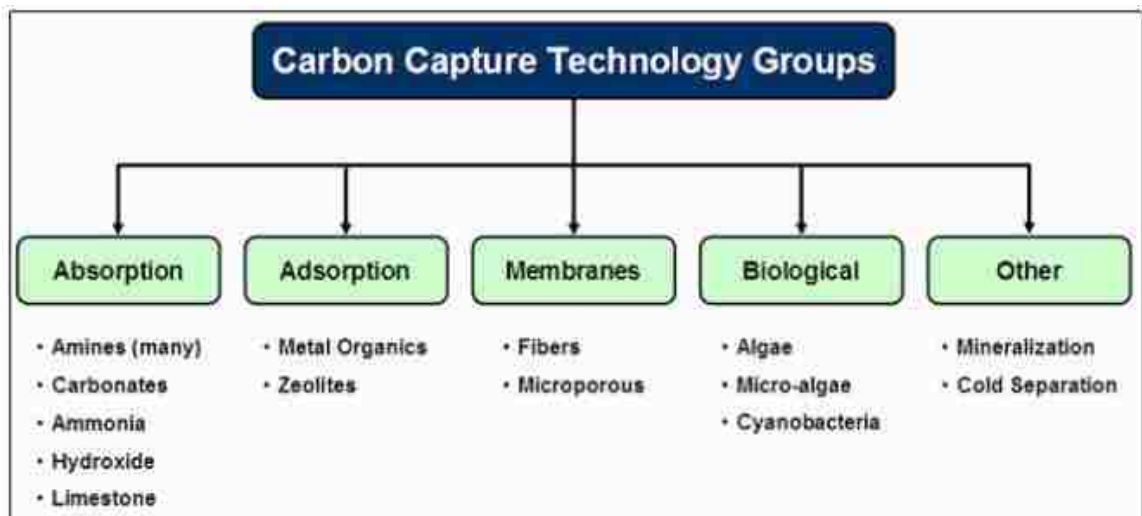


Fig 3-5. Post-combustion CO₂ capture techniques. Source:[8]

3.2.3.1 Chemical absorption methods

Currently, the most well-developed post-combustion CCS technique is based on chemical absorption of CO₂. In such a process, the flue gas is passed through an absorption column containing a CO₂-absorbing solvent. Afterwards, the CO₂ saturated solvent is regenerated at a higher temperature and the released CO₂ is then compressed for storage. The working temperature of chemical absorption is around 40 – 60 °C, the stripping temperature is around 80 – 120 °C and the working pressure is at ambient pressure[16]. In addition, it can also work with relatively low concentrations of carbon dioxide.

The most widely used absorbents are alkanolamines, including primary, secondary and ternary amines like monoethanolamine (MEA), diethanolamine (DEA) and N-methyldiethanolamine (MDEA). The commonly used sorbents are listed in the table 3-1. Generally speaking, primary amines have the highest reactivity towards CO₂, while tertiary amine shows the lowest reactivity. On the contrary, tertiary amine has the highest CO₂ loading capacity. The difference can be explained by the different reaction pathways for different amines. In the case of primary and secondary amines, a Zwitterion intermediate is formed, then it is transformed to carbamate salt, as shown from eq. 3-4 to eq. 3-7.



So the overall reaction is



For tertiary amine, the reaction can be described by eq. 3-8.



Afterwards, the intermediate is then hydrolyzed into the ammonia bicarbonate as the following.

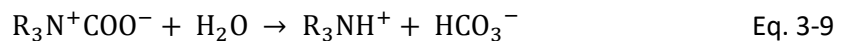




Fig 3-6. Common amine species for CO₂ absorption. Ref[16]

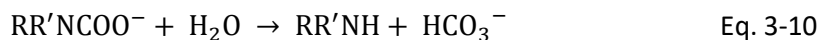
Sorbent	MEA	AEEA	PZ	MDEA	NaOH	AMP	DETA
MW (g/mol)	61.08	104.15	86.14	119.16	40	89.14	103.17
Density (g/cm ³)	1.012	1.029	1.1	1.038	1.515	0.934	0.955
Boiling point (K)	443	513	420	243	1390	438	207
Vapor pressure at 273 K (kPa)	0.0085	0.00015	0.1066	0.0013	0.4	0.1347	0.02

Vapor pressure at 393 K (kPa)	15.9	0.969	41.66	N/A	N/A	N/A	N/A
Solubility in water	Soluble	Soluble	14 wt%	Soluble	Soluble	Soluble	Soluble
Pseudo first order rate constant at 298 K (m ³ /kmol/s)	7,000	12,100	53,700	3.5	N/A	681	49,740
Activation energy (kJ/mol)	46.7	N/A	35	44.3	N/A	41.7	N/A
CO ₂ uptake (mol of CO ₂ /mol of sorbent)	0.5	1.0	1.0	1.0	0.5	1.0	1.0

Table 3-1. Physical and chemical properties of sorbents. Ref[16]

Due to their advantages and disadvantages, a mixture of amines can be used to enhance capture efficiency and lower regeneration cost. In addition, some amines with special functions are also used.

For example, though AMP is a primary amine but its steric characters destabilize the carbamate structure, leading to the hydrolysis of carbamate as the following reaction[16]:



Since another free amine molecule is generated, one mole of AMP can absorb one mole of carbon dioxide molecules. Piperazine is often used as a reaction promoter since it can form carbamate quickly with carbon dioxide molecules[28].

Though it is the most mature CCS technology today, chemical absorption still suffers from several drawbacks. The amines can degrade during the chemical absorption process of carbon dioxide. At high temperatures, dissolved oxygen in the solution can cause oxidative degradation to the amines. Carbamate polymerization can also cause loss of sorbent as well. For example, to capture a ton of carbon dioxide, 2.2 kg of MEA would be consumed in the process[16]. The absorption capacity of CO₂ is limited (up to 1:1 molar ratio), and the amine species can be degraded by SO₂ and NO₂ in the flue gas. In addition, the energy consumption during regeneration also leads to a high parasitic load on power plants.

3.2.3.2 Membrane-based separation

The membrane separation technique first appeared in the 1970s and got quickly adapted by the market after Monsanto developed the Prism for separating H_2 and N_2 in 1979[29]. Nowadays this method also used in other gas systems such as separating O_2 from N_2 , CO_2 from CH_4 and so forth[30]. The separation is driven by the different rate of permeation of different gases through the membrane (Fig 3-7). Generally, there are two types of membranes for separation, porous membranes, and dense membranes. In the porous membrane, the gas diffusion kinetics are determined by the kinetic diameter of the molecule and the pore size of the membrane, leading to different permeation rate for each gas component. For dense membranes, the gas diffusion can be described by a dissolve-diffuse model. Gas molecules are first dissolved in the membrane and diffuse to the other side, so the separation is determined by the solubility of the gas components.

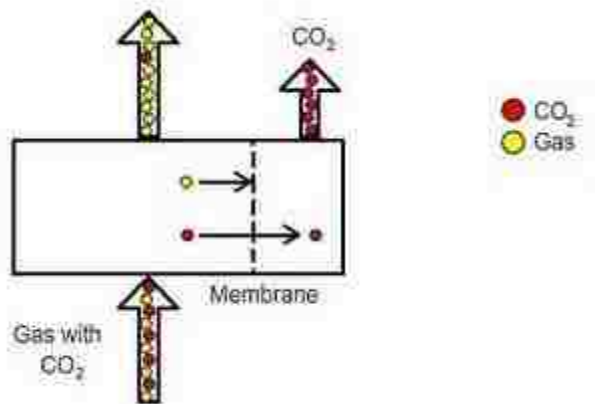


Fig 3-7. Membrane-based CO_2 separation. Source: [1]

The flue gas is pressed against the membrane and carbon dioxide is selectively permeated. In order to achieve high separation efficiency, there are some desired properties of the membrane listed below:

- High selectivity of CO_2 over other gas molecules
- High diffusion rate

- Thermal, mechanical, and chemical stability
- Long lifespan

Many efforts have been devoted to finding appropriate membrane materials for CCS. Currently, membranes can be divided into two categories, inorganic membranes, and polymer membranes. Porous and dense inorganic materials are both used as separators[31]. A porous inorganic membrane is often supported by a porous metal or ceramic support, such as alumina materials (α - and β -), zirconia, porous stainless steel. Among the porous membranes, zeolite is the most important family of materials for separation due to their unique size selectivity, chemical, and physical stability[32]. More recently, metal organic frameworks (MOFs) have also been explored as candidate materials for gas separation applications. MOF materials have intriguing properties such as highly uniform nanopores, tunable pore size, and geometry. In addition, they can also be chemically modified to enhance their carbon dioxide affinity, therefore, MOFs are good candidates for CCS purposes[33]. A dense inorganic membrane is usually an electrolyte material through which ions are transported at elevated temperatures. For example, dense molten carbonate membrane is developed recently for CO₂ separation at temperatures higher than 723 K[34]. In general, inorganic membranes have excellent thermal and physical stability. However, their operation usually requires high pressure which makes the separation process energy demanding.

Polymer membranes are also commonly used for CO₂ separation. Polyethylene (PE), polycarbonate (PC), polysulfone (PS) as well as amino groups containing polymers like polyethyleneimine, are polymers used for CO₂ separation frequently[35]. In these non-porous polymer membranes, CO₂ molecules undergo a solution-diffusion mechanism. The advantage of polymer over inorganic membranes includes low production cost, high selectivity, ease of

synthesis and so on. However, they suffer from poor thermal stability and the flue gas needs to be cooled down to around 40-60 °C before separation.

3.2.3.3 Pressure swing adsorption (PSA)

Over the past few decades, pressure swing adsorption became a well-developed technique for gas separation industry[10]. In a PSA apparatus, a porous solid sorbent is packed into spherical pellets or extruded rods in a column. The flue gas is fed through the sorbent bed in order to make contact with the porous solids. The gas component that has a low affinity toward the sorbent (N₂ in this case) will break through the column faster, while the more strongly adsorbed component (CO₂) takes longer to break through. After the sorbent in the column is saturated, the feeding gas stream is stopped and the sorbent is regenerated to release the high concentration CO₂.

In pressure swing adsorption, regeneration of the sorbent is achieved by changing the pressure in the column. Sorbents with a large difference in CO₂ uptake capacity at low partial pressure and high partial pressure are usually chosen for PSA [9]. The amount of CO₂ captured by one cycle is then determined by the capacity difference between these two pressures.

$$\Delta q = q_{feed} - q_{regen} \quad \text{Eq. 3-11}$$

For example, in Fig 3-8, sorbent material 1 with a higher Δq is more suitable for PSA than sorbent material 2.

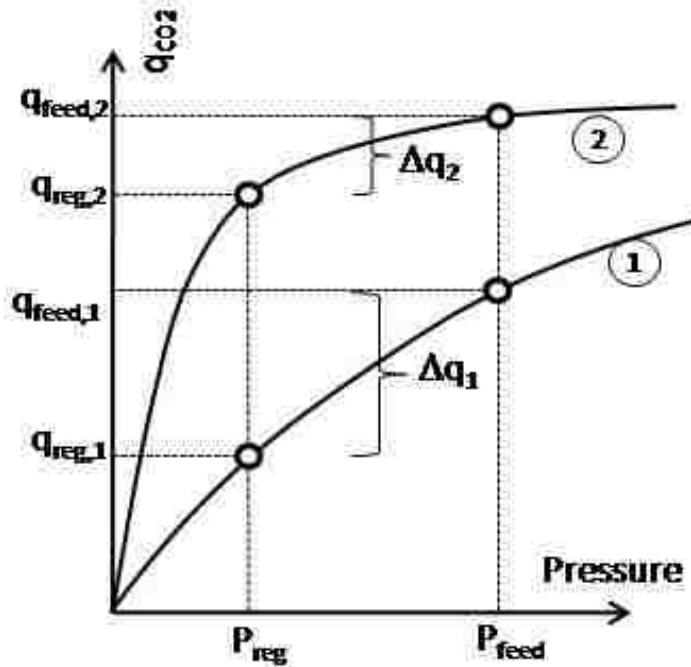


Fig 3-8. Working capacity for PSA. Ref[9]

The state-of-art PSA apparatus contains a two-column setup designed by Charles Skarstrom depicted in Fig 3-9. The gas feed input is between V1 and V2, the exhaust is between V7 and V8, the CO₂ container is between V3 and V4. The two-column setup is used to increase the working efficiency of PSA cycles. In a typical Skarstrom cycle, four steps are included[10].

- 1) Feed. Flue gas is fed through column 1 at an elevated pressure until column 1 is saturated with CO₂.
- 2) Blow. The pressure in column 1 is reduced by venting the gas into the CO₂ container.
- 3) Purge. In order to additionally remove CO₂, column 1 is purged from the exhaust of column 2 and the purging flow is driven by the pressure difference between the two columns.

4) Press. After the sorbent cleaned and ready to take more carbon CO₂, column 1 is pressurized to the adsorption pressure by the feed gas.

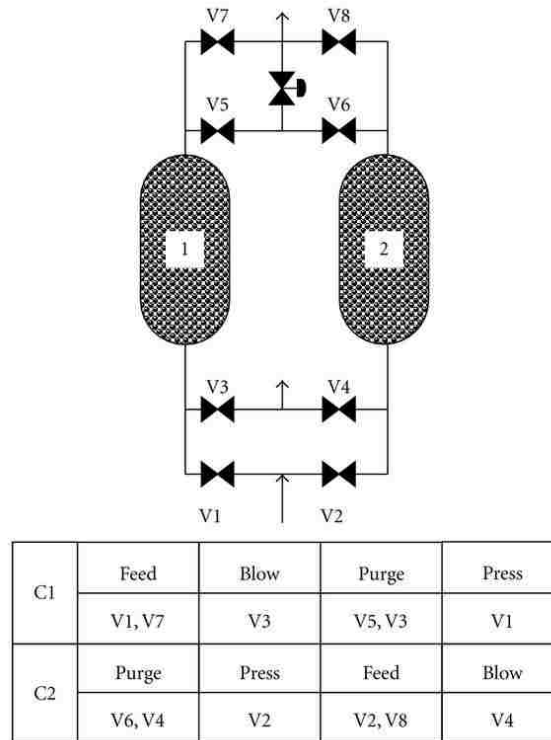


Fig 3-9. Typical PSA operating cycle. Ref[10]

These 4 steps are a cycle for column 1 to perform a PSA cycle. Meanwhile, column 2 performs the same sequence that is 2 steps apart from column 1. The combined steps from both columns give a complete PSA cycle with the ability to separating a continuous flue gas.

PSA is a general gas separation technique that can be applied to other gas mixture systems besides CCS by varying the sorbent selection. For example, the zeolite 5A, carbon molecular sieves (CMS) are used for separating nitrogen from oxygen, ETS-4 titanosilicates sorbents can selectively separate CH₄ from gases like H₂S, CO₂, and N₂[36].

3.2.3.4 Temperature swing adsorption

In addition to PSA, temperature swing adsorption (TSA) is also actively studied as the post-combustion CO₂ capture technique. TSA works in a similar pattern as PSA, using selective sorbent bed columns for the separation of CO₂ and nitrogen. Compared with PSA, in TSA the sorbent regeneration is completed via changing the temperature of the column instead of pressure[37].

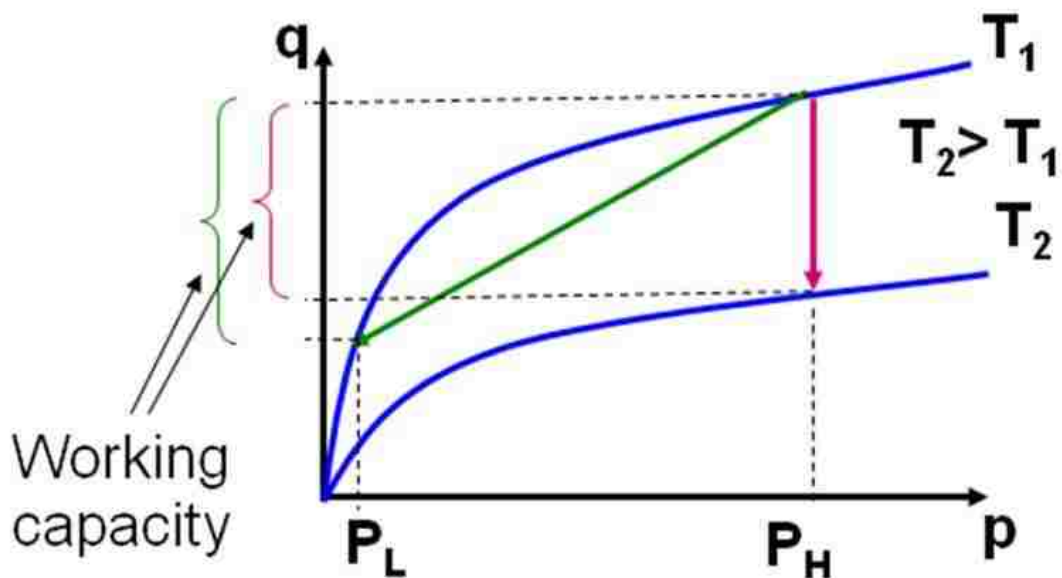


Fig 3-10. Working capacity for TSA. Image source: [6]

In TSA, the working capacity of the sorbent material is controlled by the enthalpy of adsorption capacities. For the sorbent material, the adsorption capacity decreases with temperature. The working capacity is determined by the capacity difference between the temperatures (Fig 3-10).

$$\Delta q = q_{t1} - q_{t2} \quad \text{Eq.3-12}$$

The full process is comprised of two half cycles. In the adsorption half cycle, the flue gas is fed through the sorbent bed and carbon dioxide is selectively adsorbed. After the sorbent bed is

saturated, it is regenerated by reflux or purging while heating the column. Like PSA, it can also use a two-column setup to achieve the ability of continuous operation.

Oak Ridge National Laboratory has developed a variant of TSA called electric swing adsorption (ESA)[38]. Similar to TSA, ESA also uses temperature as a driving force for regeneration of sorbent beds. In a conventional TSA process, heating and desorption are achieved by flowing hot N₂ or recovered CO₂ through the column[39, 40]. This requires a complicated heating stage for the gas feed. In ESA, the sorbent bed is specifically engineered to be electrically conductive and during the heating, stage heat is generated through resistive heating on the sorbent material according to eq. 3-13

$$P = I^2R \qquad \text{Eq. 3-13}$$

The current flows through the conductive sorbent, so heat is generated uniformly across the sorbent material. This technique eliminates the need for gas heating stages before the sorbent column and provides much more efficient heating of the sorbent, which leads to higher energy efficiency and faster regeneration speed.

In addition, TSA can also be used in conjunction with PSA to provide a system with higher working capacity[14]. As depicted in Fig 3-10, the flowing gas is fed through sorbent bed until saturation. Then the system is depressurized and heated simultaneously for the regeneration of the sorbent material. After the purging step, the column is actively cooled and pressurized again for another cycle.

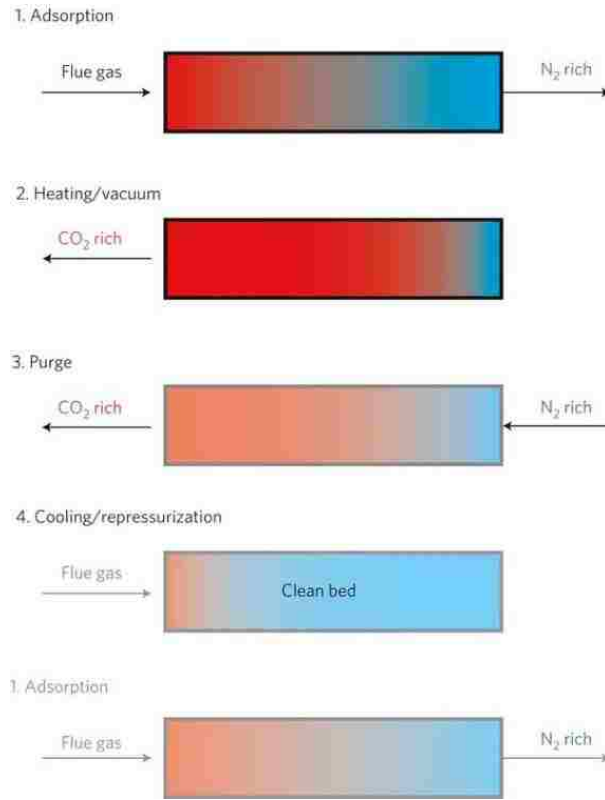


Fig 3-11. Combined TSA and PSA cycle. [14]

3.2.4 Disadvantages of current carbon capture techniques

Despite the efforts put into developing CCS techniques, current technology still has their inherent limitations. Table 3-2 is a briefly describes advantages and disadvantages for each kind of CCS technologies.

Capture techniques	Suitable application area	Advantages	Disadvantages

Pre-combustion capture	Coal-fired power plants Coal-gasification power plants	The exhaust gas contains high CO ₂ concentration, easily collected. Water-gas shift reaction apparatus is fully developed and used in industry	Requires to retrofit existing plant to accommodate hydrogen combustion, high parasitic load, high capital investment and operational cost
Oxy-fuel combustion	Coal-fired and gas-fired power plants	High CO ₂ concentration from exhaust gas, high combustion efficiency, versatile fuel choices, established oxygen separation technology	High parasitic load on the power plant, High cost of cryogenic O ₂ production, corrosion problem
Chemical absorption	Various types of CO ₂ emitting industry	High CO ₂ absorption efficiency by forming chemical bonds, currently most mature CO ₂ capture technique	Requires significant amount of energy for regeneration, sorbent might be corrosive and the environmental

			impact is also a consideration.
Membrane separation	Various types of CO ₂ emitting industry	Simple apparatus setup, continuous operation, mature technology for other separations	Stability and longevity of membrane, Needs large amount of energy to separate low CO ₂ partial pressure flue gas
Pressure swing adsorption	Various types of CO ₂ emitting industry	Fast kinetics, fully automated, continuous operation, demonstrated by pilot plants	High parasitic load, Pressure drop in the column affect adsorption efficiency
Temperature swing adsorption	Various types of CO ₂ emitting industry		Slow kinetics, heating, and cooling requires a lengthy gas pipe setup, large energy consumption for regeneration

Table 3-2. Comparison of different CCS techniques

In order to go around the limitations that these CCS techniques have currently, we have developed a fundamentally new technique called the supercapaitive swing adsorption (SSA), whose concept is based on supercapacitors. By controlling the surface charging, SSA reversibly changes the adsorption capacity of activated carbon materials. The concepts and experimental details of SSA will be described in the following chapters.

3.3 Concept of supercapacitors

Since the first patent in 1957 and the initial market deployment in 1969, supercapacitors have gained significant interest since the oil crisis the late 20th century, due to their excellent power density, long cycle life, and low production cost[41]. Currently, a number of companies, including Maxwell, EPCOS, NEC, Ness, Panasonic, are actively investing in the development and application of supercapacitors.

From a physical point of view, capacitors are devices used to store charges in an electric field. Capacitance describes a capacitor's ability to hold charges and is defined in eq 3-14.

$$C = \frac{Q}{V} \quad \text{Eq. 3-14}$$

Where:

C is the capacitance of the capacitor,

Q is the charge stored by the capacitor,

V is the voltage between the capacitor plates.

There are many types of capacitors, the most fundamental model for capacitors is a parallel plate capacitor (Fig 3-12). The parallel-plate model contains two parallel plates, separated from each other by a dielectric media with a permittivity of ϵ .

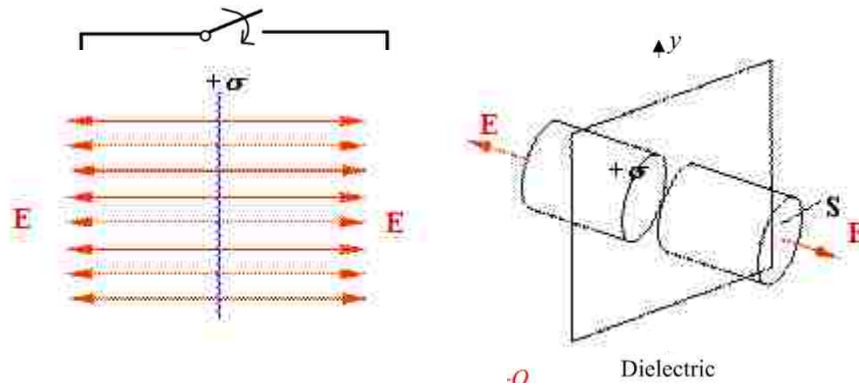


Fig 3-13. Electric flux and Gauss' Law. Source: [4]

When the capacitor is charged up, opposite charge +Q and -Q is stored in the two size of the capacitor. The capacitance of the parallel-plate model can be calculated from the Gauss' law as the following. Assuming an infinite large conductor plate with charge density + δ , the electric field flux is perpendicular to the plate (Fig 3-13 left) and point outwards on both sides of the plate. Assuming a cylinder which is intersected by the plate with an area of S (Fig 3-13 right), E is the electric field, according to Gauss' Law,

$$\oiint \vec{E} d\vec{s} = 2 E * S = \frac{Q}{\epsilon} \quad \text{Eq. 3-15}$$

$$E = \frac{\delta}{2\epsilon} \quad \text{Eq. 3-16}$$

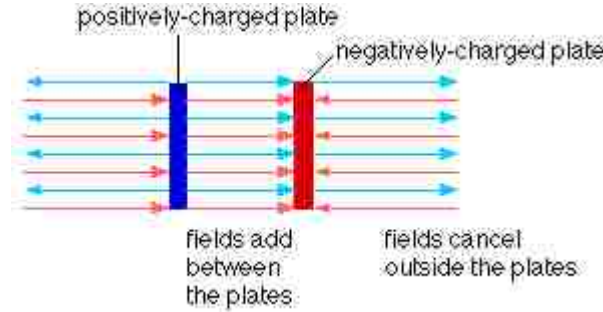


Fig 3-14. Electric fields between plates. Source:[2]

So for two parallel plates with the same charge amount but different polarity (Fig 3-14), the electric field outside the plate is canceled out and the electric field between them is added as

$$E = \frac{\delta}{\epsilon} \quad \text{Eq. 3-17}$$

Assuming a distance d between the two plates, the voltage drop between the plates is then calculated from

$$V = E * d = \frac{\delta}{\epsilon} * d \quad \text{Eq. 3-18}$$

The charge on a given area A is

$$Q = A\delta \quad \text{Eq. 3-19}$$

So the capacitance of a parallel plate capacitor is

$$C = \frac{Q}{V} = \frac{A\delta}{\frac{\delta}{\epsilon}d} = \epsilon \frac{A}{d} \quad \text{Eq. 3-20}$$

where ϵ is the combined dielectric constant, if there is no media in between, then it's the permittivity of vacuum ϵ_0 , A is the area of the parallel plate, d is the distance between the plates.

The energy total energy stored in the power density can be calculated from integrating the charging current with time until the designated charge voltage V .

$$E = \int_0^t p \, dt = \int_0^t iv \, dt = \int_0^t \frac{dq}{dt} v \, dv = \int_0^t \frac{C \, dv}{dt} v \, dt = C \int_0^t v \, dv = \frac{1}{2} CV^2 \quad \text{Eq. 3-21}$$

The maximum power a capacitor can output is dependent on the external load resistance. It is noteworthy that the internal resistance is also acting as a load. The internal resistance, which is often referred to as equivalent series resistance (ESR) consists of contact resistance between electrodes and current collectors, moving resistance of the ions, electrode resistance, etc. When calculating the discharging power, the usual practice is assuming a “matched impedance” model where the external load is equal to the internal ESR of the capacitor, with this load, half of the energy is used to perform electric work and the other half is transformed into heat. Therefore a practical power output for a capacitor can be given by eq. 3-20:

$$P_{max} = \frac{V^2}{4R} \quad \text{Eq. 322}$$

According to eq. 3-14, the capacitance is proportional to the area of the electrode and inversely proportional to the distance between the plates. In order to increase the capacitance, one has to either increase A or reduced the distance. In 1879, Helmholtz discovered a double layer ion storage process based on the separation of charged ions from electrolytes and subsequently led to the discovery of supercapacitors, or electrochemical double layer capacitors (EDLCs). There is another type of supercapacitor called pseudocapacitors, which stores energy by transferring charge in between electrode and electrolyte in Faradaic reactions[42]. However, pseudocapacitor is beyond the scope of this thesis and will not be discussed here.

Unlike conventional capacitors, supercapacitors store charges on high surface area electrode via a thin dielectric layer. A typical supercapacitor is comprised of three major components: high surface area electrode, electrolyte, and separator (optional). Electrodes are usually pressed or cast onto thin metal layer acting as the current collector. A separator membrane sits between electrodes from short-circuiting between the electrodes, if the electrodes are separated far enough from each other, the separator can be omitted. The working principle of supercapacitors

is described in Fig 3-15. By charging the capacitor through the power supply, the electrode surface is accumulated with charges, then ions in the electrolyte with opposite charge are attracted to the electrode surface, thus forming an electric double layer. Depending on the nature of electrolytes, the charging voltage is limited to prevent Faradaic reactions happening. The distance between opposite charges ranges from a few Angstroms to a few nanometers, determined by the radius of the solvation shell of electrolyte ions. The combination of large surface area and short distance of the double layer gives supercapacitors very large capacitance, up to hundreds of Farads per gram.

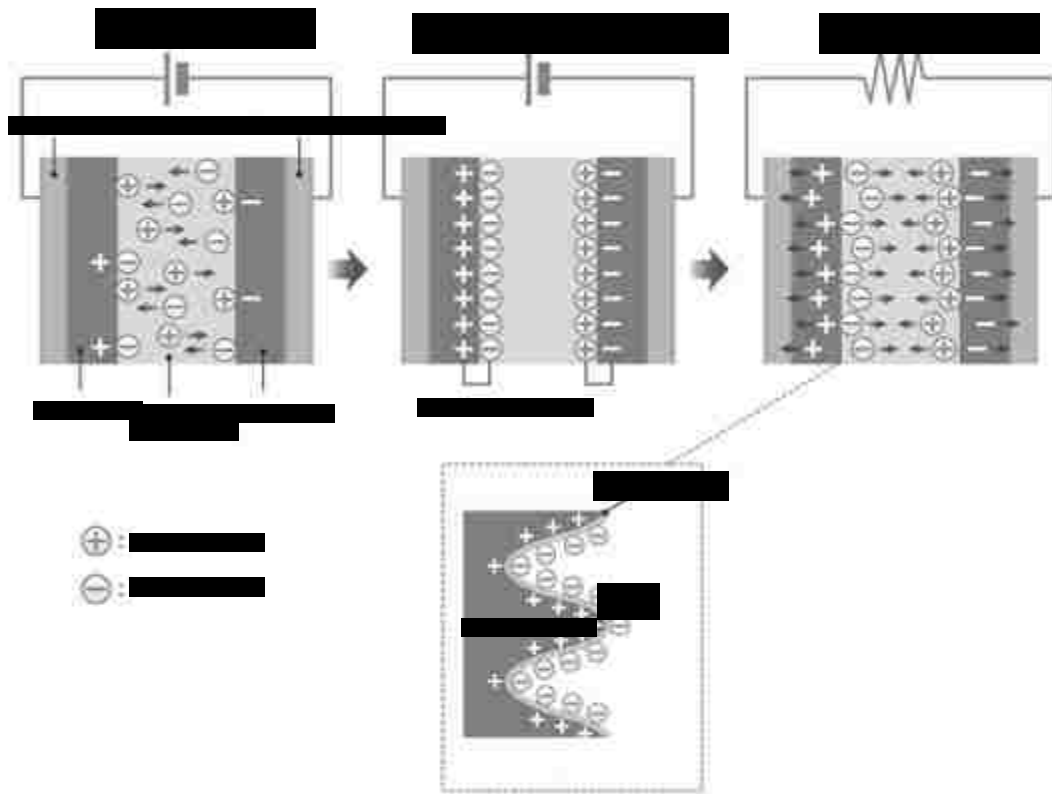


Fig 3-15. Charge and discharge cycle of EDLC. Source:[7]

Conventional capacitors have very fast charge transfer, leading to very high power densities, but the energy density is very low. Supercapacitors work on the same principle with supercapacitors with a much larger area A and much shorter dielectric distance d , which led to much larger capacitance. Compared with electrochemical batteries, charging and discharging of supercapacitors do not include Faradaic reaction, which means it has much better kinetics and power density (Fig 3-16). From a practical point of view, they have the following advantages over traditional energy storage devices, including:

- 1) Fast charge/discharge speed;
- 2) Long cycle life compared with battery, up to hundreds of thousands cycles of lifespan with no “memory effect”;
- 3) Can provide large discharge current with a high energy efficiency over 90%;
- 4) Electrode materials be manufactured relatively easily with less pollution;
- 5) Does not need complicated protective circuit for charging and discharging, amount of remaining energy is directly read out by voltage;
- 6) Wide range of working temperature, typically $-40 \sim 70$ °C.

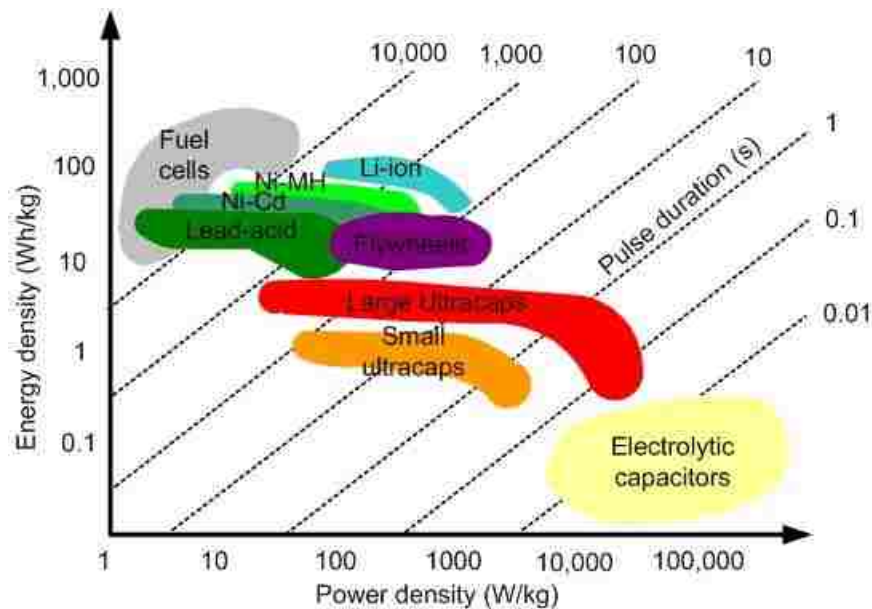


Fig 3-16. Ragone chart of energy storage systems. Ref[12]

Electrolyte choice is another key point for supercapacitor performance. Electrolytes affect the capacitance from a few perspectives. The energy stored in the capacitor is proportional with voltage squared. However, the voltage cannot be raised infinitely and is limited by the electrochemical stability window. The kinetics behavior of electrolyte has a significant impact on the ESR of the supercapacitor as well. In additions, ion concentration, ionic mobility and ion sizes are important factors for an electrolyte[41].

The most commonly used electrolytes fall into three categories: aqueous based solutions, organic compounds, and ionic liquids. Acid and base electrolytes are the usual choices for aqueous electrolytes, for example, low-cost KOH, and H₂SO₄ solutions, since K⁺ ion has the highest cation ionic conductivity after H₃O⁺, and OH⁻ has the highest anion conductivity. However, water-based solutions have a narrow stability window (up to 1.2 V). Organic electrolytes can provide a higher electrochemical window. For example, Nesscap manufactures supercapacitors with acetonitrile

electrolyte which can be charged up to 2.7 V. However, the volatility, flammability, and toxicity can be a concern for such electrolytes. In addition, ionic liquids (IL) are also being used as electrolytes. IL is the molten phase of salts consisting of cations and anions. The melting temperature of RTIL is low enough so it can stay in the liquid phase at temperatures lower than 100 °C. ILs have practically no vapor pressure and can go up to higher voltages (6V). The major drawback for IL is the low ion mobility resulted from high viscosity. They are also relatively expensive compared with inorganic and organic electrolytes.

The electrode of EDLC is mostly based on carbonaceous materials. Due to their high surface area, low cost and relatively good conductivity, activated carbons (AC) are very frequently used for as electrode material. ACs are primarily produced by physical and chemical activations from the charcoal products and more recently, renewable biomass is used to produce ACs as well, including wood, bamboo, fungi, nutshell and so forth, providing a more environmentally friendly source of EDLCs. Such activated carbons do not have a uniform pore size, but have wide pore size distribution from micropores to macropores, with surface areas up to 3000 m²/g. In addition to activated carbon, mesoporous carbon obtained from soft-templating and hard-templating routes are also excellent candidates as electrode materials for EDLCs, due to their large specific area, interconnected porous channels and tunable pore size for electrolyte entering. Hierarchical microporous-mesoporous carbon is usually used since the microporous portion provides a large surface area for electrolyte-electrode interaction, while the mesoporous portion serves as channels for rapid electrolyte ion diffusion and transportation for the electrochemical process[43]. In addition, carbon nanotubes (CNT) are also widely studied as the electrode materials for EDLC. CNT is a group of intriguing materials based on helical tubes of sp² hybridized carbon, and have attracted significant research attention since the discovery in 1991[44]. From an electrochemical perspective, one outstanding property of the sp² structured carbon is the electric conductivity,

due to the conjugation of pi electrons. Combined with excellent mechanical and thermal stability, CNTs are excellent candidates for supercapacitor electrode materials. The conductivity and high accessible surface area of CNTs can be used to produce supercapacitors with high power density. However, the surface area for CNTs is relatively small ($< 500 \text{ m}^2/\text{g}$) which limits the energy density stored in CNT supercapacitors. Researchers have tried different methods to increase the specific surface area of CNTs in order to increase the energy density. For example, CNTs can be activated by KOH to induce porosity and increase the surface area. Also, Mohamedi and co-workers have synthesized a CNT/carbon aerogel composite which has a high specific surface area of $1059 \text{ m}^2/\text{g}$ with a high specific capacitance of 524 F/g . However, the difficulties and limitations in the production of CNT limit its availability as electrode materials.

3.4 Concept of supercapacitive swing adsorption (SSA)

3.4.1 Electric field swing adsorption

From a simple chemical perspective, the carbon atom in CO_2 is electron deficient. Therefore the molecule can act as a Lewis acid. Therefore, a number of carbon dioxide capture techniques have been developed with basic sorbents, such as amine solutions like monoethanolamine (MEA), alkaline solutions, and so forth. The concept of electric field swing adsorption (EFSA) is based on the hypothesis that carbon dioxide molecule is an electron poor π -system, which will be selectively attracted to an electron rich π -system. Therefore, EFSA proposes that by charging high surface area carbon with negative charges, the adsorption affinity for CO_2 will be increased, and upon discharging, the additional adsorbed CO_2 will be desorbed. In this way, reversible CO_2 adsorption can be achieved by charging/discharging. In addition, this method could provide CO_2 selectivity over N_2 since nitrogen molecules do not bind to electron rich surfaces[45].

In a preliminary test of EFSA concept, a test device was designed and built by Dr. David Moore and Nina Jarrah, as illustrated in Fig 3-18, where a carbon electrode was charged against a counter electrode to form a parallel plate capacitor. The enclosure body and post are made of stainless steel and the insulating sleeves are made from alumina. The counter electrode is positioned with a distance to the carbon electrode so electrical breakthrough does not happen at high voltage.

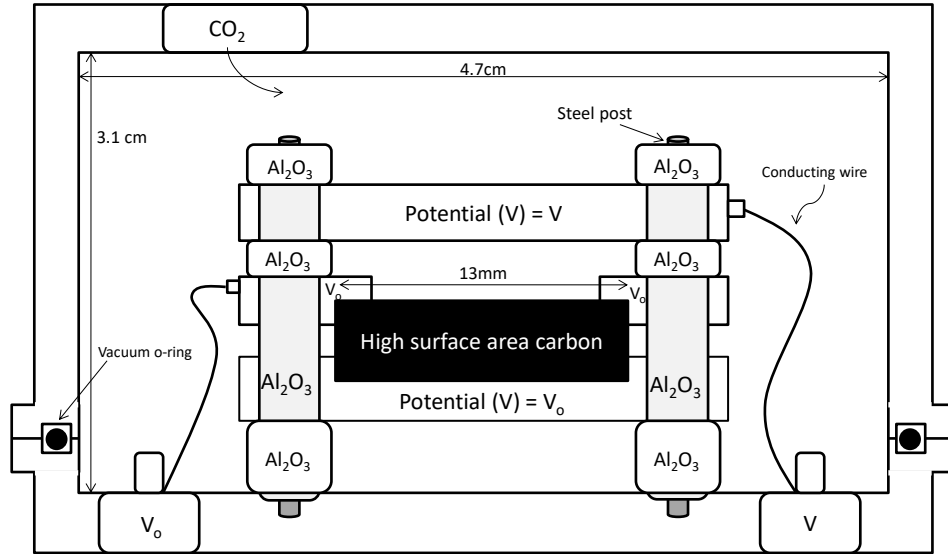


Fig 3-17. Cell design for EFSA. Image: Dr. David Moore, Nina Jarrah

However, with this setup, the concept of EFSA did not work even with voltages up to 5 kV, which corresponds to an electric field strength of $E = V/d = 5 * 10^6$ V/m. This indicates that the charge has not effectively been distributed to the pore surface of the carbon sorbent. From a physical standpoint, in a parallel plate type capacitor, the charge is distributed to the external surface of the electrode rather than the internal surface. In this scenario, the carbon pellet is made of 0.2 g BPL carbon with 13mm diameter. Therefore the external surface area is $S = \frac{\pi d^2}{4} = 1.33 * 10^{-4} m^2$. Therefore, even at an extreme voltage of 5 kV, the charge on the electrode surface can be calculated as $Q = C * V = \frac{k\epsilon S}{d} V = 2.14 * 10^{-13} C$, where k is the dielectric constant of

carbon dioxide, ϵ is the permittivity, S is the area and d is the distance. Since the charge carried by a single electron is 1.60×10^{-19} C, the charged surface has 1.34×10^6 electron pairs. Assuming each electron pair attracts one carbon dioxide molecule, which means 2.16×10^{-18} mol of CO_2 molecules will be attracted to the surface. Based on the calculations, it is clear that there would not be an obvious adsorption effect.

3.4.2 Supercapacitive swing adsorption.

To solve this issue and effectively charge the inner surface of carbon electrodes, we have developed a concept called supercapacitive swing adsorption based on the operation mechanism of an EDLC. As introduced previously, when an EDLC is charged, the electrolyte ions enter the pore surface of the electrode and are balanced by opposite charges on the electrode surface, forming an electrical double layer. In this case, the inner surface of the carbon electrode can be effectively charged. In a typical activated carbon, the surface area can go up to $1000 \text{ m}^2/\text{g}$, meaning the available surface area can be orders of magnitude higher than the EFSA setup.

In the SSA hypothesis, a microporous-mesoporous activated carbon will be used since the carbon, as the micropore is expected to provide the surface area for CO_2 adsorption, while the mesopore is expected to provide diffusion channel for electrolyte ion and CO_2 diffusion. Another potential advantage of using activated carbon is that its surface can be hydrophilic or hydrophobic depending on the terminal group. The hydrophobic sites can provide channels for CO_2 adsorption and diffusion while the hydrophilic part can interact with electrolyte. It is also anticipated that most of the electrolyte would stay in the interparticular space and mesopore region and be kept out of micropores, as the capillary force could keep the electrolyte inside the mesopore channels. When the SSA device is charged up, electrolyte ions will be pushed into the pores of the electrode by electrostatic force, correspondingly, the electron density on the pore surface will also change. It is expected that CO_2 adsorption capacity can be will be increased or decreased on the pore

surfaces depending on the charge on the surface. The cations flow into the cathode and negative charge flow to the pores, while the electron flows to the pore surface. Therefore the CO₂ affinity will be increased. On the other hand, the electron density on anode will be decreased and CO₂ affinity will be decreased accordingly. After discharging, ions will then flow back into the electrolyte in the mesopores, and the adsorption capacity of the porous electrode will revert to the original state. In addition, the electron density of non-infiltrated pores may also change due to electron delocalization in the conjugated π -electron systems of the carbon pore walls. Therefore these non-infiltrated pores could also contribute to the change of CO₂ affinity.

Potentially, SSA can have some advantages over traditional CCS technique. In SSA, there is no chemical reaction, and all adsorption/desorption is completed by physical reorganization of the electronic structure on the electrode surface. Therefore the cycle life could be very long with little performance degradation.

Since SSA concept is based on supercapacitor, the energy used for charging can be recovered after discharging, which could lead to reduced parasitic load on power plants. The electrode material (activated carbon) and electrolyte (aqueous solution) are widely available with a low cost, at the same time, they are also environment-friendly. Therefore, SSA is expected to be a low-cost CCS technique.

3.5 References

1. BELLONA. *Capture of CO₂*. [cited 2016 May]; Available from: <http://bellona.org/about-ccs/how-ccs>.
2. Seviaan, H. *Gauss' Law*. 2000 [cited 2016 May]; Available from: <http://buphy.bu.edu/py106/notes/Gauss.html>.
3. Siemens-Study. *Sustainable Power Generation: Facts and Forecasts 2014* 1 October 2014 [cited 2016 May].
4. Davis, C.L. *Capacitors*. [cited 2016 Apr]; Available from: http://www.physics.louisville.edu/cldavis/phys299/notes/elec_capacitors.html.
5. BBC. *Oil refining and fuels*. 2006 [cited 2016 May]; Available from: http://www.bbc.co.uk/schools/gcsebitesize/science/edexcel/fuels/oil_refining_fuelsrev_6.shtml.
6. Shamsuzzaman Farooq, I.K. *CO₂ Capture and Concentration for Climate Change Abatement* [cited 2016 April]; Available from: <http://www.eng.nus.edu.sg/EResnews/102010/sf2.html>.
7. TDK. *EDLC : Electric Double Layer Capacitor*. [cited 2016 May]; Available from: http://www.tdk.co.jp/techmag_c/electronics_primer/vol8.htm.
8. APEC, *BUILDING CAPACITY FOR CO₂ CAPTURE AND STORAGE IN THE APEC REGION*, A.E.W. Group, Editor 2012.
9. Grande, C.A., *Biogas Upgrading by Pressure Swing Adsorption*. Biofuel's Engineering Process Technology. 2011.
10. Grande, C.A., *Advances in Pressure Swing Adsorption for Gas Separation*. ISRN Chemical Engineering, 2012. **2012**: p. 13.
11. Koh, K., M. Sreekumar, and S. Ponnambalam, *Experimental Investigation of the Effect of the Driving Voltage of an Electrodeposition Actuator*. Materials, 2014. **7**(7): p. 4963.
12. Simon, P. and Y. Gogotsi, *Materials for electrochemical capacitors*. Nat Mater, 2008. **7**(11): p. 845-854.
13. Hansen, J., et al., *Global temperature change*. Proceedings of the National Academy of Sciences, 2006. **103**(39): p. 14288-14293.
14. Lin, L.-C., et al., *In silico screening of carbon-capture materials*. Nat Mater, 2012. **11**(7): p. 633-641.
15. Figueroa, J.D., et al., *Advances in CO₂ capture technology - The US Department of Energy's Carbon Sequestration Program*. International Journal of Greenhouse Gas Control, 2008. **2**(1): p. 9-20.
16. Yu, C.H., C.H. Huang, and C.S. Tan, *A Review of CO₂ Capture by Absorption and Adsorption*. Aerosol and Air Quality Research, 2012. **12**(5): p. 745-769.
17. Diolaiuti, G.A., et al., *Glacier retreat and climate change: Documenting the last 50 years of Alpine glacier history from area and geometry changes of Dosedè Piazzini glaciers (Lombardy Alps, Italy)*. Progress in Physical Geography, 2011. **35**(2): p. 161-182.
18. Mitchell, J.F.B., *The "Greenhouse" effect and climate change*. Reviews of Geophysics, 1989. **27**(1): p. 115-139.
19. Baird, C., *Environmental chemistry*. 1995, New York: W.H. Freeman. xix, 484 p.
20. Leung, D.Y.C., G. Caramanna, and M.M. Maroto-Valer, *An overview of current status of carbon dioxide capture and storage technologies*. Renewable and Sustainable Energy Reviews, 2014. **39**: p. 426-443.

21. Pimentel, D., et al., *Renewable Energy: Current and Potential Issues: Renewable energy technologies could, if developed and implemented, provide nearly 50% of US energy needs; this would require about 17% of US land resources*. *BioScience*, 2002. **52**(12): p. 1111-1120.
22. Steen, T.Y. and T. Mousseau, *Outcomes of Fukushima: Biological Effects of Radiation on Nonhuman Species*. *Journal of Heredity*, 2014. **105**(5): p. 702-703.
23. Bauer, N., R.J. Brecha, and G. Luderer, *Economics of nuclear power and climate change mitigation policies*. *Proceedings of the National Academy of Sciences*, 2012. **109**(42): p. 16805-16810.
24. Scheffknecht, G., et al., *Oxy-fuel coal combustion-A review of the current state-of-the-art*. *International Journal of Greenhouse Gas Control*, 2011. **5**: p. S16-S35.
25. Lee, H.J., et al., *Gas hydrate formation process for pre-combustion capture of carbon dioxide*. *Energy*, 2010. **35**(6): p. 2729-2733.
26. Franz, J. and V. Scherer, *An evaluation of CO₂ and H₂ selective polymeric membranes for CO₂ separation in IGCC processes*. *Journal of Membrane Science*, 2010. **359**(1–2): p. 173-183.
27. Samanta, A., et al., *Post-Combustion CO₂ Capture Using Solid Sorbents: A Review*. *Industrial & Engineering Chemistry Research*, 2012. **51**(4): p. 1438-1463.
28. Freeman, S.A., J. Davis, and G.T. Rochelle, *Degradation of aqueous piperazine in carbon dioxide capture*. *International Journal of Greenhouse Gas Control*, 2010. **4**(5): p. 756-761.
29. *Monsanto unveils new separation technology*. *Chemical & Engineering News Archive*, 1979. **57**(47): p. 6-7.
30. Yang, H., et al., *Progress in carbon dioxide separation and capture: A review*. *Journal of Environmental Sciences*, 2008. **20**(1): p. 14-27.
31. Pera-Titus, M., *Porous Inorganic Membranes for CO₂ Capture: Present and Prospects*. *Chemical Reviews*, 2014. **114**(2): p. 1413-1492.
32. Cheung, O. and N. Hedin, *Zeolites and related sorbents with narrow pores for CO₂ separation from flue gas*. *RSC Advances*, 2014. **4**(28): p. 14480-14494.
33. Zhang, Z., et al., *MOFs for CO₂ capture and separation from flue gas mixtures: the effect of multifunctional sites on their adsorption capacity and selectivity*. *Chemical Communications*, 2013. **49**(7): p. 653-661.
34. Songolzadeh, M., et al., *Carbon Dioxide Separation from Flue Gases: A Technological Review Emphasizing Reduction in Greenhouse Gas Emissions*. *The Scientific World Journal*, 2014. **2014**: p. 34.
35. Powell, C.E. and G.G. Qiao, *Polymeric CO₂/N₂ gas separation membranes for the capture of carbon dioxide from power plant flue gases*. *Journal of Membrane Science*, 2006. **279**(1–2): p. 1-49.
36. Delgado, J.A., et al., *Adsorption and Diffusion Parameters of Methane and Nitrogen on Microwave-Synthesized ETS-4*. *Langmuir*, 2008. **24**(12): p. 6107-6115.
37. Ntiamoah, A., et al., *CO₂ Capture by Temperature Swing Adsorption: Use of Hot CO₂-Rich Gas for Regeneration*. *Industrial & Engineering Chemistry Research*, 2016. **55**(3): p. 703-713.
38. Burchell, T.D., et al., *Use of Carbon Fibre Composite Molecular Sieves for Air Separation*. *Adsorption Science & Technology*, 2005. **23**(3): p. 175-194.
39. García, S., et al., *Cyclic operation of a fixed-bed pressure and temperature swing process for CO₂ capture: Experimental and statistical analysis*. *International Journal of Greenhouse Gas Control*, 2013. **12**: p. 35-43.

40. Ntiamoah, A., et al., *CO₂ Capture by Temperature Swing Adsorption: Use of Hot CO₂-Rich Gas for Regeneration*. *Industrial & Engineering Chemistry Research*, 2016. **55**(3): p. 703-713.
41. Kularantna, N. and Safari Books Online (Firm), *Energy storage devices for electronic systems : rechargeable batteries and supercapacitors*. First edition. ed. 1 online resource (1 volume).
42. Conway, B.E., *Electrochemical supercapacitors : scientific fundamentals and technological applications*. 1999, New York: Plenum Press. xxviii, 698 p.
43. Ye, L., et al., *A supercapacitor constructed with a partially graphitized porous carbon and its performance over a wide working temperature range*. *Journal of Materials Chemistry A*, 2015. **3**(37): p. 18860-18866.
44. Iijima, S., *Helical microtubules of graphitic carbon*. *Nature*, 1991. **354**(6348): p. 56-58.
45. Buß, F., et al., *Reversible Carbon Dioxide Binding by Simple Lewis Base Adducts with Electron-Rich Phosphines*. *Journal of the American Chemical Society*, 2016. **138**(6): p. 1840-1843.

4 Supercapacitive swing adsorption: Experimental results

4.1 Static mode SSA experiments with ionic liquid as electrolyte

4.1.1 Apparatus and experimental setup

As described in chapter 3, the concept of SSA is derived from supercapacitor technology and inherits all major components from a supercapacitor. In the SSA concept, the essential components include high surface area electrode and electrolyte. Therefore, the first SSA device was built by modifying an existing commercial supercapacitor.

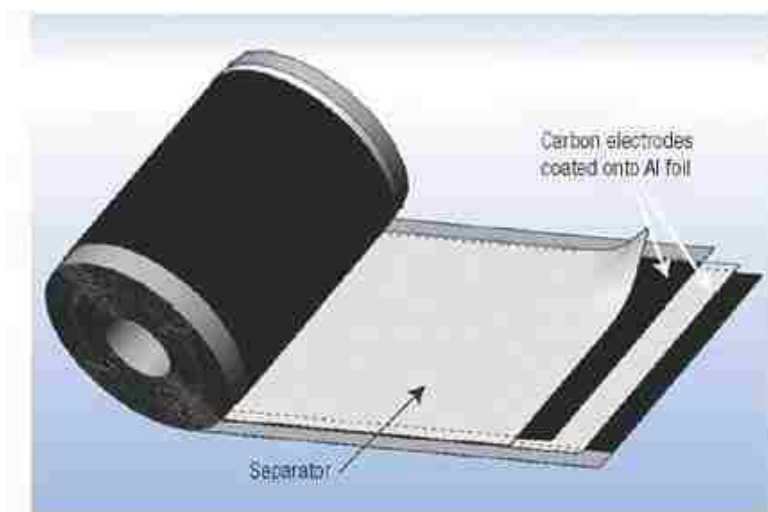


Fig 4-1. EDLC in radial configuration. Source: [1]

An ESHSR-0003C0-002R7 supercapacitor (Nesscap Corporation) was disassembled. The capacitor had a radial configuration, where high surface area carbon film was pressed onto aluminum current collectors. A separator membrane was then sandwiched by two electrodes, and the assembly was rolled up to form a radial configuration. The structure of the capacitor is depicted in Fig 4-1.

After removing the outer shell of the capacitor, it was rinsed in acetone to thoroughly remove the original electrolyte of the supercapacitor. Then it was dipped into non-volatile ionic liquid 1-Ethyl-

3-methylimidazolium tris(pentafluoroethyl) trifluorophosphate (EMIM FAP, Fig 4-2) electrolyte (Merck Chemicals). It was assumed that – due to size arguments - the cations and the anions of the ionic liquid would infiltrate the mesopores, but not the micropores. The function of the infiltrated mesopores is to ensure the supercapacitance while the function of the empty micropores is to provide adsorption sites for the CO₂ molecules.

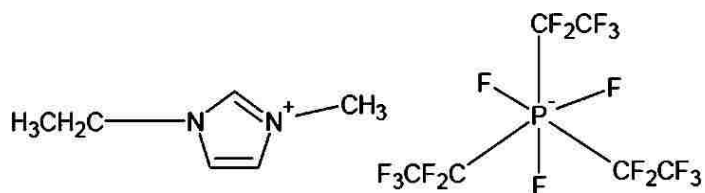


Fig 4-2. Molecular structure of EMIM FAP ionic liquid.

The experimental apparatus was designed so that the adsorption and desorption of CO₂ can be indirectly by a pressure transducer. According to the ideal gas law $pV = nRT$, where p is the pressure, V is the volume, R is the gas constant, T is the temperature, and n is the moles of gas molecules, pressure is proportional to the amount of gas molecules in a closed cell with fixed volume at constant temperature. Therefore, the gas adsorption due to the SSA effect can be monitored by measuring the pressure of the gas phase during the charging and discharging of the supercapacitor electrodes, when the electrodes are located in the gas adsorption cell.

A custom glass cell with a void volume of 108 mL was fabricated by Exeter Scientific Glass Company as illustrated in Fig 4-3. The cell had an opening port to serve as the gas inlet/outlet. In addition to the gas port, two Fe leads were fed through the glass cell. The metallic leads were used to connect the electrodes inside the cell to external power supply. A DC power supply (Extech 382260) was used to charge the electrodes. The cell was then attached to the sample port of the Autosorb-1 instrument, which was used to evacuate the cell, fill CO₂ into the cell, and to record

the pressure of the cell. Since the EMIM FAP ionic liquid does not have a significant vapor pressure at room temperature, it cannot contribute to the pressure change inside the glass cell. Therefore, the pressure change in the cell is directly related to the adsorption and desorption of CO₂ molecules.

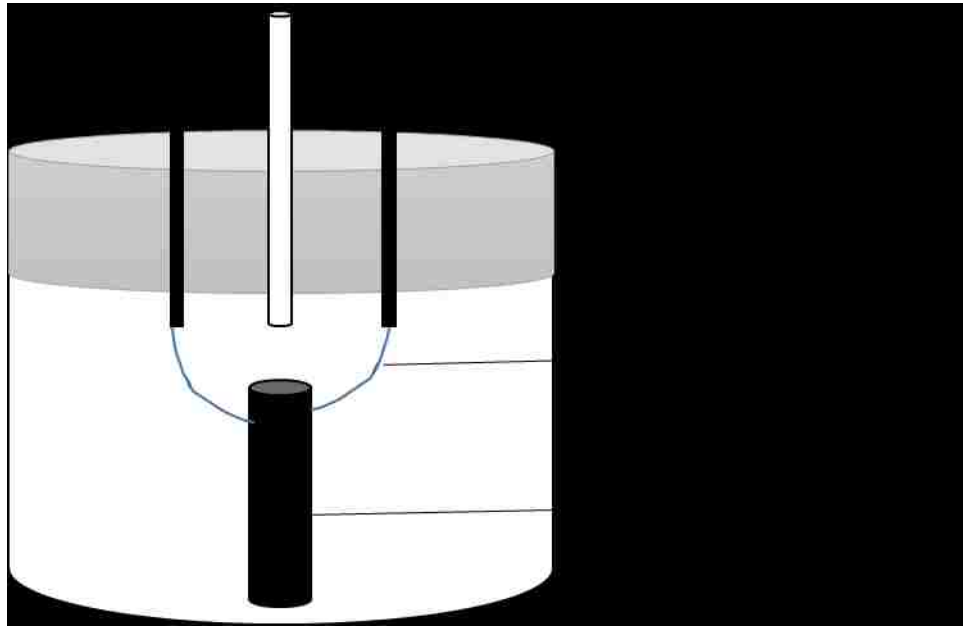


Fig 4-3 Schematic Illustration of the glass cell fabricated for testing SSA effect.

4.1.2 SSA experiment with radial type supercapacitor

The cell was evacuated and pure CO₂ was filled into the cell up to 760 mmHg, so the high surface area electrodes could be saturated with CO₂. Afterwards, the system was left for 12 hours to allow the conventional physisorption of carbon dioxide on the electrodes to fully reach equilibrium[2].

The SSA experiments were comprised of two half cycles. In the charging half-cycle, the electrodes were charged up to 1.5 V and kept for 10 min in the charged state, and in the following discharge

cycle, the electrodes were discharged and kept for 10 min in the discharged state. The pressure change was recorded versus the time. Three charge/discharge cycles with 10 min half-cycle time were recorded as shown in Fig 4-4. In an SSA cycle, a voltage of 1.5 V was applied after a waiting period of 10 mins. The voltage was kept for 10 min and then removed by short-circuiting the capacitor. After that, the system was kept at a voltage of 0 V for another 10 min. This procedure was repeated for three times (Fig 4-5). The pressure recording started 10 min before the electrodes were charged. As the voltage was turned on, the pressure dropped by 0.36 mmHg after a small initial spike. At the end of the 10 min. charging half-cycle, the capacitor was discharged by short-circuiting the two metal leads of the glass cell. Upon discharging, the pressure increased by 0.27 mmHg. The effect was repeatable for three cycles. The results can be interpreted this way: The initial pressure spike directly after turning the voltage on/off can be explained by the heat generated from the current flow upon charging/discharging of the capacitor. The pressure decrease in the charging half-cycle indicates that CO₂ was adsorbed by the electrode in the process. However, from this experiment, it was not possible to conclude whether the enhancement of adsorption happened at the cathode or the anode since both electrodes were equally exposed to CO₂ molecules. A control experiment with helium was conducted to confirm that the SSA effect observed is due to adsorption since it can be assumed that helium does not adsorb on the electrode surface at room temperature and pressure[3]. Therefore, the pressure changes in the cell would solely depend on the temperature variations.

In the control experiment, the same procedure was performed except that carbon dioxide was substituted with helium. The cell was evacuated, and refilled with helium, then equilibrated for 12 hours. 10 min after the experiment started, a 1.5 V voltage was applied to the supercapacitor. After another 10 min, the supercapacitor was discharged by short-circuiting. Overall, three cycles were recorded (Fig 4-5).

Directly after the application of the voltage, a small pressure spike was observed. When the voltage was removed, the same effect occurred. The effect can be explained by the temperature change associated with resistive heating of the capacitor. Overall, the pressure in the sorption cell was generally following the temperature trend line (green line). The fact that the reversible pressure changes occur in the CO₂ experiment but not in helium experiment strongly suggest that the pressure changes are due to adsorption and not due to other effects such as electrostriction.

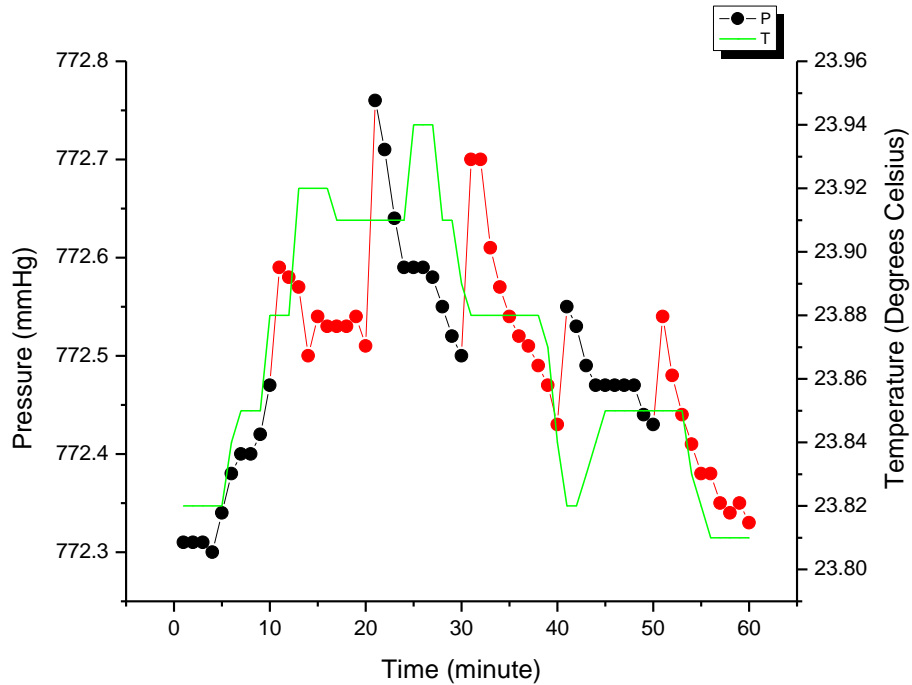


Fig 4-4. SSA experiment with CO₂, each point is taken in 1 min. Red dots: charging cycle, black dots: discharging cycle. Green line: Temperature

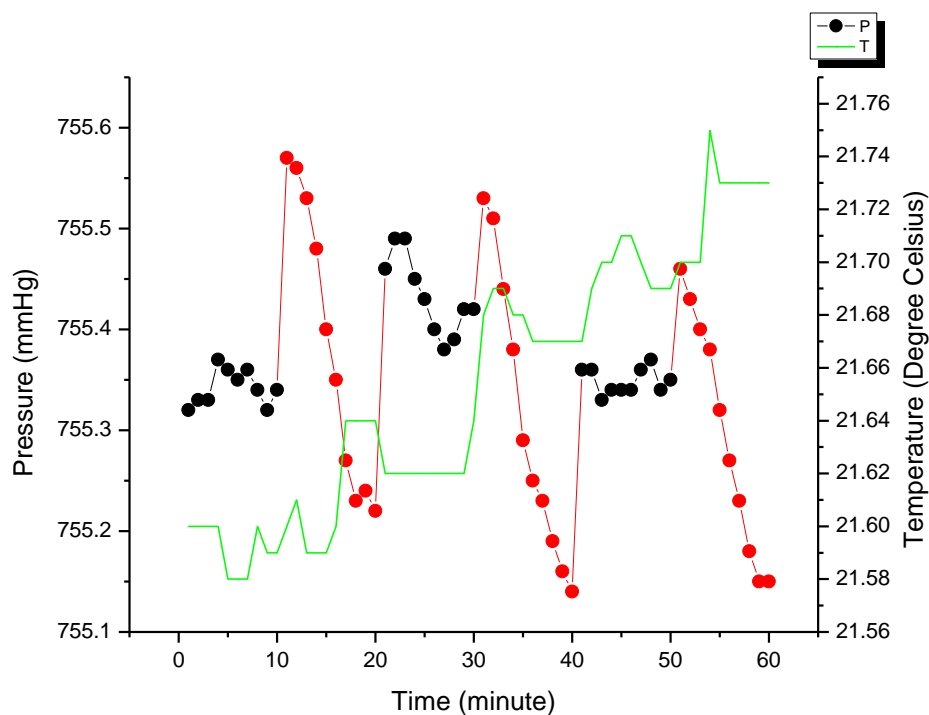


Fig 4-5. SSA experiment with Helium, each point is taken in 1 min. Red dots: Bias on, black dots: bias off.:Green line: Temperature

4.1.3 SSA experiments with asymmetrical electrode configurations

In the previous experiment, the SSA experiment was set up in a way that both electrodes of the supercapacitor had equal access to the gas phase. However, an important question remaining is how much each electrode contributes to the enhanced adsorption capacity in the charged state. It is not clear whether the cathode or the anode caused the SSA effect or both. During the charging half-cycle, the cathode surface was electron-rich and the anode surface was electron deficient. Therefore it is possible that the different surface charges direct the CO₂ adsorption behavior.

In order to test the hypothesis, a different experimental setup with asymmetrical electrode configuration was tested. A 25 Farad Nesscap ESHSR-0025C0-002R7 supercapacitor was disassembled and rinsed with acetone. Two electrodes with areas of 2 cm * 2 cm were cut out

from the original electrode. The electrode mass was measured after the SSA experiment by scraping the carbon material off the aluminum foil and determined to be 30 mg. One electrode was placed horizontally on the bottom of the sorption cell, and the other one was oriented vertically. EMIM FAP ionic liquid was used as the electrolyte. The amount of EMIM FAP filled into the sorption cell was chosen so that the flat-lying electrode was fully submerged and the perpendicular electrode was half-submerged as illustrated in Fig 4-6. The purpose of this setup was to isolate the horizontally oriented electrode from the gas phase so that only the vertically oriented electrode had contact with the electrolyte and access to carbon dioxide molecules at the same time.

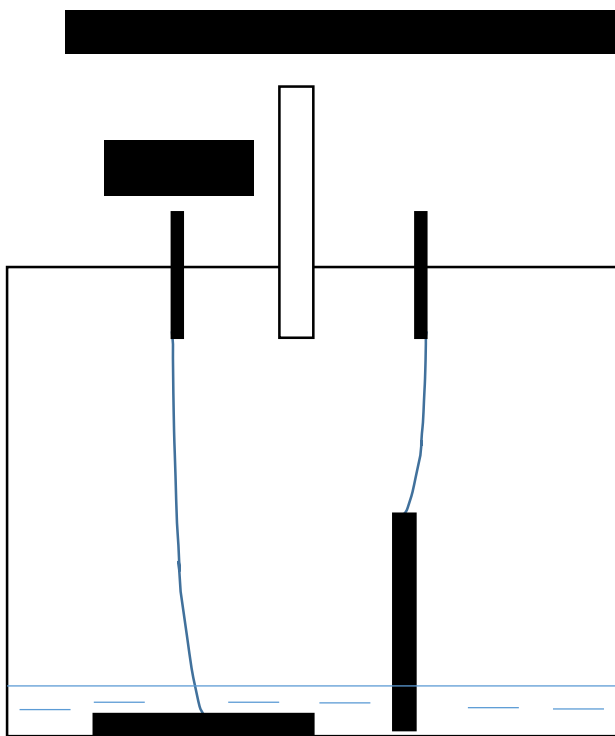


Fig 4-6. SSA experiment cell with asymmetrical electrode setup.

In the first experiment with asymmetrical electrode setup, the horizontally oriented electrode was used as cathode and the vertical electrode was used as the anode. The experiment was performed with a 2-hour cycle time (1 hour for the charging half-cycle and 1 hour for discharge half-cycle). At the start of the experiment, the pressure was recorded for 1 hour, and then a 1.5 V voltage was applied to charge the capacitor. After 1 hour, the voltage on the capacitor was removed by short-circuiting the electrodes. Three cycles were recorded in this study and the pressure was plotted versus the time (Fig 4-7).

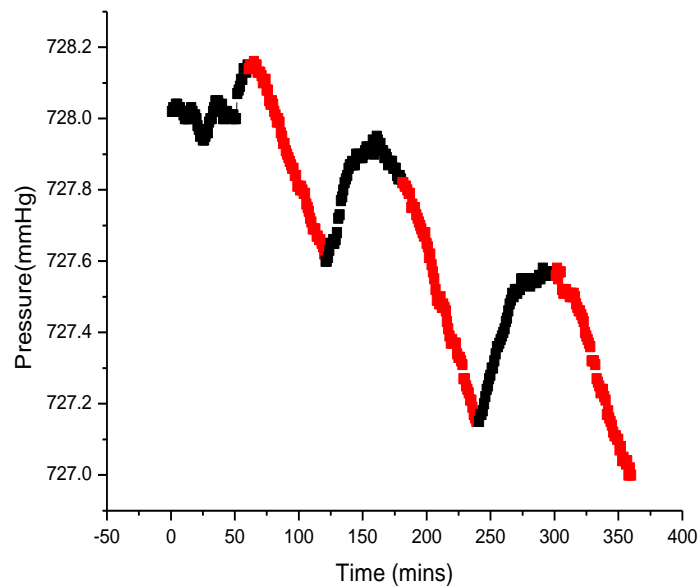


Fig 4-7. SSA experiment with asymmetrical electrode configuration. Black: discharged state, red: charged state

The pressure-time plot showed a similar pattern compared to the experiment with symmetrical electrode configuration. Before the 1st charging half cycle, the pressure was relatively stable (black in the plot) before the experiment was started. Immediately after the voltage was applied, the pressure started to drop (red). At the end of the 1-hour charging half-cycle, the pressure dropped

by 0.59 mmHg, indicating CO₂ adsorption was enhanced on the exposed electrode. Then, the electrodes were discharged and a pressure increase of 0.37 mmHg was observed, which could be contributed from CO₂ desorption of the exposed electrode. The pressure did not completely climb back to the value before the charging cycle started. This might be an indication that the desorption kinetics was slower than adsorption kinetics. The 2nd and 3rd cycle followed the same pattern. The effect was observed in all three cycles and the average pressure drop for the charge cycle was 0.63 mmHg. Control experiments were also performed with the exposed electrode as anode and submerged experiment as the cathode. However, under this configuration, the pressure did not show a clear dependence on the input voltage and the data could not be reproduced with reasonable accuracy. Therefore, it can be concluded from the SSA experiment with asymmetrical electrode configuration that when the exposed electrode is negatively charged (as cathode), the carbon dioxide adsorption capacity can be increased. This suggests that the specific changes in the electronic state of the carbon electrode are responsible for the SSA effect.

The magnitude of the SSA effect for the asymmetrical setup can be calculated the following way. The exposed electrode contains 30 mg of carbon material, the void volume of the sorption cell is 118 mL, and the gas constant is 62.36 ml mmHg K⁻¹ mmol⁻¹. According to the ideal gas law, we can calculate how much carbon dioxide has been adsorbed by the SSA effect: $\Delta p * V = \Delta n * RT$, where Δp is 0.63 mmHg, V is 118 mL, R is 62.36 ml mmHg K⁻¹ mmol⁻¹, T is 298 K, therefore $\Delta n = \Delta p * V/RT = 0.00400$ mmol. Since there was 30 mg of carbon on the exposed electrode, the SSA capacity can be calculated as $0.00400 \text{ mmol} / 30 \text{ mg} = 0.133 \text{ mmol/kg}$. Considering that in the charged state the pressure of the sorption cell did not stop dropping at the end of 1-hour charging cycle, the enhancement in the carbon dioxide sorption capacity in chemical equilibrium may actually be larger.

4.2 Static mode SSA experiments with aqueous electrolyte

4.2.1 SSA experiment with carbon monoliths

From the experiment with the radial capacitor and the asymmetrical electrode capacitors, it was clear that SSA is a novel technique that can reversibly adsorb and desorb carbon dioxide molecules by applying a voltage, and that there is potential for carbon capture and sequestration applications. However, there are some drawbacks using an ionic liquid as an electrolyte. First of all, the ionic liquid electrolyte has a very high viscosity which leads to slow kinetics in the system. This is also seen from the fact the SSA effect did not fully saturate and the pressure still had a decreasing trend at the end of 1-hour charging half-cycle. In addition, the cost and availability of the ionic liquid are also a concern. At the time of writing, the price of EMIM FAP was \$3893 per Kg from VWR, which would undoubtedly limit its application in large-scale industrial applications. In order to overcome these limitations, aqueous electrolytes were considered, owing to their low viscosity and low cost. A pH-neutral electrolyte was chosen to minimize potential corrosion problems.

To increase the pressure change between the charged state and the discharged state, carbon electrodes with much bigger mass were used. The glass cell was also modified. Two gas ports (one for inlet and one for outlet) were implemented instead of only one. Two metal feedthroughs connected the electrodes to an external power supply. In addition, a thermocouple (Omega TJ36) was added to the cell to measure the temperature in the cell during the experiment. A pressure transducer (Omega MMA015C1T3C2TA5S) was used instead of using the Autosorb-1 instrument for pressure measurement. In order to isolate the cell from the environmental temperature fluctuations, the cell was immersed in a 2 L temperature-controlled beaker (Chemglass, Fig 4-8) connected to a Neslab RTE-110 chiller set to a constant temperature of 25 °C. The sorption cell,

the pressure transducer, and the temperature-controlled beaker were all placed under a custom made Styrofoam housing with an exterior size of 75 cm * 64 cm * 45 cm and an opening of 24 cm * 24 cm, as shown in Fig 4-8. The purpose of the housing was to further thermally insulate the system from the environment.

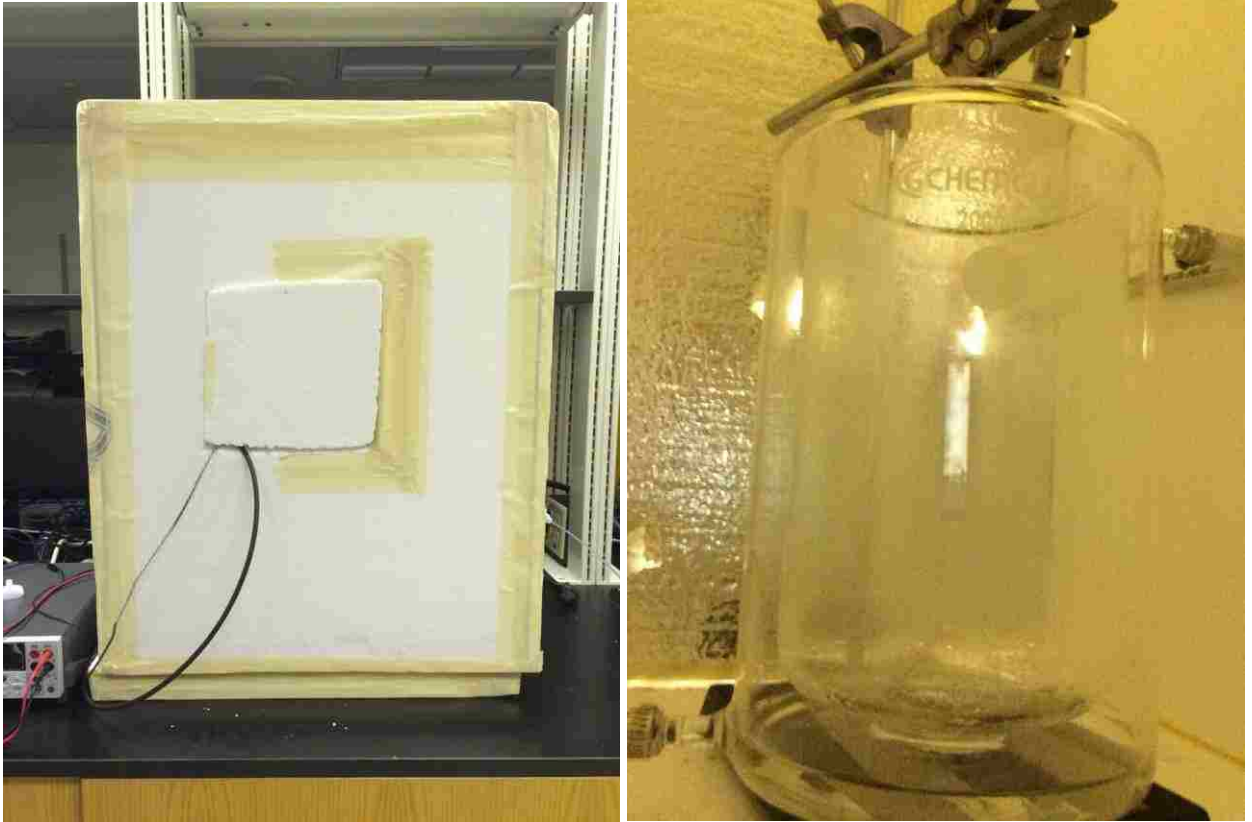


Fig 4-8. Left: Styrofoam housing for SSA experiments, right: 2L tempered beaker..

The power supply was changed to a programmable Keithley 2400 SourceMeter. This unit was a multi-functional power source which could act as a voltage source, a current source, a voltage meter, a current meter and an ohmmeter. Therefore it enabled the controlling and recording of voltage and current during the experiments. A data acquisition (DAQ) system was implemented to control the power source and log the data from the pressure and power supply system. An NI-

9125 (National Instruments) analog input module was used in conjunction an NI cDAQ-9171 (National Instruments) USB chassis to serve as the acquisition device, where the voltage signal from the transducer was converted to pressure data and recorded. The Keithley 2400 source meter was plugged in via USB interface. The thermocouple was connected to a USB-TC01 (National Instruments) adapter to monitor the temperature during the experiment. The DAQ software was implemented in National Instrument LabView 8 Platform. The basic software architecture included a controlling part, a monitoring part, and a recording part. The controlling part was controlling experimental parameters such as cycle time, cycle numbers, input voltage, voltage and current limits, while the monitoring part was responsible for displaying the parameters during the experiment. Simultaneously, the recording part logged the data points to a file on the computer.

The electrodes were fabricated from 4 x 10 mesh BPL activated carbon (Calgon Carbon Corporation). The N₂ adsorption isotherm of this BPL carbon is shown in Fig 4-9. The carbon was crushed and ground into a powder and then mixed with the binder. The binder solution was made by dispersing polyvinylidene fluoride (PVDF) polymer (average M_w ~534,000 by GPC, Sigma-Aldrich) in N-methyl-2-pyrrolidone (NMP, Alfa-Aesar) with a ratio of 1g solute:50 ml solvent. In the final mixture, the BPL carbon to PVDF ratio is 10 to 1 by weight. NaCl crystals (EMD Chemicals) were blended into the carbon electrode with a BPL: NaCl ratio of 1:1 by weight. The purpose of embedding the NaCl crystals was to introduce large pores into the system to enable better electrolyte diffusion into the carbon monoliths. After adding the BPL carbon powder, the binder, and the NaCl crystals together, the slurry was mixed in a mortar with a pestle. The excess of NMP was removed by hot air from a heat gun until the slurry became paste-like. Then a glass tube with 1.3 cm inner diameter was used to extrude the mixture into a monolith. The remaining NMP solvent in the monolith was removed by drying at 120 °C for 12 hours in an oven. The NaCl crystals

were leached out by washing the monolith in a beaker with 60 °C warm deionized water and the monolith was dried in a vacuum oven at 100 °C overnight. The weight of the carbon monolith was determined before and after the leaching to ensure complete removal of NaCl crystals.

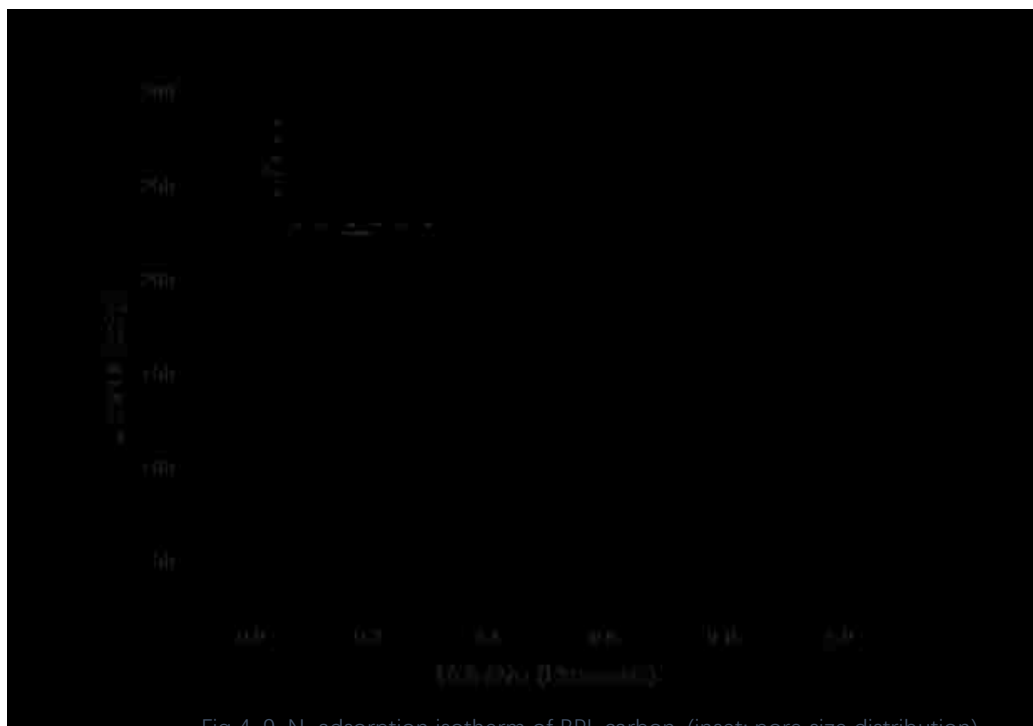


Fig 4-9. N₂ adsorption isotherm of BPL carbon. (inset: pore size distribution)

With the method described above, two carbon monoliths with 3.7 g weight, 5 cm length, and 1.3 cm diameter were made. The carbon monoliths were glued with a conducting glue (SPI LEIT-C Conductive Carbon Cement) to carbon cloth strips (AvCarb carbon fabric). Two electrodes were mounted inside the sorption cell. The two electrodes were oriented differently in the cell to achieve an asymmetrical setup. One was laid vertically so that half of the electrode was still exposed to the gas environment, the other one was placed horizontally and completely submerged in the electrolyte. 30 mL 1 M NaCl electrolyte was injected into the glass cell through a septum. The setup was illustrated in Fig 4-10.

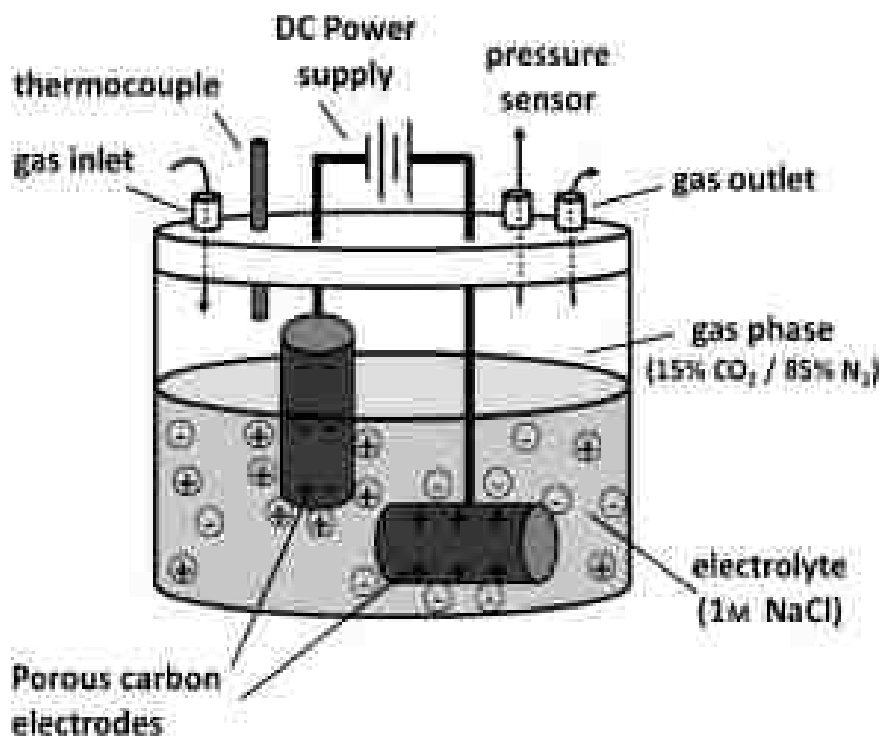
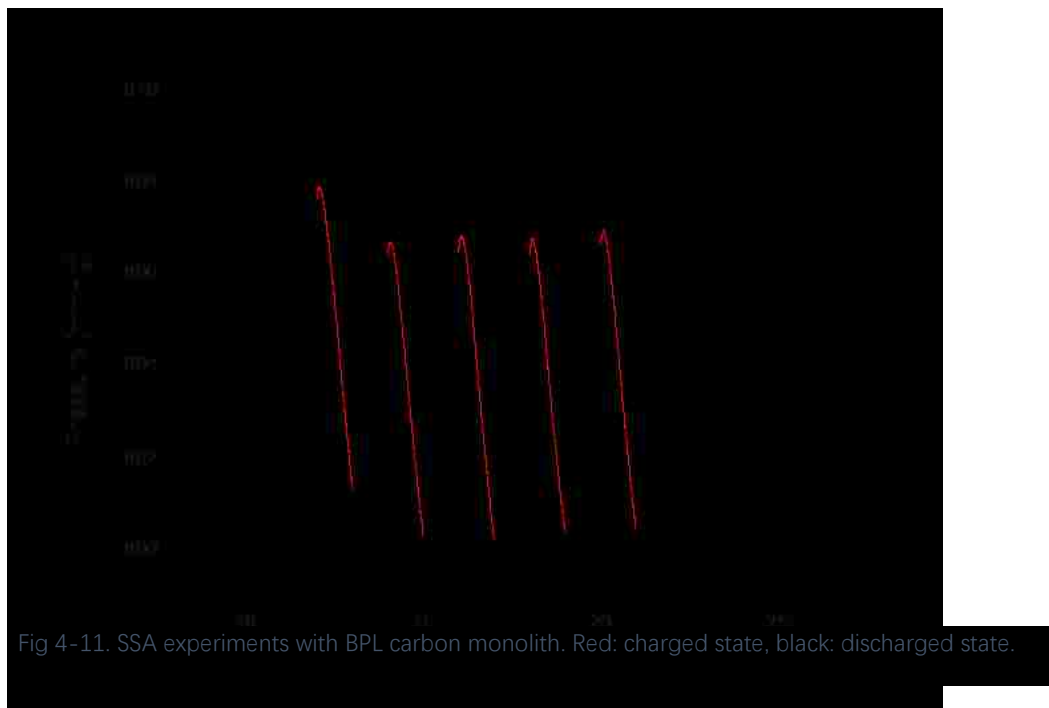
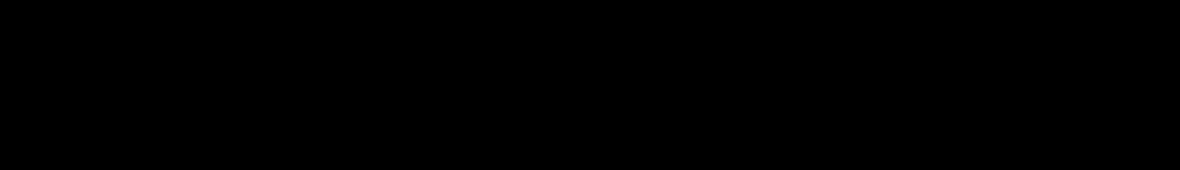
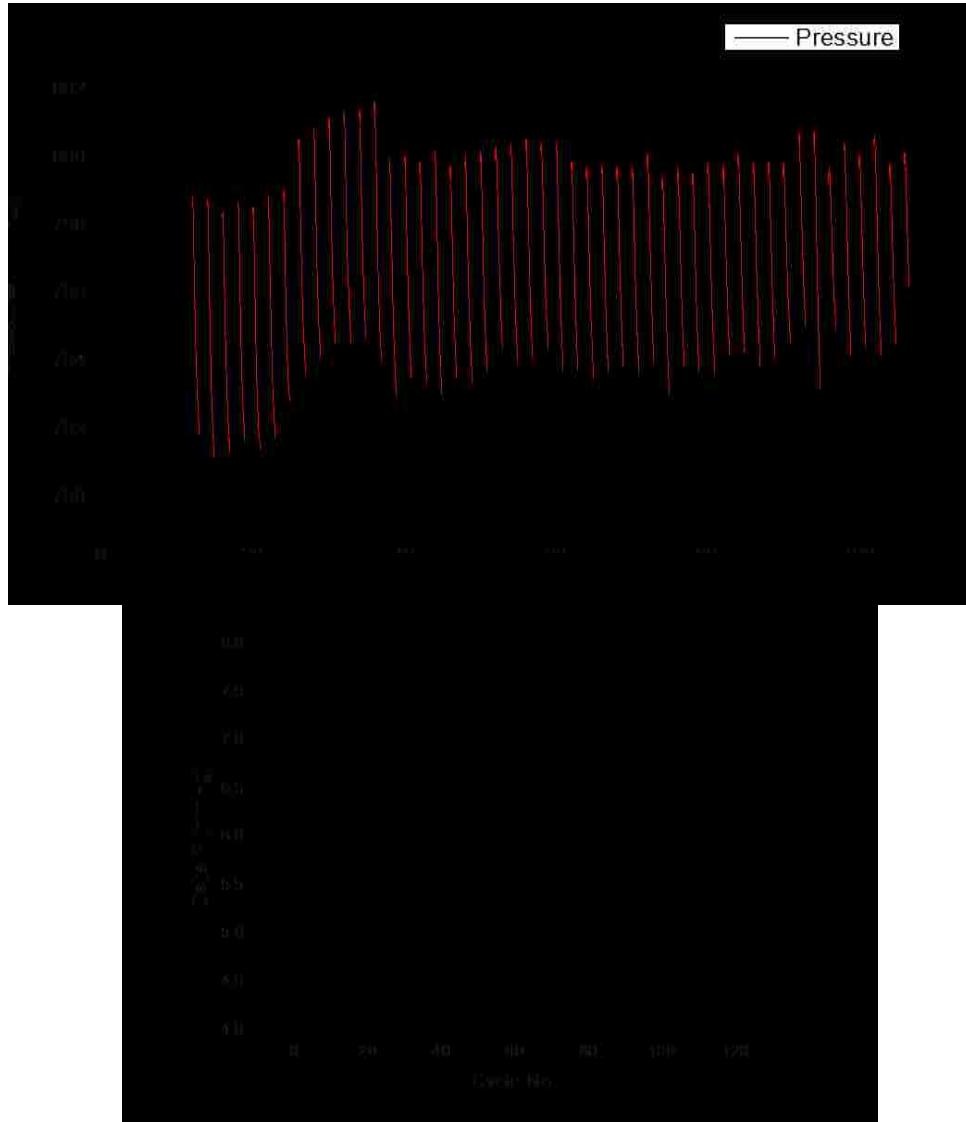


Fig 4-10. Modified SSA cell setup.

Given that it was previously established that SSA would work with pure carbon dioxide, it seemed logical to investigate if it would also work for a CO₂/N₂ mixture. In addition, the use of a gas mixture would provide information about the CO₂/N₂ selectivity of SSA. A mixture of 15% CO₂ and 85% N₂ (NI-CD15K, Airgas) was used to simulate a flue gas from fossil fuel power plant[4]. In order to saturate the carbon monolith with carbon dioxide, the inlet of the cell was connected to the gas mixture and the outlet was connected to a bubbler. The gas mixture was flown through the cell for 4 hours. Then the cell was closed, placed into the temperature-controlled beaker, and kept at 25 °C. The system was let sit for overnight (12 hrs) for full equilibration (saturation of electrolyte with CO₂ and full adsorption of CO₂ to the electrodes).

Since an aqueous electrolyte was used, the maximum input voltage on the electrodes was limited to 1.2 V to prevent the electrolysis of water[5]. A 5-cycle experiment was performed with this setup and the vertically oriented electrode was used as cathode and horizontally oriented electrode as the anode. The system responded similarly to the experiments with ionic liquid electrolyte and pure carbon dioxide. As shown in fig 4-11, when the voltage was applied to the electrodes, the pressure in the system dropped, and upon discharging the pressure of the system increased back to approximately the original value. For the average of all five cycles, the reversible pressure change was 6.65 mmHg. The SSA effect did not reach full saturation at the end of the 1-hour cycle, which means that the effect could have been larger if the cycle time had been increased. Before the 1st charging half-cycle started, the pressure was 807.78 mmHg, however, during the experiment, the pressure was not able to increase back to this value which is likely because the desorption kinetics is slower than adsorption kinetics.

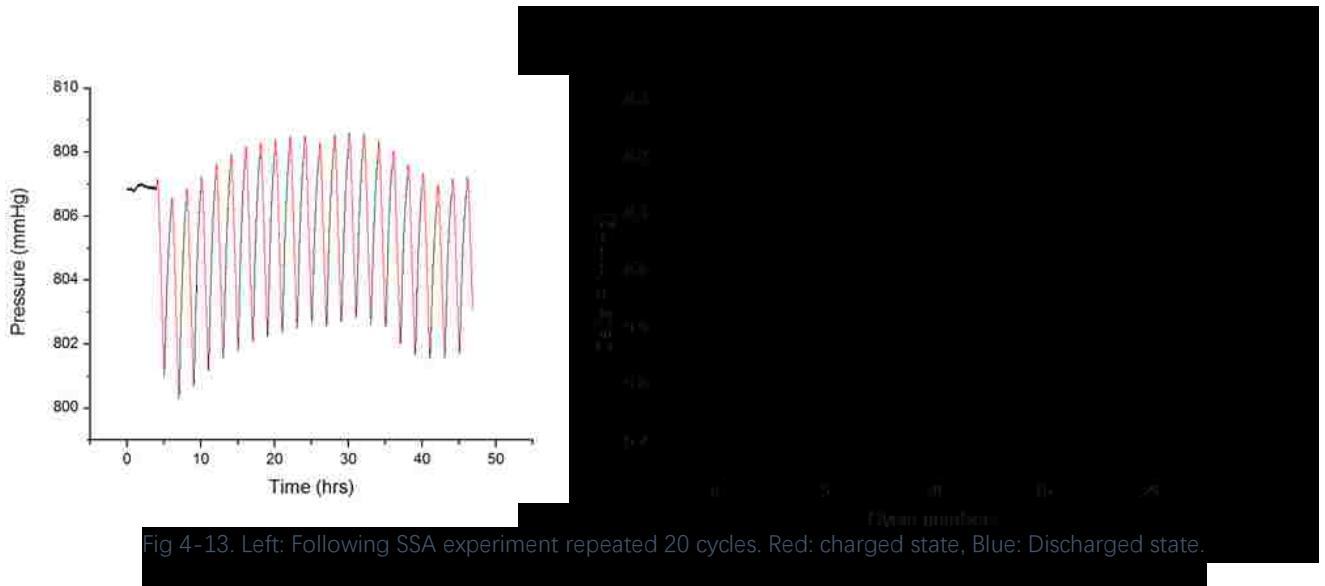




The purpose of the 5-cycle experiment was to reproduce and verify the SSA work that was done by B. Kokoszka[6]. In addition to the 5-cycle experiment, the SSA experiment was also repeated for 100 cycles to evaluate the stability and long-term performance (only 50 cycles shown), Fig 4-


12. From the graph, a decline of the SSA effect was visible as the cycle number increased. At the 100th cycle, the SSA effect had declined by 27.4% compared with the first cycle.

To find out whether the performance decline was permanent or not, the system was left untouched for 48 hours after the 110-cycle experiment was finished and then tested again for another 20 cycles as shown in Fig 4-13. After the system was sitting for the 48 h period, the system showed nearly the original SSA capacity.



The assumption that the desorption was slower than adsorption can be an explanation for the performance decline. For a given charge/discharge cycle, the CO₂ molecules adsorbed during the charge half-cycle were not fully released in the discharge half-cycle. Therefore the available SSA capacity decreases as the cycle numbers increase. The electrolyte ion diffusion kinetics could also be a possible reason for the slight performance decline over the cycles. Since the sodium and chloride ions exist in the solution as hydrated ions with solvation shells, their size could be similar or even larger than the micropore sizes. Therefore, after over 100 cycles, it was possible that a portion of pores had electrolyte ions trapped inside the pores of carbon electrodes.

In the experiment with the disassembled commercial supercapacitor, it was shown that the SSA effect can be observed for CO₂ but not for helium. In addition, it was also shown that the SSA effect is only very slight for nitrogen[6]. Therefore, it can be assumed that the pressure change in the cell was only caused by adsorption of CO₂ to the electrode.

The magnitude of the SSA effect can be calculated by the ideal gas law. The empty volume in the cell was 105 mL, and the pressure change from the SSA effect was 6.65 mmHg. R is the gas constant 62.36 ml mmHg K⁻¹ mmol⁻¹. Plugging the numbers in, the amount of CO₂ adsorbed for the charging cycle was  0.038 mmol. Since the mass of the exposed electrode was 3.7 g, which translated to an SSA capacity of 0.0102 mol kg⁻¹.

In addition, the pressure change was associated with the CO₂ composition change in the cell, the relationship can be calculated as the following. Initially, the volume percentage of carbon dioxide is 15% and the pressure is 800 mmHg with a volume of 105 mL which means there is $n = \frac{pV}{RT}$ * 0.15 = 0.68 mmol carbon dioxide and 3.84 mmol nitrogen in the cell. After 6.65 mmHg pressure change, the remaining carbon dioxide is 0.68 mmol – 0.038 mmol = 0.642 mmol. This means that the carbon dioxide concentration after the pressure drop can be calculated as % CO₂ = $\frac{\text{amount of } CO_2}{\text{amount of } N_2 + \text{amount of } CO_2} = \frac{0.642 \text{ mmol}}{3.84 \text{ mmol} + 0.642 \text{ mmol}} = 14.2\%$, which means that 6.65 mmHg change in pressure corresponds to a 15% - 14.2% = 0.8% change in carbon dioxide concentration.

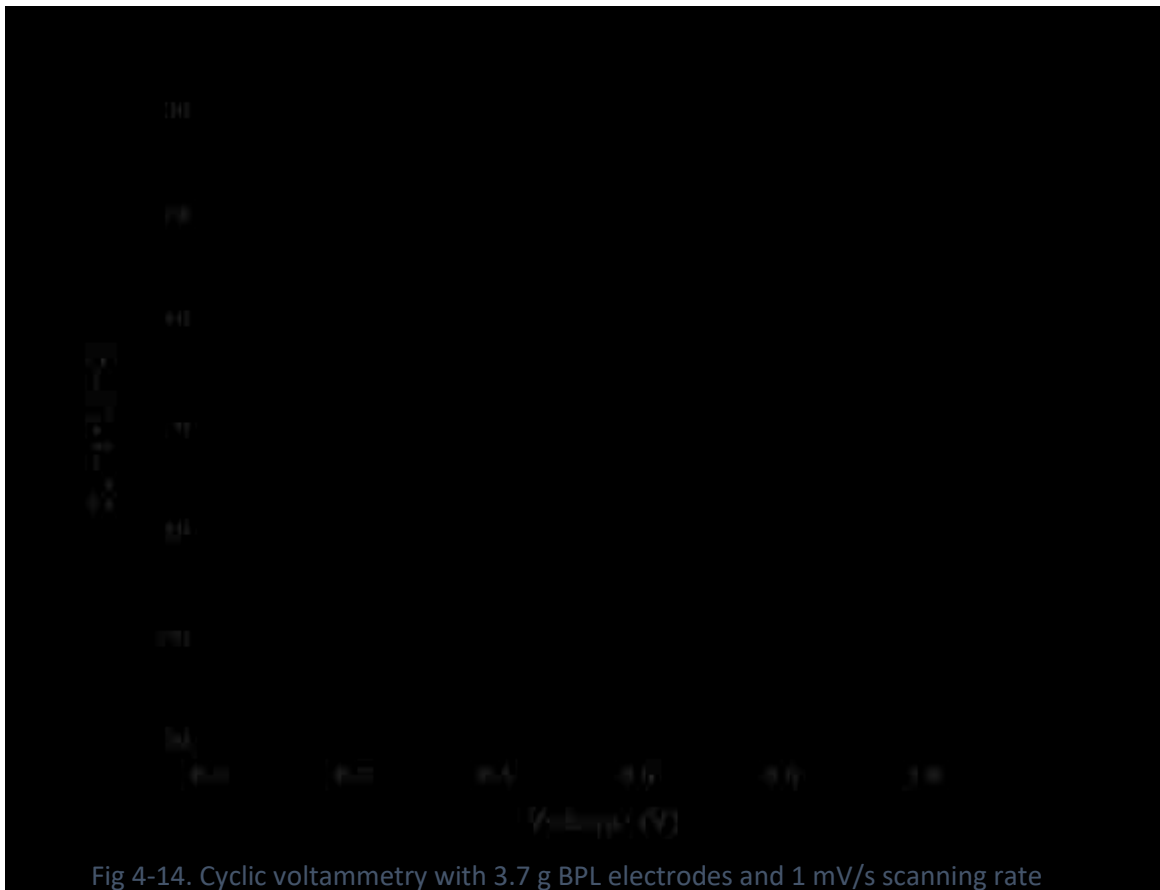
In order to determine the change of gas composition associated with the pressure change, B. Kokoszka analyzed the gas composition with the same experimental setup[6]. At the end of each charge step and discharge step, the gas composition was analyzed by a Hewlett Packard 5890 series II gas chromatograph with a thermal conductivity detector and a Supelco fused silica capillary column. 10 µL sample was taken from the sorption cell and injected into the GC. Electrodes with 3.7 g mass and 7.5 g mass were studied and the results are listed in table 4-1.

Electrode mass	3.7 g		7.5 g	
Cycle	Δp (mmHg)	Δ CO ₂ composition	Δp (mmHg)	Δ CO ₂ composition
1 st charge	-11.3	-2.1	-14.91	-2.7%
1 st discharge	+8.0	+1.1%	+12.42	+1.7%
2 nd charge	-7.9	-1.1%	-14.86	-1.9%
2 nd discharge	+7.8	+1.0%	+13.93	+1.9%
3 rd charge	-7.6	-1.1%	-15.27	-2.1%
3 rd discharge	+7.2	+1.1%	+14.88	+1.8%
4 th charge	-7.1	-1.4%	-15.48%	-2.2%
4 th discharge	+7.0	+1.0%	+15.40	+2.3%
5 th charge	-7.0	-1.4%	-15.84	-2.5%
5 th discharge	+6.9	+1.3%	+16.05	+2.8%

Table 4-1. Change in gas compositions during SSA experiment with 3.7 g and 7.5 g electrodes.

The results showed that the carbon dioxide composition change in accordance with the pressure. When the pressure in the cell dropped, so did the gas composition and vice versa. This proves the assumption that the pressure change was caused by the carbon dioxide molecules selectively adsorbed on the electrodes and further supports the SSA effect. From the test results, 6.39 mmHg pressure change correlates with 1.0% change in gas composition, which is lower from the calculated value but plausible since the change in carbon dioxide composition is larger than expected. In the calculation, carbon dioxide and nitrogen are both treated as an ideal gas and this

could be an explanation for the difference between the calculated value and experimental data. The electrochemical behavior of the system was characterized by the Gamry Potentiostat 3000 system. The cyclic voltammetry was carried out with the halfway-submerged electrode with the counter electrode and the fully-submerged electrode as the working electrode, and the voltage was scanned from 0 V to 1 V.



Comparing Fig 4-14 with a typical CV curve for supercapacitor in Fig 2-14, the CV curve did not have a “rectangular” shape which is representative for a typical supercapacitor. Even with a slow scan rate (1 mV/s), the CV curve showed the system does not have a well-defined double-layer formation step, and the diffusion kinetics of electrolyte ions was far from ideal.

The charge/discharge cycle was also performed with the halfway-submerged electrode as the counter and fully-submerged electrode as the working electrode. In the cyclic charge/discharge experiment, a constant current was used to charge the system up to 1 V and voltage was recorded against time as shown in Fig 4-15.

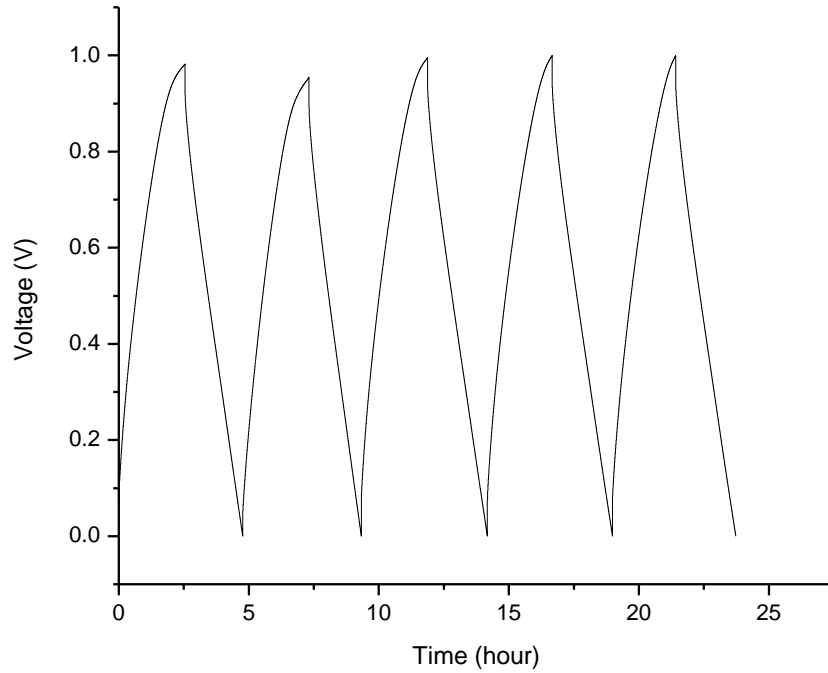


Fig 4-15. Charge/Discharge curve of 3.7 g BPL monolith electrodes with 5 mA from 0 V to 1 V.

5 charge cycles and 5 discharge cycles were plotted in the graph. In the charge half-cycle, the voltage gradually increased from 0 V to 1 V and energy flowed from the power supply to the device, and it can be calculated the following way:

$$E_{charge} = I \int_{0V}^{1V} V dt \quad Eq. 4 - 1,$$

While in the discharge half-cycle, the energy flew back could be calculated as

$$E_{discharge} = I \int_{1V}^{0V} V dt \quad Eq. 4 - 2.$$

Where E is the energy, I is the current, V is the voltage and t is time. Therefore, the energy in the charge/discharge cycles could be represented by the integral area underneath the charge/discharge curve. The capacitance of the system could also be calculated from the cyclic charge/discharge curve by the following.

$$C = \frac{Q}{V} = \frac{it}{V} \quad \text{Eq. 4 - 3.}$$

Where Q is the total charge stored on the capacitor at the end of a charging cycle, i is the charging current, V is the final voltage and t is the charging time[7]. Plug in the numbers, the capacitance of the system was $C = it/V = 0.005 \text{ A} * 7198 \text{ s} / 1 \text{ V} = 35.9 \text{ F}$ and the energy consumed in the charge step could be calculated as $E_{\text{charge}} = 0.005 \text{ A} * 6263.09 \text{ Vs} = 31.32 \text{ J}$, while the energy recovered in the discharge step is $E_{\text{discharge}} = 0.005 \text{ A} * 3377.31 \text{ Vs} = 16.89 \text{ J}$, which means the energy efficiency of the setup was 50.9 %.

While it is much lower than that of a commercial supercapacitor, there is room for optimization. The energy efficiency of a supercapacitor is closely related to the equivalent series resistance (ESR). The ESR of a supercapacitor can be measured from the voltage drop between the charge cycle and discharge cycle. With a 5 mA charge/discharge current, the ESR was measured to be 11.4 Ω . For comparison, commercial capacitors usually have very low ESR (< 0.6 Ω)[8]. The contact resistance between the electrode and current collector and non-conductive PVDF binder could contribute to a high ESR of the system.

4.3 SSA experiments in flow-through mode

4.3.1 Background and experimental setup

Previous experiments showed that SSA can separate CO₂ with N₂ in a closed glass cell where there was no gas flow. However, in order to build a functional CO₂ separation device, the SSA concept needs to work with flowing flue gas. For example, TSA and PSA techniques allow gas to flow through sorption columns packed with sorbent material. As the gas mixture advances through the column, one gas gets adsorbed and the other passes through the column. When the sorbent is saturated and the adsorbate breaks through, the column is purged and regenerated.

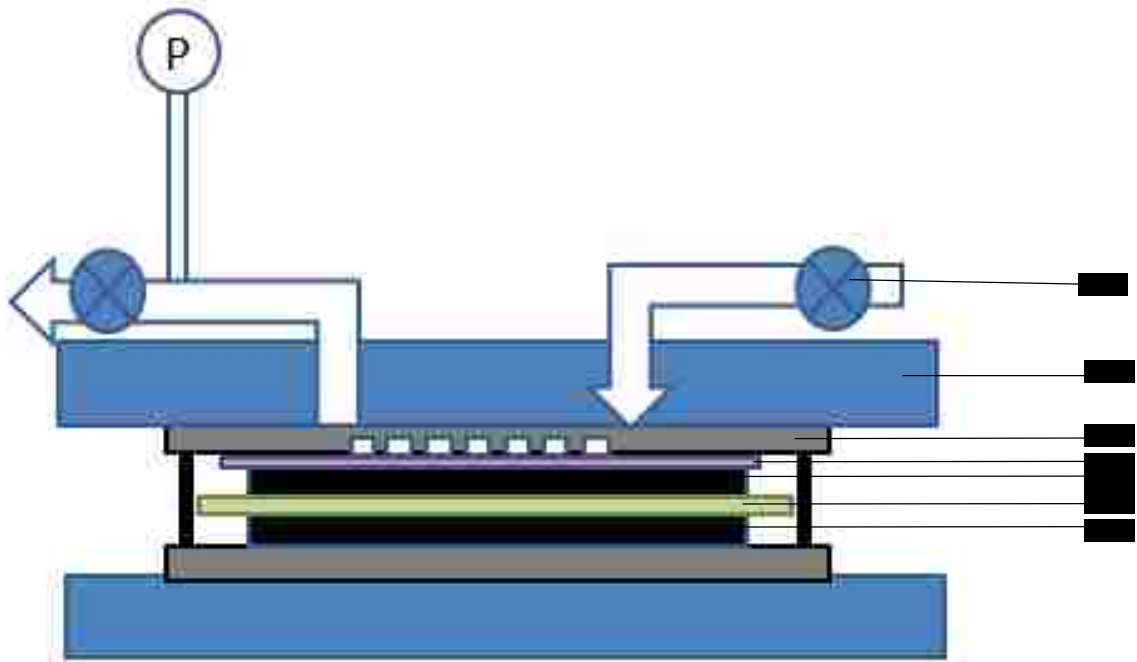


Fig 4-16. Construction of SSA gas separation device, cross-sectional view. 1. Valve, 2. Aluminum block, 3. Graphite plate with gas diffusion channels, 4. Carbon cloth, 5. Top electrode, 6. Separator, 7. Bottom electrode.

In order to make SSA a technique that is able to separate gases from a continuous gas flow, a custom gas separation device was constructed as shown in Fig 4-16. The separation device had inlet and outlet ports to allow gas flow through. The Omega pressure transducer was attached to the gas channels of the device by a dielectric joint (SS-6-DE-6, Swagelok) so that the applied voltage on the device did not interfere with the transducer electronics. Two aluminum plates (blue bar) with 3 cm*3 cm size were machined and served as mechanical support and current

collector for the device. The thickness of the top and bottom aluminum plate are 1.27 cm (1/2 inch) and 0.635 cm (1/4 inch), respectively. Both plates had 2 cm * 2 cm * 1 mm recess in the center so the graphite plates would fit inside. Two holes with 1 mm diameter were drilled in the top aluminum plate to provide gas channels for the top graphite plate. The inlet and outlet from the plate were connected to the respective source by a 1/8-inch stainless steel tube (Swagelok SS-T2-S-028-20). Two 2 cm * 2 cm * 0.635 cm (1/4 inch) sized graphite plates (grey) are in contact with the carbon electrodes. The top graphite had 1mm wide and 1mm deep gas diffusion channels as shown in Fig 4-17. At each end of the gas diffusion channel, a hole with 1 mm diameter was drilled matching the holes on the aluminum plate to serve as the gas inlet/outlet. The locations of the ports were designed so that when the top graphite plate was placed inside the top aluminum plate, the gas ports on the graphite plate were aligned with ports on the aluminum plate. A 1.4 cm * 1.4 cm carbon cloth (AvCarb 1071 HCB) was added between the top electrode and the top graphite plate to provide additional gas diffusion pathways. Between the two graphite plates, a separator membrane (Whatman filter paper, grade 2) was sandwiched between two 1.4 cm * 1.4 cm BPL carbon electrodes to form a supercapacitor. The void channel volume (the volume within the device between the inlet and outlet valve) was calculated to be 4.6 mL. The parts and materials used to build the separation are listed in the table below.

Component	Vendor	Size/Model No.
Pressure transducer	Omega	MMA015C1T3C2TA5S
Dielectric connection	Swagelok	SS-6-DE-6
Stainless steel tube	Swagelok	SS-T2-S-028-20, 1/8 in
Graphite plate	McMaster-Carr	1/4 in
Aluminum plate	McMaster-carr	1/2 in, 1/4 in
Separator membrane	Whatman	Filter paper grade 2
Rubber sealer	McMaster-Carr	High-Strength 60A EPDM rubber, 1/8 in
High vacuum grease	Apiezon	Apiezon M grease
Carbon cloth	Avcarb	1071 HCB, 20 cm * 20 cm

Table 4-2 List of materials for the gas separation device assembly.

This setup could potentially provide several benefits over the previous glass cell setup. In the previous setup, a 1 cm wide carbon cloth was used as the current collector for the carbon monolith which was not able to cover the whole monolith. The carbon monoliths were several centimeters apart, which could result in long diffusion pathways for the electrolyte ions and subsequently lead to slow kinetics. With the gas separation device setup, the electrodes were fully in contact with the graphite current collectors, and the distance between the electrodes was reduced to 0.2 mm (thickness of the separator paper), which could also improve the electrolyte diffusion kinetics. Therefore, it was expected this experimental setup could also optimize electrochemical performance and provide higher energy efficiency.

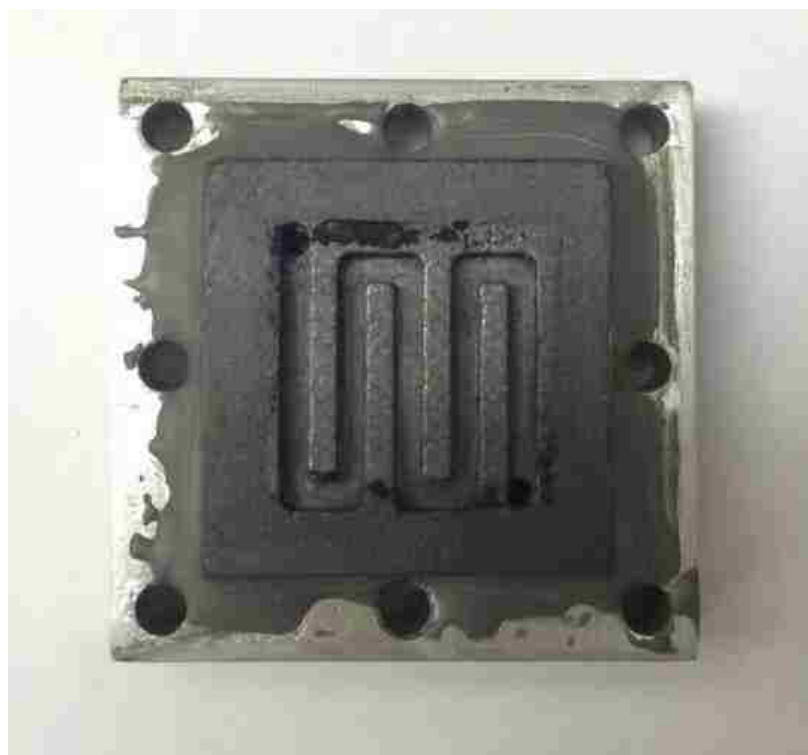


Fig 4-17. Gas channel of the top graphite plate.

The carbon electrodes were fabricated from BPL carbon powder. In a typical procedure, 0.083 g 60% Polytetrafluoroethylene (PTFE) dispersion (Sigma-Aldrich) was dispersed in 10 mL ethanol and stirred. PTFE was used as the binder instead of PVDF that was used previously because PVDF requires the use of high boiling point solvents such as NMP, dimethylformamide (DMF), and dimethylacetamide (DMA). Since PTFE preparation solution could be dispersed ethanol, it was much easier to dry the binder at room temperature. In addition, PTFE was a much better film forming binder than PVDF. After the PTFE was completely dissolved, 0.8 g BPL carbon, 0.1 g gluten (Hodgson Mill, food grade), and 0.05 g conductive carbon black (Cabot Corporation) was added to the solution. Gluten here serves as a co-binder which ensures the sufficient hydrophilicity of the binder mixture. Carbon black was added to increase the conductivity of the electrodes. The

final ratio of BPL: Carbon black: Gluten:PTFE was 80:5:10:5 by mass. The solution was then stirred at 60 °C in a vial for 2 hours. Afterwards, the vial was opened and the ethanol was evaporated at 80 °C until the mixture became a slurry. The slurry was then transferred to a flat glass panel and mixed with a metal spatula for 1 hour to allow thorough contact between the binder and the rest components. As the ethanol gradually evaporated, the slurry became a sticky dough-like substance. Then, the dough was rolled against the glass panel with a glass vial having a diameter of 2.54 cm to form a uniform film. Two 1.4 cm * 1.4 cm sheets were cut from the film as the electrode. The mass of the final electrode was adjusted by the thickness of the film. The electrode was then dried at 100 °C for 12 hours in a vacuum oven to remove any solvent residue (the pressure in the oven was ~25 mmHg).

After several trials with pure PTFE as the binder, it was discovered that gluten was a vital component for successful SSA experiments. Without gluten added, the SSA result showed unpredictable and unreproducible results. One possible reason is that PTFE is a hydrophobic polymer that could affect the wetting in the electrodes. By adding gluten, the overall hydrophilicity was increased. Another attempt was made to use only gluten as the only binder. However, by using gluten as the sole binder, it was difficult to obtain a flat electrode.

In the experimental setup, it was intended to have an exposed electrode (top electrode) and a submerged electrode (bottom electrode) in order to mimic the previous experiments with the carbon monoliths. Therefore, the bottom electrode was soaked completely in 1 M NaCl for 2 hours, and used as the anode. The top electrode was wetted with electrolyte solution on only one side so that the other side remained dry and accessible by gas molecules. After the electrodes were properly wetted with the electrolyte, the separator with a size of 1.6 cm * 1.6 cm was cut from a Whatman Grade 2 filter paper (GE Healthcare Life Sciences) and placed in between the electrodes to prevent short-circuiting between them. Then, this sandwich structure was transferred onto the

bottom graphite plate, so the fully soaked electrode was in contact with this graphite plate. A 2 cm * 2 cm rubber seal (gasket) with a 1.7 cm * 1.7 cm opening was cut from an EPDM rubber film (1/8 in, McMaster-Carr) and placed on top of the electrode sandwich. Then, high vacuum grease (Apiezon M grease) was applied to the rubber seal to prevent leaking. Then a 1.4 cm * 1.4 cm sized carbon cloth (AvCarb 1071 HCB) was placed on the top electrode. The top aluminum plate and the bottom aluminum plate was then clamped together by 8 screws. These screws were tightened evenly to 15 Nm by a torque wrench.

Then, gas mixture was flown through a bubbler containing 1 M NaCl to the cell for 2 hours. The purpose of the bubbler was to moisturize the gas mixture so that the electrode films do not get dried out. Afterwards, the system was left for equilibration overnight in the Styrofoam tent. The electrodes were then connected to the Keithley 2400 power source through the aluminum block with the top electrode as the cathode and bottom electrode as the anode.

4.3.2 Experimental results

In order to validate whether the SSA concept could work in this configuration, a “static mode” experiment was performed similarly to the experiments in 4.2.1. Two electrodes with 0.0487 g mass and 0.39 mm thickness were made and loaded into the gas separation device according to the procedure described above. A 5-cycle SSA experiment was performed with 1 h half-cycle time, shown in Fig 4-18. As the voltage was turned on, the pressure dropped very rapidly. For the 1st cycle, the pressure dropped 3.59 mmHg within 15 mins after the voltage was turned on while the total pressure drop of the cycle was 4.42 mmHg. Therefore, 80% percent of the pressure drop was completed within the first 15 min after charging. Unlike the previous SSA experiments with carbon monoliths, the pressure drop completely stopped at the end of a 1-hour charging half-cycle. In

the discharge half-cycle, the pressure increased by 4.28 mmHg in the first 15 min after discharging started. Over the 1-hour discharge cycle, the overall pressure increase was 5.24 mm Hg. At the end of the discharge cycle, the pressure was slightly higher than the pressure before the charging cycle started, which was probably caused by the temperature variance in the environment.

The result also showed that the adsorption and desorption kinetics were much faster than in the previous SSA experiment with the carbon monoliths. For comparison, in the experiment described in 4.2.1, 15 min after the charging started, the pressure dropped by 0.92 mmHg, and at the end of the 1-hour charging half-cycle the pressure drop was 6.65 mmHg, therefore after 15 mins, only 14% of the final pressure drop was reached. The improvement of faster pressure drops/increases may be explained by the gas diffusion kinetics as well as electrolyte ion diffusion kinetics. In the experiments with cylindrical carbon monoliths, CO₂ molecules have to diffuse through the monoliths with 5 cm length, and 2.54 cm in diameter. Also, the two electrodes were separated apart by several centimeters, which can lead to a long travel time for the electrolyte ions. In the gas separation device setup, the electrode films were only 0.29 mm thin, therefore the diffusion pathway for CO₂ into the electrodes was much shorter. In addition, the two films were only separated by a fraction of a millimeter. Therefore, the kinetics of ion transport was improved as well.

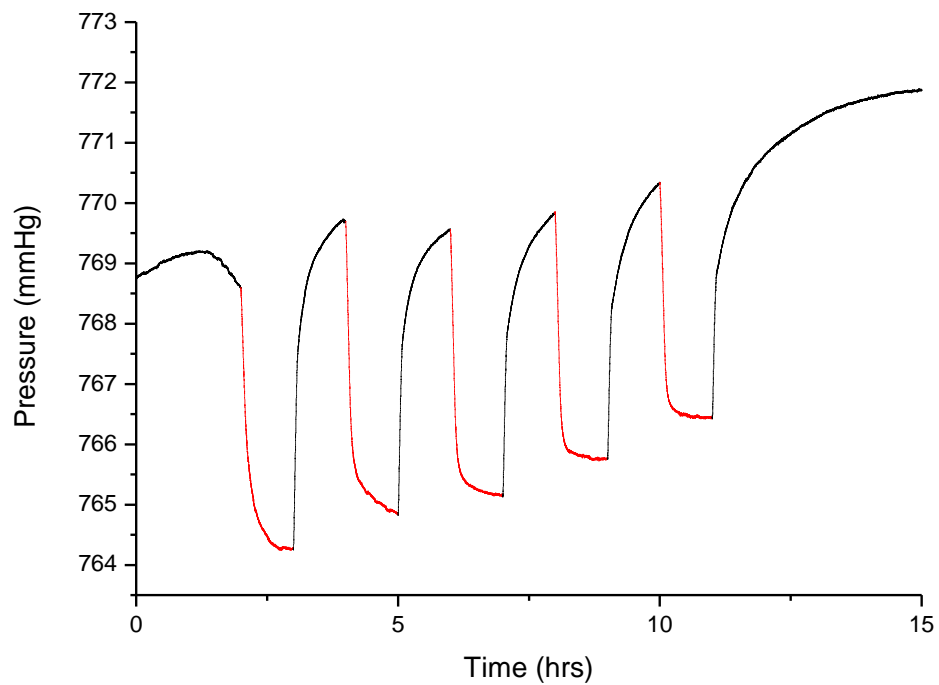


Fig 4-18. SSA experiment with electrodes having a 0.0487 g mass. Red: Charged state, black: discharged state.

In order to investigate the gas composition change during the cycles, at the end of each charge/discharge step, 10 μL gas was taken and injected into the GC for composition analysis. The average change in CO_2 concentration is 1.01% demonstrating that gas separation occurred in the constructed device.

Electrode mass	0.0487 g	
Cycle	Δp (mmHg)	CO ₂ concentration (%)
1 st charge	-4.46	15.02
1 st discharge	+5.44	15.97
2 nd charge	-4.96	14.72
2 nd discharge	+4.72	15.11
3 rd charge	-4.45	14.00
3 rd discharge	+4.73	15.73
4 th charge	-4.08	15.19
4 th discharge	+4.61	16.22
5 th charge	-3.89	15.12
5 th discharge		

Table 4-3. CO₂ composition after each charge and discharge cycle.

The next aim was to show that the SSA device can be operated in flow-through mode. The working capacity of SSA can be described as the CO₂ adsorption capacity difference between the charging half-cycle and discharging half-cycle. When doing a flow-through SSA experiment it is important to distinguish between the native CO₂ adsorption capacity due to conventional physisorption and the adsorption capacity change from the SSA effect. Because the flow-through experiments were operated at atmospheric pressure the pressure transducer is unnecessary in the experiment and

was removed from the apparatus. After pressure transducer and dielectric connection were removed, the dead volume of the device was reduced to 0.9 mL (Fig 4-19).

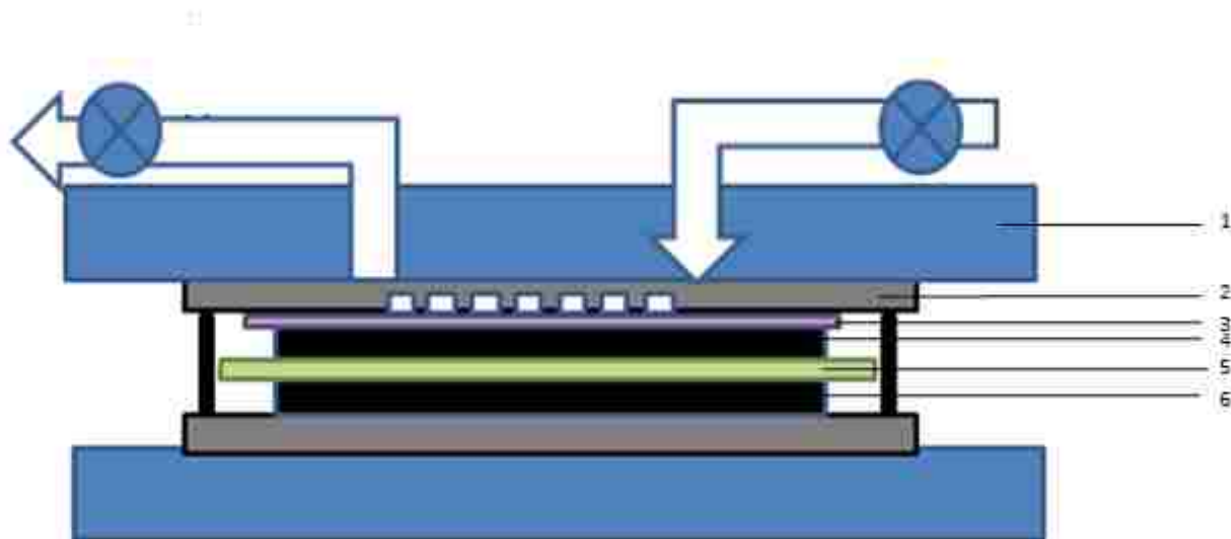


Fig 4-19. Gas separation device with pressure transducer removed. 1: Aluminum block. 2. Graphite plate with gas diffusion channels. 3. Carbon cloth. 4. Exposed electrode. 5. Separator. 6. Submerged electrode.

The experiments were performed the following way. Two 1.4 cm * 1.4 cm electrodes with 0.197 g and 0.189 g mass and 1.53 mm thickness were prepared. The 0.189 g electrode was soaked in 1 M NaCl for 2 hours and used as the bottom electrode. The other electrode was in contact with the electrode on one side and used as the top electrode, so the other side would remain dry and accessible for gas diffusion. The top electrode and bottom electrode were assembled into the gas separation device using the method described above. After the assembly, the gas mixture was flown through a bubbler with 1 M NaCl solution, and then through the gas separation device for 2 hours. The device was then let sit overnight to allow equilibration. Before the experiment, the residual mixture gas in the separation device was purged with a flow of 10 cc/min for 1 min with N₂. The high flow of 10 cc/min was to ensure rapid removal of residual gas but not to significantly

affect the CO₂ adsorption equilibrium on the BPL carbon electrodes. Afterwards, the electrodes were charged up to 1V to put the system into adsorption mode with the valves of the device closed. The power source used was the same Keithley 2400 source meter and the current was limited to 10 mA. After 10 minutes, the gas mixture was passed through the gas separation device at a rate of 0.3 cc/min, and the effluent gas composition was analyzed every two minutes by GC (Table 4-4).

Time (min)	CO ₂ concentration (%)
Before N ₂ purge	15.23
0 (10 mins after charging)	0
2	0
4	0
6	1.95
8	12.26
10	14.69
12	15.36

Table 4-4. CO₂ concentration in the effluent gas at vs time.

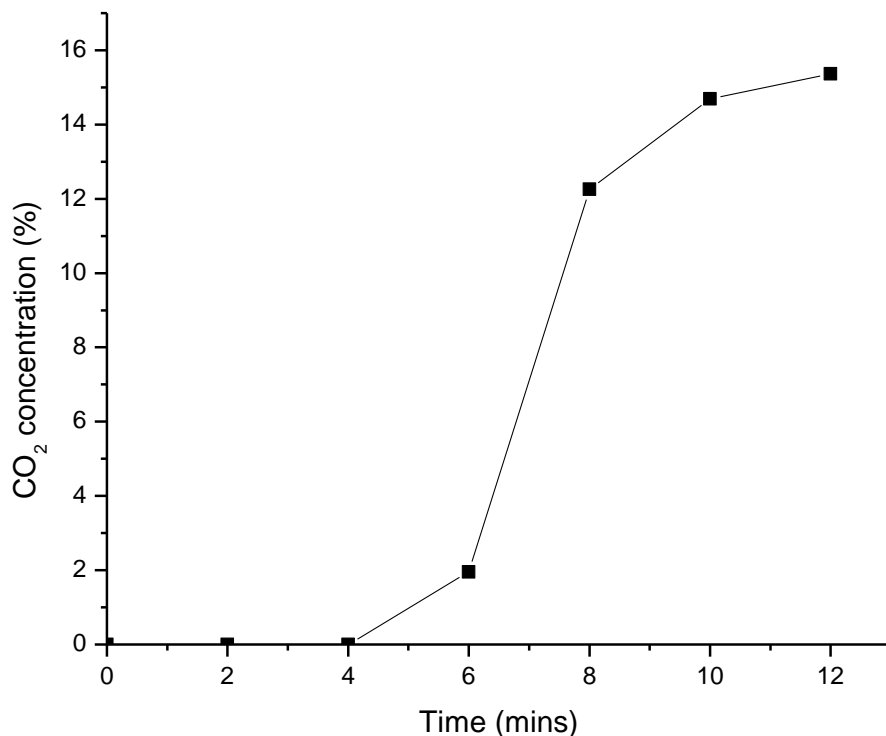


Fig 4-20. CO₂ breakthrough curve of 0.197g electrode.

As Fig 4-20 suggests, up to 4 min after the experiment started, no CO₂ was detected by GC in the effluent gas. This means that during this period, the device was absorbing CO₂. Carbon dioxide starts to breakthrough at 6 min. At 12 min, the SSA effect was completely saturated and the CO₂ concentration in effluent gas reached that of the influent gas.

It is worth considering that the 0.9 mL void volume of the separation device affects the breakthrough time. In a control experiment, after the device was purged with 10 cc/min N₂ flow for 1min, the gas mixture was flown directly through the separation device without turning on the voltage, and the effluent gas was analyzed by GC. The result is listed in Table 4-4. It can be

concluded that it took up less than 4 mins to fill up the void space of the gas separation device, which was expected considering the void volume (0.9 mL) and the gas flow rate (0.3 cc/min).

Time (mins)	CO ₂ concentration (%)
Before purging	15.39
0	0
2	8.87
4	15.45

Table 4-5. CO₂ concentration in effluent gas without SSA effect.

In order to get to get a more precise measurement of the breakthrough curve, electrodes with larger mass were used and a lower gas flow rate was used. Two electrodes with a mass of 0.290 g and 0.287 g with 2.31 mm thickness were used as the top and bottom electrode, respectively, and a low flow rate of 0.1 cc/min was chosen. All the other experimental procedures were the same as previously described. After the device was flushed with the moisturized gas mixture, it was allowed to sit overnight. Then, the system was purged with 10 cc/min N₂ flow for 1 min. Before the SSA experiment, a control experiment was performed to determine the carbon dioxide breakthrough time at a flow rate of 0.1 cc/min without the SSA effect.

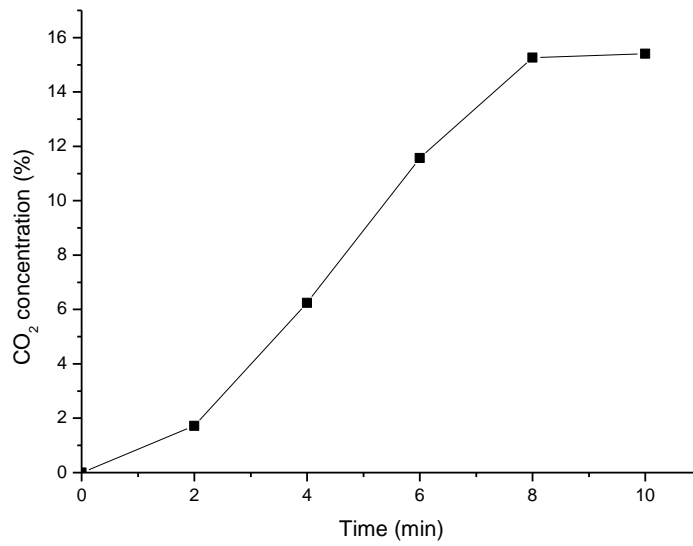


Fig 4-21. Carbon dioxide breakthrough without SSA

Time (min)	CO2 concentration (%)
0	0
2	1.72
4	6.24
6	11.57
8	15.26
10	15.41

Table 4-6. CO₂ breakthrough data from experiment without applied voltage.

According to the GC measurements in table 4-6 and Fig 4-21, it took up to 10 mins for the gas mixture to flow through the void volume, which is expected for a dead volume of 0.9 mL. In the following actual SSA experiment, after the system was purged with 10 cc/min N₂ for 1min, the device was closed and the voltage was turned on for 10 mins. Then, the device was opened and the gas mixture was flown through at a rate of 0.1 cc/min, and effluent gas composition was analyzed by GC. From the breakthrough curve in Fig 4-22, carbon dioxide was not detected until at 22 min, and the effect reached full saturation at 32 min. Considering that the void volume in the gas separation device took 10 mins to be filled by 0.1 cc/min mixture gas flow, the actual breakthrough by SSA effect happened between 12 min and 22 min.

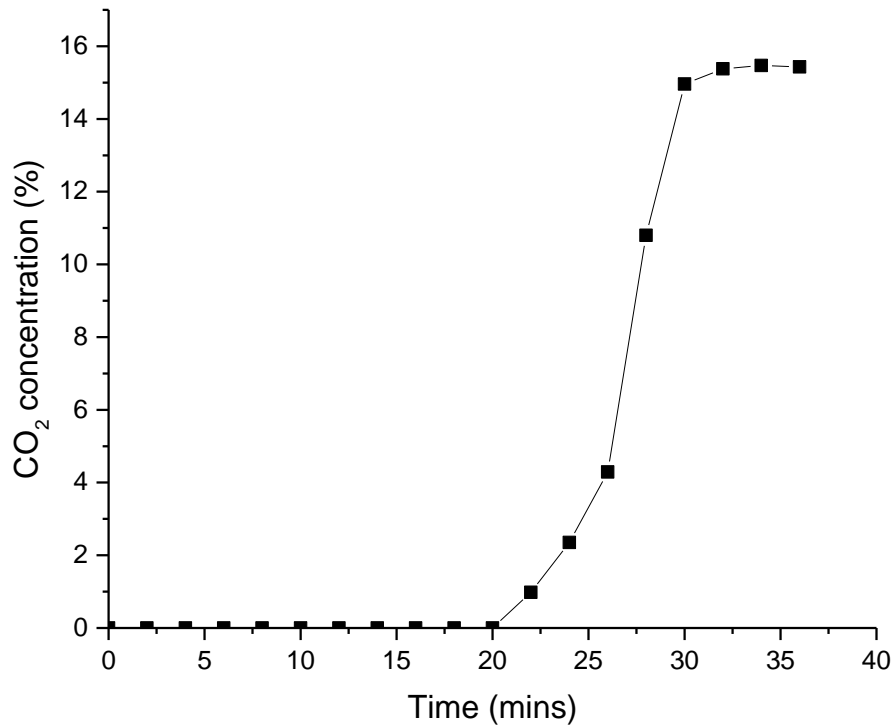


Fig 4-22. Breakthrough curve with 0.1 cc/min mixture flow.

Time (min)	CO2 concentration (%)
0	46.61
2	1.72
4	0

Table 4-7. CO₂ concentration in the desorption cycle.

In the discharging half-cycle, the device was discharged with the inlet and outlet gas valves closed for 30 mins for carbon dioxide to fully desorb. After that, pure nitrogen was used to purge carbon dioxide out of the device. To avoid the desorption of conventionally adsorbed CO₂, a fast purge rate of 1 cc/min was used, and the exhaust gas was analyzed in Table 4-7. After the discharge, the carbon dioxide concentration in the cell had increased dramatically to 46.61% and was purged out at an N₂ flow rate of 1 cc/min in less than 4 mins.

Following the first cycle, another cycle was performed to investigate the reproducibility of the SSA effect under this configuration. The CO₂ concentration in the effluent gas was plotted versus time in Fig 4-23. The breakthrough curve for the 2nd cycle was very similar to the 1st cycle. For the first 20 min, no carbon dioxide was detected, and 10 min afterwards, the SSA effect was saturated.

After the carbon dioxide got saturated, the desorption half-cycle was also performed. The inlet and outlet valves were closed and the device was discharged for 30 mins, and then the valves were opened and the device was purged by pure N₂ gas at 1 cc/min, and the GC result is shown in Table 4-8.

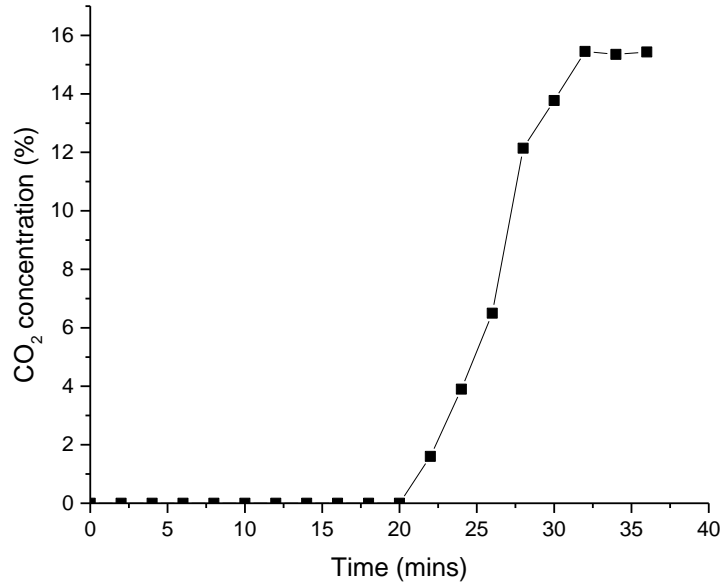


Fig 4-23. 2nd adsorption cycle with 0.1 cc/min gas flow.

Time (min)	CO ₂ concentration (%)
0	45.95
2	0.98
4	0

Table 4-8. CO₂ concentration in 2nd desorption cycle.

From the analysis of the two cycles, the separation performance of SSA is repeatable over more than one cycle. Carbon dioxide was detected 12 min after the gas mixture was flown through the device and reached saturation at 22 min. The breakthrough point is defined as the point in time at which the effluent gas concentration reaches 50% of the influent gas concentration [9, 10]. According to that the breakthrough time in our experiment is 18 min. In the desorption cycle, the CO₂ concentration increased to an average of 46.28%, which means that after the desorption cycle, 46.28% of the dead volume was carbon dioxide. Compared to the SSA experiments with the carbon monoliths the change in carbon dioxide concentration was significantly higher because the gas separation device had a much smaller dead volume.

In the adsorption half-cycle, the amount of carbon dioxide adsorbed by the SSA effect can be calculated as $0.1 \text{ cc/min} * 18 \text{ min} * 15\% = 0.27 \text{ cc (mL)}$. In the desorption half-cycle, the amount desorbed by SSA effect caused the CO₂ concentration to rise from 15% to 46.28%. Therefore the amount desorbed can be calculated as $0.9 \text{ mL} * (46.28\% - 15\%) = 0.281 \text{ mL}$. The small difference between adsorption amount and desorption amount could be caused by the measurement inaccuracy. Due to GC instrument limitations, the sample can only be taken every 2 minutes. Therefore the breakthrough time might not be completely accurate. However, this data can confirm that the adsorbed amount can be released completely during the desorption step. During the adsorption cycle, the amount of carbon dioxide was $n = pV/RT = 0.011 \text{ mmol}$, where R is 62.36 ml mmHg K⁻¹ mmol⁻¹, T is 298K, p is 760 mmHg and V is 0.27ml. Since 0.290 g carbon material was used in the top electrode, the SSA sorption capacity can be calculated by $0.011 \text{ mmol} / 0.290 \text{ g} = 0.038 \text{ mol/kg}$, which means for every kilogram of sorbent material, the SSA capacity is 0.038 mol of carbon dioxide molecules.

The electrochemical performance was also characterized by electrochemical measurements. In these measurements, the top electrode with 0.290 g mass was connected to the counter electrode of the potentiostat, while the bottom electrode was connected to the working electrode. The CV curve was plotted in Fig 4-24. Compared to Fig 4-14, the rectangular shape of the curve was much more defined, which was a sign for improved kinetics compared to the monolithic BPL electrodes.

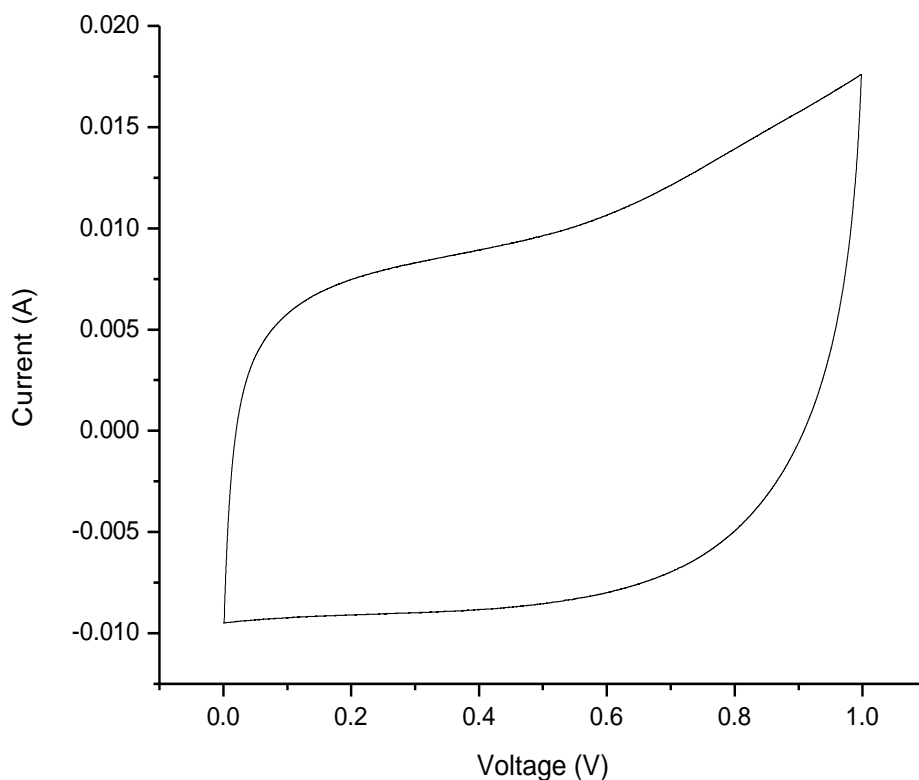


Fig 4-24. CV curve of the thin film electrodes with 1 mV/s scanning rate.

The charge/discharge curve was measured with the same electrode setup, the charging current was 1 mA and the voltage was from 0 V to 1 V. The curve is shown in Fig 4-25.

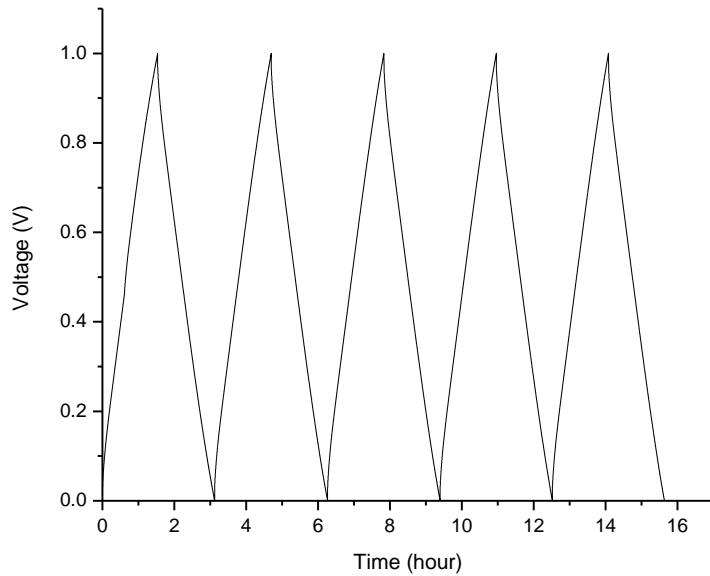


Fig 4-25. Charge/discharge curve for thin film carbon electrodes with a constant current of 1mA.

The triangular shape of the curve means the thin film electrodes had a higher charge/discharge efficiency compared to the 3.7 g BPL carbon monolith electrodes. The capacitance of the system could be calculated as $C = it/V = 0.001 \text{ A} * 5688 \text{ s} / 1 \text{ V} = 5.68 \text{ F}$. On average, in the charge cycle, the energy flown into the device was $E_{\text{charge}} = 0.001 \text{ A} * 2842.27 \text{ Vs} = 2.842 \text{ J}$, the energy recovered on the discharge cycle was $E_{\text{discharge}} = 0.001 \text{ A} * 2218.72 \text{ Vs} = 2.221 \text{ J}$, therefore the energy efficiency was $E_{\text{discharge}}/E_{\text{charge}} = 78 \%$. This was higher than the energy efficiency obtained from BPL electrodes setup in 4.2, indicating the setup with thin film electrodes was a more energy efficient setup.

4.4 Possible SSA mechanism and optimizations

In chapter 3, it was shown that earlier SSA attempts without using ionic electrolyte did not produce any CO₂ adsorption effect. Therefore, the formation of the electrical double layer between the electrolyte ions and electrode surface is critical to the SSA effect. This indicates that the enhancement of CO₂ adsorption capacity resulted from the interaction between CO₂ molecules and charges. Generally speaking, there are two routes for this interaction: 1) CO₂ molecules can diffuse to the electrode pores through the macropores and mesopores directly, 2) CO₂ molecules can diffuse to the pores through the electrolyte. In the SSA experiment with carbon monoliths, the SSA effect could not fully saturate within a 1-hour charging half-cycle. It is well known that physisorption is a very fast process, therefore the mechanism behind the SSA effect seems more complicated than that of simple physisorption. This leads to the conclusion that the SSA effect is more likely happening at the liquid-solid interface, rather than the gas-solid interface. Given that activated carbon surface could be hydrophobic due to the nature of C-C bonds, it is possible that part of carbon dioxide molecules diffused to pores through the electrode material itself, and part of the carbon dioxide molecules diffused to the pores through the electrolyte. SSA is a promising concept of carbon dioxide capture, yet it is facing some technological and engineering challenges. Although the mechanism of SSA in the above hypothesis sounds plausible, it is not directly observed. In the future, in-situ spectroscopy SSA experiments could help to understand the mechanism of SSA, specifically how CO₂ molecules are preferably adsorbed when the carbon surface is electron rich. In addition, in the current setup, the gas mixture does not flow through but flows above the sorbent and the SSA effect depends on the carbon dioxide molecules diffusing to the sorbent. This could have a negative impact on the efficiency of the SSA effect.

The energy consumed in the carbon capture process is also an important factor to consider. In the gas separation devices with 0.290 g carbon electrodes, 3.158 J of energy was consumed in the charging step and 2.465 J of energy was recovered by the discharging step. Therefore, the net energy consumption was 0.624 J. Assuming 0.011 mmol carbon dioxide was captured in the cycle, we can calculate the energy cost per ton of CO₂ as $E = \frac{0.624 J}{0.011 \text{ mmol}} = \frac{0.624 J}{0.011 * 44 \text{ mg}} = 1.28 \text{ GJ/ton}$.

In general, coal-fired powerplants generate 3.6 GJ of energy per ton of CO₂ emission[11], leading to a parasitic load of 35.7%, which was on par with amine scrubbing technology[12]. The 0.624 J consumption was measured during charge/discharge experiments, therefore the energy consumption in actual SSA cycles could be higher than 0.624 J and the parasitic load could be higher than 35.7%. The high parasitic load is mainly associated with the low charge/discharge energy efficiency. Commercial supercapacitors have over 95% efficiency compared to 78% efficiency of the gas separation device. Several factors could contribute to the low efficiency of the current system. The carbon electrode contains 10% gluten to increase its hydrophilicity, however, gluten is not a conductive material and could increase the internal resistance of the system. The 5% PTFE binder could further add to the internal resistance as well. In addition, the separator membrane used was lab grade filter paper which is not specifically engineered supercapacitors, which could add kinetic barrier for electrolyte diffusion. With proper optimizations in the future, it is foreseeable that the parasitic load of the SSA process could be lowered by a large margin.

4.5 References:

1. Simon, P. and Y. Gogotsi, *Materials for electrochemical capacitors*. Nat Mater, 2008. **7**(11): p. 845-854.
2. Rashidi, N.A., S. Yusup, and B.H. Hameed, *Kinetic studies on carbon dioxide capture using lignocellulosic based activated carbon*. Energy, 2013. **61**: p. 440-446.
3. Gumma, S. and O. Talu, *Gibbs Dividing Surface and Helium Adsorption*. Adsorption, 2003. **9**(1): p. 17-28.
4. Kikkinides, E.S., R.T. Yang, and S.H. Cho, *Concentration and recovery of carbon dioxide from flue gas by pressure swing adsorption*. Industrial & Engineering Chemistry Research, 1993. **32**(11): p. 2714-2720.
5. Wessells, C., et al., *Investigations of the Electrochemical Stability of Aqueous Electrolytes for Lithium Battery Applications*. Electrochemical and Solid-State Letters, 2010. **13**(5): p. A59-A61.
6. Kokozska, B., et al., *Supercapacitive Swing Adsorption of Carbon Dioxide*. Angewandte Chemie International Edition, 2014. **53**(14): p. 3698-3701.
7. Chen, G.Z., *Understanding supercapacitors based on nano-hybrid materials with interfacial conjugation*. Progress in Natural Science: Materials International, 2013. **23**(3): p. 245-255.
8. NESSCAP Co., L., *NESSCAP ULTRACAPACITOR TECHNICAL GUIDE 2008*.
9. Gupta, V.K., et al., *Column operation studies for the removal of dyes and phenols using a low cost adsorbent*. Global Journal of Environmental Science and Management, 2016. **2**(1): p. 1-10.
10. Mollah, A.H. and C.W. Robinson, *Pentachlorophenol adsorption and desorption characteristics of granular activated carbon—I. Isotherms*. Water Research, 1996. **30**(12): p. 2901-2906.
11. Tan, Z. and SpringerLink (Online service), *Air Pollution and Greenhouse Gases From Basic Concepts to Engineering Applications for Air Emission Control*, in *Green Energy and Technology*,. p. XXVIII, 481 p. 128 illus.
12. Massood Ramezan, T.J.S., Nsakala ya Nsakala, and Gregory N. Liljedahl, , *Carbon Dioxide Capture from Existing Coal-fired Power Plants*. U.S. Department of Energy–National Energy Technology Laboratory, DOE/NETL-401/110907,, 2007.

5 High pressure chemistry of nanoporous materials

5.1 Introduction to the high pressure chemistry of mesoporous materials

Since the successful synthesis of the M41S family molecular sieves, researchers have extensively studied and explored nanoporous materials for application in gas storage and separation[4], drug delivery[5], catalytic support[6] and so forth. For industrial applications, the structural stability of these materials is an important factor to consider. Generally speaking, the stability of nanoporous materials includes the thermal, chemical, and mechanical stability. Thermal stability of those materials has been studied extensively over the past two decades. It is well demonstrated that MCM-41 series of mesoporous silica can be stable up to 800 °C with the mesostructure retained. It was also reported for SBA-15 type mesoporous silica that even though there is thermally induced contraction of the pores upon heating, the pore structure can be stable up to 1200 °C[7]. Also, Dai et, al. has found ORNL-1 type mesoporous carbon can be heated to 2600 °C for graphitization with considerable porosity maintained[8].

On the other hand, compared with the research efforts put into the study of the thermal behavior of mesoporous materials, reports about the behavior of mesoporous materials under pressure are rather limited. For large-scale industrial applications, there is a need for porous materials with high mechanical stability. There are some scenarios where porosity is desired in a pressurized environment, for example, in high pressure gas adsorption beds that have to be packed in a confined space, in porous carbon coatings that fit inside a tiny column for gas chromatography and so forth. The first study about the structural stability of mesoporous materials under pressure was conducted by O'Brien at 1996 when MCM-41 mesoporous silica was pressurized up to 1.2 GPa by mechanical compression. It was found from N₂ adsorption and SAXS that the mesostructure started to degrade at 86 MPa and was damaged at 224 MPa[9]. In 1999, Nakata

performed similar studies on MCM-48 mesoporous material, where the material is stable up to 400 MPa. The increased mechanical stability is attributed to the interconnected three-dimensional gyroid structure of the MCM-48 material[10]. Hartmann et al. investigated the mechanical stability of SBA-1 mesoporous silica with three-dimensional globular cages forming a continuous porous network. It was found SBA-1 exhibits higher stability than MCM-41 at 217MPa. This further proves that pore structure has an impact on the mechanical stability[11].

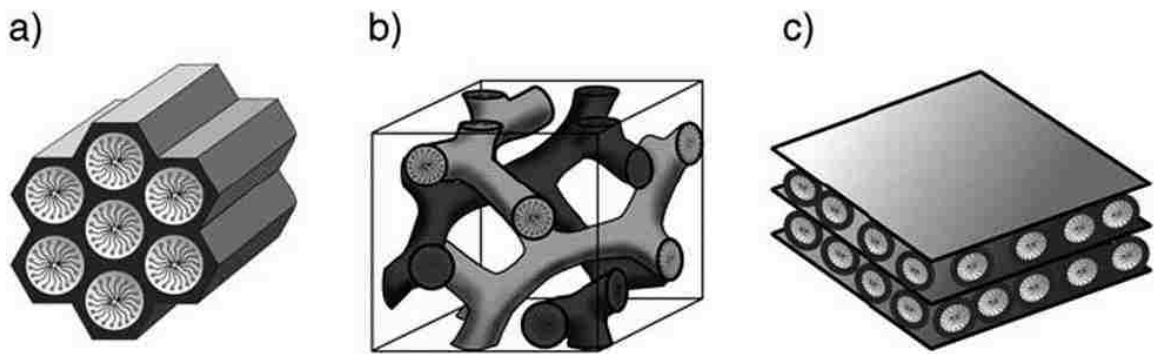


Fig 5-1. Structures of mesoporous silica: a) hexagonal, b) gyroid, c) lamellar

Hartmann also investigated the mechanical stability of SBA-15 silica and found that the pore structure was stable up to 260 MPa[12], which is higher than that of the MCM-41 material. Since SBA-15 and MCM-41 shares a similar hexagonal mesostructure, the difference in mechanical stability is likely to be a result of increased pore wall thickness of SBA-15.

In addition to pure mesoporous silica, the mechanical stability of mesoporous silica with heteroatoms is also investigated by researchers. Carrot et al. has found that inclusion of transition metal ions increases the structural stability of mesoporous silica significantly. For example, Ti-modified mesoporous silica SBA-15 can stand up to 518 MPa before the pores started to collapse, and the porous structure did not get destroyed till 814 MPa[13].

It is noteworthy that the efforts mentioned above were achieved using a piston-cylinder press which generates uniaxial pressure by applying pressure from two directions 180° apart from each other. When hydrostatic pressure was applied, the same mesoporous silica can withstand pressures in the gigapascal range. In 2000, the Tolbert group compressed an MCM-41 type silica/surfactant composite (as-synthesized silica without calcination) in a diamond anvil cell, using liquid/solid argon as a pressure media to ensure a hydrostatic pressure[14]. The composite material was able to resist pressure up to 12 GPa. In-situ XRD showed an elastic distortion of mesoporous lattice up to 4 GPa, and the distortion was recovered when the pressure was released. Even with surfactant removed the MCM-41 mesoporous silica was stable up to 8 GPa in an isostatic pressure environment. This increase can be explained by the hydrostatic pressure due to the pressure media (Argon). In a solid form, Argon can penetrate into the pores, therefore acting as a support for the porous framework, leading to a much higher stability of MCM-41 materials. From the research efforts mentioned above, one can preliminarily conclude that the stability of a porous structure is associated following parameters: 1) the pore structure and pore geometry – interconnected three-dimensional pore structure reinforce the framework against pressure, 2) pore wall thickness – thicker pore walls provide higher strength, 3) inclusion of heteroatoms can increase the strength as well, though the mechanism is unknown yet, 4) the support inside the pores can also increase the stability of the material. However, the study and understanding of the mechanical stability of mesoporous materials are rather limited until now, and some research showed contradicting results. For example, the Cassier group studied the thermal, hydrothermal and mechanical stability of a wide range of mesoporous silica, including MCM-48, KIT-1, MCM-41, SBA-15, FSM-16, PCH and HMS silicas. While they found that thermal stability is related to pore wall thickness and precursor choice and hydrothermal stability is related to wall thickness and degree of polymerization, they concluded the mechanical stability is little influenced by the

different nature of these mesoporous silicas and all of them collapsed at a maximum pressure of 450 MPa[7].

The research efforts mentioned above primarily focused on the stability of mesoporous materials under pressure, and they were limited to ambient temperature as well. It was not until recent years that researchers realized pressure could be utilized to induce crystallization of porous materials. In fact, pressure is an important thermodynamic driving force to induce crystallization of materials

However, high pressure synthetic chemistry on porous materials was limited mostly to hydrothermal conditions with pressure in the sub-GPa region. For example, Ghobarkar has synthesized a variety of natural zeolites at the pressure range from 0.05 GPa to 0.4 GPa[15]. No gigapascal level high pressure synthetic chemistry about mesoporous materials reported previously.

In recent years, the Landskron group here at Lehigh have synthesized a series of novel high pressure nanostructures from mesoporous precursors, some of which exhibit a porous structure after HPHT treatment. This endeavor has opened up a new field on the synthesis of high pressure phase materials. The use of mesoporous structure as starting materials can bring advantages over their bulk counterparts as the high surface area could lead to increased reaction activity during phase transition. It is worthwhile to investigate how the product structure will be affected by the porosity as well.

5.2 Introduction to high-pressure apparatus

The modern research of high pressure began after P.W. Bridgeman improved the high pressure apparatus to create pressures greater than 10 GPa[16], and Bridgeman later won the Nobel prize “for the invention of an apparatus to produce extremely high pressures, and for the discoveries

he made therewith in the field of high pressure physics” in 1946. The high pressure apparatus by Bridgeman later led to a series of man-made high pressure phase materials including diamond[17], stishovite[18], cubic boron nitride[19], etc. A number of functional materials such as superhard

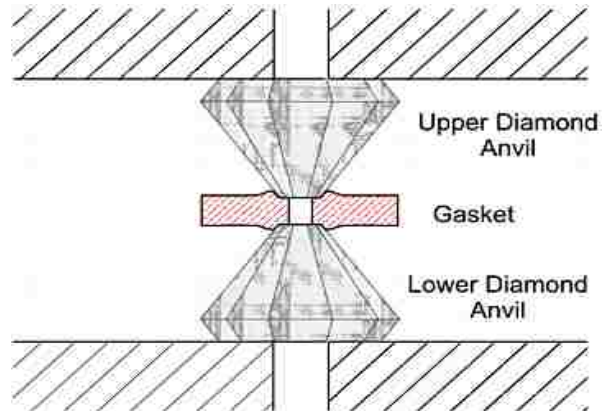


Fig 5-2. Left: Piston-cylinder press. Right: Diamond anvil cell. Ref[1]

materials[20], metal oxide superconductors[21] have been synthesized from HPHT as well.

Currently, the state-of-art high pressure apparatus usually include three types of high pressure apparatus commonly used for HPHT experiments: diamond anvil cell (DAC), piston-cylinder press and multi-anvil apparatus (MAA). In a piston cylinder apparatus, pressure is applied from two opposite sides from the piston cylinder, and uniaxial pressure up to 4 GPa is applied on the sample. It can also provide a relatively large sample volume (up to 500 mm³) as well as fast heating and cooling rates[1]. In a DAC setup, two single crystal diamonds are pressed against each other as illustrated in Fig 5-2. The tip of diamond crystals are small facets with a diameter in the micrometer range, therefore the setup can generate extreme pressures up to 550 GPa[22]. The

main drawback for diamond anvil cell is the sample volume, which is usually limited to a cylindrical shape with 50-100 μm in diameter and 10-50 μm in height.

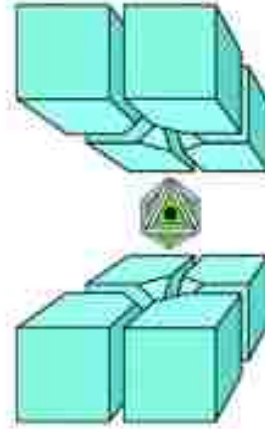


Fig 5-4. Illustration of multi-anvil assembly. Ref[2]

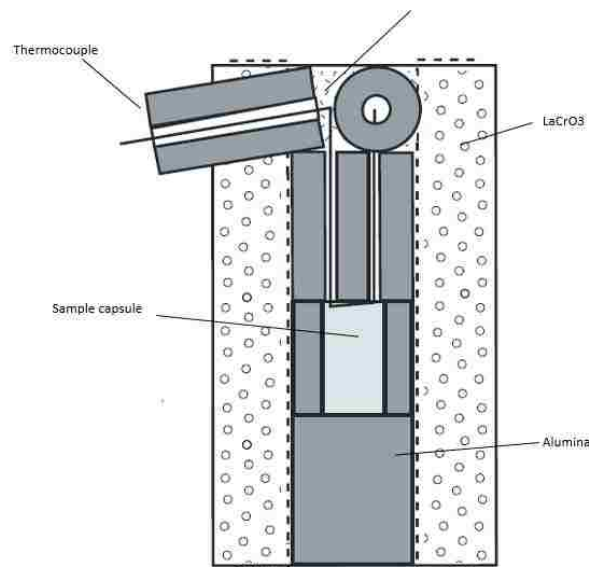


Fig 5-3. Sample assembly in a multi-anvil apparatus. Ref[3]

Most of the experiments in this thesis were done with the multi-anvil apparatus, which provides a balance between the maximum pressure and sample volume. With tungsten carbide anvils, the pressure can go up to 28 GPa. The MAA setup provides quasi-hydrostatic pressure by applying force from multiple directions as illustrated in Fig 5-3.

In a typical synthesis, the HPHT experiment was carried out in a multi-anvil assembly with a 1500-ton press. The sample was first sealed in a platinum foil, then the capsule was put into an alumina sleeve and inserted into a cylindrical rhenium heater surrounded by LaCrO_3 shell. A thermocouple was put on top of the assembly to monitor the temperature during the experiment, and zirconia oxide was used as heat insulating material.

The assembly was then transferred into a Cr_2O_3 doped magnesium oxide octahedron with an edge length of 14 mm. The octahedron was then placed in between 8 truncated tungsten carbide cubes with an edge length of 32 mm and a truncation length of 8 mm. To prevent direct contact between the cubes pyrophyllite gaskets were placed in between the cubes. Afterwards the assembly was pressurized to the designated pressure and heated up to reaction temperature.



Fig 5-5. Multi-anvil press at Geophysical Labs

5.3 Synthesis of high-pressure phases from mesoporous precursors

5.3.1 Synthesis of stishovite nanocrystals from mesoporous silica

Stishovite is a high pressure polymorph of silica with a rutile structure (Fig 5-6). Unlike other types of silica, the silicon atom in stishovite has a coordination number of 6. It is rarely found in nature. In fact, the first stishovite was synthesized by Stishov and co-workers at HPHT conditions and was named after him in 1961[18]. Later, stishovite was found in a coesite-bearing Meteor Crater in the state of Arizona, suggesting only extreme temperature and pressure generated by meteors hitting earth could produce such crystals[23]. Stishovite is the hardest oxide materials discovered and has a hardness value of 33 GPa. Due to its superior hardness, stishovite could be used as a substitute for diamond abrasive under certain chemical environments, for example, when diamond abrasive forms alloy with ferrous metal or get oxidized in air at elevated temperature. However, the cost of manufacturing currently prevents widespread application of stishovite.

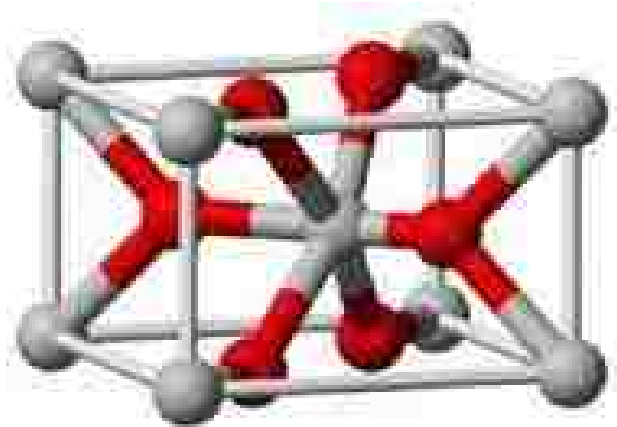


Fig 5-6. Crystal structure of Stishovite. Grey: Silicon, Red: oxygen.

Traditionally, stishovite was synthesized from bulk siliceous species, pyrophyllite, silica gel, and vitreous silica as well. Wentorf from GE laboratory in New York successfully synthesized stishovite

crystals at a pressure of 13 GPa and temperature from 1000 to 1600 °C[23]. However, the high temperature associated with the production limits the production. By using mesoporous SBA-16 as a starting material, our group has found that stishovite nanocrystals can be obtained at HTHP conditions with a pressure ramping rate of 2 GPa/h to 12 GPa and temperature ramping rate of 100 °C/min to 400 °C[24].

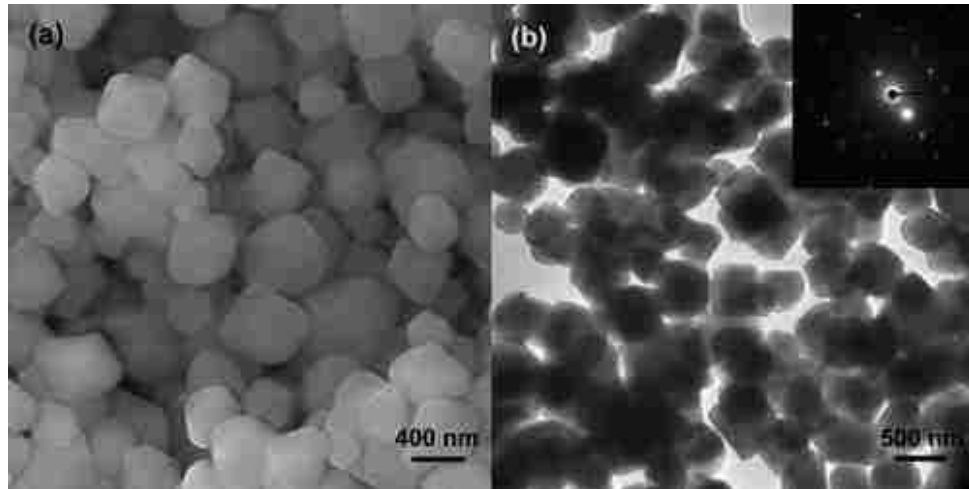


Fig 5-7. Images of stishovite nanoparticles. Left: SEM, Right: TEM

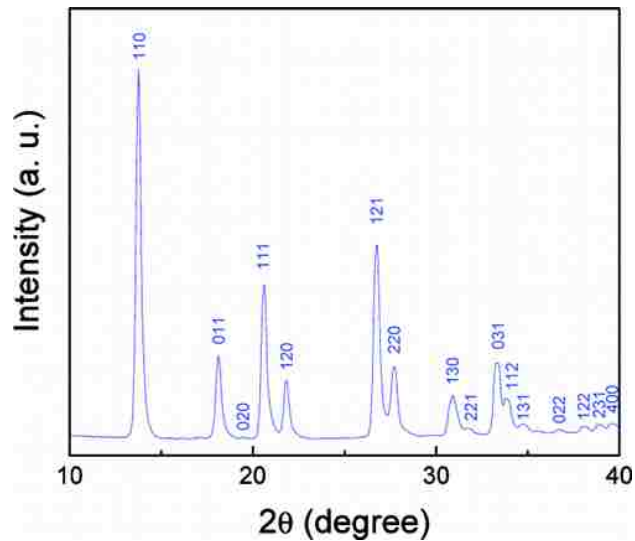


Fig 5-8. XRD spectra of stishovite nanocrystals.

Characterization data shows that the mesoporous starting material has transformed into stishovite nanocrystals at 12 GPa and 400 °C. The phase purity was confirmed with the XRD patterns (Fig5-8), which was indexed to the tetragonal crystal structure of stishovite (JCPDS 45-1374). These non-agglomerated stishovite nanocrystals have well faceted polygonal morphology with diameters from 200 – 400 nm under the electron microscope (Fig 5-7). Dynamic light scattering (DLS) analysis further showed the nanoparticles could be dispersed as individual particles in solution without aggregation and the hydrodynamic radius matched with the crystal radius obtained by electron microscopy.

Besides SBA-16, KIT-6 and SBA-15 type mesoporous silica were also investigated under the same conditions. The former had a gyroid type pore geometry and yielded stishovite nanocrystals with a similar morphology to those from SBA-16, but the diameter of the nanocrystals was larger, ranging from 400 to 800 nm (Fig 5-9 and Fig 5-10).

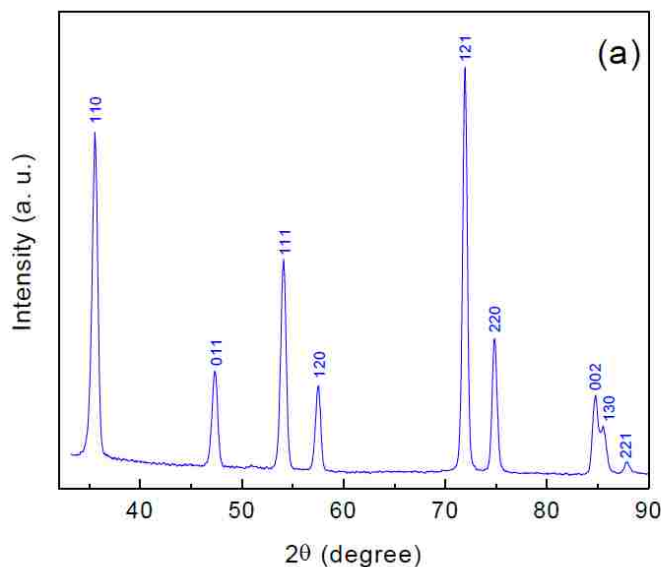


Fig 5-9. XRD of stishovite nanocrystals from KIT-6

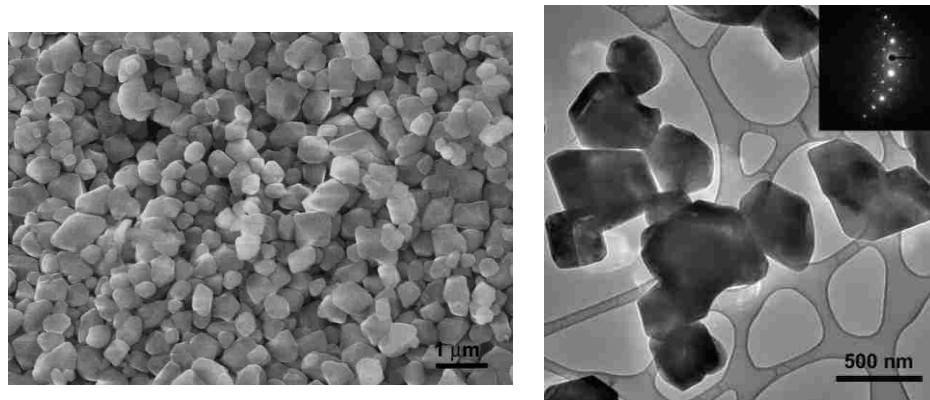


Fig 5-10. SEM(left) and TEM (right) of stishovite nanocrystals from KIT-6.

However, when the precursor is substituted by SBA-15 type mesoporous silica, at 12 GPa and 400 °C the product was coesite without well-defined morphology (Fig 5-11 and Fig 5-12).

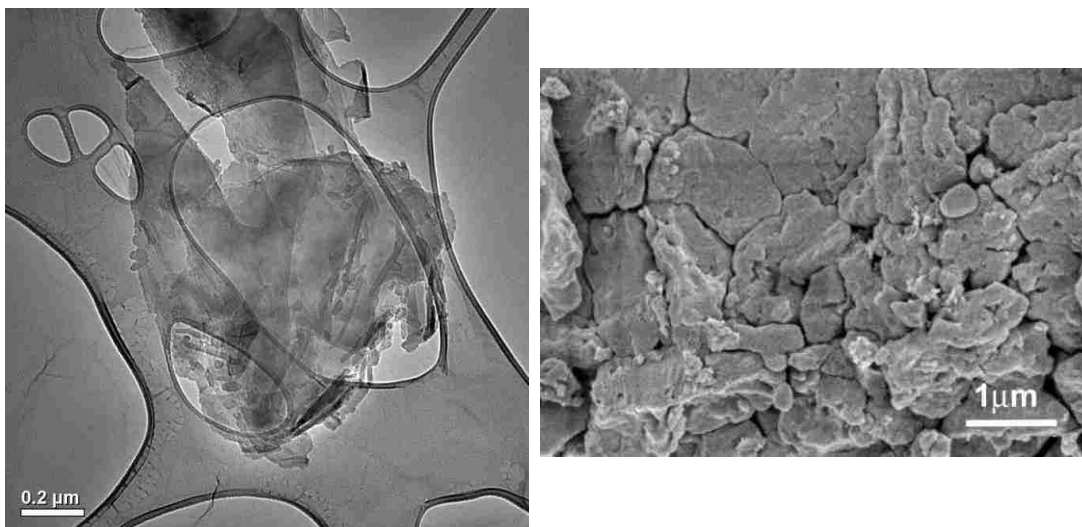


Fig 5-11. TEM(left) and SEM(right) of coesite from SBA-15.

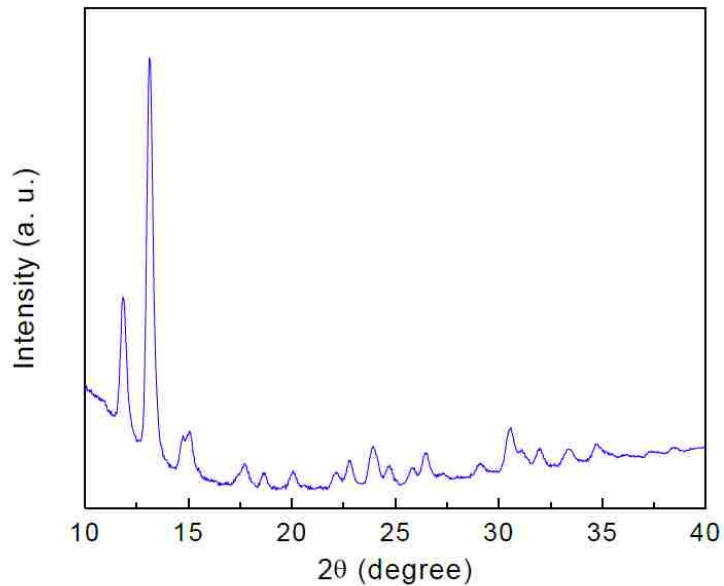


Fig 5-12. XRD spectra of coesite from SBA-15.

The result was not anticipated because from a chemical perspective, SBA-16, KIT-6 and SBA-15 are all silicon dioxide and according to the phase diagram of SiO_2 in Fig 5-10, stishovite is the stable phase at 12 GPa and 400 °C. These results indicate that these porous silicas have different reaction pathways to crystallization. A plausible explanation is that SBA-15 is first transformed to the intermediate coesite, however, since the temperature is only 400 °C, the intermediate cannot overcome the energy barrier between coesite and stishovite. This is in accordance with the Ostwald's step rule, which states that the least stable polymorph crystallizes first rather than the most stable one. In the case of SBA-16 and KIT-6, the interconnected cubic mesostructure helps directly crystalline the product in the stishovite structure without the formation of a coesite intermediate.

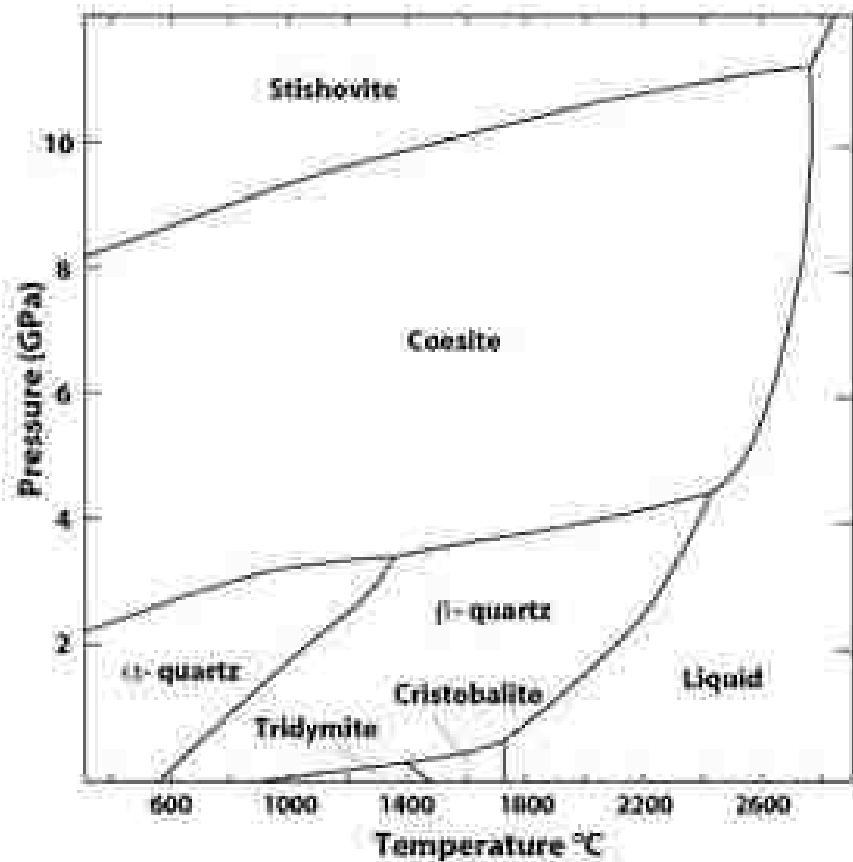


Fig 5-13. Phase diagram of silicon dioxide.

By using mesoporous silica as starting material, the temperature and pressure conditions required for stishovite synthesis can be as low as 12 GPa and 400 °C, indicating the unique structure and high reactivity can facilitate phase transition at milder temperature conditions compared with bulk starting materials.

5.3.2 Synthesis of mesoporous coesite form mesoporous silica

Coesite is another high-pressure polymorph of silicon dioxide first synthesized by Coes under HPHT conditions[25]. Coesite can be synthesized from mesoporous silica SBA-15 at 12 GPa and

300°C for 5 minutes. Surprisingly, the coesite obtained by such method is mesoporous as seen by electron microscopy in Fig 5-14 and Fig 5-15.

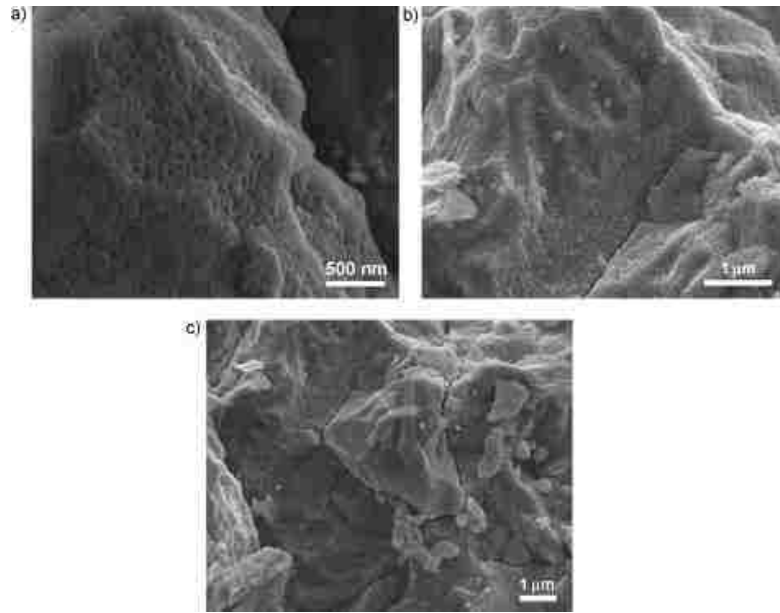


Fig 5-14. SEM images of mesoporous coesite nanocrystals

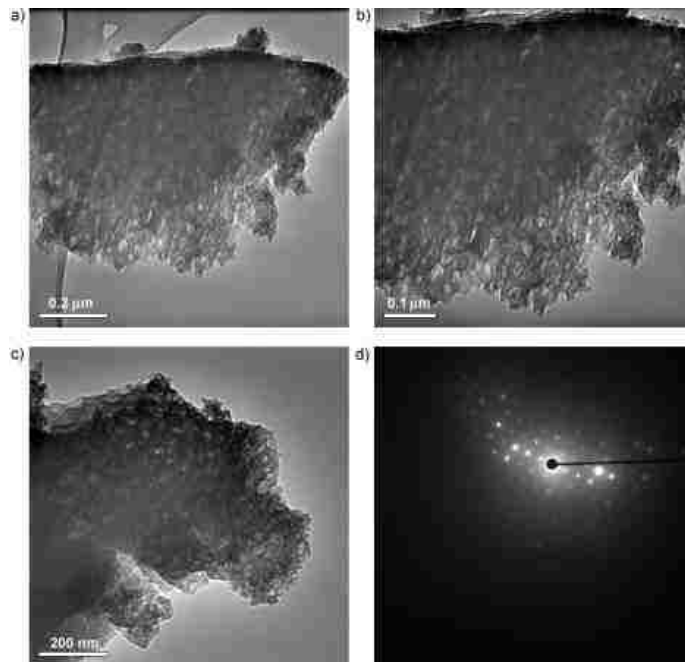


Fig 5-15. TEM (a-c) and SAED (d) of mesoporous coesite nanocrystals

There was no clear defined particle morphology under electron microscopy investigation, however, a mesoporous structure was clearly revealed from the electronic contrast in the images. The pores were elliptical shaped with size from 2 – 50 nm. The well-defined SAED spots indicate these nanoparticles are single crystals, indicating the particle size is much larger than pore size. Due to limited sample amount, gas adsorption measurements could not be performed to analyze the pore volume and pore size, but depth-sectioned electron microscopy was used to investigate the porosity of the coesite crystals.

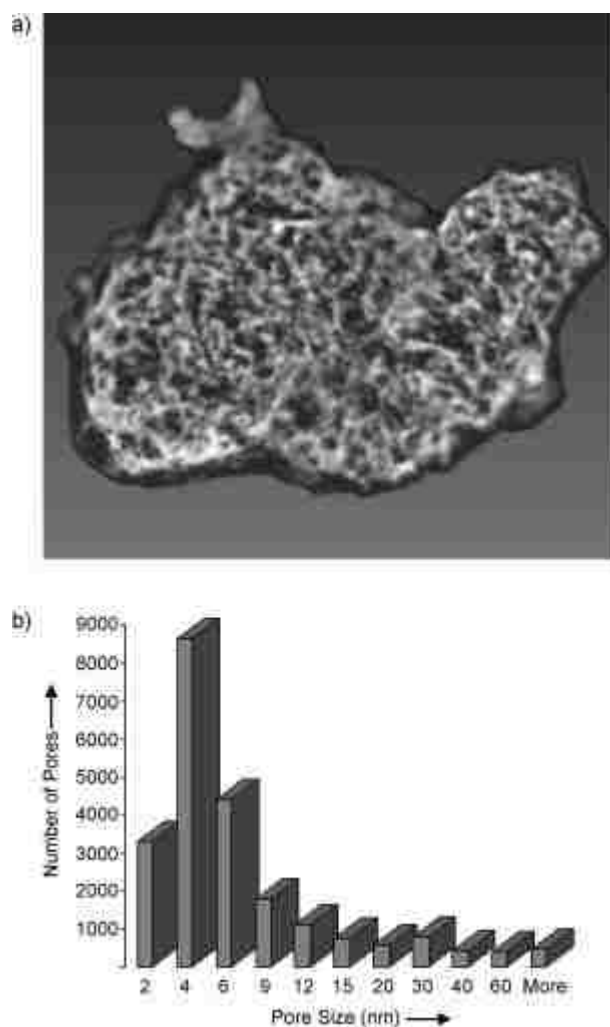


Fig 5-16. Depth sectioned TEM image (a) and pore size distribution of coesite nanocrystals

One specific particle with a total volume of $14.301 \times 10^{-14} \text{ cm}^3$ was chosen to perform a through-focal series images, and the pore size was estimated to be $6.994 \times 10^{-14} \text{ cm}^3$, which translates to a porosity of ca 49% and the surface area according to the particle was calculated to be $53 \text{ m}^2/\text{g}$. The low surface area can be explained by crystallization-induced surface smoothing and micropore collapsing during the HPHT reaction. A control experiment was performed at 12 GPa at 200 °C for the same starting material, and a glassy substance was obtained with no porosity nor crystallinity present.

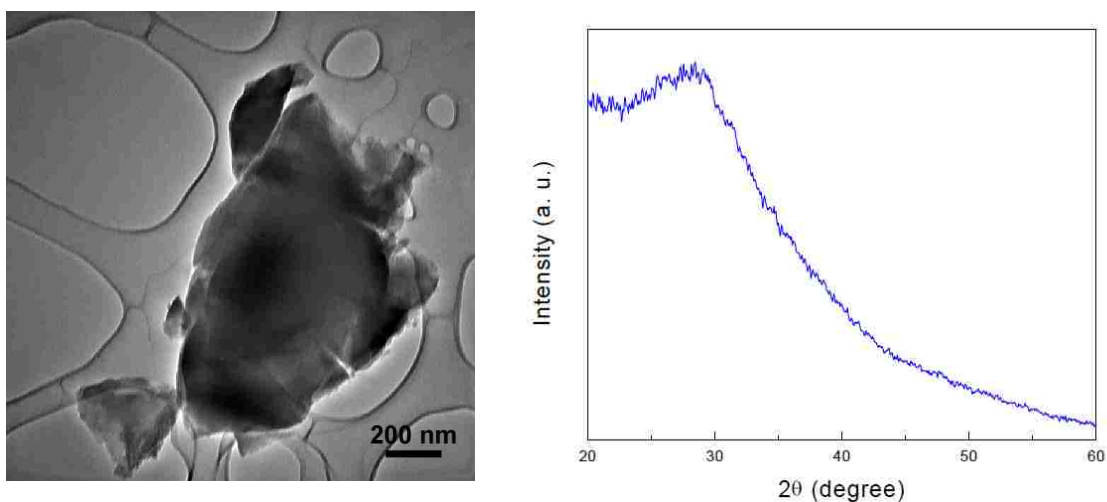


Fig 5-17. TEM (left) and XRD (right) experiment of SBA-16 treated under 12 GPa and 200 °C.

The absence of porosity from the product produced at 200 °C indicates that the mesopores in the coesite were not due to pores that did not collapse from the starting material. This suggests that phase transformation happened at the temperature between 200 and 300 °C and the pores were generated during the crystallization process. A possible mechanism for porosity can be proposed from the perspective of elastic behavior of the mesoporous silicas. It is possible that the elastic distortion of mesoporous silica plays an important role of pore reformation above 200 °C. As the

pressure increases to 12 GPa, the SBA-16 will first undergo elastic distortion and finally the pores collapse under pressure, and transforms into a glassy intermediate state. However, the elastic strain in the intermediate is not released, as a result, pores are generated during the crystallization upon heating to 300 °C to release the strain. After the formation of coesite, the pores remain metastable without collapsing, possibly due to two reasons: 1) the crystalline coesite channel walls have higher strength than amorphous silica, 2) short reaction time of 5 mins was able to produce a metastable mesoporous coesite without collapsing. The hypothesis is further supported by the polarized microscopy image of the intermediate at 200 °C, which shows an anisotropic structure.

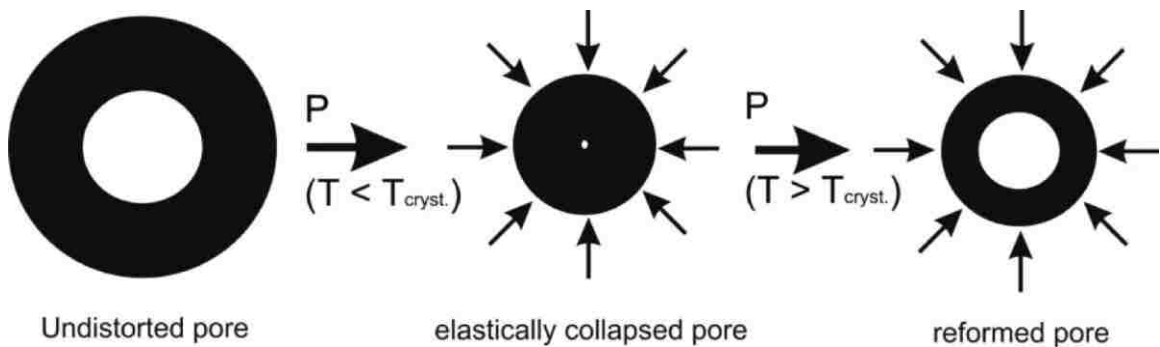


Fig 5-18. Pore collapse and reformation mechanism.

It is worth noting that 12 GPa and 300 °C is the thermodynamic stable region of stishovite in the silica phase diagram, which means that coesite is a metastable phase under this condition. This further supports the Ostwald's step rule where the least stable phase crystallizes first. The coesite formed under cannot overcome the free energy barrier at 300 °C, possibly due to the high energy barrier associated with changing the coordination number of silicon atoms.

5.3.3 Synthesis of nanopolycrystalline diamond from mesoporous carbon

Diamond is a high pressure polymorph of carbon with excellent physical properties such as high hardness, excellent thermal conductivity, and high refractive index. In an analogous effort to the studies of mesoporous silica under HPHT, the behavior of mesoporous carbon under HPHT is also investigated to find out whether the mesostructure can facilitate the phase transformation from carbon to diamond and generate new diamond nanostructures.

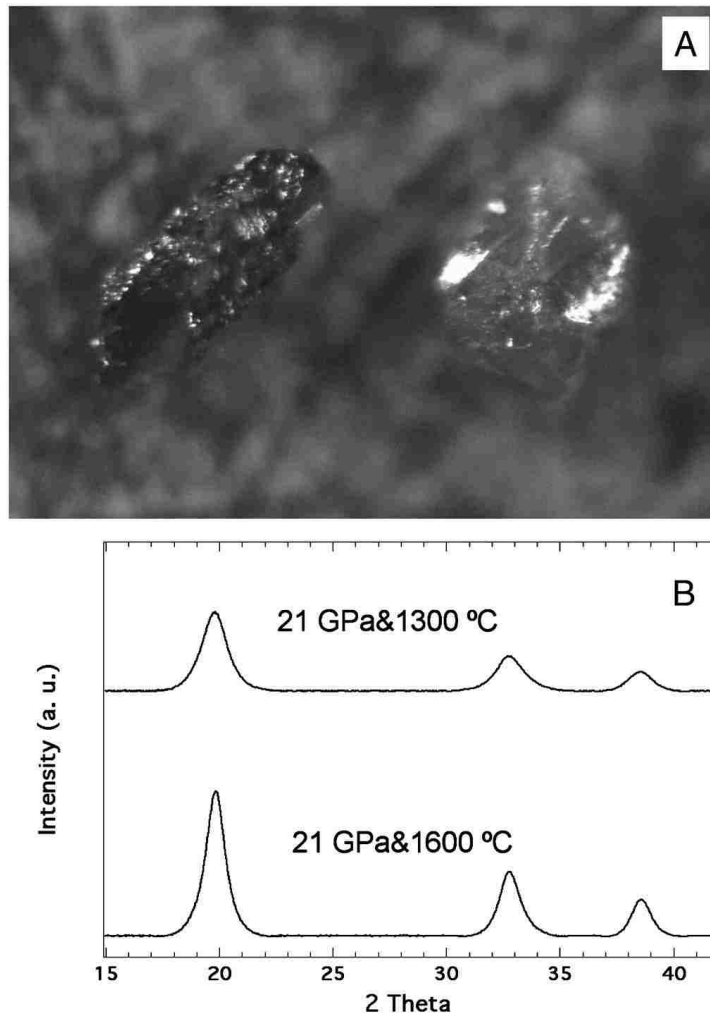


Fig 5-19. Microscopy(A) and XRD (B) of diamond nanocrystals from CMK-8.

CMK-8 mesoporous carbon was used as the carbon precursor and placed into a multi-anvil assembly inside a magnesium oxide capsule. Mesoporous CMK-8 was pressurized to 21 GPa and

heated to a series of temperature from 1100 to 1600 °C. Diamond formation was observed from the sample heated at 1300 °C. The as-synthesized diamond crystal is an optically transparent brown monolith under a microscope. The phase purity of the product is confirmed by XRD, where 111, 200 and 311 reflections of cubic diamond structure are clearly visible[26], as shown in Fig 5-19.

The monolithic and transparent nature suggested the sample was polycrystalline, which was further confirmed by the diffraction rings in the SAED. TEM images showed the product was a mesostructured material, comprised from interconnected diamond nanograins (Fig 5-20). The size of the nanograins is on the scale of ~10 nm, which is in accordance with the polycrystalline nature of the diamond. The nanograin structure was also seen from SEM image. The strong electronic contrast from the TEM image suggests the presence of porosity. Krypton adsorption experiment was performed to investigate porosity of the diamond. The BET area calculated to be 33 m²/g from the data. The relatively low surface area of the porous structure can be explained by the low surface roughness of the crystalline pore walls and lack of micropores from CMK-8 carbon, which was also observed previously on mesoporous coesite nanocrystals. It is noteworthy that the surface area measurement may not be accurate due to the limited sample amount (0.6 mg).

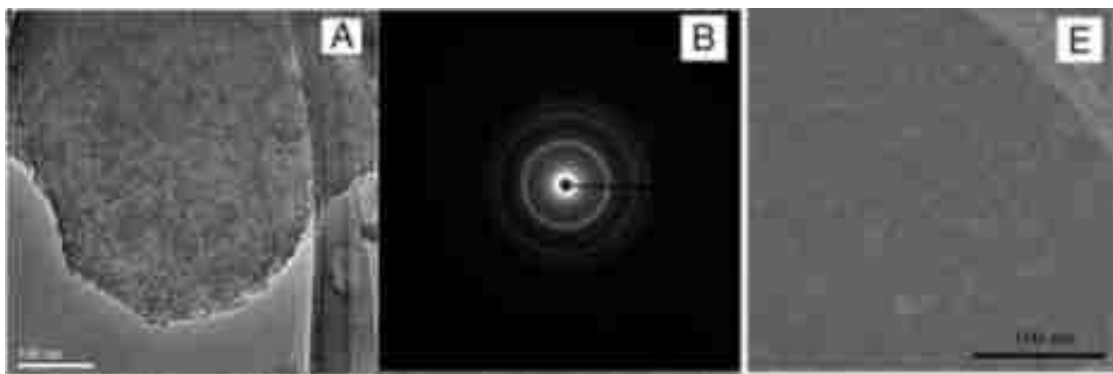


Fig 5-20. TEM (A), SAED (B) and SEM (E) of mesoporous diamond nanocrystals

The pore formation could be explained by the collapse-reformation mechanism from that proposed for the mesoporous coesite formation. Upon the pressurizing of CMK-8 carbon, the pores collapse gradually but the elastic strain is created in the intermediate, and when the temperature rises above the crystallization temperature, the strain is released during the crystallization by creating pores. The sintered polycrystalline nature of the product provided very high mechanical strength so the pores did not collapse at extreme pressures. Also, under the reaction temperature of 1300 °C, the porous diamond may not transform to a sintered high-density phase at a significant rate.

Another interesting property of diamond synthesized via this route is the polycrystalline nature. Though diamond is the hardest material known, single crystalline diamond has a low toughness due to the existence of a cleavage plane, presumably the {111} plane[4]. Polycrystalline diamond can eliminate this issue owing to the absence of a well-defined cleavage plane. Previously Irifune and co-workers have successfully synthesized polycrystalline diamond by treating pure polycrystalline graphite rod under pressures from 12 – 25 GPa and temperature from 2300 – 2500 °C[27], where the temperature is extremely high for a high-pressure synthesis. By starting with a CMK-8 mesoporous carbon, the temperature required to obtain a polycrystalline product is lowered by 1000 °C, therefore reducing the energy consumption of the HPHT process by a significant margin.

5.4 Synthesis of high pressure phase with periodic mesostructures via nanocasting at high pressure

Mesoporous silica was first synthesized by Mobil Oil in 1992 with the intention to replace zeolite materials as catalyst for petroleum cracking purposes, as their large pore channels can provide better diffusion kinetics for long-chain hydrocarbon molecules. However, this never happened

due to the lack of hydrothermal stability of the silica materials under harsh reaction environments. The problems rise from the amorphous pore walls of mesoporous silica. Unfortunately, silicate materials are extremely difficult to crystallize by temperature alone. In order to go around this issue, a concept of “nanocasting at high pressure” was developed. In this technique, mesostructured composites are used instead of mesoporous compounds. Pressure and temperature are applied to the composite materials to induce phase transformation of one or more phases of the composite material. The synthetic scheme is listed in Fig 5-21.

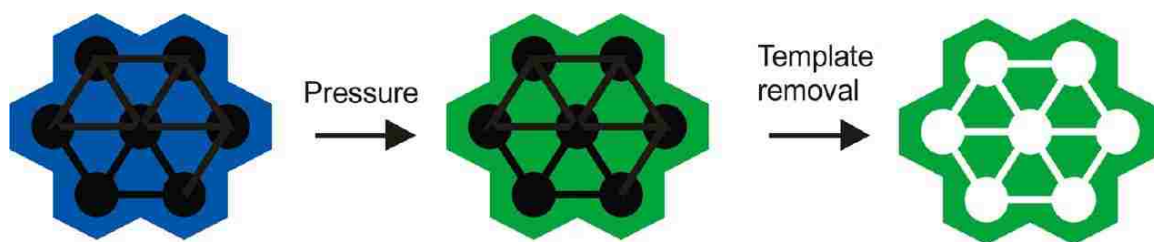


Fig 5-21. Nanocasting at high pressure.

Because the starting material is a dense material with practically no porosity there is no pore collapse during the HPHT treatment and the mesostructured is retained during the transformation. By following this route, periodic mesoporous coesite and quartz were synthesized.

5.4.1 Synthesis of periodic mesoporous coesite

The first demonstration of high pressure nanocasting was in 2009, where SBA-16/carbon composite was used as starting material[28]. The composite was made by impregnation of mesophase pitch into mesoporous SBA-16 silica by a melt-infiltration technique. The pitch was later carbonized at 900 °C under nitrogen flow to create a non-porous SBA/C composite, which is then moisturized to provide water as a mineralizer. After treating the composite at 12 GPa and

350 °C, the silica was converted into the coesite phase, while carbon in the composite acted as support for the mesostructure and prevented pore collapse. After the HPHT treatment, carbon was removed by oxidation in air to obtain a mesoporous coesite.

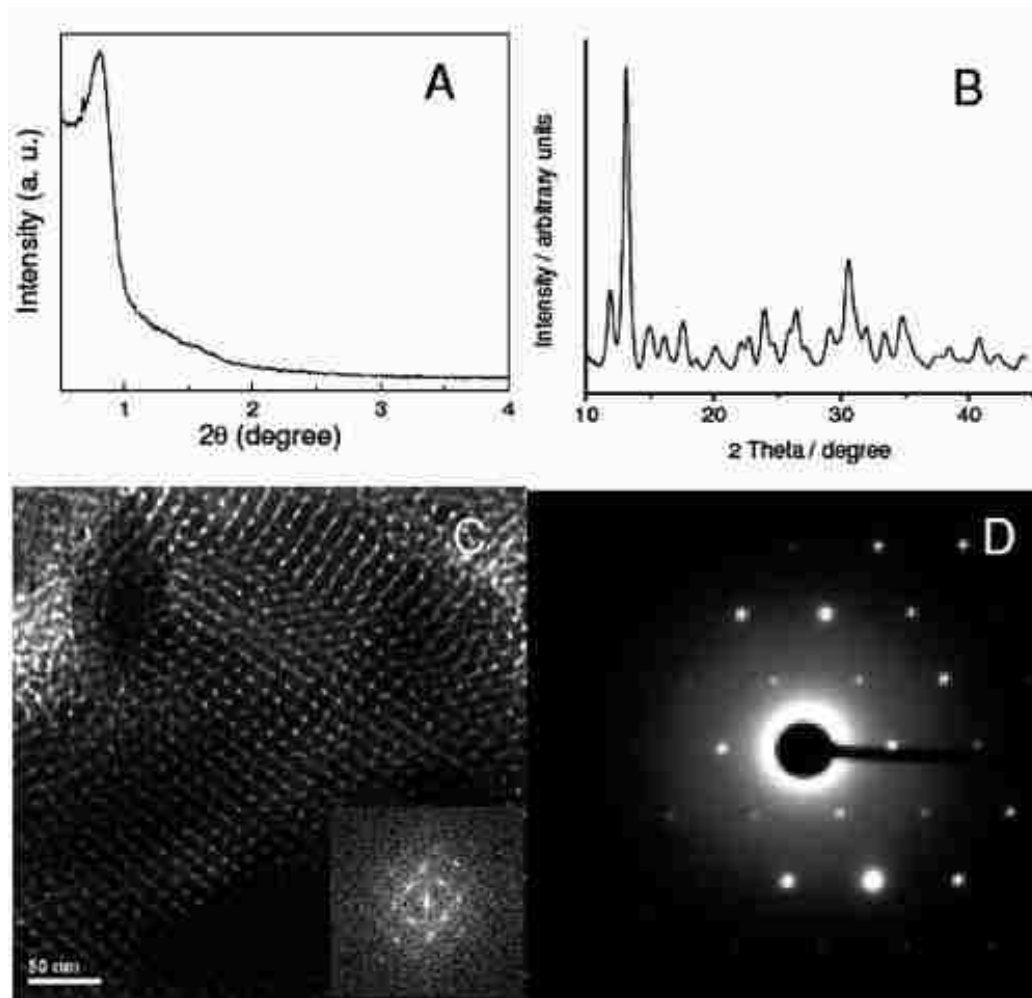


Fig 5-22. SAXS(A), XRD(B), TEM with FFT inset(C) and SAED(D) of ordered mesoporous coesite

The periodic mesostructure was clearly seen by TEM and the inset fast Fourier transform (FFT) pattern. The sharp peak in the SAXS pattern also indicated a highly ordered mesostructure. The phase purity was confirmed by XRD and SAED pattern as well (Fig 5-22). The SAED further confirms

that the coesite is single-crystalline despite having a periodic mesoporous structure. Nitrogen adsorption isotherm exhibited a type IV isotherm which is a direct indication of mesoporosity. The inset showed pore size calculated from DFT was ~ 4 nm. The pore size of the coesite material decreased slightly compared to that of the starting material (4.0 nm vs 5.0 nm), and the BET surface area was decreased as well, from 833 m^2/g to 278 m^2/g (Fig 5-23). Since the density of coesite is higher than amorphous silica, the pores could shrink during the HPHT procedure, leading to a smaller pore size. The surface area decreasing could be attributed to the collapse of micropores under pressure and the smoothing of the crystalline channel walls.

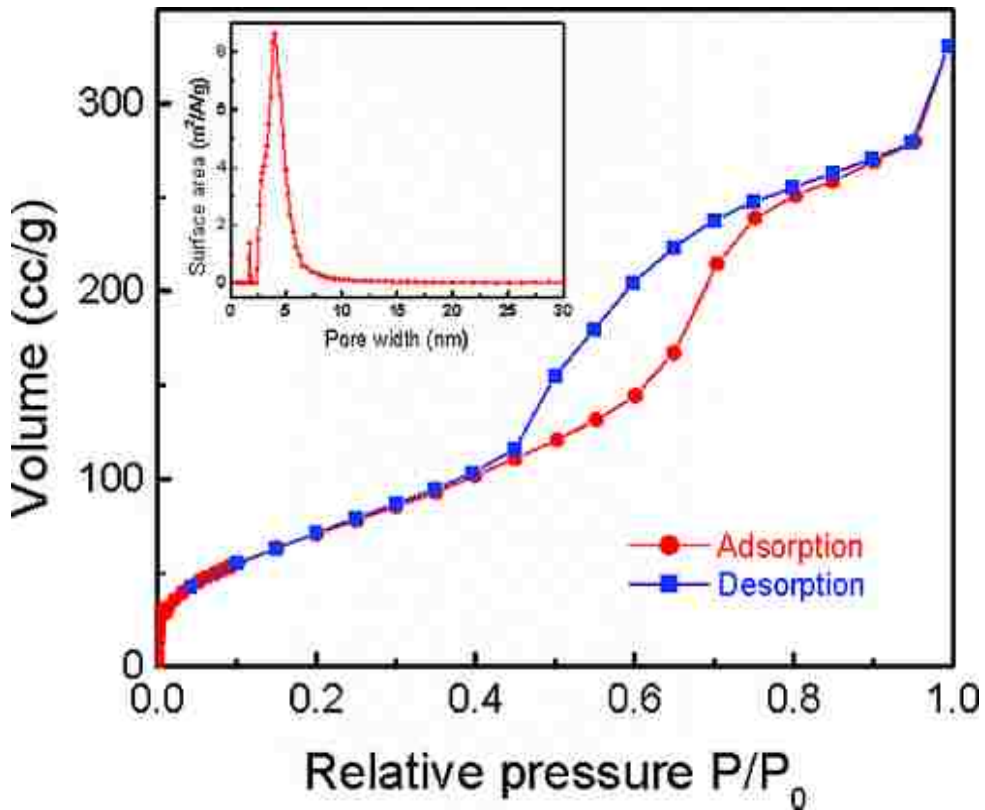


Fig 5-23. Nitrogen adsorption isotherm of mesoporous coesite(inset: pore size distribution).

5.4.2 Synthesis of periodic mesoporous quartz

Though a periodic mesoporous coesite was obtained via HPHT process, the high pressure of 12 GPa prohibits the production of such materials at large scale, so efforts were put into studying whether lower pressure can still induce the crystallization of mesoporous silica/carbon composites. In the silica phase diagram, α - and β - quartz are the stable crystalline phases below coesite, therefore an effort was made to obtain periodic mesoporous quartz via high pressure nanocasting.

Large pore FDU-12 was used for this study and was also infiltrated with mesophase pitch as support. FDU-12/carbon composite was treated at 4 GPa, 2 GPa, and 1 GPa respectively at a reaction temperature of 750 °C[29]. After the HPHT experiments, carbon was removed by oxidizing the product in air. The composite treated at 4 GPa successfully converted to quartz with the mesostructure retained, as seen from SAXS and XRD in Fig 5-26. The phase purity is also confirmed from the clear diffraction spots in the SAED in TEM images and the FFT pattern also shows pore ordering on the mesoscale (Fig 5-24). The porous structure is seen from SEM images as well. The formation of quartz rather than thermodynamic stable phase coesite can be explained by the same Ostwald's step rule mentioned above.

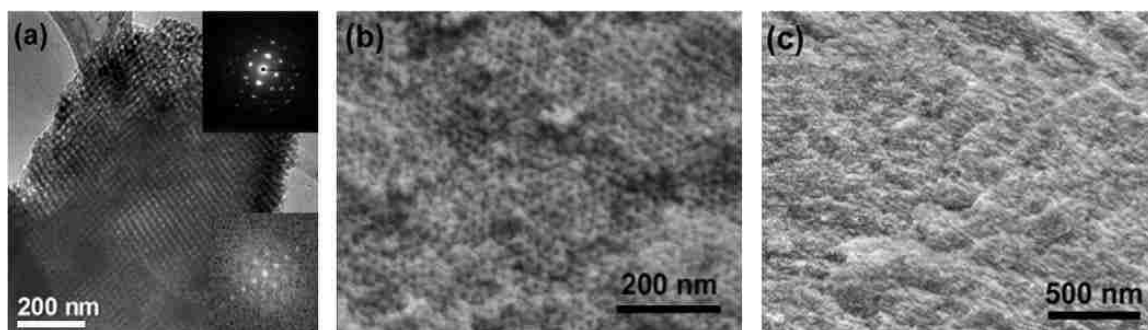


Fig 5-24. TEM (a) and SEM (b,c) of mesoporous quartz produced at 4 GPa.

The porous structure is also confirmed by N_2 adsorption isotherm (Fig 5-25), from which the BET surface area, pore volume, and pore size distribution is calculated. The surface area decreased

from 350 m²/g to 238 m²/g, and the pore volume decreased from 0.79 cc/g to 0.7 cc/g. These can be attributed to the smoothing of the pore surface by crystallization.

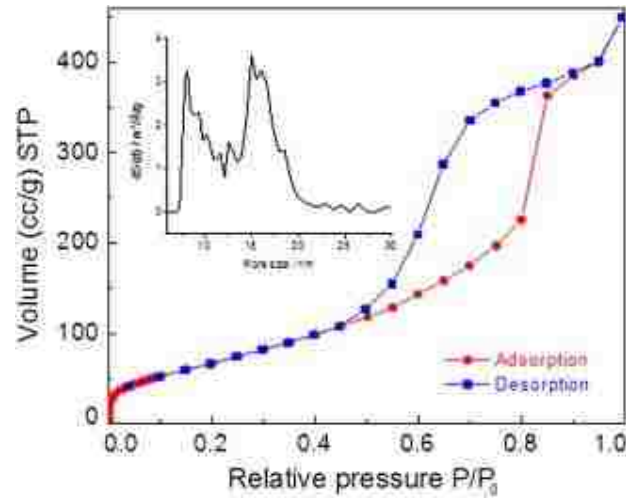


Fig 5-26. Nitrogen adsorption isotherm of mesoporous quartz (inset: pore size distribution).

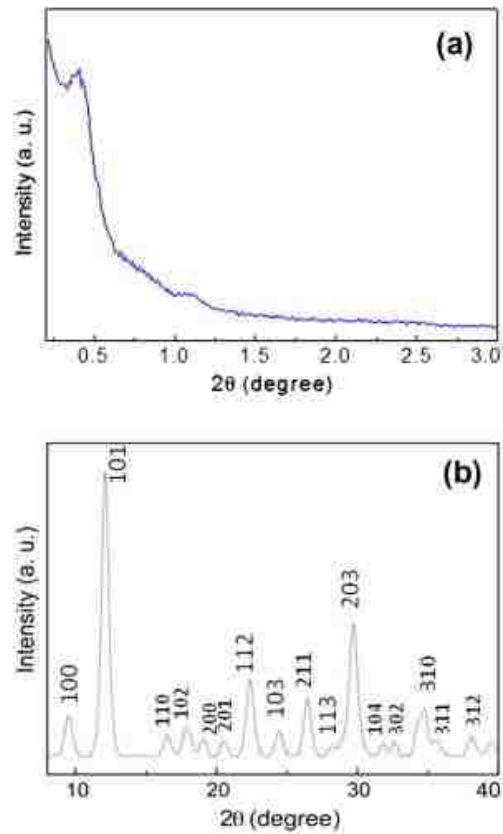


Fig 5-25. SAXS(a) and XRD(b) of mesoporous quartz.

At pressures of 2 GPa and 1 GPa, the lowering of pressure allows a much simpler piston-cylinder apparatus compared with the multi-anvil apparatus. The composite treated at 1 GPa remained amorphous while the 2 GPa sample was transformed into quartz phase as seen in Fig 5-28, indicating the phase transition pressure lies between 1 GPa and 2 GPa. The mesoscale order on the 2 GPa sample was lower than that of 4 GPa sample (), due to the piston-cylinder setup which provides uniaxial pressure instead of a hydrostatic pressure from the multi-anvil setup. Despite this, the sample prepared at 2 GPa still showed a typical type IV isotherm (Fig 5-27). The pore size calculated by DFT for spherical pore models was 18 nm with a pore entrance of 8 nm, the BET surface area is 234 m²/g, which are in agreement with the sample prepared at 4 GPa.

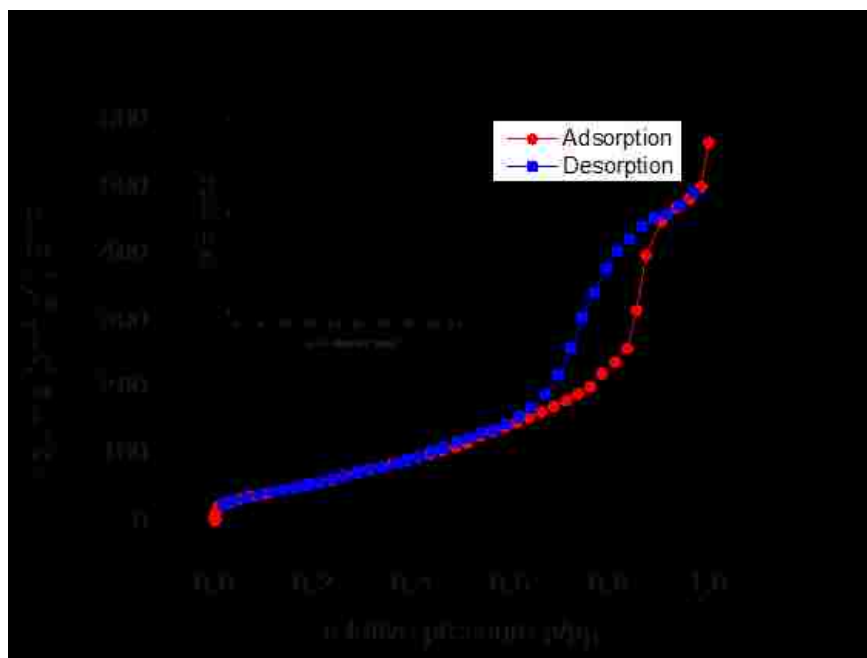


Fig 5-27. Nitrogen isotherm of mesoporous quartz produced under 2 GPa

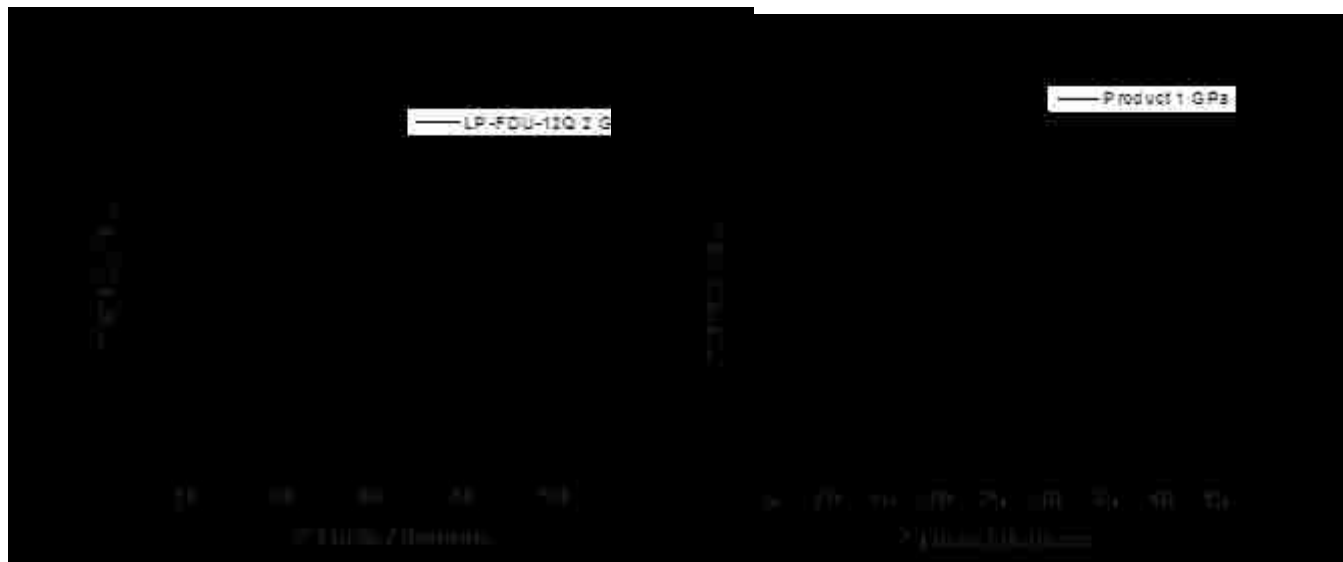


Fig 5-29. XRD products produced at 2 GPa(left) and 1 GPa(right).

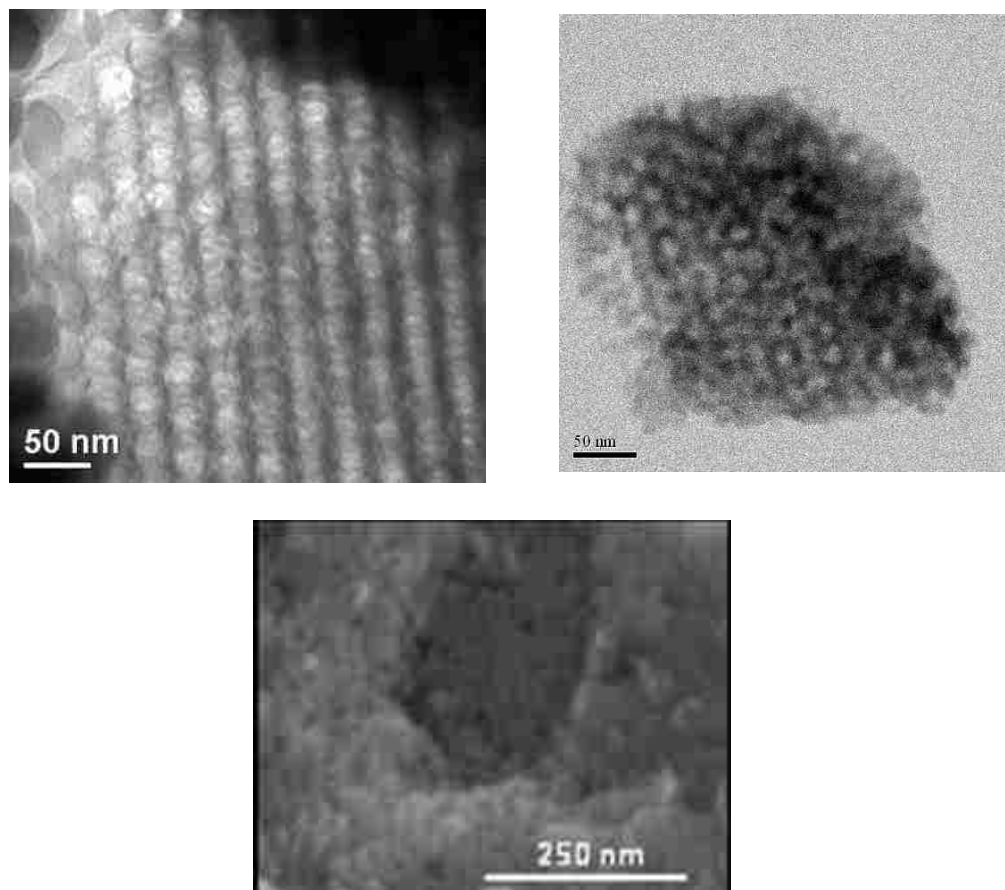


Fig 5-28. TEM (top left and right) and SEM of mesoporous quartz produced at 2 GPa

Due to the crystalline channel walls, the hydrothermal stability of mesoporous quartz is greatly improved over amorphous mesoporous silica precursor. Both samples were subjected to H₂O steam with a vapor pressure of 1 atm at 800 °C for 2 h. Electron microscopy in Fig 5-27 results shows that the sample prepared at 2 GPa retained the porosity and mesoscale ordering during the hydrothermal treatment (Fig 5-30). The precursor material, however, had decomposed and volatilized with the water steam, leaving practically nothing in the alumina boat.

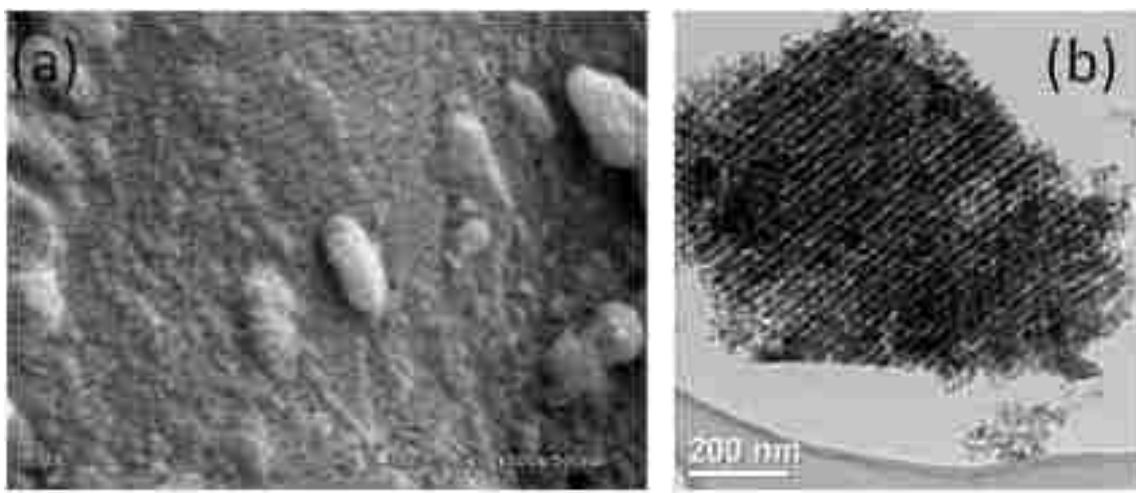


Fig 5-30. SEM(left) and TEM(right) of quartz obtained at 2 GPa after hydrothermal treatment.

Compared to zeolites which are the traditional catalyst for petroleum cracking, mesoporous quartz still requires a relatively high pressure (gigapascals) to synthesis. However, materials produced by this method have much larger pores to provide larger transport channels for long hydrocarbon molecules, and solid hydrothermal stability as well. These excellent properties may justify the high cost of production associated with HPHT synthesis, and it may be possible to lower the required pressure and temperature by further optimizations.

5.5 Summary

By using a mesoporous material as starting materials, a series of novel nanostructures was synthesized. Monodisperse stishovite nanocrystals may be used as abrasive materials under certain chemical environments not suitable for diamond. Mesoporous nanopolycrystalline diamond was obtained from CMK-8 carbon which might be used as carriers for drug delivery due to their porosity and biocompatibility. Mesoporous coesite was obtained directly from mesoporous silica, which is the first known mesoporous material formed under extreme pressure.

High pressure phase	P/T required from nanoporous precursor	P/T required from traditional precursors
Stishovite	12 GPa, 400 °C	13 GPa, 1000-1600 °C
Coesite	12 GPa, 300 °C (mesoporous)	3.5 GPa, 700 °C
Polycrystalline diamond nanocrystals	21 GPa, 1300 °C	12-25 GPa, 2300-2500 °C

Table 5-1. Comparison of bulk precursor and nanoporous precursor for HPHT synthesis.

The results mentioned above have shown that by starting with a mesoporous precursor the temperature required for low pressure phase to transform into high pressure phase is greatly reduced, in some case the required pressure is reduced as well. The increased reaction activity can be attributed to the high porosity of these nanoporous materials. In addition, different pore geometry (cubic, gyroid, hexagonal) are likely to provide reaction pathways along the free energy surface that are not available in bulk precursors, which leads the creation of new nanostructures that have not been observed previously. Nanocasting at high pressure offers a synthetic scheme for the synthesis of mesostructured high pressure phase materials that are otherwise difficult to produce. This concept may be extended to a variety of mesostructured material as well.

Following the work of this chapter, cubic boron nitride nanocrystals were synthesized from mesoporous cubic boron nitride, and diamond mesowires were made by the nanocasting process, details will be discussed in the following chapters.

5.6 References

1. Akella, J., *The diamond anvil cell: Probing the behavior of metals under ultrahigh pressures*. Journal Name: Science and Technology Review; Other Information: PBD: Mar 1996, 1996: p. Medium: X; Size: pp. 17-27.
2. Horvath-Bordon, E., et al., *High-pressure chemistry of nitride-based materials*. Chemical Society Reviews, 2006. **35**(10): p. 987-1014.
3. van Westrenen, W., et al., *Assessment of temperature gradients in multianvil assemblies using spinel layer growth kinetics*. Geochemistry, Geophysics, Geosystems, 2003. **4**(4): p. 1036.
4. Chang, F., et al., *Microporous and mesoporous materials for gas storage and separation: a review*. Asia-Pacific Journal of Chemical Engineering, 2013. **8**(4): p. 618-626.
5. Manzano, M. and M. Vallet-Regi, *New developments in ordered mesoporous materials for drug delivery*. Journal of Materials Chemistry, 2010. **20**(27): p. 5593-5604.
6. Chiu, J.J., et al., *Friedel–Crafts alkylation properties of aluminosilica SBA-15 meso/macroporous monoliths and mesoporous powders*. Journal of Catalysis, 2004. **221**(2): p. 400-412.
7. Cassiers, K., et al., *A Detailed Study of Thermal, Hydrothermal, and Mechanical Stabilities of a Wide Range of Surfactant Assembled Mesoporous Silicas*. Chemistry of Materials, 2002. **14**(5): p. 2317-2324.
8. Wang, X., C. Liang, and S. Dai, *Facile Synthesis of Ordered Mesoporous Carbons with High Thermal Stability by Self-Assembly of Resorcinol–Formaldehyde and Block Copolymers under Highly Acidic Conditions*. Langmuir, 2008. **24**(14): p. 7500-7505.
9. Gusev, V.Y., et al., *Mechanical Stability of Pure Silica Mesoporous MCM-41 by Nitrogen Adsorption and Small-Angle X-ray Diffraction Measurements*. The Journal of Physical Chemistry, 1996. **100**(6): p. 1985-1988.
10. Tatsumi, T., et al., *Mechanical Stability of Mesoporous Materials, MCM-48 and MCM-41*. Journal of Porous Materials. **6**(1): p. 13-17.
11. Vinu, A., V. Murugesan, and M. Hartmann, *Pore Size Engineering and Mechanical Stability of the Cubic Mesoporous Molecular Sieve SBA-1*. Chemistry of Materials, 2003. **15**(6): p. 1385-1393.
12. Hartmann, M. and A. Vinu, *Mechanical Stability and Porosity Analysis of Large-Pore SBA-15 Mesoporous Molecular Sieves by Mercury Porosimetry and Organics Adsorption*. Langmuir, 2002. **18**(21): p. 8010-8016.
13. Galacho, C., M.M.L. Ribeiro Carrott, and P.J.M. Carrott, *Evaluation of the thermal and mechanical stability of Si-MCM-41 and Ti-MCM-41 synthesised at room temperature*. Microporous and Mesoporous Materials, 2008. **108**(1–3): p. 283-293.
14. Wu, J., X. Liu, and S.H. Tolbert, *High-Pressure Stability in Ordered Mesoporous Silicas: Rigidity and Elasticity through Nanometer Scale Arches*. The Journal of Physical Chemistry B, 2000. **104**(50): p. 11837-11841.
15. Ghobarkar, H., O. Schäf, and P. Knauth, *Zeolite Synthesis by the High-Pressure Hydrothermal Method: Synthesis of Natural 6-Ring Zeolites with Different Void Systems*. Angewandte Chemie International Edition, 2001. **40**(20): p. 3831-3833.
16. Bridgman, P.W., *The physics of high pressure. New impression with supplement*. International text-books of exact science. 1952, London,: G. Bell. vii, 445 p.
17. Bovenkerk, H.P., et al., *Preparation of Diamond*. Nature, 1959. **184**(4693): p. 1094-1098.

18. Stishov, S.M. and S.V. Popova, *New dense poly- morphic modification of silica*. Geokhimiya, 1961. **10**: p. 837-839.
19. Wentorf, R.H., *Synthesis of the Cubic Form of Boron Nitride*. The Journal of Chemical Physics, 1961. **34**(3): p. 809-812.
20. Hubert, H., et al., *High-Pressure, High-Temperature Synthesis of Superhard Boron Suboxide*. MRS Online Proceedings Library Archive, 1995. **410**: p. 191.
21. Kumar, A., R.P. Tandon, and V.P.S. Awana, *Spin-glass and cluster ferromagnetism in RuSr₂Y_{1.5}Ce_{0.5}Cu₂O₁₀ magneto-superconductor synthesized by HPHT*. Cryogenics, 2012. **52**(12): p. 764-766.
22. Zhai, S. and E. Ito, *Recent advances of high-pressure generation in a multianvil apparatus using sintered diamond anvils*. Geoscience Frontiers, 2011. **2**(1): p. 101-106.
23. Wentorf, R.H., *Stishovite synthesis*. Journal of Geophysical Research, 1962. **67**(9): p. 3648-3648.
24. Mohanty, P., et al., *Synthesis of Stishovite Nanocrystals from Periodic Mesoporous Silica*. Journal of the American Chemical Society, 2009. **131**(8): p. 2764-2765.
25. Coes, L., *A New Dense Crystalline Silica*. Science, 1953. **118**(3057): p. 131-132.
26. Zhang, L., et al., *Catalyst-free synthesis of transparent, mesoporous diamond monoliths from periodic mesoporous carbon CMK-8*. Proceedings of the National Academy of Sciences, 2010. **107**(31): p. 13593-13596.
27. Irifune, T., et al., *Materials: Ultrahard polycrystalline diamond from graphite*. Nature, 2003. **421**(6923): p. 599-600.
28. Mohanty, P., Y. Fei, and K. Landskron, *Synthesis of Periodic Mesoporous Coesite*. Journal of the American Chemical Society, 2009. **131**(28): p. 9638-9639.
29. Mohanty, P., et al., *Large-pore periodic mesoporous silicas with crystalline channel walls and exceptional hydrothermal stability synthesized by a general high-pressure nanocasting route*. Microporous and Mesoporous Materials, 2012. **152**: p. 214-218.

6 Synthesis of cubic BN from nanoporous precursors

6.1 Introduction to boron nitride materials.

Materials with superior hardness are widely used for engineering applications, such as drilling, abrasives, cutting and grinding. Therefore, superhard materials are sought by scientists which have led to significant scientific discoveries[2]. The most commonly used superhard material is diamond. It is still the hardest material known[4], despite many experimental and theoretical efforts to find harder ones[5]. However, diamond has its own inherent limitations with regard to its chemical stability, listed as the following:

- Diamond is the unstable phase of carbon under ambient pressure and starts to convert back to graphite at starting at 900 °C[3].Diamond is prone to oxidation in air at 600 °C owing to the chemical nature of carbon.
- Diamond tends to dissolve in ferrous metal (Fe, Co, Ni) and their alloys at temperatures above 700 °C by carbide formation[6]

Due to these limitations, it is not possible to use diamond as grinding materials for certain applications, for example, grinding hardened steel. In light of this, alternatives for diamond are explored and a common alternative used today is cubic boron nitride[3].

Boron nitride (BN) is a chemical compound containing an equal number of boron and nitrogen atoms. BN is isoelectronic to carbon and it has polymorphs that are similar to carbon allotropes structurally - hexagonal boron nitride (hBN) and cubic boron nitride (cBN). Like graphite, h-BN is comprised of stacks of hexagonal rings made of alternating boron and nitrogen atoms with sp^2 hybridization. On the other hand, cubic boron nitride shares the same structure with diamond with sp^3 hybridized atoms with a coordination number of four. In other words, one can view hBN and cBN as graphite and diamond crystals with half atoms substituted by nitrogen and the other

half substituted by boron. More interestingly, some of their properties and applications are also similar. For example, similar to graphite, hBN is also a good lubricant and is often used as a substitute for graphite under oxidative conditions. On the other hand, cBN is one of the hardest materials known today like diamond. There are also similar phase transition behaviors between boron nitride and carbon. Shown in Fig 6-1 is the phase transition of graphite to diamond (top) and hBN to cBN (bottom), both of them go from a hexagonal lattice to a cubic lattice.

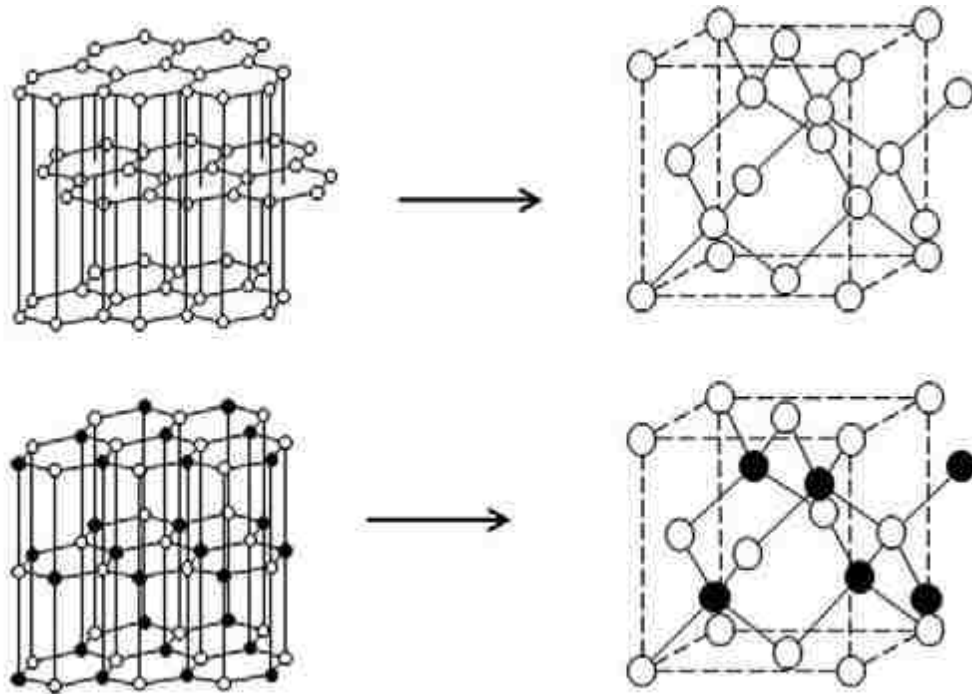


Fig 6-1. Phase transition schematics. Top: from graphite to diamond, Bottom: from hBN to cBN (white: boron, black: nitrogen). Ref[3]

Different from diamond, cBN is first discovered by HPHT synthesis and later found in nature[7]. In 1957, Wentorf Jr. from GE laboratory made the first cBN from mixtures containing boron and nitrogen at 8.6 GPa and 1800 °C[8]. Since then, cBN has been prepared from various BN precursors, like amorphous boron nitride[9], high purity hBN[10], pyrolytic graphite-like boron nitride[11] and so forth.

Therefore, from both scientific curiosity and a practical point of view, the investigation of nanoporous boron nitride under HPHT conditions is of significant interest. First of all, given the similarity of boron nitride and carbon in many ways, it is worthwhile to study the phase transition behavior of mesoporous boron nitride under similar conditions compared with mesoporous carbon. Secondly, since single-crystalline diamond nanoparticles and nanopolycrystalline diamond crystals have been produced from mesoporous carbon, and the same morphology may be formed from boron nitride as well. It is also worthwhile to investigate whether mesoporous boron nitride is more active in HPHT reactions than its bulk counterpart. This effort was a collaborative project between me and Dr. Manik Mandal in which we both contributed to the synthesis of the precursors and I performed most of the characterization. Dr. Mandal performed the high-pressure high-temperature syntheses at the Carnegie Institution of Washington.

6.2 Experimental setup and procedures:

The nanoporous hBN precursor was made by the nanocasting scheme described in Chapter 1. Firstly, SBA-15 type mesoporous carbon (mC) was prepared by a soft assembly route reported by Dai. Then borazane ($\text{BH}_3\cdot\text{NH}_3$) was infiltrated into the pore channels of the carbon template. The amount of borazane was chosen according to the pore volume of the carbon so it can fill the pores completely. After the infiltration, the composite was heated in N_2 to convert borazane to boron nitride. Finally, the carbon template was removed by heating in NH_3 flow to obtain a mesoporous boron nitride (mBN). Then, the pure mBN was transformed into cubic boron nitride under HPHT conditions.

6.2.1 Synthesis of C-ORNL-1 mesoporous carbon template

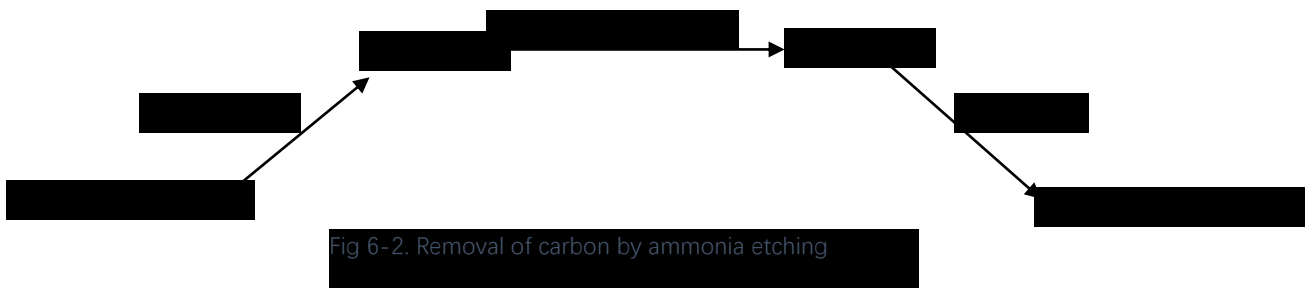
The synthesis of mesoporous carbon templated was reported by Dai and co-workers[12]. Resorcinol (Sigma-Aldrich), formaldehyde (Sigma-Aldrich), F127 surfactant (BASF) and HCl (EMD Chemicals, Inc.) was obtained without further purification. In the synthesis procedure, 2.2 g F127 was dissolved in a mixture of 9.0 ml 3 M HCl and 9.0 ml EtOH under stirring, then 2.2 g resorcinol was added to the solution for dissolution. After continuous stirring for ~ 11 min, the solution turned into a cloudy mixture. After 40 min, the gel phase was separated by centrifuging at 3000 rpm and transferred onto a Petri dish for subsequent drying at 80 °C and 120 °C for 24 h respectively. The dried gel was scrubbed from the Petri dish, transferred into an alumina crucible and heated to 350 °C for 2 h at 1 °C/min for decomposition of F127 and subsequently to 850 °C for 2h for the carbonization of the resorcinol-formaldehyde polymer. The as-obtained carbon template was denoted as C-ORNL-1 and characterized by SEM, TEM, gas adsorption, and SAXS.

6.2.2 Synthesis of mesoporous carbon / borazane composite

$\text{BH}_3\cdot\text{NH}_3$ was used as the source for boron nitride. To infiltrate BN complex into the template, 0.5 g $\text{BH}_3\cdot\text{NH}_3$ was taken and stirred in 2.0 g tetrahydrofuran (THF) to obtain a borazane suspension. To this mixture, 1.4 g mesoporous carbon was added and sonicated for 30 min. Then the mixture was left at 40 °C overnight for the evaporation of THF. A borazane/ carbon composite was obtained afterward. The borazane / carbon complex was heated up to 1000 °C with a heating rate of 5 °C/min under nitrogen flow to form hBN.

6.2.3 Removal of the carbon template

Ammonia was used to remove carbon from the composite material. The composite material was heated up in nitrogen atmosphere at 10 °C/min. When the temperature reached 1000 °C, the flowing gas was switched to ammonia to etch the carbon from the composite for 24h. Afterwards, the sample was cooled down in a nitrogen flow. The scheme is shown in Fig 6-2. After the treatment, mesoporous boron nitride was obtained and used as the precursor for HPHT experiments.



6.2.4 HPHT experiments

The precursor was pressurized to the designated pressure at a ramp of 2 GPa/h at room temperature and subsequently heated up to the final temperature at a rate of 50 C°/min. Then the pressure and temperature were kept for 3 h during experiments. After the experiment, the pressure was gradually released at 2 GPa/h. The sample was extracted from the assembly at ambient pressure and temperature for characterization. Several pressure/temperature combinations were chosen to investigate the effect of pressure and temperature on the phase transition of mesoporous BN precursors.

6.3 Product characterization and analysis:

Gas adsorption measurements were taken with Quantachrome AS-1 Surface Area and Pore Size Analyzer. The sample was degassed at 200 °C prior to measurement. XRD pattern was acquired on an imaging plate using Bruker D8 Discover in Geophysical Laboratory instrument with Cu K_α as X-ray source. The sample was mounted inside a 0.5 mm diameter capillary tube. TEM images were taken with JEOL 2000FX microscope with lanthanum hexaboride filament as electron source operating at 200 kV. The samples were ground and dispersed in acetone, then drop cast onto copper grid supported carbon film (SPI supplies). SEM was performed with Hitachi S4200 and Zeiss 1550 with field emission electron source, operated at the voltage of 2-5 kV. The sample was coated with iridium with ~ 5nm thickness to increase electrical conductivity on sample surfaces. Three-dimensional TEM was performed by the Arslan Group at Pacific Northwest National Laboratory to analyze the pore size distribution of the cubic boron nitride products. Three-dimensional TEM is a technique where a tilt-series of 2D TEM images are collected and later used to reconstruct a 3D image of the sample[13].

The nanocrystal size and particle size distribution was analyzed by the Liu group at the University of Akron using dynamic light scattering (DLS) techniques. A BI-9000 AT digital time correlator was used to monitor the intensity-intensity time correlation function. The constrained regularized CONTIN method was used to analyze the field correlation function $G(\Gamma)$ to get the characteristic line width Γ . The hydrodynamic radius R_h of the nanocrystals was calculated with Stokes-Einstein equation:

$$R_h = kT/(6\pi\eta D),$$

where:

k is the Boltzmann constant,

η is the viscosity of the solvent at temperature T ,

D is translational diffusion coefficient.

With D calculated by the following equation:

$$D = \frac{\Gamma}{q^2},$$
$$q = \frac{4\pi n}{\lambda} \sin(\theta/2),$$

where:

n is the refractive index of the sample,

λ is the incident laser wavelength,

θ is the scattering angle.

The particle size distribution is then obtained by plotting $\Gamma G(\Gamma)$ against R_h .

6.3.1 Characterization of the mesoporous carbon template C-ORNL-1

The as-synthesized mesoporous carbon (mC) template was examined by TEM, SEM, and gas adsorption techniques. Electron microscopy showed the mesoporous structure was successfully synthesized by the soft-templating route. The as-synthesized mesoporous carbon template has one-dimensional pore channels packed hexagonally with a diameter of ~ 7 nm. N_2 isotherm showed a typical type IV isotherm with capillary condensation. From the adsorption isotherm, the BET surface area was calculated to be $780 \text{ m}^2/\text{g}$, and NLDFT gave a pore size estimation of 6.5 nm.

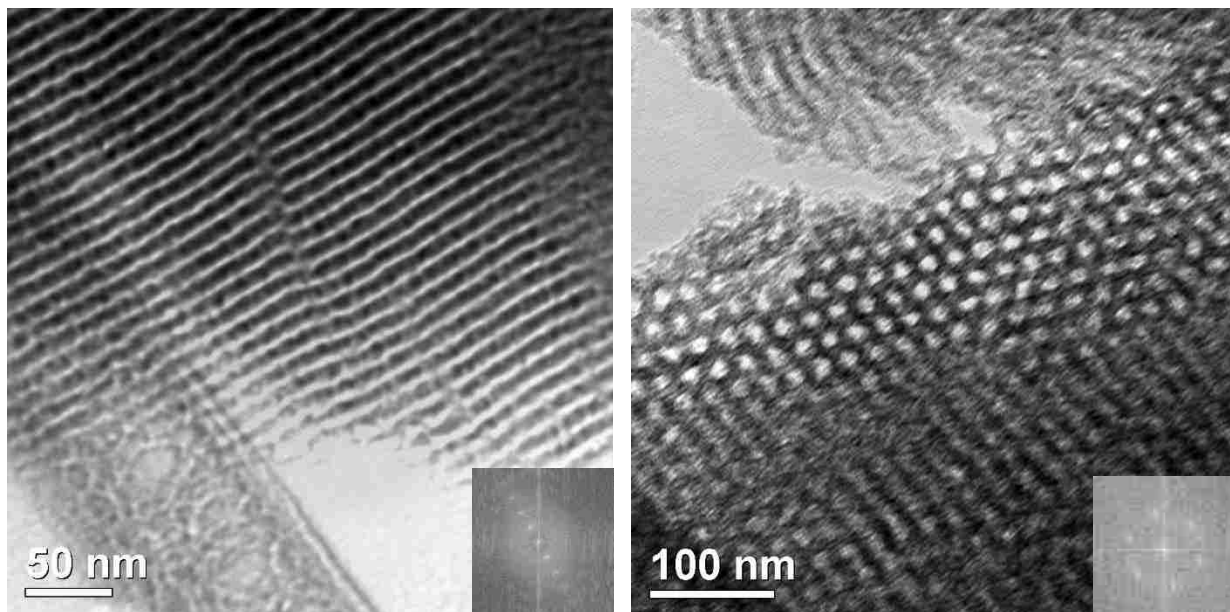


Fig 6-3. TEM images of the mesoporous carbon template with FFT inset.

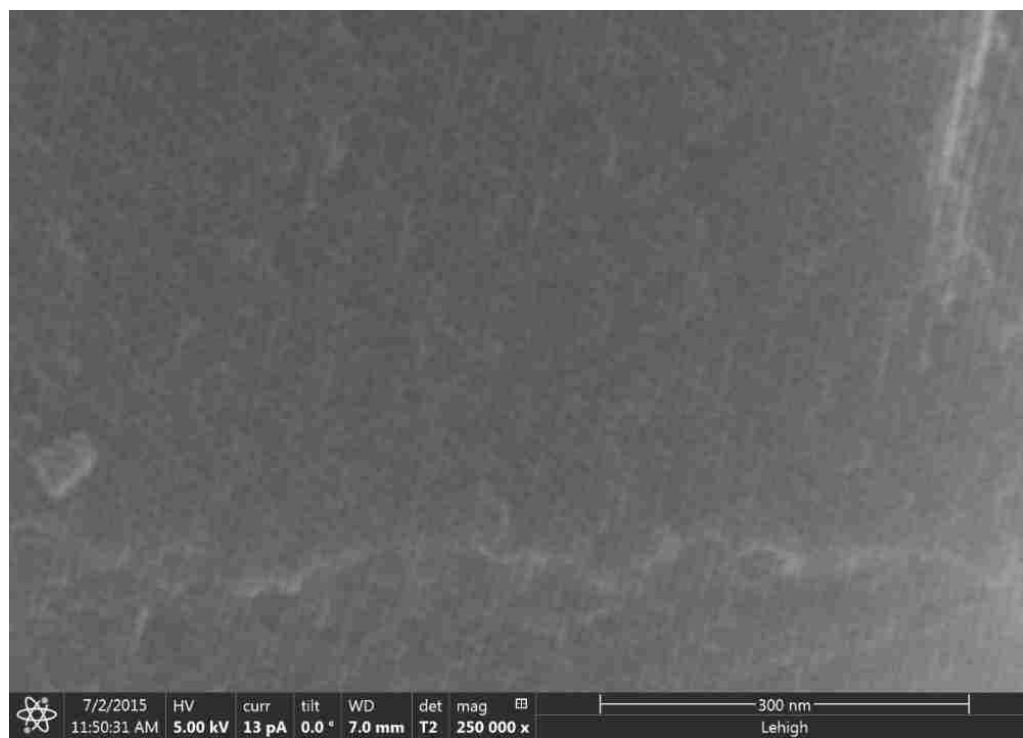


Fig 6-4. SEM of mesoporous carbon template

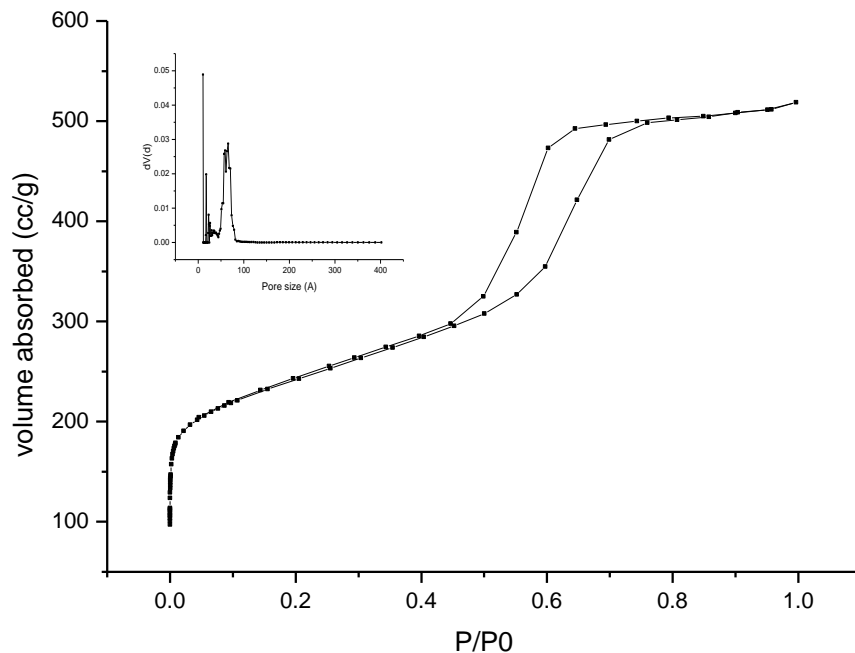


Fig 6-5. Nitrogen adsorption isotherm of mesoporous carbon template. (Inset: pore size distribution)

6.3.2 Characterization of mC/mBN composite

After infiltration of borazine into the template, the mC/mBN was inspected by gas adsorption measurements to ensure the pore volume of the carbon template was effectively filled with boron nitride.

The BET surface area of mC/mBN composite was calculated from the adsorption isotherm in Fig 6-7 was 43.8 m²/g, which is only 5.6% compared with that of the carbon template, showing the successful infiltration process. The rather small electronic contrast from TEM images in Fig 6-6 indicates the same as well.

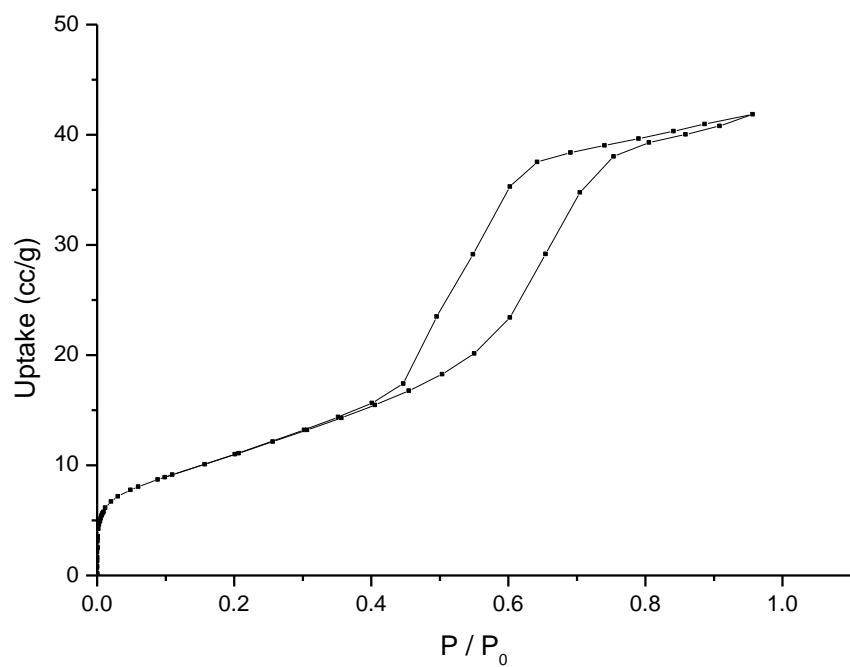


Fig 6-7. Nitrogen adsorption isotherm of mC/mBN composite

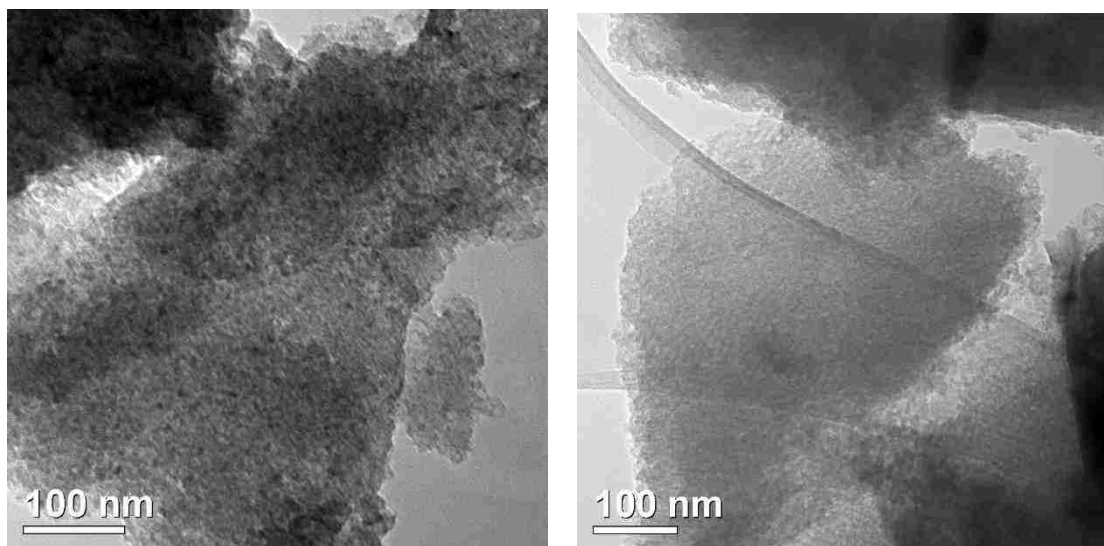


Fig 6-6. TEM image of mC/mBN nanocomposite

6.3.3 Characterization of mesoporous boron nitride precursor

After the removal of carbon template by ammonia, a pure mesoporous boron nitride was obtained. Its porous structure was confirmed by TEM microscopy in Fig 6-8 and nitrogen adsorption isotherm in Fig 6-9. The BET surface area of mBN was $610 \text{ m}^2/\text{g}$ with a pore size of 5.2 nm calculated from NLDFT.

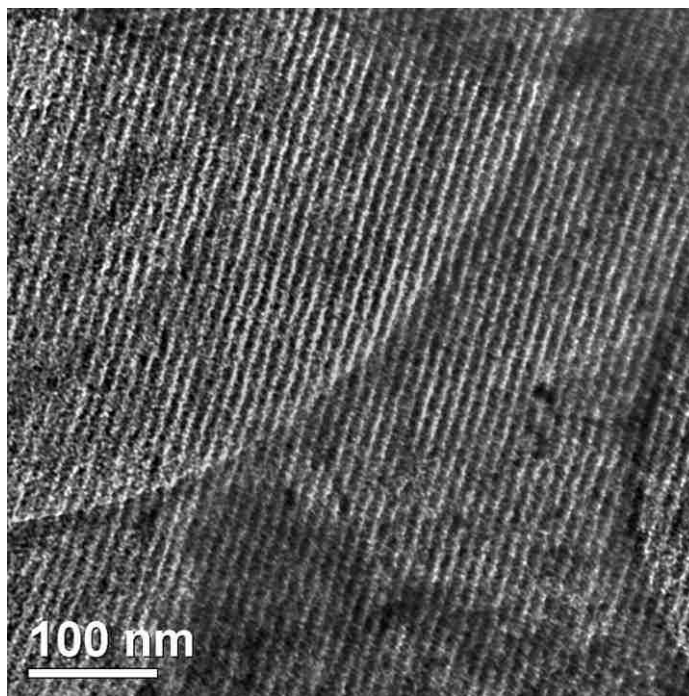


Fig 6-8. TEM image of mBN precursor

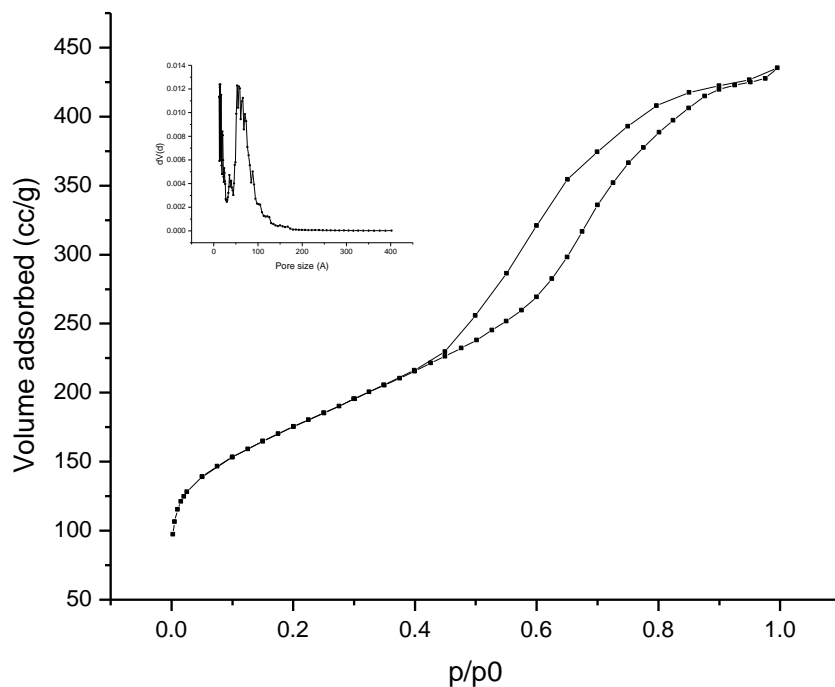


Fig 6-9. Nitrogen adsorption isotherm for mBN precursor. (Inset: pore size distribution)

6.3.4 Single-crystalline mBN nanoparticles obtained at 14 GPa and 1300 °C

The precursor treated at 14 GPa, 1300 °C for 3h transformed to cBN successfully, as indicated by the XRD pattern in Fig 6-10 showing the 111, 200, 220 and 311 reflections of cubic lattice of boron nitride, with a lattice constant of 3.6154 Å. The product morphology was characterized by TEM in and SEM in Fig 6-11 and Fig 6-12. TEM revealed the as-synthesized cBN are faceted nanocrystals with a particle size of ~50 nm. The same was observed with SEM as well.

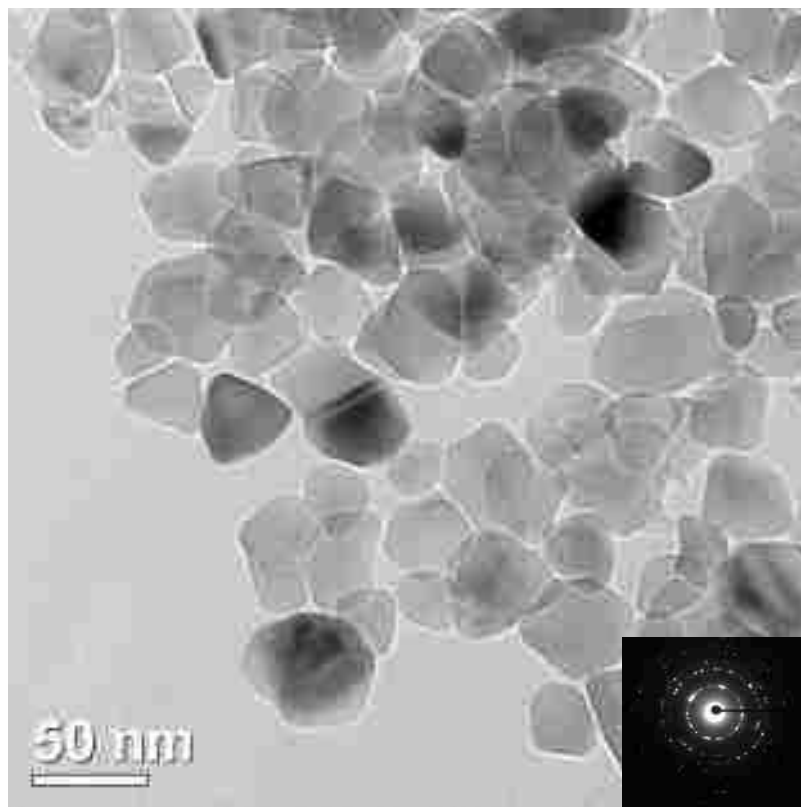


Fig 6-11. TEM of mBN treated at 14 GPa and 1300 °C (inset: SAED).

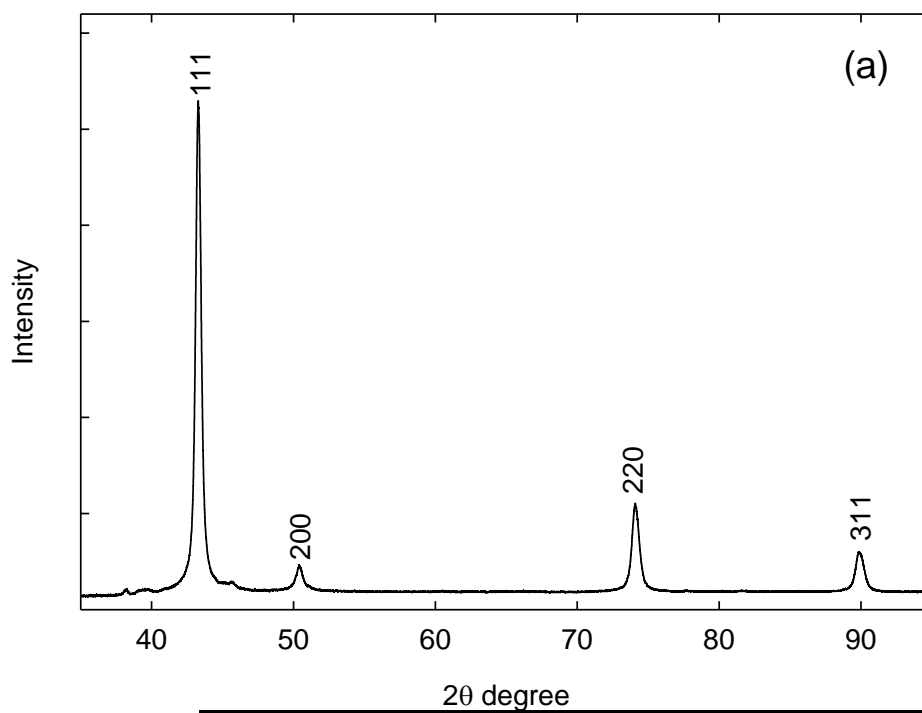


Fig 6-10. XRD of mBN treated at 14 GPa and 1300 °C

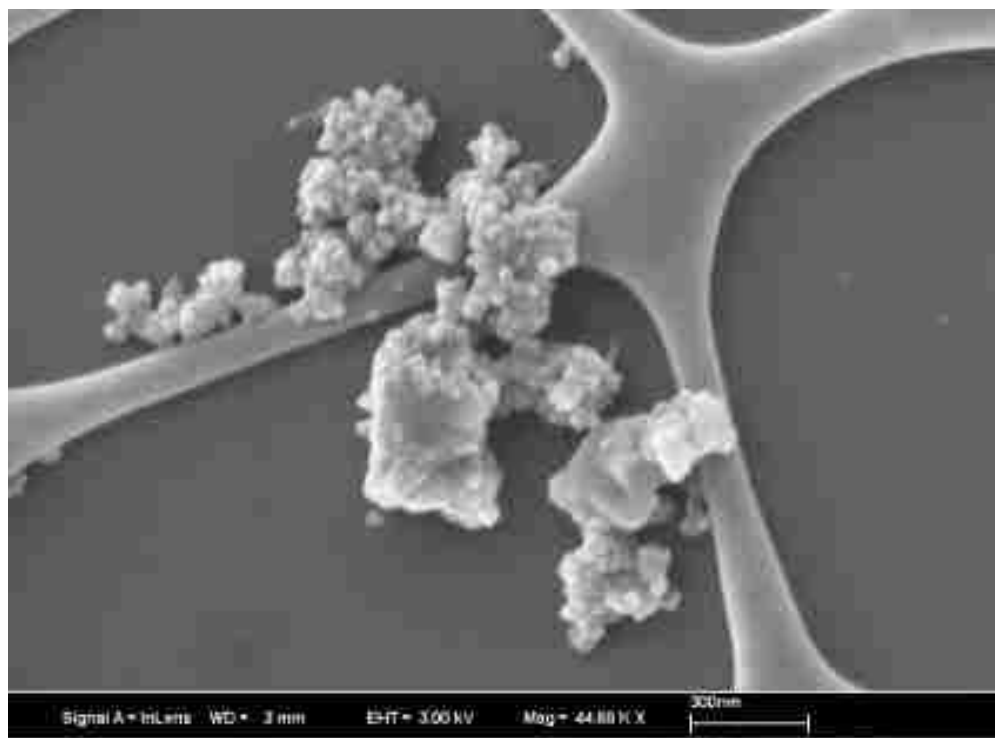


Fig 6-12. SEM of mBN treated at 14 GPa and 1300 °C

To find whether these nanoparticles are free standing, the cBN were dispersed in acetone and analyzed with DLS. The measurement was performed at different scattering angles from 45° to 120°. The hydrodynamic radius R_h of the dispersed nanoparticles was determined by CONTIN algorithm. The average nanoparticle was found to be ~70 nm, which is slightly larger than the observation from TEM and SEM. Slight aggregation and the solvation shell of these particles could be a possible explanation for this discrepancy. In DLS, the particles can be surrounded by solvent molecules, therefore the solvation shell could lead to the hydrodynamic radius. The DLS measurement indicates the cBN nanoparticles in the solvent is slightly aggregated but still solution processable (Fig 6-13).

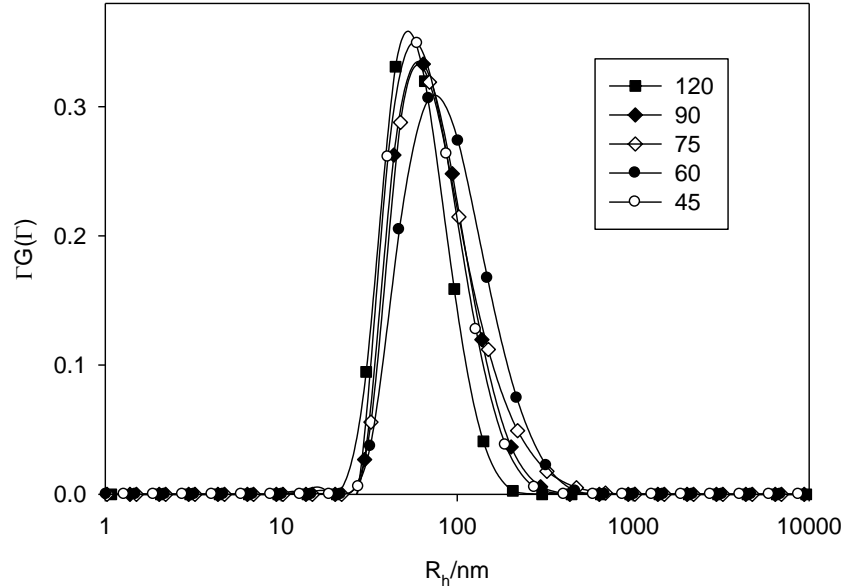


Fig 6-13 DLS particle size of cBN obtained at 14 GPa and 1300 °C

6.3.5 Nanopolycrystalline cBN obtained at 10 GPa and 1000 °C

In another experiment, the mBN precursor was treated at 10 GPa and 1000 °C for 30 min to investigate if the phase transition can still happen at lower temperature and pressure. The XRD pattern in Fig 6-16 confirmed that cBN formed under this condition. The crystal morphology was investigated by TEM and SEM. The results show the cBN formed at 10 GPa and 1000 °C is in aggregated form. According to TEM images in Fig 6-14, the product is aggregated from cBN nanoparticles of ~20 nm diameter, making the product a nanopolycrystalline material. This is confirmed by SEM images as well, as seen in Fig 6-15. This sample was also investigated by DLS in Fig 6-17, and the hydrodynamic radius calculated from CONTIN algorithm is ~500 nm, which shows that the nanograins are aggregated to form a polycrystalline material.

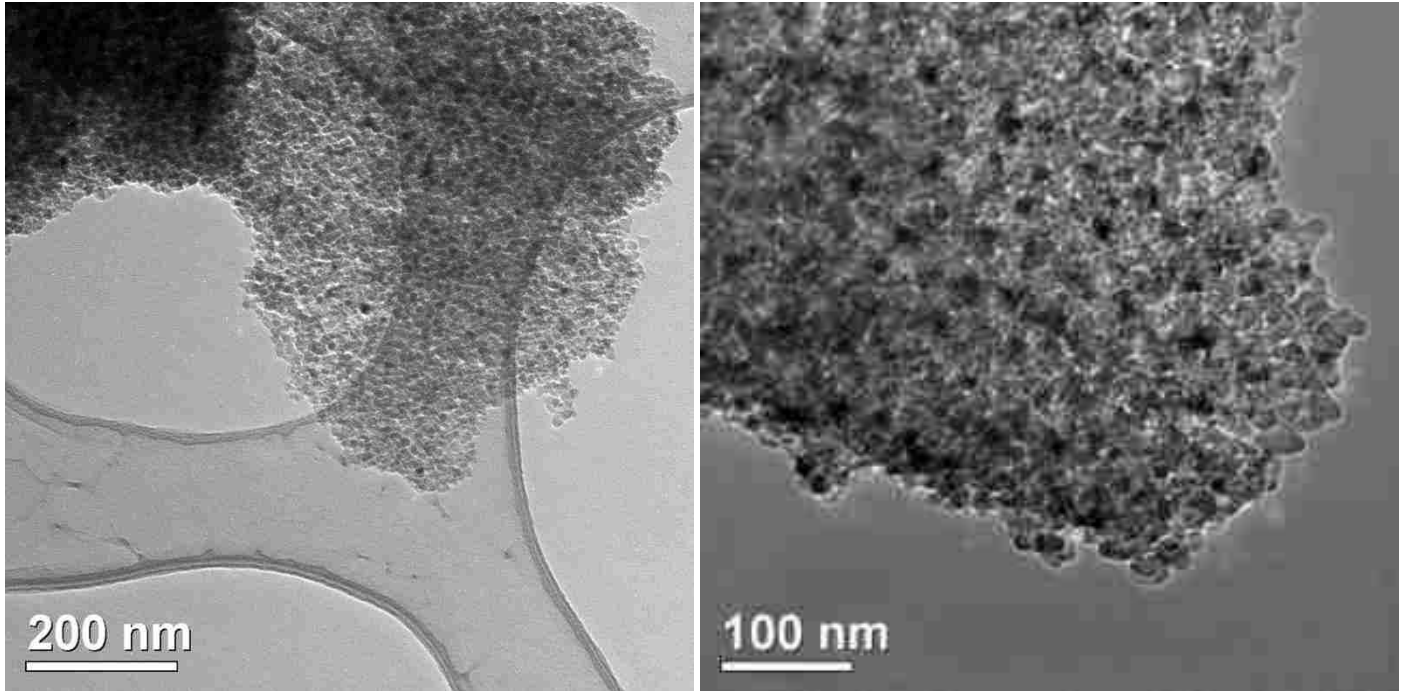


Fig 6-14. TEM images of mBN treated at 10 GPa and 1000 °C

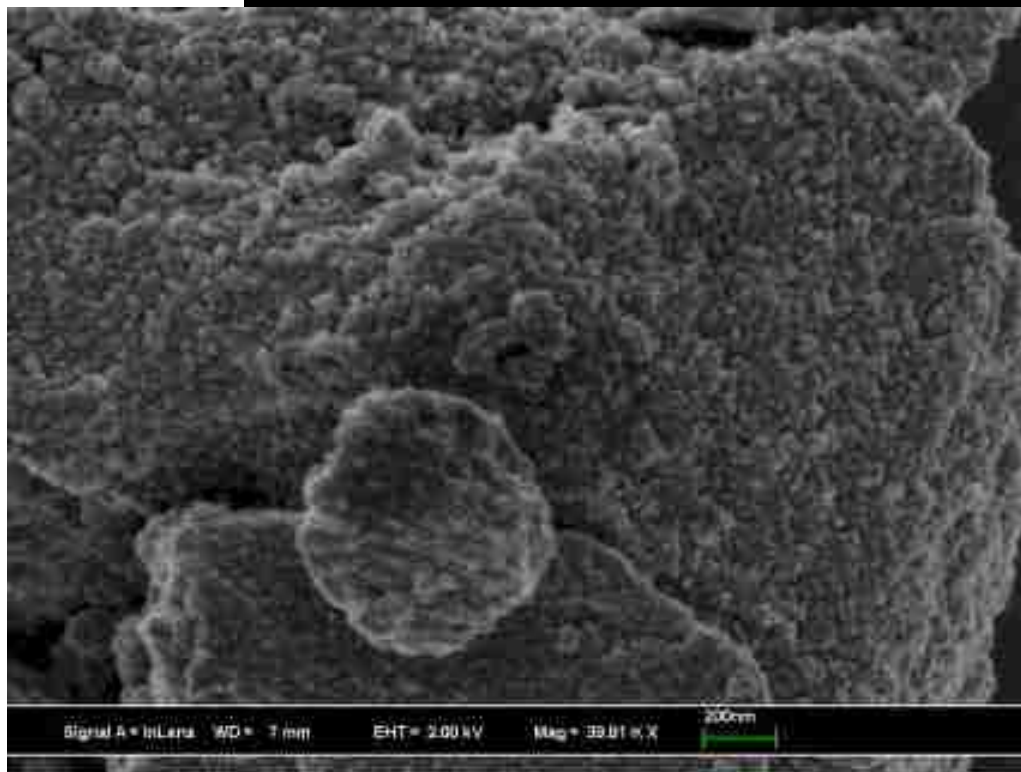


Fig 6-15. SEM image of mBN treated at 10 GPa and 1000 °C

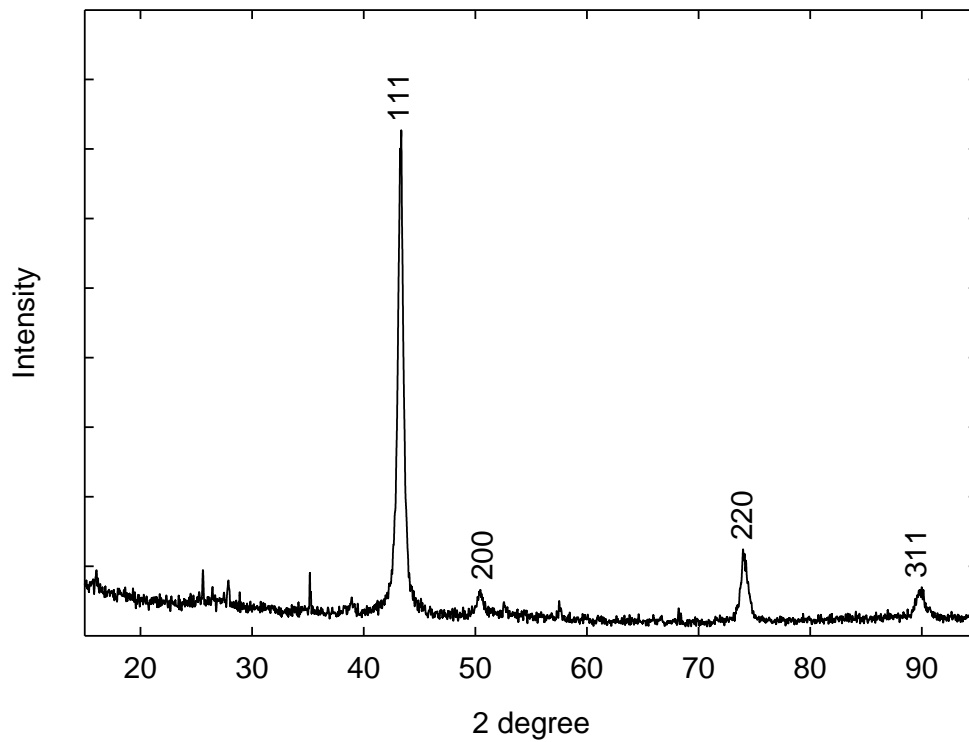


Fig 6-16. XRD spectra of mBN treated at 10 GPa and 1000 °C

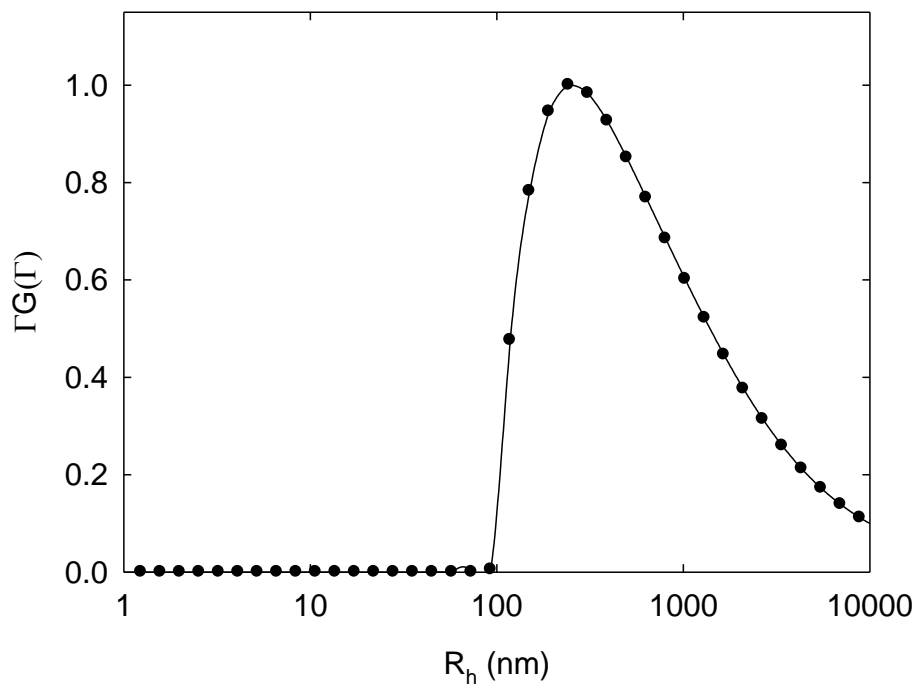


Fig 6-17. DLS CONTIN of mBN treated at 10 GPa and 1000 °C

It was ambiguous if the electronic contrast from TEM images would come from porosity or from grain boundaries. The bright areas around a nanocrystal can be interpreted as grain boundary, and the bright area between the particles may indicate porosity. Therefore, N₂ adsorption isotherm and three-dimensional TEM investigation were performed. From the nitrogen adsorption isotherm shown in Fig 6-18, the BET surface area was calculated to be 44.9 m²/g. The adsorption hysteresis occurs over a wide pressure range, indicating a relatively broad pore size distribution. The pore size distribution ranged from 3 to 8 nm and the pore volume was 0.05 cc/g calculated from NLDFT. The AS-1 instrument provides several adsorbate/adsorbent models for NLDFT calculation, but there is no option for boron nitride adsorbent. Therefore, only a N₂ adsorption on carbon with slit pores model could be used which may not have given accurate results.

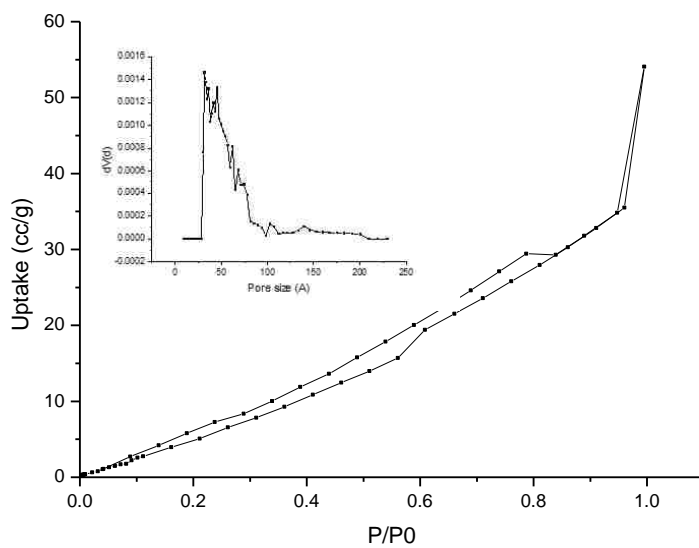


Fig 6-18. Nitrogen adsorption isotherm of mBN treated at 10 GPa and 1000 °C

The schematics of 3D TEM investigation can be illustrated by Fig 6-19. A series of images were collected at different tilting angles, and the images were later combined to construct a 3D

representation of the sample. Shown in Fig 6-20 is one slice of the images obtained from the sample treated at 10 GPa and 1000 °C. The black area surrounded by white area represents the pores in the sample. By measuring the pore size from multiple images, a statistical pore size distribution was obtained in Fig 6-21.

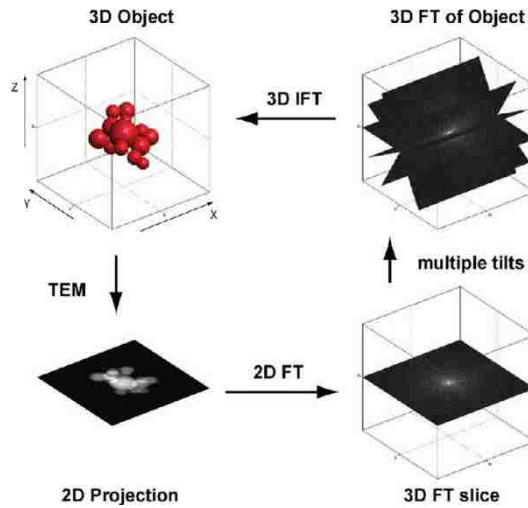


Fig 6-19. The principle of 3D TEM by tilting. Ref[1]

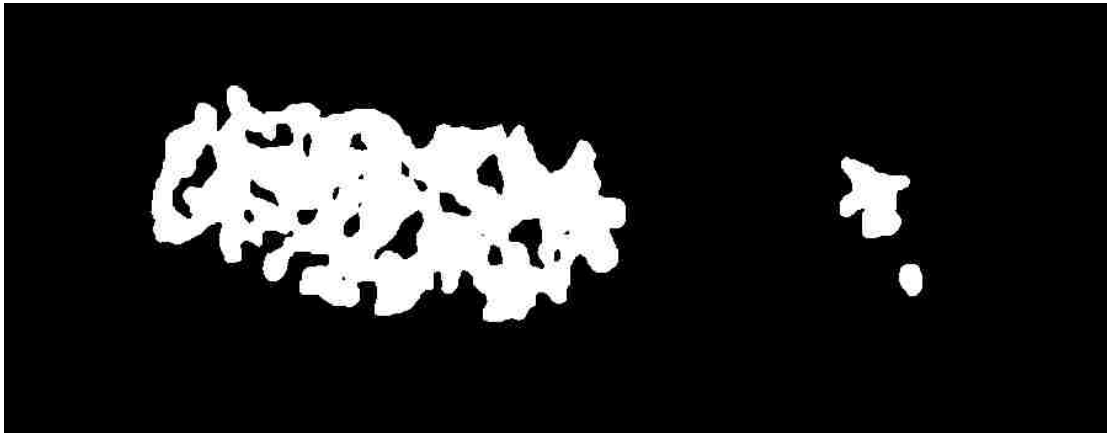


Fig 6-20. One slice from 3D TEM images. (No scale bar shown)

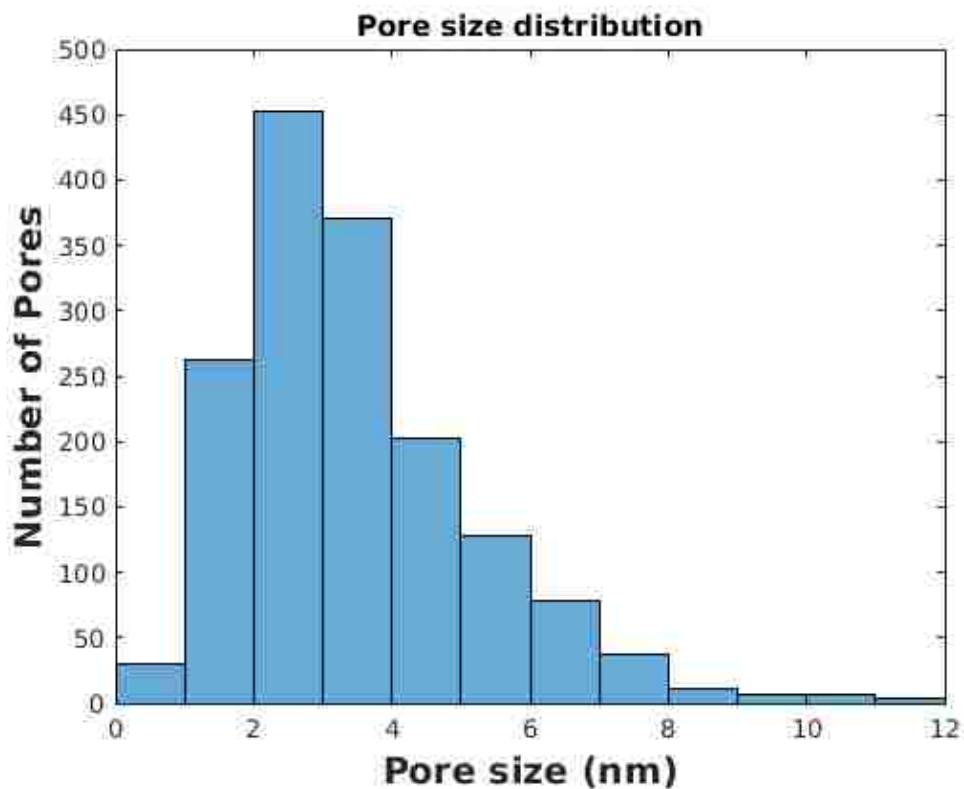


Fig 6-21. Pore size distribution of mBN treated at 10 GPa and 1000 °C

According to calculations from 3D TEM, the sample surface area is 122 m²/g, with 10.2% porosity and 0.0331 cc/g pore volume. The surface area here is larger than the surface area calculated from gas adsorption isotherm, indicating a large portion of pores is closed pores that are not accessible for gas molecules.

6.3.6 Mesoporous boron nitride treated at 8 GPa and 1000 °C

In order to find the lower pressure boundary for the phase transition, another HPHT experiment was carried out at the 8 GPa and 1000 °C for 30 min. Under this condition, the mBN precursor transformed to hexagonal boron nitride as indicated by the XRD pattern in Fig 6-22. According to

TEM and SEM in Fig 6-23, the product is vesicular shaped nanoparticle with an average size of $\sim 0.5\text{-}1\ \mu\text{m}$. DLS analysis showed the average particle size is $1\ \mu\text{m}$ (Fig 6-24), which is in accordance with TEM and SEM observations. These results indicate that the minimal phase transition pressure for mBN precursor is between 8 and 10 GPa.

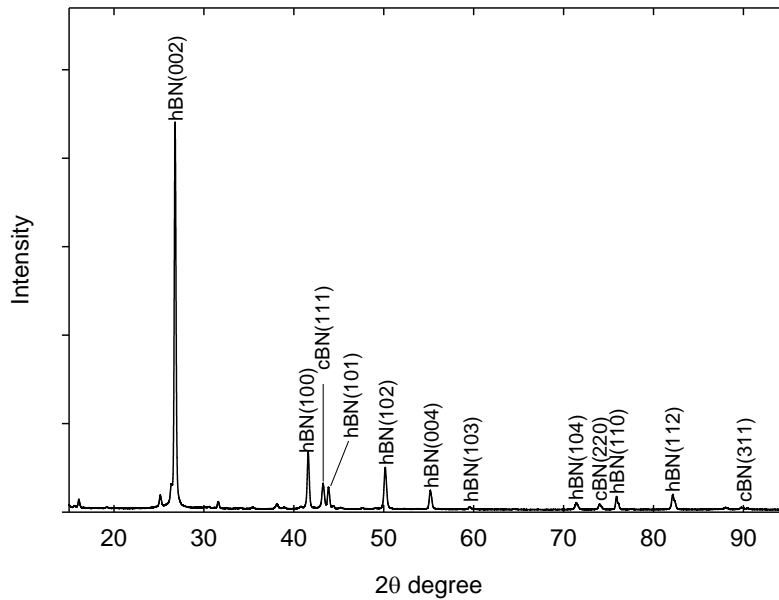


Fig 6-23. XRD of mBN treated at 8 GPa and 1000 °C

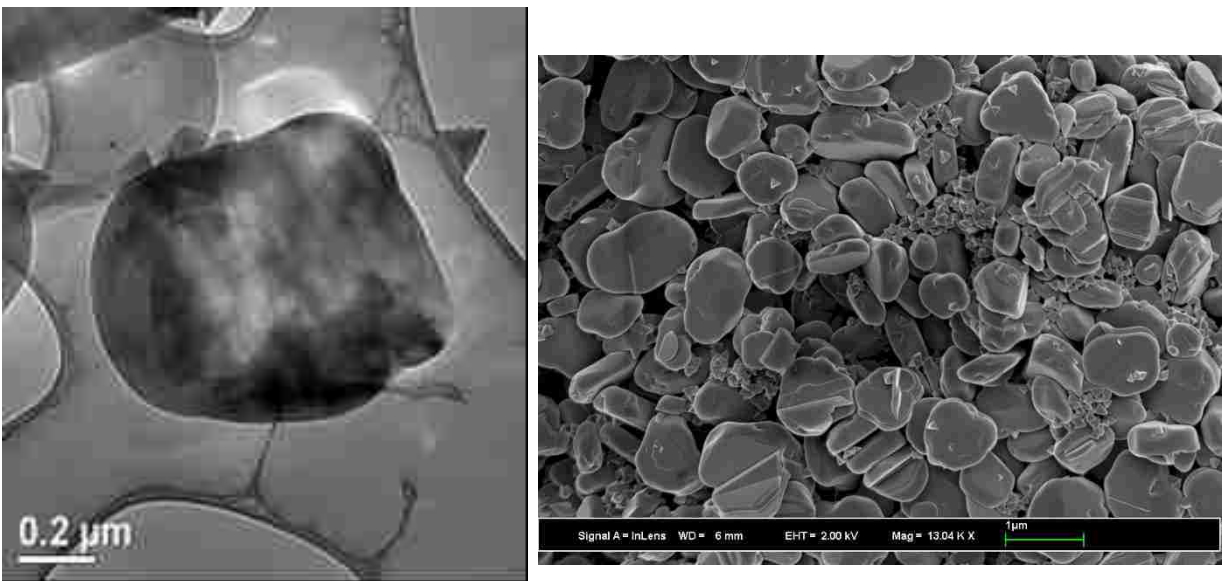


Fig 6-22. TEM (left) and SEM (right) of mBN treated at 8 GPa and 1000 °C

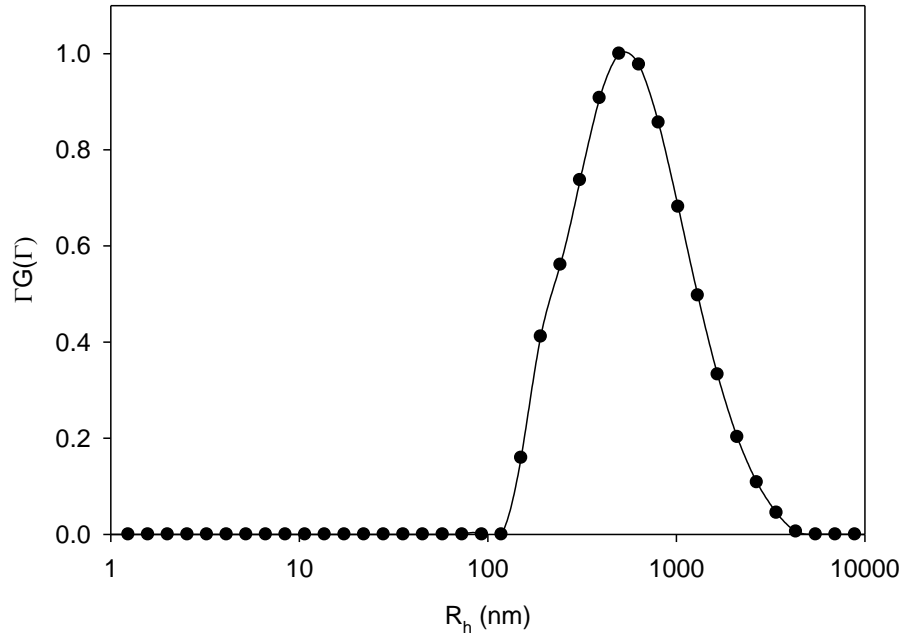


Fig 6-24. DLS CONTIN analysis of mBN treated at 8 GPa and 1000 °C

6.4 Discussion and conclusion:

Similar to single crystalline diamond nanoparticles produced from mesoporous carbon[14], single crystalline cBN nanoparticles can also be obtained from mesoporous boron nitride precursor without the aid of catalysts. The cBN products obtained from 14 GPa and 1300 °C experiment are isotropic nanoparticles with ~50 nm grain size and have well-defined crystal edges and facets. In addition, these nanoparticles are solution processable since they can be dispersed in acetone.

On the other hand, the mesoporous nanopolycrystalline cBN produced from 10 GPa and 1000 °C experiment is similar to the report of mesoporous nanopolycrystalline diamond obtained from CMK-8 carbon[15]. The as-synthesized cBN is made of sintered nanoparticles with ~20 nm grain size. Measured by DLS, the average hydrodynamic radius of the particles is ~500 nm. The as-synthesized has a surface area of 122 m²/g, which is significant for high-pressure phase materials, though some portion of the surface area is not accessible. High pressure and porosity seem to

contradict to each other, but the presence of porosity might be explained by the collapse-reformation mechanism described in Chapter 6. It is well studied that mesoporous silica exhibits elastic behavior under pressure[16], the same might apply for mBN as well. Upon pressurization, the mesopores are elastically distorted, ultimately leading to partial or complete pore deformation in the intermediate. Upon crystallization as cBN, the strain can be released by pore creation. At a relatively mild temperature (1000 °C), the strength of cBN might be well enough to support the porous structure against the pressure of 10 GPa. Additionally, the volume shrinkage during crystallization can also induce porosity.

From a practical standpoint, the use of mBN precursor brings several of benefits to the production of cBN materials. Firstly, according to the Hall-Petch effect (also called grain-boundary strengthening), grain boundaries can impede dislocations within the material. Therefore, the mechanical strength of the cBN is reversely related to the grain size. Previously, Irifune has reported this effect for nanopolycrystalline diamonds[17]. Due to nanopolycrystalline nature of the product produced at 10 GPa and 1000 °C, the materials could be much stronger than conventional cBN with micron meter sized grains. However, it needs to be considered that porosity tends to decrease mechanical strength and that the grain boundaries may be weak due to the mild temperature applied.

Secondly, the temperature and pressure conditions required for mBN to convert to cBN is much lower compared with conventional precursors. For example, the Solozenko group reported the synthesis of nanopolycrystalline cBN from a BN precursor which has a similar structure to polycrystalline graphite at 20 GPa and ~1500 °C[18] and the Ogi group obtained similar products from high purity hBN and pyrolytic BN at pressures between 9–20 GPa and temperatures between 1500-2300 °C[19], while our method only required 10 GPa and 1000 °C, lowering the energy

consumption and cost during the synthesis, therefore making the whole process potentially more scalable.

The high reactivity of nanoporous precursor in HPHT reactions have also been observed in the synthesis of diamond materials[14, 15, 20] and silicon dioxide materials as well[21, 22]. From the perspective of thermodynamics, it is likely the high surface area and ordered porous structures can provide reaction pathways with low activation barrier that are not available for bulk materials, therefore the pressure and temperature conditions are lowered and novel cBN nanostructures are obtained from the precursor. For example, the high surface area may provide more active sites and the pore volume may provide extra space for contraction/expansion during the phase transformation, which is not applicable for conventional bulk precursors.

However, it is not clear how the porosity can exactly facilitate the phase transformation and how the product morphology is governed by the reaction conditions. Based on the results reported in this chapter, one can design further experiments, for example, *in-situ* HPHT experiments with XRD/SAXS measurements in a diamond anvil cell to study intermediate states and reaction pathways. Also, computational modeling of phase transformation might help as well. Hopefully, these future experiments can provide detailed mechanistic information to help us design and optimize the synthesis of high pressure phases from nanoporous precursors.

6.5 References

1. Friedrich, H., et al., *Electron Tomography for Heterogeneous Catalysts and Related Nanostructured Materials*. Chemical Reviews, 2009. **109**(5): p. 1613-1629.
2. Brazhkin, V.V., A.G. Lyapin, and R.J. Hemley, *Harder than diamond: Dreams and reality*. Philosophical Magazine A, 2002. **82**(2): p. 231-253.
3. Monteiro, S.N., et al., *Cubic boron nitride competing with diamond as a superhard engineering material – an overview*. Journal of Materials Research and Technology, 2013. **2**(1): p. 68-74.
4. Kaner, R.B., J.J. Gilman, and S.H. Tolbert, *Designing Superhard Materials*. Science, 2005. **308**(5726): p. 1268-1269.
5. Teter, D.M., *Computational Alchemy: The Search for New Superhard Materials*. MRS Bulletin, 1998. **23**(01): p. 22-27.
6. Coelho, R.T., et al., *The application of polycrystalline diamond (PCD) tool materials when drilling and reaming aluminium based alloys including MMC*. International Journal of Machine Tools and Manufacture, 1995. **35**(5): p. 761-774.
7. Dobrzhinetskaya, L.F., et al., *Qingsongite, natural cubic boron nitride: The first boron mineral from the Earth's mantle*. American Mineralogist, 2014. **99**(4): p. 764-772.
8. Wentorf, R.H., *Synthesis of the Cubic Form of Boron Nitride*. The Journal of Chemical Physics, 1961. **34**(3): p. 809-812.
9. Huang, J.Y. and Y.T. Zhu, *Atomic-Scale Structural Investigations on the Nucleation of Cubic Boron Nitride from Amorphous Boron Nitride under High Pressures and Temperatures*. Chemistry of Materials, 2002. **14**(4): p. 1873-1878.
10. Sumiya, H., S. Uesaka, and S. Satoh, *Mechanical properties of high purity polycrystalline cBN synthesized by direct conversion sintering method*. Journal of Materials Science, 2000. **35**(5): p. 1181-1186.
11. Dubrovinskaia, N., et al., *Superhard nanocomposite of dense polymorphs of boron nitride: Noncarbon material has reached diamond hardness*. Applied Physics Letters, 2007. **90**(10): p. 101912.
12. Wang, X., C. Liang, and S. Dai, *Facile Synthesis of Ordered Mesoporous Carbons with High Thermal Stability by Self-Assembly of Resorcinol-Formaldehyde and Block Copolymers under Highly Acidic Conditions*. Langmuir, 2008. **24**(14): p. 7500-7505.
13. Koster, A.J., et al., *Three-Dimensional Transmission Electron Microscopy: A Novel Imaging and Characterization Technique with Nanometer Scale Resolution for Materials Science*. The Journal of Physical Chemistry B, 2000. **104**(40): p. 9368-9370.
14. Mandal, M., et al., *Size tunable synthesis of solution processable diamond nanocrystals*. Chemical Communications, 2014. **50**(77): p. 11307-11310.
15. Zhang, L., et al., *Catalyst-free synthesis of transparent, mesoporous diamond monoliths from periodic mesoporous carbon CMK-8*. Proceedings of the National Academy of Sciences, 2010. **107**(31): p. 13593-13596.
16. Wu, J., X. Liu, and S.H. Tolbert, *High-Pressure Stability in Ordered Mesoporous Silicas: Rigidity and Elasticity through Nanometer Scale Arches*. The Journal of Physical Chemistry B, 2000. **104**(50): p. 11837-11841.
17. Sumiya, H. and T. Irifune, *Hardness and deformation microstructures of nanopolycrystalline diamonds synthesized from various carbons under high pressure and high temperature*. Journal of Materials Research, 2007. **22**(08): p. 2345-2351.

18. Solozhenko, V.L., O.O. Kurakevych, and Y. Le Godec, *Creation of Nanostructures by Extreme Conditions: High-Pressure Synthesis of Ultrahard Nanocrystalline Cubic Boron Nitride*. *Advanced Materials*, 2012. **24**(12): p. 1540-1544.
19. Nagakubo, A., et al., *Elasticity and hardness of nano-polycrystalline boron nitrides: The apparent Hall-Petch effect*. *Applied Physics Letters*, 2014. **105**(8): p. 081906.
20. Pauzauskie, P.J., et al., *Synthesis and characterization of a nanocrystalline diamond aerogel*. *Proceedings of the National Academy of Sciences*, 2011. **108**(21): p. 8550-8553.
21. Mohanty, P., et al., *Synthesis of Stishovite Nanocrystals from Periodic Mesoporous Silica*. *Journal of the American Chemical Society*, 2009. **131**(8): p. 2764-2765.
22. Mohanty, P., et al., *Direct Formation of Mesoporous Coesite Single Crystals from Periodic Mesoporous Silica at Extreme Pressure*. *Angewandte Chemie*, 2010. **122**(25): p. 4397-4401.

7 Synthesis of diamond nanowires by nanocasting at high pressure with a hard template

7.1 Introduction and background

Low-dimensional materials have a long history in physics, chemistry, and material science. They can be defined as materials that are finite in at least one dimension, for example, zero-dimensional quantum dots[6], one-dimensional nanowires[7, 8], and two-dimensional (2D) sheet structures[9]. The past few decades have witnessed the progress on low-dimensional carbon materials with sp^2 hybridization, namely the discovery of 0D fullerene[10, 11], 1D carbon nanotube[12] and 2D graphene[13], as shown in Fig 7-1.

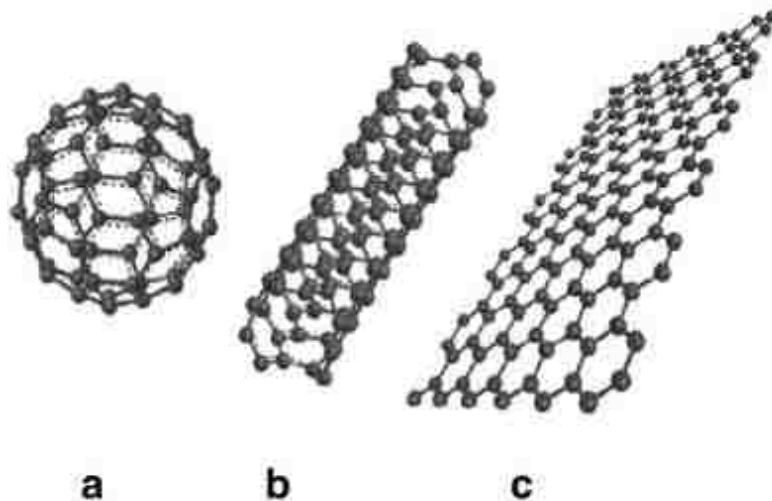


Fig 7-1. Low-dimensional sp^2 carbon structure. Fullerene (a), carbon nanotube (b), graphene (c).
Ref[5]

These low-dimensional carbon structures have remarkable chemical and physical properties, for example, carbon nanotubes have a very high Young's modulus and high tensile strength. In addition, depending on their structure, they can be tuned to be metallic conductors or semiconductors [14]. Therefore, large amounts of effort have been devoted to producing them and fabricating new devices from these materials.

On the other hand, low dimensional sp^3 carbon structures are much less studied. For example, the sp^3 analogue of the carbon nanotube, the diamond nanowire, also holds promises for several important applications, as it also possesses interesting properties like high strength, biocompatibility, and high thermal conductivity[2]. The unique physiochemical features suggest applications as reinforcements in nanocomposites, heat dissipation materials, as well as electronic devices. Recently, the Badding group at Penn State University has synthesized one-dimensional diamond nanowires made of a strand of zig-zag shaped “cyclohexane” rings of six atoms with sp^3 -hybridization[15]. Theoretical calculations have shown that this structure is remarkably strong yet light[1], which makes it potentially suitable for building “space elevators” (Fig 7-2).

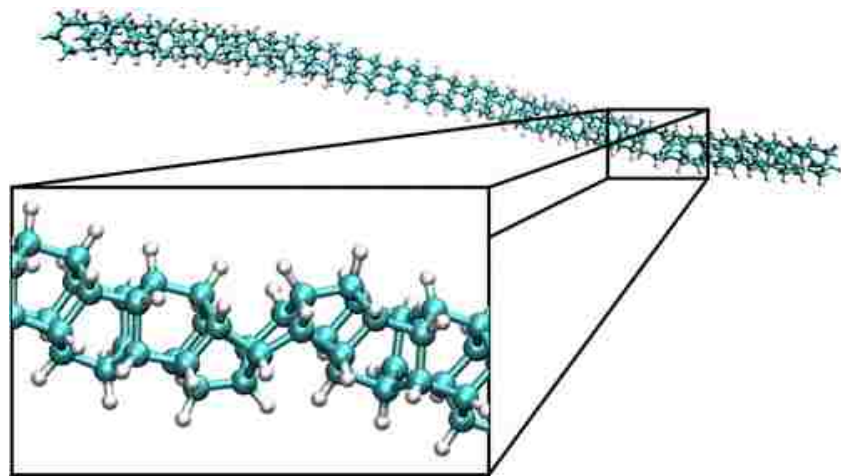


Fig 7-2. One dimensional sp^3 carbon structure, blue: carbon, white: hydrogen. Ref[1]

However, current synthesis methodologies for this type of one-dimensional structure are relatively limited. The production of diamond nanowires can be categorized into two approaches: top-down and bottom-up. The top-down approach is the common technique in nanomaterials synthesis, especially for semiconductor devices. The basic concept of top-down is to reduce the

initial structure from a macroscopic level to the nanoscopic level by externally controlled forces like etching through mask and milling.

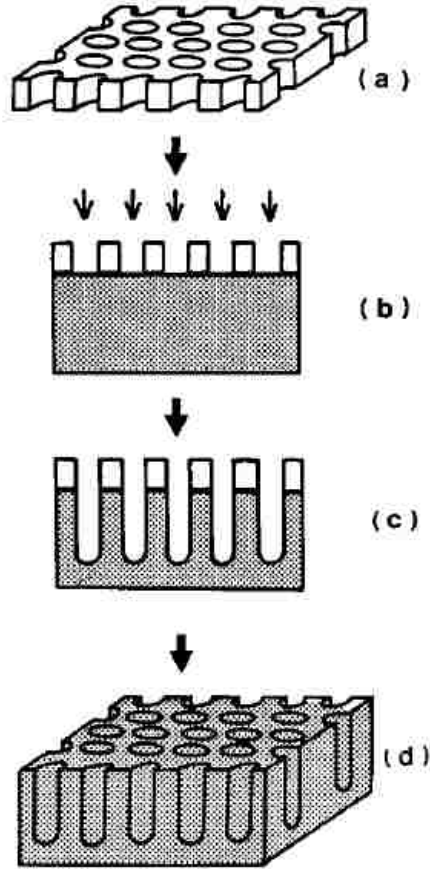


Fig 7-3. Production of diamond nanowire by masked etching. Ref[4]

One of the early efforts to make diamond nanowires by etching was reported by the Shiomi group, where reactive ion etching (RIE) by oxygen plasma was used to produce diamond rod structures with 300 nm length and 10 nm diameter[16]. Masuda proposed a general route for producing diamond nanowires from the etching of chemical vapor deposition (CVD) diamond film by oxygen plasma through anodic aluminum oxide (AAO) mask, as in Fig 7-3. Since the etching rate of the AAO template is negligible, the plasma is able to selectively remove carbon content by oxidation, producing one-dimensional diamond nanopillars with high aspect ratio[4].

On the other hand, the bottom-up approach builds nanostructures on the foundation of atoms and molecules, for example, molecular self-assembly, atomic layer deposition, epitaxy, and so forth. The Masuda group also studied the bottom-up approach diamond nanowire synthesis with AAO template. Diamond nanoparticles with ~50 nm size were used as seeds, and the product is deposited through the channels of the template (Fig 7-4).

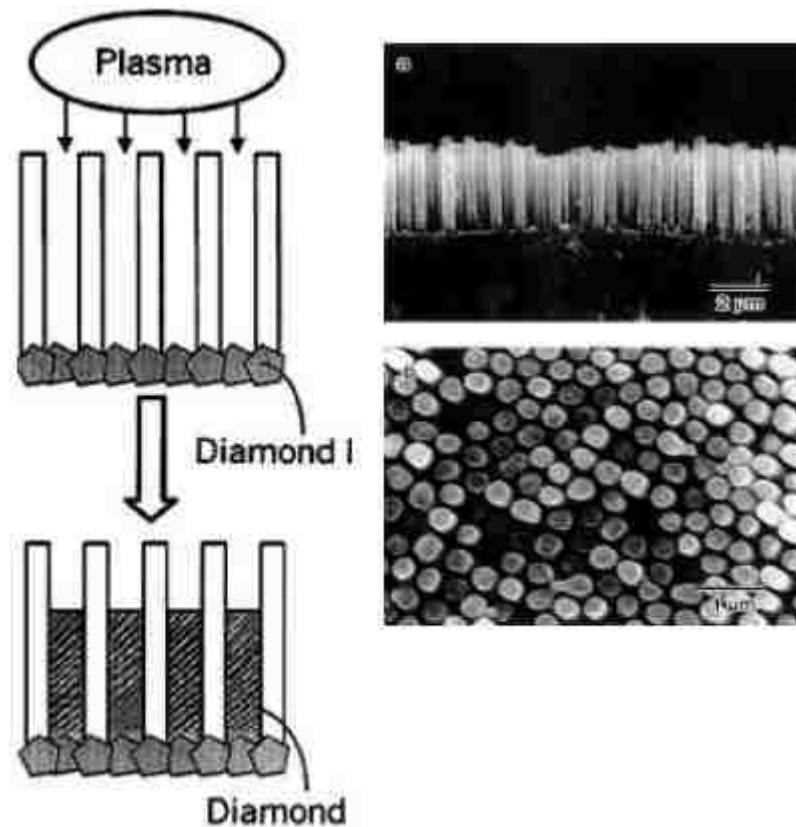


Fig 7-4. Mask deposition of diamond nanowires. Left: scheme, right: SEM image. Ref[3]

However, these methods have their inherent drawbacks. For example, in a top-down approach, the mask has to be perfectly aligned with the substrate and lithographic equipment can be costly. The bottom-up CVD approach also requires complex setup and rises a cost concern as well. In addition, both of them are surface techniques that are difficult to scale up.

In order to go around these limitations, we proposed a novel route using the high pressure nanocasting concept to provide an efficient and scalable method for producing individual free standing diamond nanowires. The concept of high-pressure nanocasting was introduced in chapter 5 where a mesostructured nanocomposite is used as the precursor in an HPHT experiment to obtain a high-pressure phase material with periodically ordered structures. In such a process, one phase remains stable to act as the supporting material while the other phase is transformed into a high pressure phase. Up to date, this concept has been applied only to the synthesis of high pressure SiO_2 materials, such as periodic mesoporous stishovite[17], periodic mesoporous coesite[18], periodic mesoporous quartz[19], and periodic mesoporous aluminosilica[20]. It is worthwhile to investigate whether this concept can be extended to one-dimensional carbon structures.

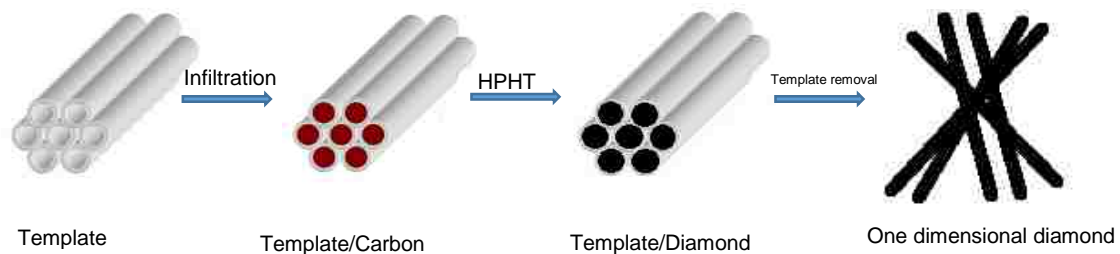


Fig 7-5. Proposed synthetic scheme for 1D diamond nanostructures.

Herein, a simple synthetic scheme to produce one-dimensional diamond nanostructures by the high-pressure nanocasting concept as illustrated in Fig 7-5 is presented. First, a template with cylindrical channels is chosen and filled with a carbon precursor. Afterwards, the template/carbon composite is treated at HPHT conditions, where carbon is transformed into diamond and the template remains unchanged. Finally, the template is etched from the template/diamond

composite to obtain pure one-dimensional diamond nanowires. Anodized aluminum oxide (AAO) is chosen as the template as it has well-defined hexagonal, non-interconnected, porous channels that would be optimal for producing diamond nanowires. Before HPHT treatment, AAO can be converted to the most stable alpha-alumina phase to ensure the one-dimensional structure does not undergo phase transformations during the high pressure experiment. Polyaromatic mesophase pitch is chosen as the carbon source as it can yield dense, non-microporous carbon, so that there is minimal morphological change during the phase transition reaction.

7.2 Materials and experimental procedures

The ACSAAO50 template was purchased from ACS Materials and used without further treatment. The as-obtained AAO membranes are transparent circular disks with 1.2 cm diameter and a thickness of 50 μm . Inspected by SEM, the one-dimensional pore channels are packed in a hexagonal order and the pore diameter is 50 nm as shown in Fig 7-6 and 7-7.

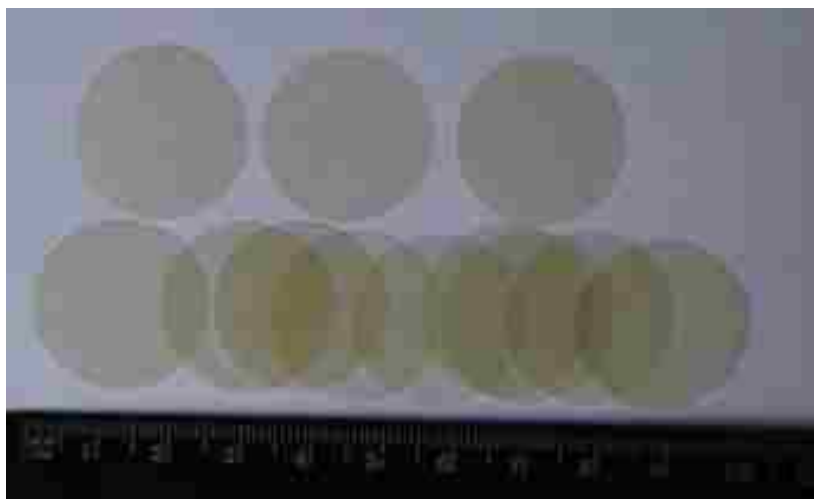


Fig 7-6. The Double-Pass AAO Templates obtained from ACS materials.

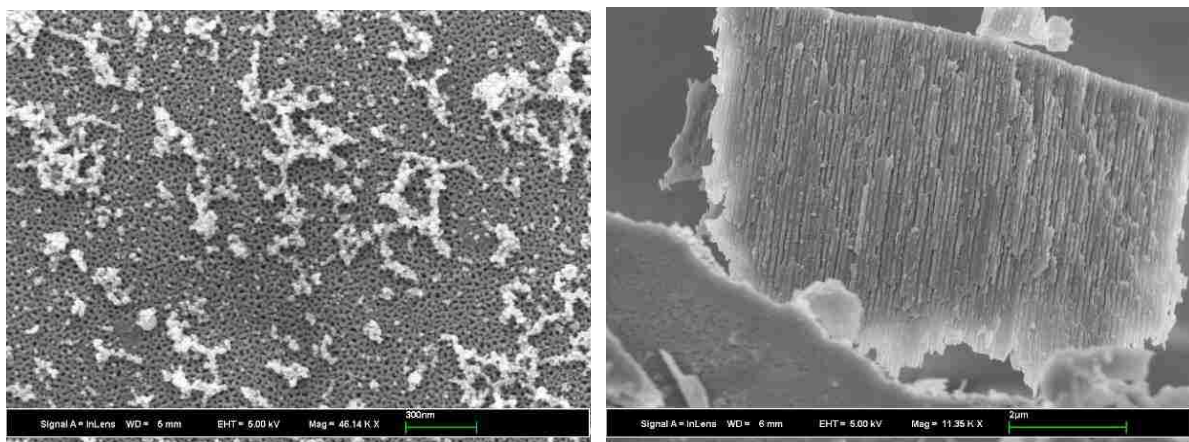


Fig 7-7. SEM image of top (left) and cross-sectional (right) view of ACSAAO50 template.

Mesophase AR pitch from Mitsubishi Gas Chemical, Inc. was used as the carbon source. 0.2g of AAO template was crushed into a powder, then mixed with 0.052 g mesophase pitch and ground. Then, the mixture was transferred into a vial with 10 mL ethanol added. The vial was sonicated for 30 mins and stirred at 40 °C overnight to evaporate the ethanol. The mass of mesophase pitch was chosen according to the pore volume of AAO template, so it can infiltrate the pore channels effectively. The composite was then heated up to 302 °C under nitrogen atmosphere with a heating rate of 1 °C/min and kept for 3 hours to allow the mesophase pitch to melt and infiltrate into the template pores. The composite was further heated up to 850 °C at a rate of 5 °C/min and kept for 2 hours for the carbonization of mesophase pitch.

The AAO/C composite was then investigated by SEM and gas adsorption isotherm for pore filling. The nitrogen adsorption isotherm result is plotted in Fig 7-9. According to the isotherm, the BET surface area of the AAO template was 320 m²/g, and the surface area dropped to 3.9 m²/g after carbon precursor was filled to the template, which indicates that the infiltration process was

effective. In addition, the SEM images in Fig 7-8 also show that the carbon precursor had infiltrated into the pore structure of the AAO templates.

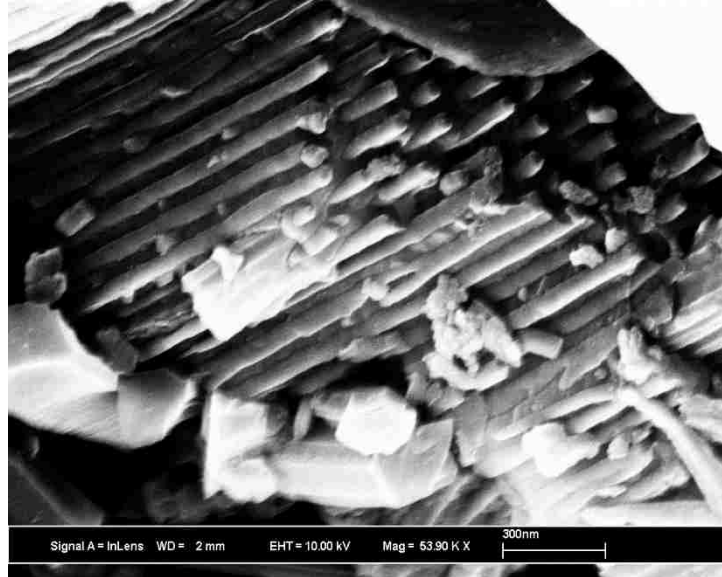


Fig 7-8. SEM image of AAO/C composite

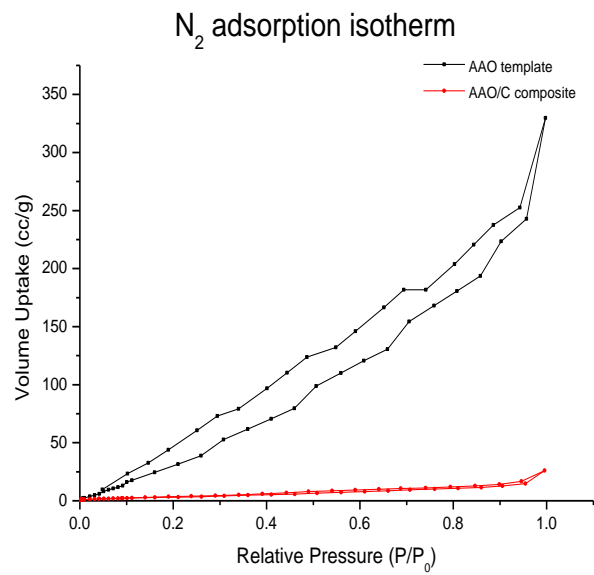


Fig 7-9. N₂ adsorption isotherm of the AAO template before and after the infiltration of mesophase pitch.

Afterwards, the composite was heated up 1300°C for 2h under argon atmosphere to convert aluminum oxide in the composite into the alpha phase. Since α -alumina is thermodynamically stable at high-pressure and does not make phase transformations, it is expected that the template will remain stable during the HPHT reaction. The XRD of the materials in Fig 7-10 confirmed the α -alumina and the morphology of the composite remained unchanged after the treatment, as suggested by SEM images in Fig 7-11.

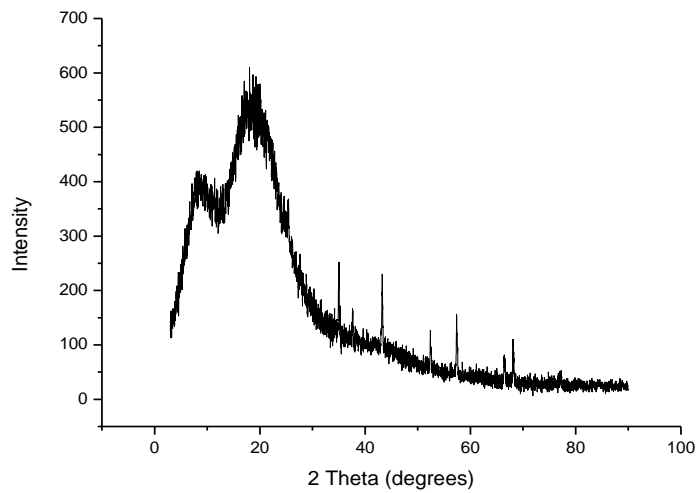


Fig 7-10. XRD of AAO/C composite before HPHT. The diffraction peaks correspond to alpha-alumina (PDF 46-1212).

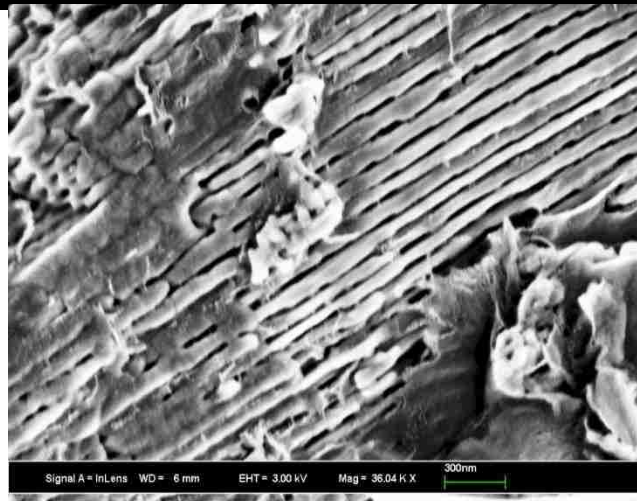


Fig 7-11. AAO/C composite after heat treatment at 1300 °C.

After characterization, the AAO/C composite was then used as the precursor for HPHT studies. The experiments were carried out in a multi-anvil apparatus as described in chapter 5. The pressure was ramped up to the designated pressure with a ramping rate of 2 GPa/h at room temperature and was then heated to the designated temperature at a heating rate of 50 °C/min. The samples were treated for 3h at the final temperature. After the experiment, the sample was quenched and the pressure released at a rate of 2 GPa/h. Then, the sample was extracted from the capsule. These experiments were done in a collaborative effort with Dr. Manik Mandal, whereby I prepared the precursor material and characterized the product, while Dr. Mandal performed the high pressure experiments at Carnegie Institution of Washington.

7.3 Product characterization and analysis

The gas adsorption isotherm in this project was measured with Quantachrome AS-1 surface area and pore size analyzer, with the sample heated to 200 °C for 2 hours under vacuum before measurement. XRD pattern was acquired on an imaging plate using Rigaku Miniflex benchtop XRD. The sample was crushed into powders and loaded onto a zero background sample holder made of single-crystalline silicon. Copper K α radiation was used. The SEM images were recorded with a Zeiss LEO 1550 with a Schottky field emission electron source. For the best dispersion, the sample was ground in acetone and drop cast onto a copper grid supported carbon film, and later coated with a 5 nm Iridium layer for conductivity.

7.3.1 Treatment of sample at 14GPa and 1300°C

In the first attempt, the AAO/C composite was treated at the pressure of 14 GPa and 1300°C for 3 hours since diamond nanocrystals have been obtained at similar conditions previously [21, 22].

After the experiment, the product investigated by XRD to check for diamond formation during the HPHT process. According to the diffraction pattern in Fig 7-12, diamond is absent, which suggests that diamond did not form under such pressure and temperature conditions. All the peaks in the spectrum could be assigned to alpha alumina peaks (2θ equals 25° , 34° , 37° , 43° , 52° , 57° , 66° , 68° , 76°).

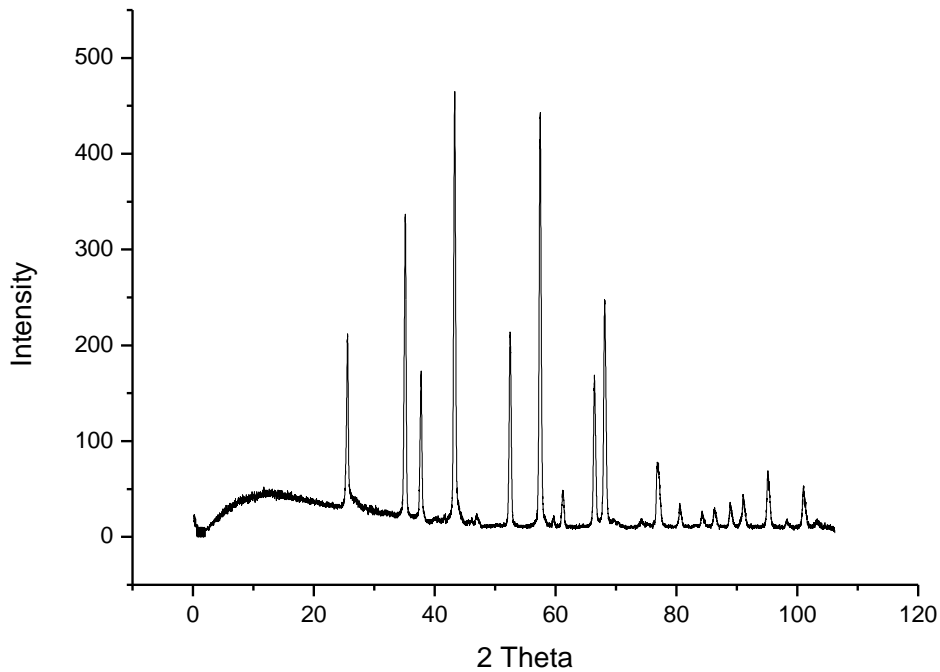


Fig 7-12. AAO/C composite after 14 GPa and 1300 °C.

7.3.2 Treatment of composite at 14 GPa and 1600 °C

In another attempt, the temperature of the HPHT experiment was increased to 1600°C while other conditions were kept the same. The aim of the temperature increase was to promote the reactivity of the diamond precursor during the high pressure conditions. According to the XRD pattern in Fig 7-13, the AAO/C had transformed into an AAO/Diamond composite at the condition of 1600°C and 14 GPa. Due to instrument limitations, the scan was limited up to $2\theta = 60^\circ$, but

the (111) reflection around 44° is clearly visible. In addition, Raman spectroscopy in Fig 7-14 also shows a strong peak at 1335 cm^{-1} , which is indicative of diamond formation.

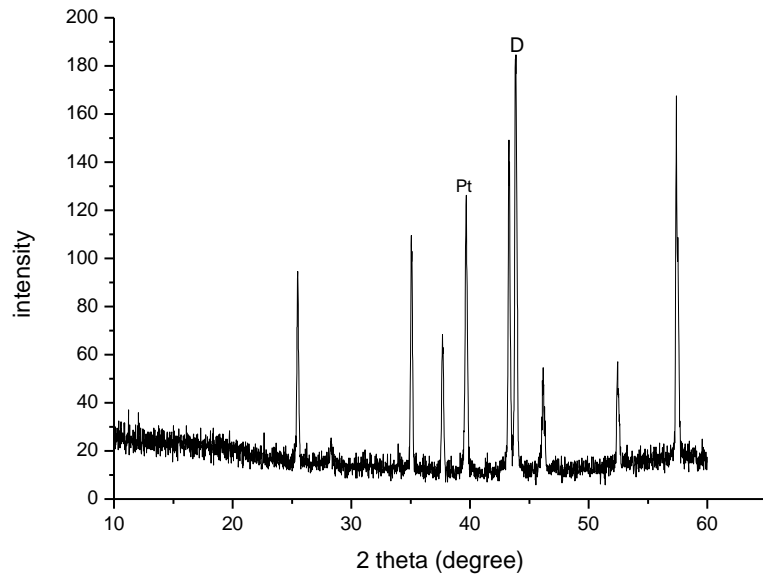


Fig 7-13. XRD of the AAO/diamond composite. D refers to diamond, Pt refers to Platinum, all other peaks can be assigned to alpha alumina (PDF 46-1212).

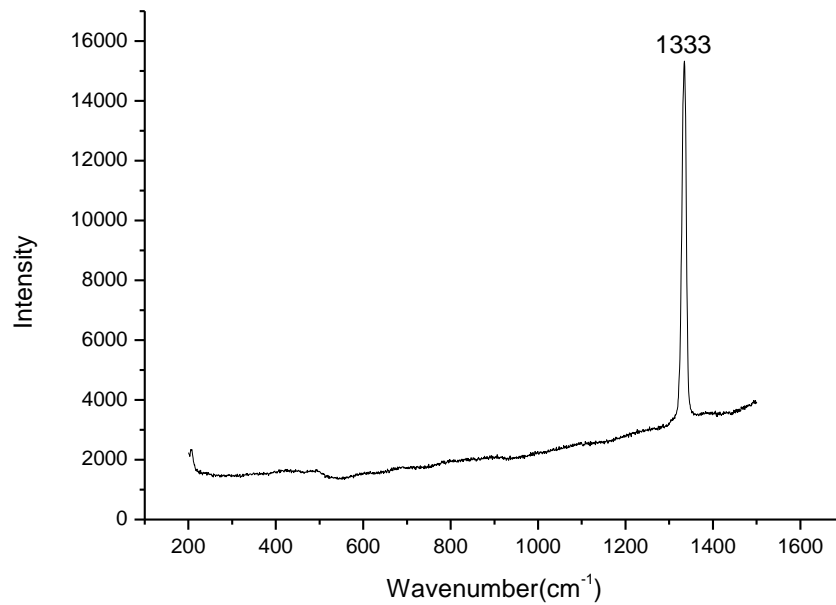


Fig 7-14. Raman spectra of AAO/Diamond after HPHT.

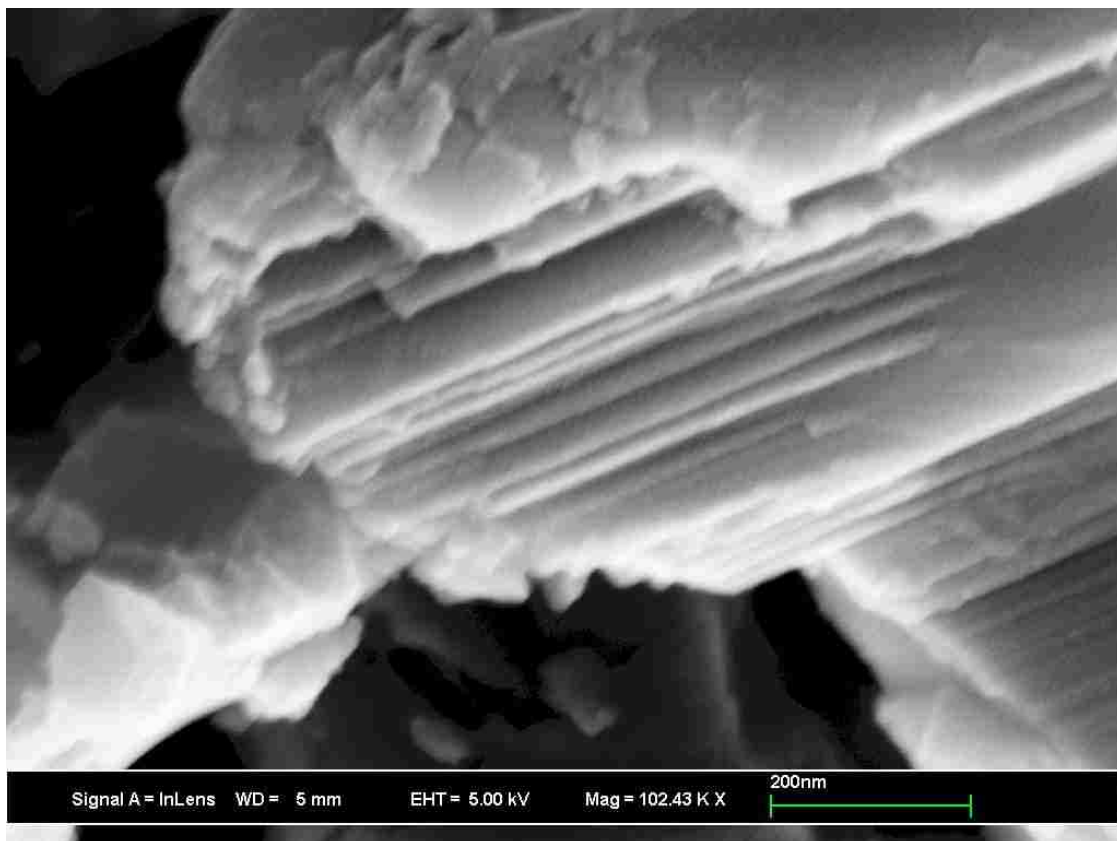


Fig 7-15. SEM of AAO/Diamond composite.

The removal of the AAO template was accomplished by base etching. 100 mg of sample was mixed with 2 g NaOH and transferred into a glassy carbon crucible. The crucible was put into a tube furnace and heated at 550 °C for 3 days under argon flow. Afterwards, the product was taken out, washed with deionized water, and filtered through a fritted glass funnel. The residue from the glass filter was collected. Due to the limited sample amount, only electron microscopy images were taken. As shown in the image in Fig 7-15, the product is monodispersed diamond nanowires with 43 nm diameter. The slight reduction in diameter is expected since diamond has the highest density among carbon polymorphs, therefore the volume could shrink during the phase transformation.

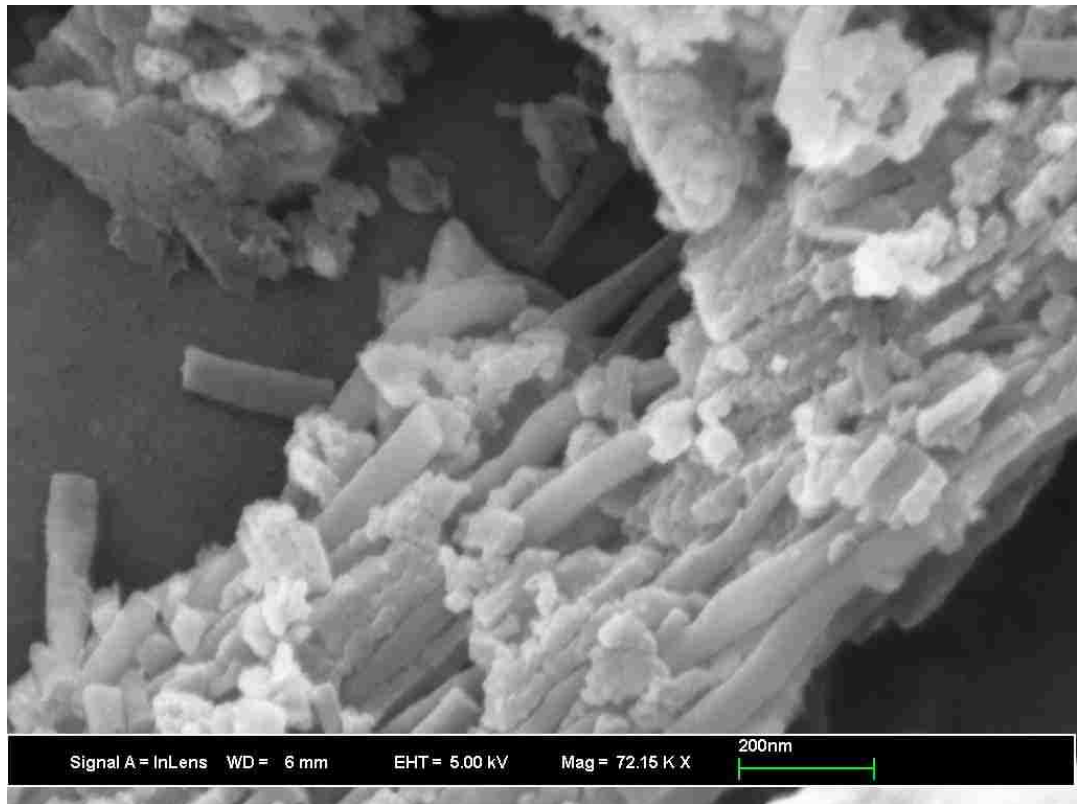


Fig 7-16. SEM image of AAO/Diamond after etching.

7.4 Discussion and conclusions:

It is well demonstrated that ordered mesoporous materials exhibit high activity in many chemical reactions[23-26], as well as in HPHT reactions as introduced in chapter 5. This can be explained by the high surface to volume ratio of the mesoporous materials since the high surface area can lead to a large number of unsaturated surface atoms and active sites.

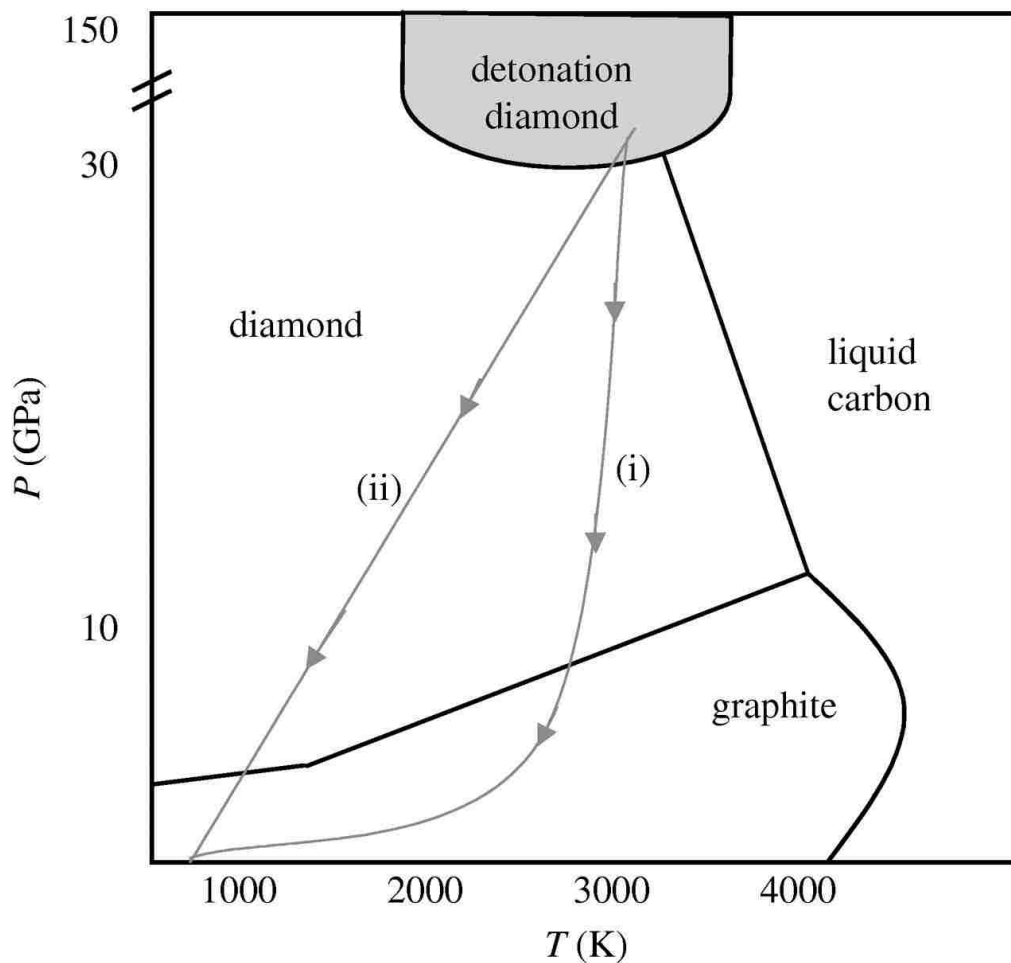


Fig 7-17. Carbon phase diagram. Source: [2]

Unlike the previous discovery that mesoporous carbon can be transformed into diamond at the condition of 14 GPa and 1300 °C, the carbon in the AAO/C composite did not form diamond under the same conditions. As indicated by the phase diagram of carbon in Fig 7-17, such condition is in the stability region of diamond, which indicates the reactivity of AAO/C is lower than mesoporous carbon-like CMK-8[21]. One possible explanation for the reduction of activity could be the lack of surface area from the precursor. Though the AAO and carbon rods have high surface area themselves, the AAO/C composite had a minimal surface area, therefore the reactivity is less than

a pure mesoporous carbon precursor. Upon raising the reaction condition to 14 GPa and 1600 °C, the carbon content in the composite transformed into diamond, which further indicates the lack of surface area has decreased the reactivity.

However, the possibility of synthesizing diamond nanowires at lower temperatures should not be ruled out completely. A similar study was conducted by Peter Pauzauskie et, al. at Lawrence Livermore National labs, where carbon aerogel was pressurized in a diamond anvil cell (DAC) apparatus to obtain diamond aerogels. As a commonly used pressure transmitting medium, neon was filled into the DAC and under such high pressure conditions, neon can flow and infiltrate into the pore system[27], effectively forming a Neon/Carbon composite system. Upon heating to a temperature of 1307 ± 30 °C and pressure greater than 21 GPa, the carbon transformed to diamond with the aerogel morphology maintained. This indicates it is feasible to achieve amorphous to diamond transformation around 1300 °C, though the authors did not explore lowest possible pressure conditions.

In summary, the concept of high pressure nanocasting enables the production of monodisperse diamond nanowires in bulk with the help of a template. Novel scientific and industrial applications are expected of the diamond nanowires due to their high strength and thermal conductivity.

Compared with the surface techniques like CVD and masked etching, the nanocasting route can be scale up more easily. If the pressure and temperature conditions can be lowered by optimization, this method could be potentially useful for synthesizing the diamond wires in larger quantities. This method could be extended to a general and flexible technique to obtain diamond nanostructures that are otherwise hard to achieve. For example, the diameter of the diamond nanowires can be easily adjusted by choosing AAO template with different pore diameters. In addition, by using mesoporous alumina with different pore geometry[28], this method can potentially lead to a corresponding diamond nanostructure.

7.5 Reference

1. Roman, R.E., K. Kwan, and S.W. Cranford, *Mechanical Properties and Defect Sensitivity of Diamond Nanothreads*. Nano Letters, 2015. **15**(3): p. 1585-1590.
2. Holt, K.B., *Diamond at the nanoscale: applications of diamond nanoparticles from cellular biomarkers to quantum computing*. Philosophical Transactions of the Royal Society of London A: Mathematical, Physical and Engineering Sciences, 2007. **365**(1861): p. 2845-2861.
3. Masuda, H., et al., *Synthesis of Well-Aligned Diamond Nanocylinders*. Advanced Materials, 2001. **13**(4): p. 247-249.
4. Masuda, H., et al., *Fabrication of a Nanostructured Diamond Honeycomb Film*. Advanced Materials, 2000. **12**(6): p. 444-447.
5. Zhou, C., et al., *Graphene's cousin: the present and future of graphane*. Nanoscale Research Letters, 2014. **9**(1): p. 1-9.
6. Algar, W.R., A.J. Tavares, and U.J. Krull, *Beyond labels: A review of the application of quantum dots as integrated components of assays, bioprobes, and biosensors utilizing optical transduction*. Analytica Chimica Acta, 2010. **673**(1): p. 1-25.
7. Hu, J., T.W. Odom, and C.M. Lieber, *Chemistry and Physics in One Dimension: Synthesis and Properties of Nanowires and Nanotubes*. Accounts of Chemical Research, 1999. **32**(5): p. 435-445.
8. Wang, Q.H., et al., *Low Dimensional Carbon Materials for Applications in Mass and Energy Transport*. Chemistry of Materials, 2014. **26**(1): p. 172-183.
9. Zhang, H., *Ultrathin Two-Dimensional Nanomaterials*. ACS Nano, 2015. **9**(10): p. 9451-9469.
10. Iijima, S., *Direct observation of the tetrahedral bonding in graphitized carbon black by high resolution electron microscopy*. Journal of Crystal Growth, 1980. **50**(3): p. 675-683.
11. Kroto, H.W., et al., *C₆₀: Buckminsterfullerene*. Nature, 1985. **318**(6042): p. 162-163.
12. Iijima, S., *Helical microtubules of graphitic carbon*. Nature, 1991. **354**(6348): p. 56-58.
13. Novoselov, K.S., et al., *Electric Field Effect in Atomically Thin Carbon Films*. Science, 2004. **306**(5696): p. 666-669.
14. Popov, V.N., *Carbon nanotubes: properties and application*. Materials Science and Engineering: R: Reports, 2004. **43**(3): p. 61-102.
15. Fitzgibbons, T.C., et al., *Benzene-derived carbon nanothreads*. Nat Mater, 2015. **14**(1): p. 43-47.
16. Hiromu, S., *Reactive Ion Etching of Diamond in O₂ and C F₄ Plasma, and Fabrication of Porous Diamond for Field Emitter Cathodes*. Japanese Journal of Applied Physics, 1997. **36**(12S): p. 7745.
17. Stagno, V., et al., *High-pressure synthesis of mesoporous stishovite: potential applications in mineral physics*. Physics and Chemistry of Minerals, 2015. **42**(6): p. 509-515.
18. Mohanty, P., Y. Fei, and K. Landskron, *Synthesis of Periodic Mesoporous Coesite*. Journal of the American Chemical Society, 2009. **131**(28): p. 9638-9639.
19. Mohanty, P., et al., *Large-pore periodic mesoporous silicas with crystalline channel walls and exceptional hydrothermal stability synthesized by a general high-pressure nanocasting route*. Microporous and Mesoporous Materials, 2012. **152**: p. 214-218.
20. Mandal, M., et al., *A high-pressure synthesis of hydrothermally stable periodic mesoporous crystalline aluminosilica materials*. RSC Advances, 2016. **6**(9): p. 7396-7402.

21. Zhang, L., et al., *Catalyst-free synthesis of transparent, mesoporous diamond monoliths from periodic mesoporous carbon CMK-8*. Proceedings of the National Academy of Sciences, 2010. **107**(31): p. 13593-13596.
22. Mandal, M., et al., *Size tunable synthesis of solution processable diamond nanocrystals*. Chemical Communications, 2014. **50**(77): p. 11307-11310.
23. Linares, N., et al., *Mesoporous materials for clean energy technologies*. Chemical Society Reviews, 2014. **43**(22): p. 7681-7717.
24. Corma, A., *From Microporous to Mesoporous Molecular Sieve Materials and Their Use in Catalysis*. Chemical Reviews, 1997. **97**(6): p. 2373-2420.
25. Taguchi, A. and F. Schüth, *Ordered mesoporous materials in catalysis*. Microporous and Mesoporous Materials, 2005. **77**(1): p. 1-45.
26. AlOthman, Z., *A Review: Fundamental Aspects of Silicate Mesoporous Materials*. Materials, 2012. **5**(12): p. 2874.
27. Pauzuskie, P.J., et al., *Synthesis and characterization of a nanocrystalline diamond aerogel*. Proceedings of the National Academy of Sciences of the United States of America, 2011. **108**(21): p. 8550-8553.
28. Mitra, A., D. Jana, and G. De, *A facile synthesis of cubic (Im[3 with combining macron]m) alumina films on glass with potential catalytic activity*. Chemical Communications, 2012. **48**(27): p. 3333-3335.

VITA

Cong Liu was born in Hubei, China. After completing high school, he attended the University of Science and Technology of China in 2005, where he obtained a B.S. in materials science. In 2009, he joined Lehigh University to pursue a Ph.D. degree in chemistry. During the study at Lehigh, he worked on developing a new method for carbon dioxide capture called supercapacitive swing adsorption and synthesizing new nanomaterials by high pressure, high temperature techniques.